Multivariate population balance for turbulent gas-liquid flows

Politecnico di Torino

Department of Applied Science and Technology
Ph.D. in Chemical Engineering
XXV cycle (2010-2012)

MULTIVARIATE POPULATION BALANCE FOR TURBULENT GAS-LIQUID FLOWS

PhD Student

Antonio Buffo

Supervisors
Prof. Daniele Marchisio
Prof. Marco Vanni

Second Referee:
Prof. Giuseppina Montante

Coordinator:
Prof. Vito Specchia

Abstract

This dissertation focuses on the development of computational tools capable of predicting the complex fluid dynamics behavior of industrial scale gas-liquid systems. In the past, the description of such systems for design purposes was performed through the use of correlations, formulated by means of very expensive experimental campaigns. The limits of this approach can be overcome by the use of modern simulation tools, such as Computational Fluid Dynamics (CFD). However the momentum and mass transfer description of gas-liquid systems is characterized by the intrinsic poly-dispersity of the gas phase, namely the different dispersed bubbles are usually distributed over a certain range of size, velocity and chemical composition values. Then a proper methodology must be applied to tackle this issue: Population Balance Modeling (PBM), originally formulated for crystallization problems, can be successfully adopted to describe any generic dispersed system in which the combination of different phenomena (i.e., physical space advection, diffusion, aggregation, breakage, growth, nucleation) determines the state of the dispersed system.

All these considerations explain the interest of the multiphase flow community in efficient coupled PBM-CFD methods, especially when such methodologies are employed to investigate large scale systems with complex phenomena involved, such as mass transfer and chemical reactions. Moreover, the knowledge of more than one property of the disperse phase can be required to properly describe the problem (i.e., multivariate description instead of monovariate), as in the case of reacting multiphase systems, and this fact represents a challenge from the modeling point of view. At this point, it is very important to reduce the computational costs introduced by the Population Balance Equation (PBE), by recurring to approximate but reliable methods. In this sense, it is also recent the formulation of Quadrature-Based Moments Methods (QBMM) for particulate flows, a class of solution methods particularly suitable for the purposes of this work. Therefore in this dissertation the issues related to the application of these methods for the description of industrial scale bubble columns and aerated stirred tank reactors will be discussed.

In the first part of this work, the derivation of PBE and the Eulerian-Eulerian methodology for gas-liquid systems is shown, especially concerning the description of the mass transfer problem in air-water system, in which the information on the bubble size distribution is needed to estimate the interfacial area and the distribution of bubble composition may be required to calculate the local mass transfer driving force. Moreover the QBMM solution methods, both for monovariate and multivariate cases, are here presented and dis-

cussed in detail. In the second part, a preliminary study of QBMM stability and accuracy for simplified zero-dimensional systems is performed through comparison with accurate PBE solution methods, then the implementation is verified through the simulation of one and two-dimensional systems in order to point out the numerical issues than may arise when physical space advection is considered. Eventually, the simulation of realistic gas-liquid systems (i.e., a stirred tank reactor and a bubble column), for which experimental data are available relating to the local bubble size distribution (BSD) and mass transfer, are performed for validation purposes. The shown results prove the effectiveness of the proposed PBM-CFD approach: in general a very good agreement with the experimental data is observed with a reasonable computational costs.

Contents

Chapter 1

Introduction

Turbulent gas-liquid flows are very common in the chemical, pharmaceutical, food and biochemical industries. Many gas-liquid reactions, such as oxidation, hydrogenation, halogenation and biological fermentation are usually performed in aerated stirred tank reactors and bubble columns. Turbulent flow conditions, under which most of these processes are carried out, are essential to improve the overall performance, increasing the gas dispersion and enhancing heat and mass transfer rates.

The engineering approach on design and scale-up of these systems is historically based on many empirical or semi-empirical correlations formulated by means of numerous experiments performed through the last sixty years. However, the limitations of this approach may be several: first, the use of correlations for estimating heat and mass transfer rates is restricted to specific vessel geometries and operating conditions close to those under which they were derived. Second, these correlations are usually based on well-mixed models, considering only volume-averaged quantities over the entire equipment and neglecting the effect of spatial inhomogeneities that may exist even in small scale vessels. The last aspect one has to consider is that the optimization of these gas-liquid systems through standard correlations and experimental campaigns is usually very time consuming and expensive.

Gas-liquid systems are usually characterized by the interactions between the continuous phase and the disperse phase, and between the different bubbles constituting the disperse phase. These interactions can be classified as continuous or discontinuous depending on the time and length scale chosen to observe the system: a continuous process will result, considering an infinitesimal time scale, in an infinitesimal change of properties of the dispersion, whereas a discontinuous event leads to a finite change of the system status. The dynamics of aerated stirred tank reactors is an illuminating example: on one hand bubble coalescence and breakage events "instantaneously" modify the local interfacial area determining the volumetric mass transfer coefficient ($k_L a$), and on the other one mass transfer continuously changes the composition of liquid phase until the equilibrium is reached. Moreover, the relationship between these phenomena and the fluid dynamics of the system should not be ignored, because it is the reason behind the different flow regimes usually studied.

Another aspect to consider is the local nature of the interactions between the different

phases. The example of gas-liquid stirred reactors is here always relevant: in fact, the Bubble Size Distribution (BSD) varies from point to point in the vessel according to the flow conditions imposed by the stirrer motion. As a consequence of such flow pattern, bubbles near the impeller break-up due to the high shear experienced and the BSD is skewed towards lower diameters, whereas bubbles accumulate and coalesce in stagnant zones, resulting in a BSD shifted to larger bubble diameters. Very different conditions take place in gas-liquid bubble columns, where the complex oscillating motion of the dispersion is completely determined by the interaction between the rising bubbles and the surrounding fluids. Furthermore, every single bubble has its own size, velocity and composition and, in order to correctly predict the evolution in space and time of the disperse phase, including local and global mass transfer fluxes, all these issues related to the local fluid dynamic behavior must be addressed.

In the latest years, with the rapid increasing of computing power, Computational Fluid Dynamics (CFD) emerged as an essential tool for the study and design of the industrial scale equipments. While for the single-phase systems only few aspects still need to be clarified, gas-liquid flow modeling represents an open challenge: since for such system a trivial extension of single phase models is not feasible, different approaches for different purposes are formulated and discussed in the literature (for a complete review see van Wachem and Almstedt, 2003). Tracking-interface methods are able to capture with good approximation the evolution of the gas-liquid interface, but they can be used only for small regions of large systems and just including a few bubbles inside. Lagrangian-Eulerian methods allow the evaluation of the motion of larger number of bubbles in a continuous media, however this number may not be sufficient to simulate most of practical cases. With Eulerian-Eulerian methods, both gas and liquid phases are treated as continuous interpenetrating media through volume fractions, and this approach is suitable for the study of industrial problems with realistic geometries.

In order to obtain an accurate description of a multiphase system, an important role is played by the phase-coupling terms. Many studies have been conducted on interfacial forces (like drag, virtual mass, lift, Basset and turbulent dispersion forces) acting on bubbles or swarms of bubbles. As observed in the work of Scargiali et al. (2007), in aerated stirred tanks the drag force gives the most important contribution in determining the local gas hold-up, whereas all the other forces are negligible. Different models considering the rise of a bubble in a stagnant liquid are present in literature for the estimation of drag force (Tomiyama et al., 1998; Deen et al., 2002; Scargiali et al., 2007) and the effect of turbulence on terminal velocity or drag coefficient has been also accounted for (Bakker and Van den Akker, 1994; Lane et al., 2005). Recently a drag law formulated in terms of the terminal velocities, exposed by Montante et al. (2007), has been modified in order to account for both turbulence and the presence of other bubbles, and was proven to be capable of describing flow transitions between different regimes (Petitti et al., 2009). For bubble columns, on the contrary, all the phase-coupling terms may play an important role in the fluid dynamic description as experimentally observed by Deen et al. (2001), although from the modeling point of view there are still some issues about their relative importance (Diaz et al., 2008). Fur-

thermore, turbulence modeling in both cases plays an important role in the prediction of the multiphase flow: Large Eddy Simulation (LES) and Direct Numerical Simulation (DNS) were successfully applied to bubbly flows (Derksen and Van den Akker, 1999; Hartmann et al., 2004), but they are typically used to simulate small scale systems due to their computational cost. For this reason, the well-known Reynolds-Averaged Navier-Stokes equation (RANS) approach has been adapted to gas-liquid systems (Lopez de Bertodano and Saif, 1997), since it is now well established in the simulation of industrial equipments, with or without terms accounting for bubble turbulence (Zhang et al., 2006).

It should be highlighted that in past studies the bubble population was usually described by resorting to a non-physical mono-disperse bubble size distribution, constant in space and time, with optimal bubble size chosen by a tedious fitting procedure. The presence of a BSD was firstly considered by Bakker and Van den Akker (1994), who formulated a balance for the number of bubbles that undergo coalescence and breakage in a gas-liquid stirred tank; this model is based on the solution of an additional equation for the bubble number density with one-way coupling between gas and liquid, considering bubbles collisions with a very simplified approach based on the critical Weber number. With this approach, the local bubble size may be different from point to point in the domain, but in every single point a nonphysical mono-disperse distribution is still considered. Almost at the same time, the mathematical framework of Population Balance Equation (PBE), originally formulated for crystallization and spray systems, was generalized to other dispersed systems (Ramkrishna, 2000). With this equation is possible to track the evolution of the disperse phase not only in physical space, but also in the space generated by the considered properties of the population (traditionally referred to as internal coordinates). Different formulation exists, namely monovariate and multivariate PBEs. In the first case only one internal coordinate is sufficient for describing the state of the dispersed system, while in the second case two or even more coordinates are adopted. The aforementioned continuous and discontinuous processes typical of gas-liquid systems, find with this method a proper phenomenological and deterministic description through the formulation of probabilities and rates for bubble-bubble and bubble-eddy interactions, contributing to determine the evolution of the bubble distribution ad its physical properties in space and time.

However, due to its complex integro-differential form, the solution of the PBE is not straightforward, especially when the model is complicated by the fact that more than one bubble property is considered and spatial inhomogeneities are introduced. Most of the developed methods for solving the PBE belong to one of the following groups: classes or sectional, Monte Carlo and moment-based methods. The first group the PBE is solved by discretizing internal coordinates space: the Classes Methods (CM) were firstly developed for the solution of monovariate cases, in which the state of the population is characterized by a single property or variable (Kostoglou and Karabelas, 1994; Vanni, 2000) and were recently extended to multivariate cases, in which two or more variables are needed for describing the disperse system (Kumar et al., 2008; Nandanwar and Kumar, 2008). The main drawback of these methods is the high computational costs required to obtain an acceptable

accuracy, when also the inhomogeneities in the physical space are taken into account. It is worth mentioning that Finite Volume Methods (Gunawan et al., 2004) and Finite Element Methods (Godin et al., 1999) belong to the group of classes methods and hence they, too, show the aforementioned limitations in the applicability to realistic inhomogeneous cases. Monte Carlo Methods (MCM) are based on the solution of stochastic differential equations that are able to reproduce a finite number of artificial realizations of the system under investigation (Zhao et al., 2007). In order to have a solution very close to reality, the number of artificial realizations is often very high, resulting in unsustainable computational costs. For this reason, these methods are usually employed for validation (Zucca et al., 2007) in simplified cases.

The Method of Moments was originally formulated and applied to particulate systems in the pioneering work of Hulburt and Katz (1964). The idea behind this method is the integration of the PBE in the space of the internal coordinates, leading to a set of equations that can be solved only for some lower-order moments. For realistic processes, it is not always possible to write the governing equations in terms of the moments themselves, generating what is known as "closure problem"; many closures were proposed in order to overcome this issue and our work is focused on a particular class of methods called Quadrature-Based Moments Methods (QBMM), in which the Number Density Function (NDF) representing the population is assumed to be a summation of some basis function (very often Dirac delta functions) centered on the zeros of the orthogonal polynomials of a Gaussian Quadrature. Although the quadrature approximation is always very accurate, comparison with alternative methods (Marchisio et al., 2003b; Zucca et al., 2007) is always suggested when different processes are considered in the description. In general, acceptable accuracy can be achieved with a very low number of nodes ($N \leq 4$) (Marchisio et al., 2003b; Marchisio and Fox, 2005). The main advantage of QBMM is represented by the possibility to be coupled with CFD solvers, and so they are capable of describing industrial scale systems characterized by strong spatial heterogeneity and a high degree of poly-dispersity in the internal coordinates with an optimal balance between accuracy and computational costs (Marchisio et al., 2003a; Fan et al., 2004; Zucca et al., 2006; Petitti et al., 2010).

QBMM can be subdivided into two main groups: in the former the evolution of moments is calculated and the quadrature approximation is determined through a specific inversion algorithm; in the latter the quadrature (in terms of its weights and nodes) is directly evolved in space and time by mimicking the evolution of some moments. For monovariate PBE, these two methods correspond to the quadrature method of moments (QMOM) (McGraw, 1997) and to the direct quadrature method of moments (DQMOM) (Marchisio and Fox, 2005), respectively. For multivariate PBE, DQMOM can be easily extended, while QMOM, with its standard inversion algorithms, can not be used as it is not capable of dealing with the mixed-order moments that arise from multivariate populations. Among the recently proposed inversion algorithms for multivariate problems (Brute-Force, Wright et al. (2001); Tensor Product, Yoon and McGraw (2004b,a); Fox (2009); Conditional Quadrature Method of Moments, CQMOM, Yuan and Fox (2011)), CQMOM was proven to perform excellently.

As far as the coupling to Computational Fluid Dynamics (CFD) codes is concerned, some issues for both methods still need to be addressed. The generation of invalid sets of moments may arise with QMOM/CQMOM when high-order spatial discretization schemes are used for transporting the moments of the NDF (Wright Jr, 2007). A set of moments is valid if there exists a NDF resulting in that specific set of moments: in this way the calculated nodes are always in the domain of internal-coordinate space and the weights are always positive. If the inversion algorithm were used with invalid moment sets, unrealizable quadratures would be calculated (because no realizable NDF corresponds to an invalid set), jeopardizing the stability of the simulation. Wright Jr (2007) proposed an iterative algorithm to correct a corrupted set of moments, based on the convexity principle, but this algorithm is only capable to restore the set, not to prevent and solve the corruption problem. Recently Vikas et al. (2011) introduced a class of high-order numerical schemes, based on the kinetic finite volume schemes, that guarantees the realizability of a set of moments. DQMOM does not exhibit the corruption problem (Marchisio and Fox, 2005), since the resulting moments tracked by the method will always be realizable as long as the weights are non-negative, but, under certain conditions, the method may be unable to calculate properly the moments. In fact, if the moment transport equation is purely hyperbolic (i.e. pure advection of the NDF) or there are spatial discontinuities in the quadrature, the spatial continuity assumption used to derive the method is no more valid and DQMOM fails (Mazzei et al., 2010, 2012). Even if the spatial solution is smooth, problems may arise whenever the moment transport equation contains spatial diffusion terms that are smaller than or comparable with the numerical diffusion that every Finite-Volume scheme (FV) introduces. In fact, in this case the correction proposed by Marchisio and Fox (2005) is difficult to be calculated since the numerical diffusion coefficient cannot be determined accurately. Very recently, a slight modification of the DQMOM formulation, the so-called DQMOM-Fully Conservative (Buffo et al., 2013), was proposed allowing the proper solution in space of the evolution of important conservative quantities as moments of NDF.

Although the coupled CFD-QBMM methodology can be applied to any dispersed multiphase system, the focus of this work, as previously pointed out, is on turbulent gas-liquid systems, in which spatial inhomogeneities, bubble collisions and mass transfer play an important role in the determination of the state of the system. In such a system the mass transfer rate strongly depends on the size of the bubbles (mass transfer from small bubbles is faster than for larger ones) and at least a second internal coordinate related to the bubble composition is needed in addition to bubble size, in order to determine accurately the evolution of the population. Therefore this dissertation is organized as follows:

- in Chapter 2 the generalized population balance framework is introduced, with particular attention to specific characteristics of gas-liquid systems. Moreover the solution algorithms used are here presented and discussed in detail;

- in Chapter 3 an overview of CFD methodology for gas-liquid systems including the treatment of phase coupling and turbulence is given. Furthermore, the details relating

to the coupling of QBMM with CFD are reported;

- in Chapter 4 the results of a preliminary study of QBMM stability and accuracy for simplified spatially zero-dimensional systems are shown, revealing the pros and cons of different multivariate methods compared with a detailed Monte Carlo solution. Also a very simple mono-dimensional system is examined, in order to point out the difficulties that may arise when the advection in physical space is considered.

- in Chapter 5 results of the implementation of QBMM for realistic systems are shown. A two-dimensional bubble column is investigated for model verification purposes. Moreover, the results obtained in the simulation of experimentally studied systems, a stirred tank reactor (Laakkonen et al., 2006) and a partially aerated rectangular bubble column (Cachaza Gianzo, 2011), are eventually validated.

References

Bakker, A., Van den Akker, H., 1994. Gas-liquid contacting with axial flow impellers. Chemical Engineering Research and Design 72, 573–582.

Lopez de Bertodano, M.A., Saif, A.A., 1997. Modified k-ϵ model for two-phase turbulent jets. Nuclear Engineering and Design 172, 187–196.

Buffo, A., Vanni, M., Marchisio, D., Fox, R.O., 2013. Multivariate quadrature-based moments methods for turbulent polydisperse gas-liquid systems. International Journal of Multiphase Flow 50, 41–57.

Cachaza Gianzo, E.M., 2011. Hydrodynamics and mass transfer effects in bubble columns. Ph. D. Thesis. Universidad de Salamanca. Salamanca, Spain.

Deen, N., Solberg, T., Hjertager, B., 2001. Large eddy simulation of the gas-liquid flow in a square cross-sectioned bubble column. Chemical Engineering Science 56, 6341–6349.

Deen, N., Solberg, T., Hjertager, B., 2002. Flow generated by an aerated rushton impeller: two-phase PIV experiments and numerical simulations. Canadian Journal of Chemical Engineering 80, 1–15.

Derksen, J., Van den Akker, H.E.A., 1999. Large eddy simulations on the flow driven by a rushton turbine. American Institute of Chemical Engineering Journal 45, 209–221.

Diaz, M.E., Montes, F.J., Galan, M.A., 2008. Experimental study of the transition between unsteady flow regimes in a partially aerated two-dimensional bubble column. Chemical Engineering and Processing 47, 1867–1876.

Fan, R., Marchisio, D.L., Fox, R.O., 2004. Application of the direct quadrature method of moments to polydisperse gas–solid fluidized beds. Powder Technology 139, 7–20.

Fox, R.O., 2009. Optimal moment sets for multivariate direct quadrature method of moments. Industrial & Engineering Chemistry Research 48, 9686–9696.

Godin, F.B., Cooper, D.G., Rey, A.D., 1999. Numerical methods for a population-balance model of a periodic fermentation process. American Institute of Chemical Engineering Journal 45, 1359–1364.

Gunawan, R., Fusman, I., Braatz, R.D., 2004. High resolution algorithms for multidimensional population balance equations. American Institute of Chemical Engineering Journal 50, 2738–2749.

Hartmann, H., Derksen, J., Montavon, C., Pearson, J., Hamill, I., van den Akker, H., 2004. Assessment of large eddy and RANS stirred tank simulations by means of LDA. Chemical Engineering Science 59, 2419–2432.

Hulburt, H., Katz, S., 1964. Some problems in particle technology: A statistical mechanical formulation. Chemical Engineering Science 19, 555–574.

Kostoglou, M., Karabelas, A., 1994. Evaluation of zero order methods for simulating particle coagulation. Journal of Colloid and Interface Science 163, 420–431.

Kumar, J., Peglow, M., Warnecke, G., Heinrich, S., 2008. The cell average technique for solving multi-dimensional aggregation population balance equations. Computers and Chemical Engineering 32, 1810–1830.

Laakkonen, M., Alopaeus, V., Aittamaa, J., 2006. Validation of bubble breakage, coalescence and mass transfer models for gas–liquid dispersion in agitated vessel. Chemical Engineering Science 61, 218–228.

Lane, G., Schwarz, M., Evans, G., 2005. Numerical modelling of gas-liquid flow in stirred tanks. Chemical Engineering Science 60, 2203–2214.

Marchisio, D.L., Dennis Vigil, R., O. Fox, R., 2003a. Implementation of the quadrature method of moments in CFD codes for aggregation–breakage problems. Chemical Engineering Science 58, 3337–3351.

Marchisio, D.L., Fox, R.O., 2005. Solution of population balance equations using the direct quadrature method of moments. Journal of Aerosol Science 36, 43–73.

Marchisio, D.L., Vigil, R., Fox, R.O., 2003b. Quadrature method of moments for aggregation–breakage processes. Journal of Colloid and Interface Science 258, 322–334.

Mazzei, L., Marchisio, D.L., Lettieri, P., 2010. Direct quadrature method of moments for the mixing of inert polydisperse fluidized powders and the role of numerical diffusion. Industrial & Engineering Chemistry Research 49, 5141–5152.

Mazzei, L., Marchisio, D.L., Lettieri, P., 2012. New quadrature-based moment method for the mixing of inert polydisperse fluidized powders in commercial CFD codes. American Institute of Chemical Engineering Journal 58, 3054–3069.

McGraw, R., 1997. Description of aerosol dynamics by the quadrature method of moments. Aerosol Science and Technology 27, 255–265.

Montante, G., Paglianti, A., Magelli, F., 2007. Experimental analysis and computational modelling of gas - liquid stirred vessels. Chemical Engineering Research and Design 85, 647–653.

Nandanwar, M.N., Kumar, S., 2008. A new discretization of space for the solution of multi-dimensional population balance equations. Chemical Engineering Science 63, 2198–2210.

Petitti, M., Marchisio, D., Vanni, M., Baldi, G., Mancini, N., Podenzani, F., 2009. Effect of drag modeling on the prediction of critical regime transitions in agitated gas-liquid reactors with bubble size distribution modeling. Multiphase Science and Technology 21, 95–106.

Petitti, M., Nasuti, A., Marchisio, D.L., Vanni, M., Baldi, G., Mancini, N., Podenzani, F., 2010. Bubble size distribution modeling in stirred gas–liquid reactors with QMOM augmented by a new correction algorithm. American Institute of Chemical Engineering Journal 56, 36–53.

Ramkrishna, D., 2000. Population Balances: Theory and Applications to Particulate Systems in Engineering. Academic Press, San Diego (CA), USA. 1 Edition.

Scargiali, F., D'Orazio, A., Grisafi, F., Brucato, A., 2007. Modelling and simulation of gas - liquid hydrodynamics in mechanically stirred tanks. Chemical Engineering Research and Design 85, 637–646.

Tomiyama, A., Kataoka, I., Zun, I., Sakaguchi, T., 1998. Drag coefficients of single bubbles under normal and micro gravity conditions. JSME international journal. Ser. B, Fluids and thermal engineering 41, 472–479.

Vanni, M., 2000. Approximate population balance equations for Aggregation–Breakage processes. Journal of Colloid and Interface Science 221, 143–160.

Vikas, V., Wang, Z., Passalacqua, A., Fox, R., 2011. Realizable high-order finite-volume schemes for quadrature-based moment methods. Journal of Computational Physics 230, 5328–5352.

van Wachem, B., Almstedt, A., 2003. Methods for multiphase computational fluid dynamics. Chemical Engineering Journal 96, 81–98.

Wright, D.L., McGraw, R., Rosner, D.E., 2001. Bivariate extension of the quadrature method of moments for modeling simultaneous coagulation and sintering of particle populations. Journal of Colloid and Interface Science 236, 242–251.

Wright Jr, D.L., 2007. Numerical advection of moments of the particle size distribution in eulerian models. Journal of Aerosol Science 38, 352–369.

Yoon, C., McGraw, R., 2004a. Representation of generally mixed multivariate aerosols by the quadrature method of moments: I. statistical foundation. Journal of Aerosol Science 35, 561–576.

Yoon, C., McGraw, R., 2004b. Representation of generally mixed multivariate aerosols by the quadrature method of moments: II. aerosol dynamics. Journal of Aerosol Science 35, 577–598.

Yuan, C., Fox, R.O., 2011. Conditional quadrature method of moments for kinetic equations. Journal of Computational Physics 230, 8216–8246.

Zhang, D., Deen, N., Kuipers, J., 2006. Numerical simulation of the dynamic flow behavior in a bubble column: A study of closures for turbulence and interface forces. Chemical Engineering Science 61, 7593–7608.

Zhao, H., Maisels, A., Matsoukas, T., Zheng, C., 2007. Analysis of four monte carlo methods for the solution of population balances in dispersed systems. Powder Technology 173, 38–50.

Zucca, A., Marchisio, D.L., Barresi, A.A., Fox, R.O., 2006. Implementation of the population balance equation in CFD codes for modelling soot formation in turbulent flames. Chemical Engineering Science 61, 87–95.

Zucca, A., Marchisio, D.L., Vanni, M., Barresi, A.A., 2007. Validation of bivariate DQMOM for nanoparticle processes simulation. American Institute of Chemical Engineering Journal 53, 918–931.

Chapter 2

Population balance

In this chapter, the population balance framework needed to describe a generic polydisperse multiphase flows is introduced: a generic definition of number density function (NDF) and population balance equation (PBE) will be given, with a particular attention to the modeling of aggregation-breakage processes that characterize the evolution of multiphase systems.

The discussion of the governing equations will be limited to the particular system under investigation, namely gas-liquid flows, where dispersed bubbles may coalesce, break-up and exchange mass with the surrounding liquid. It will be shown, under certain reasonable assumptions, how to model the collisional events between bubbles and the mass transfer of chemical species for a air-pure water system.

Finally, the solution methods for PBE used in this dissertation, Direct Simulation Monte Carlo (DSMC) and Quadrature-based Methods of Moments (QBMM), will be explained in detail. Although these methods can be used for solving any defined PBE, here the discussion will focus in particular focused on the solution of governing equations for gas-liquid systems. Moreover, particular emphasis will be given to the distinction between monovariate and multivariate methods and on the difficulties derived by the introduction of different parts of the physics in the solution of the investigated system.

2.1 General definition of Population Balance Equation

Dispersed systems are generally constituted by a continuous phase and a number of discrete elements (or particles) composing the disperse phase. These elements may interact with each other or with the continuous phase: general properties of the system determine the nature of such interactions. As for the continuous phase, also each single element of the disperse phase can be identified by a certain number of properties. In population balance theory these properties are usually indicated as coordinates (Ramkrishna, 2000; Marchisio and Fox, 2013). Coordinates are classified into two groups:

- external (i.e., the spatial coordinates: the position of a element in physical space is not an intrinsic property this element);

- internal (i.e., intimate properties of the elements, as their volumes, their velocities, their temperature, their chemical composition, etc.).

The entire population of discrete elements can be described with a functional called Number Density Function (NDF), containing information about how the population of particles inside an infinitesimal control volume is distributed over the properties of interest. By using a rigorous notation, this infinitesimal volume is in general indicated with its position $\mathbf{x} = (x_1, x_2, x_3)$ and its measure $\mathrm{d}\mathbf{x} = \mathrm{d}x_1\mathrm{d}x_2\mathrm{d}x_3$, while $\boldsymbol{\xi} = (\xi_1, \xi_2, \ldots, \xi_N)$ and $\mathrm{d}\boldsymbol{\xi} = \mathrm{d}\xi_1\mathrm{d}\xi_2 \ldots \mathrm{d}\xi_N$ represent respectively the internal-coordinate vector containing the N properties of interest and the infinitesimal volume of the internal-coordinate space (i.e. the space generated by the N properties of the population, or phase space). The NDF definition, $n_{\boldsymbol{\xi}}(\boldsymbol{\xi}; \mathbf{x}, t)$, stems on the fact that the following quantity:

$$n_{\boldsymbol{\xi}}(\boldsymbol{\xi}; \mathbf{x}, t)\, \mathrm{d}\mathbf{x}\, \mathrm{d}\boldsymbol{\xi} \tag{2.1}$$

represents the expected number of elements contained inside the physical volume $\mathrm{d}\mathbf{x}$ and in the internal-coordinate space $\mathrm{d}\boldsymbol{\xi}$ at time t. This quantity should be considered as an ensemble average of infinite number of realizations of the dispersed system; consequently the NDF is a smooth and differentiable function with respect to time, physical space and internal-coordinate space (for a detailed discussion about the NDF definition see Ramkrishna, 2000). By means of the NDF, it is possible to describe a dispersed system in a deterministic way; in fact, the NDF identifies the entire population of particles at any instant and at any given point in the computational domain and considers the probability associated with the state of each of these particles. As already mentioned, sometimes the population of particles is described by only one internal coordinate, for example particle length (i.e., $\xi = L$), and the NDF is called monovariate. When two internal coordinates are needed, for example particle size and surface area (i.e., $\xi = (L, a)$), the NDF is bivariate. More generally, higher-dimensional cases are referred to as multivariate.

By considering a generic control volume in physical space $\Omega_{\mathbf{x}}$ and in internal-coordinate space $\Omega_{\boldsymbol{\xi}}$ with boundaries indicated respectively with $\partial\Omega_{\mathbf{x}}$ and $\partial\Omega_{\boldsymbol{\xi}}$, and by omitting the dependency in space and time, it possible to write a balance equation for the number of elements contained in this control volume (i.e., number density) as

$$\begin{aligned}\frac{\partial}{\partial t}\left(\int_{\Omega_{\mathbf{x}}} \mathrm{d}\mathbf{x} \int_{\Omega_{\boldsymbol{\xi}}} \mathrm{d}\boldsymbol{\xi}\; n_{\boldsymbol{\xi}}\right) + \int_{\Omega_{\boldsymbol{\xi}}} \mathrm{d}\boldsymbol{\xi} \int_{\partial\Omega_{\mathbf{x}}} \left(n_{\boldsymbol{\xi}}\mathbf{v}\right) \cdot \mathrm{d}\mathbf{A}_{\mathbf{x}} \\ + \int_{\Omega_{\mathbf{x}}} \mathrm{d}\mathbf{x} \int_{\partial\Omega_{\boldsymbol{\xi}}} \left(n_{\boldsymbol{\xi}}\dot{\boldsymbol{\xi}}\right) \cdot \mathrm{d}\mathbf{A}_{\boldsymbol{\xi}} = \int_{\Omega_{\mathbf{x}}} \mathrm{d}\mathbf{x} \int_{\Omega_{\boldsymbol{\xi}}} \mathrm{d}\boldsymbol{\xi}\; h_{\boldsymbol{\xi}}\end{aligned} \tag{2.2}$$

where $\mathbf{v}$ is the advection velocity vector of the dispersed phase, assumed to be known (i.e., in some way linked to the local velocity of the continuous phase), $\dot{\boldsymbol{\xi}}$ represents the continuous rate of change in the internal-coordinate space and $h_{\boldsymbol{\xi}}$ is the functional representing discrete events that may locally change the number of elements. In addition to the advection velocity

in physical and phase space, also diffusive-flux terms can be included in Eq. (2.2) as other particular higher-order terms according to the investigated system, here neglected in this very general case only to simplify the notation and the expressions.

It is clear that the first term of Eq. (2.2) is an integral over the control volume (physical and phase space) and represents accumulation in time of the total number of elements. The second term indicates the net flux of number density due to advection in physical space; for this reason the is surface integral is performed over the boundary of the physical space and $\mathrm{d}\mathbf{A}_{\mathbf{x}}$ represents the infinitesimal surface unit vector with magnitude equal to the measure of the infinitesimal surface of the physical control volume and direction defined by the vector normal to this surface. The third term is analogue to the second one and represents advection in phase space; if it is possible to calculate the physical advection as $\mathbf{v} = {}^{\mathrm{d}\mathbf{x}}/_{\mathrm{d}t}$, at the same time the phase space velocity vector can be written as $\dot{\boldsymbol{\xi}} = {}^{\mathrm{d}\boldsymbol{\xi}}/_{\mathrm{d}t}$ and it is composed in each component by the rate of change of the i^{th} internal coordinate due to continuous processes. Any discrete event that cause discontinuous jumps in phase space is instead represented by the term on the right-hand side of Eq. (2.2).

The difference between continuous and discrete/discontinuous processes is based on the time and space scales of interest. In principle, all processes can be treated as discrete at molecular level, but, when a process is characterized by changes in internal coordinates with time scales much smaller than the one characterizing the change in the NDF can be modeled as continuous. A typical example is the growth of a solid crystal: the size of the particle grows due to surface deposition of molecules which occurs at time and length scales much smaller than the scales related to the change in size of the crystal. Another example could be the absorption of a chemical species in a gas-liquid system. On the contrary when two particles collide, and as a consequence of collision they aggregate, the length scale of this process is of the same order of the variation of particle size, thus causing a discontinuous jump in phase space.

Since $n_{\boldsymbol{\xi}}$ is a continuous function by definition, it is possible to write the surface integrals as volume integrals by applying the Reynolds-Gauss theorem (Aris, 1962) to Eq. (2.2):

$$\begin{aligned}\frac{\partial}{\partial t}\left(\int_{\Omega_{\mathbf{x}}}\mathrm{d}\mathbf{x}\int_{\Omega_{\boldsymbol{\xi}}}\mathrm{d}\boldsymbol{\xi}\, n_{\boldsymbol{\xi}}\right)+\int_{\Omega_{\mathbf{x}}}\mathrm{d}\mathbf{x}\int_{\Omega_{\boldsymbol{\xi}}}\mathrm{d}\boldsymbol{\xi}\,\frac{\partial}{\partial\mathbf{x}}\cdot\left(n_{\boldsymbol{\xi}}\mathbf{v}\right)\\ +\int_{\Omega_{\mathbf{x}}}\mathrm{d}\mathbf{x}\int_{\Omega_{\boldsymbol{\xi}}}\mathrm{d}\boldsymbol{\xi}\,\frac{\partial}{\partial\boldsymbol{\xi}}\cdot\left(n_{\boldsymbol{\xi}}\dot{\boldsymbol{\xi}}\right)=\int_{\Omega_{\mathbf{x}}}\mathrm{d}\mathbf{x}\int_{\Omega_{\boldsymbol{\xi}}}\mathrm{d}\boldsymbol{\xi}\, h_{\boldsymbol{\xi}},\end{aligned}\tag{2.3}$$

where $\frac{\partial}{\partial\mathbf{x}}$ and $\frac{\partial}{\partial\boldsymbol{\xi}}$ are the gradient in physical and internal-coordinate space, defined respectively as

$$\frac{\partial}{\partial\mathbf{x}}=\left(\frac{\partial}{\partial x_1},\frac{\partial}{\partial x_2},\frac{\partial}{\partial x_3}\right),\qquad\frac{\partial}{\partial\boldsymbol{\xi}}=\left(\frac{\partial}{\partial\xi_1},\ldots,\frac{\partial}{\partial\xi_N}\right).$$

Since $\Omega_{\mathbf{x}}$ and $\Omega_{\boldsymbol{\xi}}$ compose a generic control volume of the balance, from Eq. (2.3) derive the following relation:

$$\frac{\partial n_{\xi}}{\partial t} + \frac{\partial}{\partial \mathbf{x}} \cdot \left(n_{\xi} \mathbf{v}\right) + \frac{\partial}{\partial \boldsymbol{\xi}} \cdot \left(n_{\xi} \dot{\boldsymbol{\xi}}\right) = h_{\xi}, \tag{2.4}$$

which is known generally as Population Balance Equation (PBE); for further details on this derivation, see Ramkrishna (2000); Marchisio and Fox (2013). When the elements do not share a unique velocity field but are characterized by their own velocity distribution, the velocity of the dispersed phase is treated as internal coordinate of the NDF $n(\boldsymbol{\xi}, \mathbf{v}; \mathbf{x}, t)$ and Eq. (2.4) becomes (omitting the dependencies on internal and external coordinates):

$$\frac{\partial n}{\partial t} + \frac{\partial}{\partial \mathbf{x}} \cdot (n\mathbf{v}) + \frac{\partial}{\partial \mathbf{v}} \cdot (n\mathbf{A}) + \frac{\partial}{\partial \boldsymbol{\xi}} \cdot \left(n\dot{\boldsymbol{\xi}}\right) = h, \tag{2.5}$$

where $\mathbf{A}$ is now the continuous rate of change of particle velocity due to external forces per unit mass acting on particles (e.g., gravity, fluid drag, etc.). Eq. (2.5) is usually called Generalized Population Balance Equation (GPBE) (Marchisio and Fox, 2013).

In order to solve PBE or GPBE, initial conditions for n_{ξ} at starting time and boundary conditions in physical space $\Omega_{\mathbf{x}}$ and in phase space Ω_{ξ} must be specified; however, analytical solutions are available for a few special cases and only under some very simple hypotheses. In most cases of practical interest, numerical methods must be used to solve these equations, providing knowledge of the NDF for each time instant and at every physical point in the computational domain, as well as at every point in phase space. In Section 2.3, these methods will be introduced and discussed with particular focus on less demanding methods from the computational point of view, as the Method of Moments (MOM).

Starting from the general definition of NDF, it is possible to define an arbitrary moment of the NDF introducing the moment transform as follows:

$$M_{\mathbf{k}} = \int_{\Omega_{\xi}} \xi_1^{k_1} \cdots \xi_N^{k_N} n_{\xi}(\boldsymbol{\xi}; \mathbf{x}, t) \, \mathrm{d}\boldsymbol{\xi} \tag{2.6}$$

where $\mathbf{k} = (k_1, \ldots, k_N)$ is a vector containing the order of the moments with respect to each of the components of $\boldsymbol{\xi}$ and Ω_{ξ} indicates all the possible values of the internal-coordinate vector $\boldsymbol{\xi}$. Through this definition, important integral quantities of the distribution may be identified: for example, the total number of elements per unit volume located at time t and at point $\mathbf{x}$ (i.e., the total number concentration) is the moment of order $\mathbf{0} = (0, \ldots, 0)$ as follows:

$$M_{\mathbf{0}} = \int_{\Omega_{\xi}} n_{\xi}(\boldsymbol{\xi}; \mathbf{x}, t) \, \mathrm{d}\boldsymbol{\xi}. \tag{2.7}$$

It is clear that, by using moments, internal-coordinate dependencies of NDF are integrated out losing some piece of information of the distribution (e.g., the detailed shape), but important variables from the engineering point of view (e.g., distribution averages or covariances)

can be expressed as a function of the moments themselves. However, it is possible to apply the moment transform defined in Eq. (2.6) to Eq. (2.4), obtaining:

$$\frac{\partial M_{\mathbf{k}}}{\partial t} + \frac{\partial}{\partial \mathbf{x}} \cdot \left(M_{\mathbf{k}} \mathbf{v} \right) = - \int_{\Omega_\xi} (\xi_1^{k_1} \cdots \xi_N^{k_N}) \frac{\partial}{\partial \boldsymbol{\xi}} \cdot \left(n_\xi \dot{\boldsymbol{\xi}} \right) \mathrm{d}\boldsymbol{\xi} + \int_{\Omega_\xi} (\xi_1^{k_1} \cdots \xi_N^{k_N}) \, h_\xi \, \mathrm{d}\boldsymbol{\xi}, \tag{2.8}$$

which the so-called moment transport equation. It should be mentioned that in this case the physical velocity vector $\mathbf{v}$ is not a function of NDF or its internal coordinates. In the case of GPBE (Eq. (2.5)), the moment transport equation is the following one:

$$\frac{\partial M_{\mathbf{k}}}{\partial t} = - \int_{\Omega_\xi} (\xi_1^{k_1} \cdots \xi_N^{k_N}) \frac{\partial}{\partial \mathbf{x}} \cdot (n\mathbf{v}) \, \mathrm{d}\boldsymbol{\xi} - \int_{\Omega_\xi} (\xi_1^{k_1} \cdots \xi_N^{k_N}) \frac{\partial}{\partial \mathbf{v}} \cdot (n\mathbf{A}) \, \mathrm{d}\boldsymbol{\xi} - \int_{\Omega_\xi} (\xi_1^{k_1} \cdots \xi_N^{k_N}) \frac{\partial}{\partial \boldsymbol{\xi}} \cdot \left(n\dot{\boldsymbol{\xi}} \right) \mathrm{d}\boldsymbol{\xi} + \int_{\Omega_\xi} (\xi_1^{k_1} \cdots \xi_N^{k_N}) \, h \, \mathrm{d}\boldsymbol{\xi}. \tag{2.9}$$

It should be noticed that in both Eq. (2.8) and Eq. (2.9) the unclosed terms are moved on the right side: in fact, the functional forms of n_ξ, $\dot{\boldsymbol{\xi}}$, h_ξ and n, $\mathbf{v}$, $\dot{\boldsymbol{\xi}}$, h are in general not known and must be assumed in order to solve these equations. This is the so-called "closure problem" that Hulburt and Kats explicated in their pioneering work on Methods of Moments (Hulburt and Katz, 1964). Furthermore, although the PBE solution methods based on moment transport equation could be applied to different problems (rather distinguishing between monovariate and multivariate cases), the expression of different terms of Eq. (2.8) and Eq. (2.9) strongly depends on the modeled dispersed system. For this reason, in the next sections the NDF for gas-liquid system will be introduced and how to solve in practice the PBE for this case will be discussed. However, for aggregation-breakage problem (e.g., solid particles, drops or bubbles in fluids), the term relating to discontinuous events may have a general expression and this will be provided in the following section.

2.1.1 Birth and death functions

As previously remarked, the discontinuous events term h is used to model all those processes that have an instantaneous impact on the NDF, causing a discontinuous jump in phase space. Such processes are usually divided into three groups (Marchisio and Fox, 2013):

- zero-order process, in which the jump depends only on the state of the continuous phase (i.e., nucleation);
- first-order process, in which the jump is due to an interaction of a element of disperse phase with the continuous phase (i.e., breakage);
- second-order process, in which the jump is due to an interaction of two different elements of disperse phase with the continuous phase (i.e., aggregation).

It should be noticed that higher-order processes are in general neglected because the simultaneous interaction of three or more dispersed elements is very unlikely compared to the interaction of two elements in the same infinitesimal interval of time. Moreover it is important to remark that different elements do not directly interact between each other, but always by means of the action of the continuous phase. In other words, the state of the continuous phase strongly determines the rate of different processes.

A very common way to model similar processes is to use birth and death functions (Ramkrishna, 2000): according to the considered process, in fact, a certain number of elements may appear inside the control volume (e.g., as a consequence of a particle breakage or nucleation of new particles) while other elements may disappear (e.g., when two aggregating elements). By using the mathematical formalism, it is possible to state what follows:

$$h_i = h_i^+ - h_i^- \tag{2.10}$$

where h_i^+ represent the rate of production and h_i^- the rate of loss of particle due to i^{th} discontinuous event. Since the aim of this work is related to the description of bubbles in liquids, in the following part the formulation of similar functions for aggregation and breakage processes will be presented and discussed. Readers interested in more details for other particulate systems are referred to the specialized literature (Marchisio and Fox, 2013).

Birth and death due to breakage

A first-order process, as the bubble breakage is generally described by the following term:

$$b(\boldsymbol{\xi}, \boldsymbol{\xi}_c; \mathbf{x}, t)\mathrm{d}t \tag{2.11}$$

which is the probability that a particle with internal coordinates $\boldsymbol{\xi}$ in a fluid characterized by the physical state $\boldsymbol{\xi}_c$ undergoes the process under investigation in the infinitesimal time interval dt. The quantity b is a frequency and so has units of inverse of time, and its dependence on the particle and fluid properties. According to this definition, the number of particles per

unit volume disappearing because of this process can be readily written as (suppressing the t and $\mathbf{x}$ dependence for clarity):

$$h_b^-(\xi, \xi_c) = b(\xi, \xi_c)\, n(\xi). \tag{2.12}$$

As far as the rate of formation of particles due to breakage is concerned, an additional function must be defined. This is usually introduced as a conditional probability density function (PDF) that states the probability of formation of a daughter element with internal coordinates ξ' from a mother element with ξ . This function usually depends only on the state of the disperse phase (Patruno et al., 2009; Marchisio and Fox, 2013); however the dependence on continuous phase ξ_c can be easily included in the definition. In any case, this PDF has to be normalized in a way that:

$$\int_{\Omega_{\xi'}} P(\xi'|\xi)\, \mathrm{d}\xi' = 1, \tag{2.13}$$

which states that the sum of all probabilities of producing the daughter particle ξ' starting from the mother particle ξ is unity. However, the conditional PDF does not contain any information regarding the number of particles formed during the breakage process; for this reason the corresponding conditional number density function $N(\xi'|\xi)$, generally known as daughter distribution function, is defined as follows:

$$\int_{\Omega_{\xi'}} N(\xi'|\xi)\mathrm{d}\xi' = \nu(\xi), \tag{2.14}$$

where ν is the total number of new elements formed by the breakage process. It is clear that the relationship between Eq. (2.13) and Eq. (2.14) is a simple renormalization. Now it is possible to describe the formation of new elements due to breakage in the following way:

$$h_b^+(\xi, \xi_c) = \int_{\Omega_{\xi'}} N(\xi'|\xi) b(\xi', \xi_c) n(\xi')\mathrm{d}\xi'. \tag{2.15}$$

The overall breakage rate $h_b(\xi, \xi_c)$ is therefore expressed as:

$$h_b(\xi, \xi_c) = h_b^+(\xi, \xi_c) - h_b^-(\xi, \xi_c) = \int_{\Omega_{\xi'}} N(\xi'|\xi) b(\xi', \xi_c) n(\xi')\mathrm{d}\xi' - b(\xi, \xi_c)\, n(\xi) \tag{2.16}$$

It should be remarked that the formulation of daughter distribution function N and the breakage frequency b is problem-dependent. In Section 2.2.2, some common functional forms for gas-liquid system will be reported.

Birth and death due to aggregation

In a second-order process, such as particle aggregation, one element with center of mass at position $\tilde{\mathbf{x}}$ characterized by internal-coordinate vector $\tilde{\boldsymbol{\xi}}$ interacts with another element with center of mass in the physical point $\mathbf{x}'$ and internal-coordinate vector $\boldsymbol{\xi}'$, in a continuous phase characterized by state vector $\boldsymbol{\xi}_c$. As already seen for breakage process, it is possible to define the frequency of the aggregation process a in a way that

$$a(\tilde{\mathbf{x}}, \tilde{\boldsymbol{\xi}}; \mathbf{x}', \boldsymbol{\xi}'; \boldsymbol{\xi}_c)\, \mathrm{d}t \tag{2.17}$$

represents the probability of elements undergoing the second-order process in a time interval $\mathrm{d}t$; as a standard frequency this quantity has unit of inverse of time. An important property assumed for this frequency is the symmetry with respect to element permutation, resulting in:

$$a(\tilde{\mathbf{x}}, \tilde{\boldsymbol{\xi}}; \mathbf{x}', \boldsymbol{\xi}'; \boldsymbol{\xi}_c) = a(\mathbf{x}', \boldsymbol{\xi}'; \tilde{\mathbf{x}}, \tilde{\boldsymbol{\xi}}; \boldsymbol{\xi}_c) \tag{2.18}$$

Starting from this aggregation frequency, it is possible to calculate the total number of events N_e occurring per unit time and unit volume involving elements in the infinitesimal range of $(\tilde{\mathbf{x}}, \tilde{\boldsymbol{\xi}})$, as follows:

$$N_e(\tilde{\mathbf{x}}, \tilde{\boldsymbol{\xi}}, \boldsymbol{\xi}_c, t) = \int_{\Omega_{\mathbf{x}'}} \int_{\Omega_{\boldsymbol{\xi}'}} a(\tilde{\mathbf{x}}, \tilde{\boldsymbol{\xi}}; \mathbf{x}', \boldsymbol{\xi}'; \boldsymbol{\xi}_c)\, n^{(2)}(\tilde{\mathbf{x}}, \tilde{\boldsymbol{\xi}}; \mathbf{x}', \boldsymbol{\xi}'; t)\, \mathrm{d}\mathbf{x}'\, \mathrm{d}\boldsymbol{\xi}', \tag{2.19}$$

where $n^{(2)}$ is the so-called pair number density function, defined in such a way that:

$$n^{(2)}(\tilde{\mathbf{x}}, \tilde{\boldsymbol{\xi}}; \mathbf{x}', \boldsymbol{\xi}'; t)\, \mathrm{d}\tilde{\mathbf{x}}\, \mathrm{d}\tilde{\boldsymbol{\xi}}\, \mathrm{d}\mathbf{x}'\, \mathrm{d}\boldsymbol{\xi}, \tag{2.20}$$

represents the expected number of element pairs with state $(\tilde{\mathbf{x}}, \tilde{\boldsymbol{\xi}})$ and $(\mathbf{x}', \boldsymbol{\xi})$ at time t. The evolution of $n^{(2)}$ can be described in turn by a balance equation similar to PBE for the NDF; however its solution involves the knowledge of $n^{(3)}$ generating another closure problem. For this reason the following closure is used[1]:

$$n^{(2)}(\tilde{\mathbf{x}}, \tilde{\boldsymbol{\xi}}; \mathbf{x}', \boldsymbol{\xi}'; t) \approx n(\tilde{\mathbf{x}}, \tilde{\boldsymbol{\xi}}, t)\, n(\mathbf{x}', \boldsymbol{\xi}', t). \tag{2.21}$$

Moreover, in most practical cases the distance in physical space between the two interacting elements (i.e., $|\mathbf{x}' - \tilde{\mathbf{x}}|$) is of the order of magnitude of element diameter and within this distance the NDF does not change significantly. Therefore, it is possible to assume that:

$$n^{(2)}(\tilde{\mathbf{x}}, \tilde{\boldsymbol{\xi}}; \mathbf{x}', \boldsymbol{\xi}; t) \approx n(\tilde{\mathbf{x}}, \tilde{\boldsymbol{\xi}}, t)\, n(\tilde{\mathbf{x}}, \boldsymbol{\xi}', t). \tag{2.22}$$

[1] In statistical mechanics this is known as Boltzmann *Stosszahlansatz* (Marchisio and Fox, 2013)

By substituting what expressed in Eq. (2.22) into Eq. (2.19), it is possible to write:

$$N_e(\tilde{\mathbf{x}}, \tilde{\boldsymbol{\xi}}, \boldsymbol{\xi}_c, t) = \int_{\Omega_{\boldsymbol{\xi}'}} \alpha(\tilde{\mathbf{x}}, \tilde{\boldsymbol{\xi}}, \boldsymbol{\xi}', \boldsymbol{\xi}_c)\, n(\tilde{\mathbf{x}}, \tilde{\boldsymbol{\xi}}, t)\, n(\tilde{\mathbf{x}}, \boldsymbol{\xi}', t)\, \mathrm{d}\boldsymbol{\xi}', \tag{2.23}$$

where

$$\alpha(\tilde{\mathbf{x}}, \tilde{\boldsymbol{\xi}}, \boldsymbol{\xi}', \boldsymbol{\xi}_c) = \int_{\Omega_{\mathbf{x}'}} a(\tilde{\mathbf{x}}, \tilde{\boldsymbol{\xi}}; \mathbf{x}', \boldsymbol{\xi}'; \boldsymbol{\xi}_c)\, \mathrm{d}\mathbf{x}' \tag{2.24}$$

is the so-called aggregation kernel and has dimensions of spatial volume per unit time. This derivation was necessary in order to define the rate of production of new elements due to aggregation:

$$h_a^+(\tilde{\mathbf{x}}, \boldsymbol{\xi}, \boldsymbol{\xi}_c, t) = \frac{1}{M} \int_{\Omega_{\boldsymbol{\xi}'}} \alpha(\tilde{\mathbf{x}}, \tilde{\boldsymbol{\xi}}, \boldsymbol{\xi}', \boldsymbol{\xi}_c)\, n(\tilde{\mathbf{x}}, \tilde{\boldsymbol{\xi}}, t)\, n(\tilde{\mathbf{x}}, \boldsymbol{\xi}', t) J(\tilde{\boldsymbol{\xi}}, \boldsymbol{\xi})\, \mathrm{d}\boldsymbol{\xi}' \tag{2.25}$$

where $(\tilde{\mathbf{x}}, \boldsymbol{\xi})$ is the state vector of the new element, generated by aggregation of $(\tilde{\mathbf{x}}, \boldsymbol{\xi}')$ and $(\tilde{\mathbf{x}}, \tilde{\boldsymbol{\xi}})$. The integer number M is the symmetry factor to used to avoid multiple pairs counting, and is equal to two for identical particles and one for different particles, in the case of aggregation. While $J(\tilde{\boldsymbol{\xi}}, \boldsymbol{\xi})$ is the Jacobian of the variable transformation relating to the internal-coordinate space before aggregation $\tilde{\boldsymbol{\xi}}$ and after aggregation $\boldsymbol{\xi}$, defined as follows:

$$J(\tilde{\boldsymbol{\xi}}, \boldsymbol{\xi}) = \left| \frac{\partial \tilde{\boldsymbol{\xi}}}{\partial \boldsymbol{\xi}} \right| = \begin{vmatrix} \dfrac{\partial \tilde{\xi}_1}{\partial \xi_1} & \cdots & \dfrac{\partial \tilde{\xi}_1}{\partial \xi_N} \\ \vdots & \ddots & \vdots \\ \dfrac{\partial \tilde{\xi}_N}{\partial \xi_1} & \cdots & \dfrac{\partial \tilde{\xi}_N}{\partial \xi_N} \end{vmatrix} \tag{2.26}$$

where N is the total number of internal coordinates considered. It should be noticed that the final expression of the Jacobian changes according to the internal coordinates of interest of a particular problem.

The rate of loss of elements due to aggregation $h_a^-(\mathbf{x}, \boldsymbol{\xi}, \boldsymbol{\xi}_c, t)$ follows from Eq. (2.23), and can be easily expressed as:

$$h_a^-(\tilde{\mathbf{x}}, \boldsymbol{\xi}, \boldsymbol{\xi}_c, t) = \int_{\Omega_{\boldsymbol{\xi}'}} \alpha(\tilde{\mathbf{x}}, \tilde{\boldsymbol{\xi}}, \boldsymbol{\xi}', \boldsymbol{\xi}_c)\, n(\tilde{\mathbf{x}}, \tilde{\boldsymbol{\xi}}, t)\, n(\tilde{\mathbf{x}}, \boldsymbol{\xi}', t)\, \mathrm{d}\boldsymbol{\xi}'. \tag{2.27}$$

The overall aggregation rate $h_a(\tilde{\mathbf{x}}, \boldsymbol{\xi}, \boldsymbol{\xi}_c, t)$ is below reported:

$$\begin{aligned} h_a(\tilde{\mathbf{x}}, \boldsymbol{\xi}, \boldsymbol{\xi}_c, t) = h_a^+(\tilde{\mathbf{x}}, \boldsymbol{\xi}, \boldsymbol{\xi}_c, t) - h_a^-(\tilde{\mathbf{x}}, \boldsymbol{\xi}, \boldsymbol{\xi}_c, t) = \\ \frac{1}{M} \int_{\Omega_{\boldsymbol{\xi}'}} \alpha(\tilde{\mathbf{x}}, \tilde{\boldsymbol{\xi}}, \boldsymbol{\xi}', \boldsymbol{\xi}_c)\, n(\tilde{\mathbf{x}}, \tilde{\boldsymbol{\xi}}, t)\, n(\tilde{\mathbf{x}}, \boldsymbol{\xi}', t) J(\tilde{\boldsymbol{\xi}}, \boldsymbol{\xi})\, \mathrm{d}\boldsymbol{\xi}' \\ - \int_{\Omega_{\boldsymbol{\xi}'}} \alpha(\tilde{\mathbf{x}}, \tilde{\boldsymbol{\xi}}, \boldsymbol{\xi}', \boldsymbol{\xi}_c)\, n(\tilde{\mathbf{x}}, \tilde{\boldsymbol{\xi}}, t)\, n(\tilde{\mathbf{x}}, \boldsymbol{\xi}', t)\, \mathrm{d}\boldsymbol{\xi}'. \end{aligned} \tag{2.28}$$

For a more detailed discussion on second-order process modeling, reader should consult specialized text (Ramkrishna, 2000; Marchisio and Fox, 2013). As pointed out for breakage frequency, the aggregation kernel formulation depends on the particular system under investigation; in Section 2.2.2 the most common kernels for bubble coalescence will be reported.

2.2 PBE for gas-liquid systems

A generic turbulent gas-liquid system can be thought of as a dispersion of bubbles, each one characterized by its size L, composition $\boldsymbol{\phi}_\mathrm{b}$ and velocity $\mathbf{U}_\mathrm{b}$. Bubble enthalpy (or temperature) is out of the description because the aim of this work is to model an isothermal system; however, this is not a serious limitation since other properties may be taken into the population balance description (Buffo et al., 2012).

Recurring to the general definition of NDF given in Eq. (2.1), in a case of dispersed gas-liquid system, it is possible to state that:

$$\hat{n}(L, \boldsymbol{\phi}_\mathrm{b}, \mathbf{U}_\mathrm{b}; \mathbf{x}, t)\, \mathrm{d}L\, \mathrm{d}\boldsymbol{\phi}_\mathrm{b}\, \mathrm{d}\mathbf{U}_\mathrm{b}\, \mathrm{d}\mathbf{x}, \tag{2.29}$$

represents the expected number of bubbles with size between L and $L+\mathrm{d}L$, composition between $\boldsymbol{\phi}_\mathrm{b}$ and $\boldsymbol{\phi}_\mathrm{b}+\mathrm{d}\boldsymbol{\phi}_\mathrm{b}$ (considering N chemical species), velocity between $\mathbf{U}_\mathrm{b}$ and $\mathbf{U}_\mathrm{b}+\mathrm{d}\mathbf{U}_\mathrm{b}$ contained inside the physical volume $\mathrm{d}\mathbf{x}$ at time t. As previously remarked, a similar bubble distribution is called multivariate because is characterized with more than two internal coordinates. Moreover, the generic moment of the NDF is what follows:

$$M_{k,\mathbf{l},\mathbf{m}}(\mathbf{x}, t) = \int_{\Omega_L} \int_{\Omega_{\boldsymbol{\phi}_\mathrm{b}}} \int_{\Omega_{\mathbf{U}_\mathrm{b}}} L^k \boldsymbol{\phi}_\mathrm{b}^{\mathbf{l}} \mathbf{U}_\mathrm{b}^{\mathbf{m}}\, \hat{n}(L, \boldsymbol{\phi}_\mathrm{b}, \mathbf{U}_\mathrm{b}; \mathbf{x}, t)\, \mathrm{d}L\, \mathrm{d}\boldsymbol{\phi}_\mathrm{b}\, \mathrm{d}\mathbf{U}_\mathrm{b}, \tag{2.30}$$

where Ω_L, $\Omega_{\boldsymbol{\phi}_\mathrm{b}}$ and $\Omega_{\mathbf{U}_\mathrm{b}}$ are respectively the spaces generated by all possible values of bubble size, composition and velocity, while k, $\mathbf{l} = (l_1, \ldots, l_N)$ and $\mathbf{m} = (m_1, m_2, m_3)$ are the integer values representing respectively the order of moment with respect to bubble size, composition and velocity.

As seen for Eq. (2.5), it is possible to write a continuity statement for the NDF. This is the GPBE for the investigated system:

$$\frac{\partial \hat{n}}{\partial t} + \frac{\partial}{\partial \mathbf{x}}(\hat{n}\, \mathbf{U}_\mathrm{b}) + \frac{\partial}{\partial \mathbf{U}_\mathrm{b}}(\hat{n}\, \mathbf{A}_\mathrm{b}) + \frac{\partial}{\partial L}(\hat{n}\, G) + \frac{\partial}{\partial \boldsymbol{\phi}_\mathrm{b}}(\hat{n}\, \dot{\boldsymbol{\phi}}_\mathrm{b}) = \widehat{h}(L, \boldsymbol{\phi}_\mathrm{b}, \mathbf{U}_\mathrm{b}; \mathbf{x}, t), \tag{2.31}$$

where the meaning of the different terms is similar to that of the terms of Eq. (2.4) and Eq. (2.5): on the left-hand side the different rates of change of the NDF due to continuous events are represented, while the right-hand side term takes into account the discontinuous events.

At this point, the discussion necessarily stops being general and some assumptions based on physical reality are needed, not only to simplify the model for reducing computational costs, but also to properly describe the system of interest. In other words, the functional

form for $\mathbf{U}_\mathrm{b}$, $\mathbf{A}_\mathrm{b}$, G, $\dot{\boldsymbol{\phi}}_\mathrm{b}$ and $\widehat{h}$ of Eq. (2.31) are not general but problem-dependent. The final purpose of this work is to describe in detail the oxygen mass transfer from gas to liquid in an isothermal air-water industrial-scale contactor, and the following assumptions are made:

- thermal effects are neglected as the system is isothermal. This means that no energy equation is solved for the continuous phase and for the dispersed bubbles. Moreover, there is no phase transition of any chemical component (e.g., condensing or boiling);
- advection is considered the only mechanism responsible of bubble motion in physical space. This assumption is based on the fact that (turbulent) diffusive transport of momentum is negligible compared to advection, due to range of bubble sizes examined in this work (as remarked in Section 3.2.3) usually larger than characteristic turbulent scale;
- the shape of all bubble population is assumed spherical in first approximation. As explained in section Section 3.2.3, this assumption is correct for very small bubbles up to 1 mm of equivalent diameter, while other shapes are observed for larger bubbles. This means that the bubble interfacial area calculated as $k_A L^2$ and the bubble volume calculated as $k_V L^3$, with $k_A = \pi$ and $k_V = \pi/6$ the areic shape factor and volumetric shape factor for a sphere, are slightly underestimated. However, this is not a limitation of the model because it is possible to tackle this issue by introducing a deformation factor, function of the state of the bubble (see Bakker and Van den Akker, 1994);
- gas phase is constituted by oxygen and nitrogen, where only one transfers between phases (i.e., oxygen) and the other is inert (i.e., nitrogen). For this reason, the composition vector $\boldsymbol{\phi}_\mathrm{b}$ becomes a scalar quantity ϕ_b;
- bubble oxygen composition ϕ_b is defined as the total number of oxygen moles. This physical quantity is chosen due to its conservation property, namely the total number of moles is conserved after bubble breakage or coalescence;
- mass transfer resistance in gas phase can be neglected, namely mass transfer coefficient k_L is estimated considering a flat oxygen profile in gas phase;
- advection in internal-coordinate space is represented by $G = \mathrm{d}L/\mathrm{d}t$ (i.e., the rate of bubble size change due to growth/shrink) and by $\dot{\phi}_\mathrm{b} = \mathrm{d}\phi_\mathrm{b}/\mathrm{d}t$ (i.e., the rate of bubble composition change). In general, these terms are function of all the internal coordinates; in this case, instead, are expressed only in terms of bubble size L and oxygen composition ϕ_b since only mass transfer is able to continuously change size and composition of bubbles. In other words, bubble velocity $\mathbf{U}_\mathrm{b}$ does not influence phase space advection terms;
- bubble coalescence and break-up are treated as an aggregation-breakage problem and therefore modeled by using the term $\widehat{h}$. As indicated in Eq. (2.31), bubble collisional phenomena may depend on size, composition and velocity (besides space and time);

however the dependence on bubble velocity $\mathbf{U}_\mathrm{b}$ can be neglected for a turbulent system, as explained in Section 2.2.2.

The description can be simplified by integrating out the bubble velocity:

$$n(L, \phi_\mathrm{b}; \mathbf{x}, t) = \int_{\Omega_{\mathbf{U}_\mathrm{b}}} \hat{n}(L, \phi_\mathrm{b}, \mathbf{U}_\mathrm{b}; \mathbf{x}, t) \mathrm{d}\mathbf{U}_\mathrm{b}, \tag{2.32}$$

in which the detailed information relating to the bubble velocity distribution is integrated out, reducing the number of internal coordinates of the problem. Eq. (2.31) must be rewritten in order to take into account the former definition of NDF (omitting the dependence on space and time for clarity):

$$\frac{\partial n}{\partial t} + \frac{\partial}{\partial \mathbf{x}}(n\, \check{\mathbf{U}}_\mathrm{b}) + \frac{\partial}{\partial L}(n\, G) + \frac{\partial}{\partial \phi_\mathrm{b}}(n\, \dot{\phi}_\mathrm{b}) = h(L, \phi_\mathrm{b}), \tag{2.33}$$

where $\check{\mathbf{U}}_\mathrm{b}$ is defined as follows:

$$\check{\mathbf{U}}_\mathrm{b}(L, \phi_\mathrm{b}) = \frac{\displaystyle\int_{\Omega_{\mathbf{U}_\mathrm{b}}} \hat{n}(L, \phi_\mathrm{b}, \mathbf{U}_\mathrm{b}; \mathbf{x}, t)\, \mathbf{U}_\mathrm{b}\, \mathrm{d}\mathbf{U}_\mathrm{b}}{\displaystyle\int_{\Omega_{\mathbf{U}_\mathrm{b}}} \hat{n}(L, \phi_\mathrm{b}, \mathbf{U}_\mathrm{b}; \mathbf{x}, t)\, \mathrm{d}\mathbf{U}_\mathrm{b}}, \tag{2.34}$$

representing the average bubble velocity conditioned over the values of bubble size and composition. It is interesting for solution purposes the case in which the spatial gradient vanishes (i.e., spatially homogeneous system), leading to the following equation:

$$\frac{\partial n}{\partial t} + \frac{\partial}{\partial L}(n\, G) + \frac{\partial}{\partial \phi_\mathrm{b}}(n\, \dot{\phi}_\mathrm{b}) = h(L, \phi_\mathrm{b}). \tag{2.35}$$

Eq. (2.33) and Eq. (2.35) are respectively the continuity statement of the bivariate NDF defined in Eq. (2.32) for spatially inhomogeneous and homogeneous systems, and these equations will be solved in Chapter 4 and Chapter 5 by means of the solution methods reported in Section 2.3. It should be noticed that the dependence on $\mathbf{A}_\mathrm{b}$ of Eq. (2.31) disappears due to the operation defined in Eq. (2.32). However, $\check{\mathbf{U}}_\mathrm{b}$ must be determined according to the Stokes number of the dispersed system, namely the ratio between the relaxation time of the bubble and of the fluid. For bubbly flows, the Stokes number is usually small but not zero so a differential model for calculating the velocity is needed. Reader refers to Chapter 3 for further details on bubble velocity calculation. In the following sections, the formulation of G, $\dot{\phi}_\mathrm{b}$ and h of Eq. (2.33) and Eq. (2.35) will be presented and discussed.

It is worth mentioning the case in which also the dependence on bubble composition ϕ_b is integrated out as follows:

$$\tilde{n}(L; \mathbf{x}, t) = \int_{\Omega_{\phi_\mathrm{b}}} n(L, \phi_\mathrm{b}; \mathbf{x}, t)\, \mathrm{d}\phi_\mathrm{b}, \tag{2.36}$$

leading to the following continuity statement:

$$\frac{\partial \tilde{n}}{\partial t} + \frac{\partial}{\partial \mathbf{x}}(\tilde{n}\,\breve{\mathbf{U}}_{\mathrm{b}}) + \frac{\partial}{\partial L}(\tilde{n}\,\widetilde{G}) = \widetilde{h}(L), \tag{2.37}$$

or in the case of homogeneous system:

$$\frac{\partial \tilde{n}}{\partial t} + \frac{\partial}{\partial L}(\tilde{n}\,\widetilde{G}) = \widetilde{h}(L), \tag{2.38}$$

which is the well-known monovariate PBE for a gas-liquid system, in which the bubble size is the only internal coordinate considered. It is important to remark that the bubble growth/shrink term $\widetilde{G}$ is formally equivalent to G, but in this case an average composition over all bubble is used for estimating mass transfer instead the actual bubble composition distribution.

2.2.1 Continuous events modeling

Referring to Eq. (2.33), the terms G and $\dot{\phi}_{\mathrm{b}}$ can be thought of as rates responsible of the advection of NDF in the internal-coordinate space generated by L and ϕ_{b}. They are also called "drift terms". With these terms it is possible to account for all the types of physical and chemical processes (such as mass transfer, chemical reactions, evaporation and condensation, etc.) that continuously modify the populations of bubbles. As previously remarked, in this work only oxygen mass transfer from air bubbles to water will be studied, by means of a bivariate population balance that gives the knowledge of bubble size and composition distribution in all the computational domain.

A detailed discussion of mass transfer theory is out of the aim of this work and can be found in specialized literature (Cussler, 1997). However, in this part the mesoscale model for G and $\dot{\phi}_{\mathrm{b}}$ will be shown starting from very basic assumptions. By using the Fick law, it is possible to describe the mass exchange of a generic chemical component A through the interface of bubble in a liquid (in the case of chemical absorption, without chemical reaction):

$$J_A = \mathscr{D}_A \left(\frac{\partial C_A}{\partial x} \right)_{x=0}, \qquad [\mathrm{mol/m^2\,s}] \tag{2.39}$$

where J_A is the molecular flux of chemical component A and $\mathscr{D}_A$ is the molecular diffusion coefficient for A in such system. It should be noticed that the molecular flux depends on a spatial composition gradient on x-direction perpendicular to the gas-liquid interface. Since in most cases the exact position of the interface is not known, it is possible to the define the mass transfer coefficient k in the following way:

$$k = \left| \frac{J_A}{C_A^{in} - \hat{C}_A} \right|, \qquad [\mathrm{m/s}] \tag{2.40}$$

where C_A^{in} is the molar concentration of A at the interface while $\hat{C}_A$ represents the concen-

tration of A at the bulk. Eq. (2.40) says that concentration variation between phase bulk and interface can be modeled by this coefficient, without specifying the concentration profile approach the interface from both phase sides. However, the continuity condition must be imposed in this way:

$$J_A = k_G(\hat{C}_{G,A} - C^{in}_{G,A}) = k_L(C^{in}_{L,A} - \hat{C}_{L,A}), \tag{2.41}$$

where subscripts G and L for gas and liquid phases respectively are introduced. By assuming the thermodynamical equilibrium at the interface, it is possible to apply the Henry law:

$$C^{in}_{L,A} = H_A C^{in}_{G,A}, \tag{2.42}$$

where H_A is the dimensionless Henry constant (in contrast with the common definition of Henry constant, which has dimensions of $\mathrm{Pa\,m^3/mol}$). In this manner, it is possible to eliminate the dependence on interface concentration in Eq. (2.41):

$$J_A = \left(\frac{1}{k_L} + \frac{H_A}{k_G}\right)^{-1} (H_A\hat{C}_{G,A} - \hat{C}_{L,A}). \tag{2.43}$$

Moreover, in this case it is possible to assume a flat concentration profile in gas phase, very common situation where pure gases or oxygen in air are considered. In this way, Eq. (2.43) becomes:

$$J_A = k_L(H_A\hat{C}_{G,A} - \hat{C}_{L,A}). \tag{2.44}$$

It is now clear that k_L models the concentration profile from the gas-liquid interface to the liquid bulk. Many correlations are available in the literature in order to estimate the mass transfer coefficient k_L (for a detailed review, see Gimbun et al., 2009). The most common ones are the so-called "penetration models", based on the work of Higbie (1935), considering the gas-liquid interface covered by elements of fluid. These elements return in the bulk zone after the contact time τ and new elements reach the surface with the concentration of the bulk. In the case of no or negligible turbulence the contact time τ can be expressed as:

$$\tau = \frac{d_b}{U_{slip}} \tag{2.45}$$

where d_b is the bubble diameter and U_{slip} is the relative velocity between bubble and liquid. According to this theory, it is possible to derive that:

$$k_L = 2\sqrt{\frac{\mathscr{D}\ U_{slip}}{\pi\ d_b}}. \tag{2.46}$$

A modification of Higbie theory was proposed by Danckwerts (1951), considering that substitution of fluid elements at the interface is randomly independent of the length of the contact with the interfacial surface. Defining with s the fraction of fluid elements replaced at surface

per unit time, it is possible to write:

$$k_L = \sqrt{\mathscr{D}\ s} \tag{2.47}$$

In the work of Lamont and Scott (1970), a formulation for s based on the local value of the turbulent dissipation rate was assumed, giving:

$$k_L = \mathscr{C}_L \sqrt{\mathscr{D}\sqrt{\frac{\epsilon}{\nu_c}}} \tag{2.48}$$

where $\mathscr{C}_L$ is a fitting constant (assumed equal to 0.4 by the authors or equal to 1.13 as in the work of Kawase et al., 1987), ν_c is the kinematic viscosity of the continuous phase and ϵ is the local value of the turbulent dissipation rate.

Now that the mass transfer coefficient is introduced, the functions G and $\dot{\phi}_b$ of Eq. (2.33) can be easily formulate. By considering a spherical bubble of size L, total number of oxygen moles ϕ_b, interfacial area $k_A L^2$ and mass $\rho_b k_V L^3$, it is possible to write the continuous rate of change of bubble composition, $\dot{\phi}_b$, due to mass transfer as:

$$\dot{\phi}_b(L, \phi_b; \mathbf{x}, t) = k_L k_A L^2 \left(C_c - H \frac{\phi_b}{k_V L^3} \right), \tag{2.49}$$

Furthermore, the term G, representing the bubble growth/shrink rate, can be evaluated by a simple mass balance on a single bubble:

$$G(L, \phi_b; \mathbf{x}, t) = \frac{2 k_L M_w}{\rho_b} \left(C_c - H \frac{\phi_b}{k_V L^3} \right), \tag{2.50}$$

where M_w is the molecular weight of the transferring solute (oxygen), C_c is the molar concentration of solute in the continuous phase and H is the dimensionless Henry constant.

2.2.2 Discontinuous events modeling

In this part, the functional form of the collisional term $h(L, \phi_b; \mathbf{x}, t)$ of Eq. (2.33) for coalescence and breakage of bubbles in liquid will be shown. A thorough discussion for a generic PBE can be found in Section 2.1.1, here only the final expression is reported (the dependencies on space and time will be omitted for clarity):

$$\begin{aligned} h(L,\phi_b) = \frac{1}{2}\int_0^L \int_0^{\phi_b} \alpha\left((L^3-\lambda^3)^{\frac{1}{3}},\lambda\right) n\left((L^3-\lambda^3)^{\frac{1}{3}},\phi_b-\phi_{b,\lambda}\right) \\ \times n\left(\lambda,\phi_{b,\lambda}\right)\frac{L^2}{(L^3-\lambda^3)^{\frac{2}{3}}}\mathrm{d}\lambda\mathrm{d}\phi_{b,\lambda} - n(L,\phi_b)\iint_0^\infty \alpha(L,\lambda)n(\lambda,\phi_{b,\lambda})\mathrm{d}\lambda\mathrm{d}\phi_{b,\lambda} \\ + \int_L^\infty\int_{\phi_b}^\infty \beta(\lambda)P(L,\phi_b|\lambda,\phi_{b,\lambda})n(\lambda,\phi_{b,\lambda})\mathrm{d}\lambda\mathrm{d}\phi_{b,\lambda} - \beta(L)n(L,\phi_b), \end{aligned} \tag{2.51}$$

where α, β and P are respectively the coalescence kernel, the breakage kernel and the daughter distribution function that must be formulated for properly describing the collisional phenomena between bubbles.

Many models for these terms, specifically for bubble coalescence and break-up in disperse gas-liquid systems, were proposed in the last years. In this part of the work, the most used formulations will be presented, however a detailed analysis of these models is out of the aims of this work. It must be remarked that usually these kernels are derived from a mixture of theoretical and empirical considerations and for this reason they may have a limited range of validity, corresponding to the experimentally investigated operating conditions for a specific equipment.

Breakage frequency

Bubble breakage is a complex phenomenon involving a balance between external stresses that tend to break the bubble and viscous and interfacial forces that oppose to its deformation. Most likely stresses causing instability on gas-liquid interface are turbulent fluctuations and shear rates on continuous phase.

The study on this kind of process is usually conducted on liquid-liquid systems due to the easy of controlling the experimental setting (in comparison to gas-liquid systems), however the conclusions can be extended to other fluid-fluid systems. Narsimhan et al. (1979) proposed a model for drops breakage in a liquid-liquid system based on the fact that the eddies arrival at drop surface and the consequent break-up event may be considered as instantaneous processes and independent of the history of the various drops. Moreover, only eddies smaller than the droplets and with sufficient energy are able to break the drop, while bigger eddies only contribute to the transport of the dispersed particles.

Based on the theory of Narsimhan, Lee et al. (1987) proposed the following model for bubble break-up:

$$\beta(V_L) = C_1\epsilon^{1/3}L^{-2/3}\left[\frac{1}{L}\int_0^L 1 - F(X_c)\mathrm{d}\lambda\right], \tag{2.52}$$

where $\beta(V_L)$ indicates the breakage frequency of a bubble of volume V_L (with diameter equal to L), ϵ is the turbulent dissipation of kinetic energy rate of the continuous phase and $F(X_c)$ represents the Chi-squared distribution function with three degrees of freedom, with X_c defined as:

$$X_c = C_2 \frac{\sigma L^2}{\rho_c \epsilon^{2/3}} \lambda^{-11/3}, \tag{2.53}$$

where σ is the surface tension, ρ_c is the density of the continuous phase. It is important to notice that C_1 and C_2 are two parameters to be obtained through experiments.

Alopaeus et al. (2002) extended the model of Narsimhan for drops in liquid, introducing an additional term for considering viscous forces opposing to breakage proportional to the viscosity of the dispersed phase. The proposed expression was the following:

$$\beta(L) = C_1 \, \epsilon^{1/3} \mathrm{erfc}\left(\sqrt{C_2 \frac{\sigma}{\rho_c \epsilon^{2/3} L^{5/3}} + C_3 \frac{\mu_d}{\sqrt{\rho_c \rho_d} \epsilon^{1/3} L^{4/3}}} \right), \tag{2.54}$$

where C_1, C_2 and C_3 are three fitting parameters, $\mathrm{erfc}(x)$ indicates the complementary error function and ρ_d and μ_d are respectively density and viscosity of the disperse phase.

Laakkonen et al. (2006) proposed a modification of this kernel in order to consider also gas-liquid systems, substituting the dependence on disperse phase viscosity with the continuous one, obtaining the following expression:

$$\beta(L) = C_1 \, \epsilon^{1/3} \mathrm{erfc}\left(\sqrt{C_2 \frac{\sigma}{\rho_c \epsilon^{2/3} L^{5/3}} + C_3 \frac{\mu_c}{\sqrt{\rho_c \rho_d} \epsilon^{1/3} L^{4/3}}} \right). \tag{2.55}$$

In this way, the viscous forces contrasting the bubble breakage are considered proportional to the viscosity of the continuous phase, as experimentally observed by Walter and Blanch (1986). Moreover, Laakkonen et al. (2006) performed an extensive experimental studies on a gas-liquid stirred tank reactor in order to find the proposed fitting parameter: $C_1 = 6.0$, $C_2 = 0.04$ and $C_3 = 0.01$. However, the validity range these values is strictly defined by the experimentally investigated operating conditions for such equipment.

Another popular kernel for binary bubble breakage was formulated by Luo and Svendsen (1996):

$$\beta(V_L) = C_1 (1 - \alpha_d) \left(\frac{\epsilon}{L^2} \right)^{1/3} \int_{\zeta_{min}}^{1} \frac{(1+\zeta)^2}{\zeta^{11/3}} \exp\left[-\frac{C_2 \sigma C_f(f)}{\rho_c \epsilon^{2/3} L^{5/3} \zeta^{11/3}} \right] \mathrm{d}\zeta, \tag{2.56}$$

where α_d is the volume fraction of the disperse phase and $\zeta = \lambda_e / L$ is the ratio between the dimension of eddies able to break the bubble and the size of the bubble itself. The function C_f is defined as follows:

$$C_f(f) = f^{2/3} + (1-f)^{2/3} - 1, \tag{2.57}$$

where f represent the ration between the volume of a daughter bubble an the volume of the mother bubble. It should be noticed that this kernel, despite of others, also includes information on the daughter distribution function. The value ζ_{min} is linked to the minimum eddie size according to Kolmogorov scale:

$$\zeta_{min} = \frac{\lambda_{e,min}}{L} = \frac{11.4}{L}\left(\frac{\mu_c^3}{\rho_c^3\,\epsilon}\right)^{1/4}. \tag{2.58}$$

The two parameters C_1 and C_2 are chosen by fitting with the experiments.

In conclusion, it is worth mentioning a model without parameters proposed by Lehr et al. (2002) and successfully validated for gas-liquid bubble columns:

$$\beta(L) = \frac{1}{2}\frac{L^{5/3}\rho_c^{7/5}\epsilon^{19/15}}{\sigma^{7/5}}\exp\left(-\sqrt{2}\frac{L^3\epsilon^{6/5}\rho_c^{9/5}}{\sigma^{9/5}}\right). \tag{2.59}$$

Among all these formulations, it is possible to recognize the characteristics needed for the implementation in a population balance solution code. In fact, the numerical solution of the PBE is a very demanding task from the computational point of view, especially if the final aim is to couple the PBM with the CFD description for industrial scale equipment. For this reason, formulations involving the numerical solution of integrals or without fitting parameters must be avoided because they lack of flexibility and computational speed compared to others. Eq. (2.55) of Laakkonen et al. (2006) has all the main characteristic of a good kernel formulation for this dissertation purpose and therefore in this work will be used and investigated.

Daughter distribution function

As indicated in Section 2.1.1, it is necessary to indicate not only the frequency of the breakage event, but also the number of bubbles generated by such event in order to give a complete description of the break-up phenomenon. In general, the daughter distribution function depends on the size of the mother bubble and on local turbulence intensity; the breaking bubble may divide into two or more bubbles according to gas redistribution mechanism caused by bubble internal pressure and external stresses: the number of fragments depends on the density difference between the continuous and the disperse phase and on the viscosity of the disperse phase. When this difference is significant (and the disperse phase is not very viscous), like in bubbly flows, binary breakage is the most likely event (Andersson and Andersson, 2006), although the dimension of the daughter bubbles may be very different.

Lehr et al. (2002) formulated a daughter distribution function based on local fluid properties and turbulence, as well as the size of mother bubble λ, assuming a binary breakage:

$$P(V_L|V_\lambda) = \begin{cases} \dfrac{6}{\pi^{3/2}L^3} \dfrac{\exp\left[-\dfrac{9}{4}\left(\ln\left[2^{2/5}\left(\dfrac{L\rho_c^{3/5}\epsilon^{2/5}}{\sigma^{3/5}}\right)\right]\right)^2\right]}{1+\mathrm{erf}\left[\dfrac{3}{2}\left(2^{1/15}\left(\dfrac{\lambda\rho_c^{3/5}\epsilon^{2/5}}{\sigma^{3/5}}\right)\right)\right]} & \text{with } 0 \le V_L \le \dfrac{V_\lambda}{2}; \\ P(V_L - V_\lambda, V_\lambda) & \text{with } \dfrac{V_\lambda}{2} \le V_L \le V_\lambda. \end{cases} \tag{2.60}$$

This model, combined with breakage kernel of Eq. (2.59), was successfully validated for the experimentally investigated bubble column by Lehr et al. (2002).

Another model based on phenomenological evidence was formulated by Luo and Svendsen (1996), and must be specifically combined with the corresponding breakage frequency shown on Eq. (2.56):

$$P(V_L|V_\lambda) = \frac{2\displaystyle\int_{\zeta_{min}}^{1}(1+\zeta)^2\zeta^{-11/3}\exp(-x_c)d\zeta}{\nu_L\displaystyle\int_0^1\int_{\zeta_{min}}^{1}(1+\zeta)^2\zeta^{-11/3}\exp(-x_c)d\zeta df} \tag{2.61}$$

where x_c is a dimensionless representing the breakage critical energy and ζ is the same quantity defined in Eq. (2.56).

In contrast with these complex models, Laakkonen et al. (2006) proposed a daughter distribution function based on a common statistical distribution, the $\beta-$Probability Density Function (β-PDF), normalized on the number of fragments generated by the process as follows:

$$P(L|\lambda) = N_f\left(9+\frac{33}{2}C+9C^2+\frac{3}{2}C^3\right)\left(\frac{L^2}{\lambda^3}\right)\left(\frac{L^3}{\lambda^3}\right)^2\left(1-\frac{L^3}{\lambda^3}\right)^C, \tag{2.62}$$

where λ and L are respectively the size of the mother and of the daughter bubble, and $N_f = 4/3 + C/3$ is a factor calculated by imposing two essential conditions:

$$\begin{cases} \displaystyle\int_0^\infty P(L|\lambda)\mathrm{d}L = N_f, \\ \displaystyle\int_0^\infty P(L|\lambda)L^3\mathrm{d}L = \lambda^3. \end{cases} \tag{2.63}$$

This model was proposed in order to avoid heavy numerical calculations (when PBE is solved) due to complex dependence on fluid properties, still giving results similar to other formulations: β-PDF was successfully validated in a case of aerated stirred tanks (Laakkonen et al., 2006; Petitti et al., 2010), and due to its flexibility can be extended also in the case of bubble columns. However a validation process with experiments is still needed.

A slight modification of this functional was proposed by Buffo et al. (2013), in which

the dependence on bubble composition ϕ_b (i.e., the total number of moles of a chemical component) was included:

$$P(L, \phi_b | \lambda, \phi_{b,\lambda}) = \frac{1}{12}(C+1)^2(C+2)^2(C+3)^2(C+4)^2 \times \frac{\phi_b^2}{\phi_{b,\lambda}^3}\left(1-\frac{\phi_b}{\phi_{b,\lambda}}\right)^C \frac{L^2}{\lambda^3}\left(\frac{L^3}{\lambda^3}\right)^2\left(1-\frac{L^3}{\lambda^3}\right)^C, \quad (2.64)$$

where λ and $\phi_{b,\lambda}$ represent respectively the size and the number of moles of the parent bubble, while L and ϕ_b are the properties of the daughter bubble. C is a parameter that indicates the type of breakage and is equal to two for binary breakage, the most common situation in the case of gas bubbles (Andersson and Andersson, 2006). It is clear that this formulation will be used in a bivariate case, while Eq. (2.62) will be used when a monovariate PBE will be solved.

Coalescence kernel

Bubble coalescence is a mechanism composed by three steps: approach and collision between two bubbles, drainage of the liquid film separating the bubbles and their final union consequent to the breakage of the liquid film. The first step brings very close the two colliding bubbles, trapping a film of liquid between them: this phase is controlled by the external forces acting on the bubbles and their motion. The next step is the controlling one: in fact, the trapped liquid must be drained out to reach the critical thickness at which break-up occurs, caused by fluid instabilities. Moreover, there are numerous mechanisms that may induce bubble collision: turbulent eddies may cause relative motion and the subsequent collision between bubbles, velocity gradients of the continuous phase may make bubbles approach and collide or a smaller bubble trapped into the wake of a bigger rising bubble may reach the other one due to buoyancy and coalesce. The first two mechanisms are prevailing in the case of turbulent systems or when the continuous phase moves as a consequence of agitation, while in the case of stagnant liquid and low turbulent fluctuations the third mechanism is predominant. A model for bubble coalescence kernels must contain the information relating to the frequency of collision due to various mechanisms, and the efficiency of collision due to the breakage of the liquid film, considering that not all bubble collisions may generate a new bubble (Jakobsen, 2008; Marchisio and Fox, 2013).

A generic form of the coalescence kernel is generally derived in analogy with the kinetic theory of gases (Marchisio and Fox, 2013), and its calculation is based on the number of bubbles swept by one bubble moving in a collisional cylinder with diameter equal to the summation of the radii of the two colliding bubbles. For two bubbles of sizes L and λ, the kernel can be approximated by:

$$\alpha(\lambda, L, \mathbf{U}_r) = \frac{\pi}{4}(\lambda + L)^2 |\mathbf{U}_r| \eta(\mathbf{U}_r) \quad (2.65)$$

where the first term represents the section of the collisional cylinder and the second term involving $\mathbf{U}_r = \mathbf{U}_\lambda - \mathbf{U}_L$ quantifies the relative velocity of two colliding bubbles. Furthermore, the function $\eta(\mathbf{U}_r)$ says how efficient is the collision to produce coalescence. This term is proportional to the ratio between the collision time interval and the coalescence time interval: there is coalescence only if the two bubbles are in contact for a time sufficient to allow liquid drainage for reducing the film thickness up to the critical value. Collisional time is linked to the turbulence characteristic scale and the rate of turbulence dissipation energy ϵ. Coalescence time depends on the mobility of bubble surface: for example in high viscosity systems, coalescence times are bigger due to the drainage in laminar regime. In general, other aspects may influence the coalescence time interval, as the presence of surfactant or impurities in the continuous phase.

It is possible to introduce bubble velocity into the population balance description by solving Eq. (2.31), while in Eq. (2.33) the dependence on velocity disappeared due to integration process, reducing the computational costs for the problem solution. Moreover, the knowledge of the velocities of colliding bubbles is in general not needed when turbulence prevails over other collisional mechanism. In the work of Coulaloglou and Tavlarides (1977), a very popular kernel based on isotropic turbulence theory was derived:

$$\alpha(\lambda, L) = C_1\, \epsilon^{1/3}(\lambda + L)^2(\lambda^{2/3} + L^{2/3})^{1/2}\eta(\lambda, L), \tag{2.66}$$

where C_1 is a constant of the model and ϵ is the local turbulent dissipation rate. The expression proposed for the coalescence efficiency is the following:

$$\eta(\lambda, L) = \exp\left(-C_2\sqrt{\frac{2\rho_c\epsilon^{2/3}}{\sigma}\frac{\lambda L}{\lambda + L}}\right) \tag{2.67}$$

in which the inertia of the draining liquid and the surface tension σ are considered the most important factors generating the breakage of the film between the two colliding bubbles. Prince and Blanch (1990) proposed another formulation for the efficiency, based on the fact that bubble surfaces are stationary during liquid drainage:

$$\eta(\lambda, L) = \exp\left(-C_2\,\frac{\mu_c\rho_c\epsilon}{\sigma^2}\left(\frac{\lambda L}{\lambda + L}\right)^4\right). \tag{2.68}$$

In the work of (Laakkonen et al., 2006; Petitti et al., 2010), Eq. (2.66) combined with Eq. (2.68) was used for simulate the evolution of a disperse phase in an aerated stirred tank, showing a good match with the experimental data by using $C_1 = 0.88$ and $C_2 = 6 \cdot 10^9$. When the relative importance of turbulent approaching mechanism decreases as in bubble columns, the value of C_1 must be changed in order to reduce the coalescence frequency. The value tested in this work is $C_1 = 0.28$, but further tests are necessary to ensure the correctness of a similar procedure.

As it is possible to see in Eq. (2.66), the coalescence kernel for a pure air-water sys-

tem depends only on bubble size; the same dependence is observed in Eq. (2.55) for bubble breakage frequency. However, other systems may exhibit an effect of composition. As previously said, a remarkable example is the contaminated gas-liquid systems, where the presence of impurities accumulating at the gas-liquid interface may significantly increase the coalescence time reducing the coalescence efficiency. Although the effect of composition on kernels is clear from a qualitative point of view, there is still a lack of knowledge regarding the kernel formulation under such conditions. For this reason, it is worth testing the accuracy and the robustness of the investigated multivariate population balance by introducing kernels with a dependence on bubble composition. In the proposed kernel based on the work of Marshall Jr. et al. (2011), a composition-dependent term is multiplied by the classical size-dependent kernel, amplifying or hindering coalescence, according to the specific chemical affinity of components in the disperse phase. Although this model does not represent any realistic gas-liquid system, the purpose of accuracy assessment of the solution methods is still valid. In fact, similar kernel formulation may be interesting in other application areas (e.g., solid-liquid or gas-solid flows). The functional form of the composition dependent kernel is the following:

$$\alpha(\lambda, L, \xi_\lambda, \xi_L) = \alpha_1(\lambda, L)\,\alpha_2(\xi_\lambda, \xi_L), \tag{2.69}$$

where ξ_λ and ξ_L are respectively the molar fractions of oxygen in the bubbles of size λ and L. The composition factor $\alpha_2(\xi_\lambda, \xi_L)$ is defined in the following way:

$$\alpha_2(\xi_\lambda, \xi_L) = \exp\{C_1\xi_\lambda\xi_L + C_2(1-\xi_\lambda)(1-\xi_L) + C_3(\xi_\lambda + \xi_L - 2\xi_\lambda\xi_L)\}, \tag{2.70}$$

where the constants C_1, C_2 and C_3 influence the frequency of coalescence (positive values to amplify, negative values to hinder) in case of preferential oxygen-oxygen, nitrogen-nitrogen and oxygen-nitrogen coalescence respectively. Here the following values are assumed: $C_1 = 3$, $C_2 = -2$ and $C_3 = 2$, representing the case in which oxygen-oxygen is the most likely coalescence event over oxygen-nitrogen, while nitrogen-nitrogen is unlikely.

2.3 Solution methods

In the previous sections, the general concept of PBE and a specific formulation for a gas-liquid systems were introduced. As explained in Section 2.2, it is possible for this particular case to derive a bivariate PBE (with bubble size and composition of a chemical component as internal coordinates), Eq. (2.33) and Eq. (2.35), by integrating out the dependence on bubble velocity $\mathbf{U}_\mathrm{b}$ of the GPBE indicated in Eq. (2.31), losing therefore the information about velocity distribution and simplifying the description of the system. Moreover, by using the same procedure it is possible to obtain a monovariate PBE, Eq. (2.37) and Eq. (2.38), considering all the bubbles have the same composition. In Chapter 3, a method for calculating the bubble velocity conditioned over the values of bubble size and composition, $\check{\mathbf{U}}_\mathrm{b}(L, \phi_\mathrm{b}; \mathbf{x}, t)$ defined in Eq. (2.34) is explained in detail; in this part of this dissertation the velocity of

bubbles is assumed to be known.

As remarked in Section 2.1, it is possible to deterministically characterize the evolution of NDF in space and time by solving the PBE; however the analytical solution is available only for very simple systems considering particular initial and boundary conditions and simplified or no discontinuous events (Hulburt and Katz, 1964). As seen in Section 2.2.1 and Section 2.2.2, where functional forms for realistically modeling of oxygen absorption in liquid and of collisional events for air bubbles in water are introduced, the nature of the PBE can be intrinsically non-linear. Therefore, numerical methods are in practical cases the only approach available.

An overview of different numerical methods for the solution of PBE can be found in Chapter 1. Here it is important to remind that these methods can be classified according to the adopted solution strategy: Sectional Methods (SM), in which the internal-coordinate space is discretized using different strategies (Classes Methods (Vanni, 2000; Kumar et al., 2008), Finite Volume Methods (Gunawan et al., 2004) and Finite Element Methods (Godin et al., 1999) belong to this group); Methods of Moments (MOM) (Hulburt and Katz, 1964), in which the dependence on internal coordinates is integrated out by solving the transport equation only for some moments of NDF; Monte Carlo Methods (MCM) (Liffman, 1992; Zhao et al., 2007), i.e., direct numerical simulations describing the evolution of a certain number of notional bubbles assumed to be statistically significant for the entire population.

As already pointed out in this dissertation, MOM are very promising due to their low computational load among these numerical methods, and can be coupled with CFD in order to obtain prediction of industrial scale systems with affordable computational costs. However, it is important to remark that MOM are approximated methods requiring the assessment of the accuracy through comparison with other detailed solution methods, at least for simplified cases (Zucca et al., 2007; Buffo et al., 2013).

Besides this classification, it is important to remind that solution methods for monovariate NDF (i.e., with only one internal coordinate) and bivariate or in general multivariate NDF (i.e., with two or more internal coordinates) can be very different in terms of algorithms or strategies. In fact, while MCM maintain the same solution structure in both cases (increasing only the memory requirements), the extension of methods originally formulated for monovariate to multivariate descriptions, as SM and MOM, is not straightforward. As said in Chapter 1, SM for multivariate PBE introduce the problem of the discretization for a generic N-dimensional phase space, that can be solved in different ways (Kumar et al., 2008; Nandanwar and Kumar, 2008) however, increasing enormously the computational costs compared to the monovariate case. Also in this case, MOM seem to be the only way feasible for predicting the evolution of a multivariate NDF in a large scale multiphase equipment (Buffo et al., 2012; Petitti et al., 2012), although solution methods are different with respect to the monovariate case.

A definition of a generic-order moment for a very general NDF is expressed in Eq. (2.6), while in Eq. (2.30) the definition is reported of a generic-order moment according to the NDF written as in Eq. (2.29) for a bubble population distributed over size, composition and

velocity. Since in this section the solution methods used in this work will be presented, it is crucial to define these quantities:

$$M_{k,l}(\mathbf{x},t) = \iint_0^\infty n(L,\phi_\mathrm{b};\mathbf{x},t) L^k \phi_\mathrm{b}^l \,\mathrm{d}L\,\mathrm{d}\phi_\mathrm{b}, \tag{2.71}$$

$$M_k(\mathbf{x},t) = \int_0^\infty \tilde{n}(L;\mathbf{x},t) L^k \mathrm{d}L, \tag{2.72}$$

representing respectively the moment of order k with respect to bubble size and order l with respect to bubble oxygen composition according to the bivariate NDF defined in Eq. (2.32) and the moment of order k with respect to bubble size according to the monovariate NDF defined in Eq. (2.36).

By applying the moment transform as defined in Eq. (2.71) for all the terms reported in Eq. (2.33), the transport equation for a generic moment can be written (since both number density functions and moments depend on space and time, the dependencies are omitted for clarity):

$$\frac{\partial M_{k,l}}{\partial t} = -\frac{\partial}{\partial \mathbf{x}}(M_{k,l}\check{\mathbf{U}}_{k,l}) + \int_0^\infty k\, L^k\, G(L,\phi_\mathrm{b})\, n(L,\phi_\mathrm{b})\,\mathrm{d}L + \int_0^\infty l\, \phi_\mathrm{b}^l\, \dot{\phi}_\mathrm{b}(L,\phi_\mathrm{b})\, n(L,\phi_\mathrm{b})\,\mathrm{d}\phi_\mathrm{b} + H_{k,l}, \tag{2.73}$$

where the velocity of the generic moment $\check{\mathbf{U}}_{k,l}$ and the collisional term $H_{k,l}$ are defined as follows:

$$\check{\mathbf{U}}_{k,l} = \frac{\iint_0^\infty \check{\mathbf{U}}_\mathrm{b}(L,\phi_\mathrm{b})\, n(L,\phi_\mathrm{b})\, L^k \phi_\mathrm{b}^l \,\mathrm{d}L\,\mathrm{d}\phi_\mathrm{b}}{\iint_0^\infty n(L,\phi_\mathrm{b})\, L^k \phi_\mathrm{b}^l \,\mathrm{d}L\,\mathrm{d}\phi_\mathrm{b}}, \tag{2.74}$$

$$H_{k,l} = \iint_0^\infty h(L,\phi_\mathrm{b})\, L^k \phi_\mathrm{b}^l \,\mathrm{d}L\,\mathrm{d}\phi_\mathrm{b}. \tag{2.75}$$

As seen in Eq. (2.35), spatial gradients vanish in a closed spatially homogeneous system and Eq. (2.73) becomes:

$$\frac{\mathrm{d}M_{k,l}}{\mathrm{d}t} = \int_0^\infty k\, L^k\, G(L,\phi_\mathrm{b})\, n(L,\phi_\mathrm{b})\,\mathrm{d}L + \int_0^\infty l\, \phi_\mathrm{b}^l\, \dot{\phi}_\mathrm{b}(L,\phi_\mathrm{b})\, n(L,\phi_\mathrm{b})\,\mathrm{d}\phi_\mathrm{b} + H_{k,l}. \tag{2.76}$$

In analogy with the bivariate case, it is possible to write for a generic moment of the monovariate PBE the following transport equations for the inhomogeneous and homoge-

neous systems respectively:

$$\frac{\partial M_k}{\partial t} = -\frac{\partial}{\partial \mathbf{x}}(M_k \check{\mathbf{U}}_k) + \int_0^\infty k\, L^k\, G(L)\, n(L)\, \mathrm{d}L + H_k, \tag{2.77}$$

$$\frac{\mathrm{d}M_k}{\mathrm{d}t} = \int_0^\infty k\, L^k\, G(L)\, n(L)\, \mathrm{d}L + H_k, \tag{2.78}$$

where now the velocity of the generic moment $\check{\mathbf{U}}_k$ and the collisional term H_k are defined as:

$$\check{\mathbf{U}}_k = \frac{\displaystyle\int_0^\infty \check{\mathbf{U}}_\mathrm{b}(L)\, n(L)\, L^k\, \mathrm{d}L}{\displaystyle\int_0^\infty n(L)\, L^k\, \mathrm{d}L}, \tag{2.79}$$

$$H_k = \int_0^\infty h(L)\, L^k \mathrm{d}L. \tag{2.80}$$

It is clear that Eq. (2.73) and Eqs. (2.76) to (2.78) are not closed, because the functional form of the underlying NDF is in general not known. This is the so-called "closure problem" pointed out in the first work on MOM of Hulburt and Katz (1964). As already reported in Chapter 1, a closure was proposed by assuming the functional form of the NDF as a summation of delta functions centered on nodes of Gaussian quadrature approximation (McGraw, 1997; Marchisio and Fox, 2013). By using this approach, the following expression can be written for the bivariate case:

$$n(L, \phi_\mathrm{b}) = \sum_{i=1}^{N} w_i\, \delta(L - L_i)\, \delta(\phi_\mathrm{b} - \phi_{\mathrm{b},i}), \tag{2.81}$$

and for the monovariate case:

$$n(L) = \sum_{i=1}^{N} w_i\, \delta(L - L_i). \tag{2.82}$$

From the physical point of view, Eq. (2.81) can be easily explained: the entire bubble population is divided into N different groups, each one of them contains bubbles of uniform size and composition and corresponds to a node of the quadrature approximation. The meaning of each term is the following: w_i is the number density (i.e., the number of bubbles per unit of total volume, consequently to the definition of number density function n) of the bubbles with size equal to L_i and composition equal to $\phi_{\mathrm{b},i}$. In the monovariate case, the explanation is straightforward.

By using the quadrature approximation expressed in Eq. (2.81) and Eq. (2.82), it is possible write all the unclosed terms of Eq. (2.73) and Eq. (2.78) (and, of course, their homogenous system counterparts) as a function of N quadrature weights and nodes. By applying

the moment transform to the collisional term reported Eq. (2.51) and then substituting NDF dependence with Eq. (2.81), it is possible to write (omitting all the passages):

$$H_{k,l} = \frac{1}{2}\sum_{i=1}^{N}\sum_{j=1}^{N}\alpha(L_i,L_j)w_i w_j\left[(L_i^3+L_j^3)^{k/3}\left(\phi_{\mathrm{b},i}+\phi_{\mathrm{b},j}\right)^l - L_i^k\phi_{\mathrm{b},i}^l - L_j^k\phi_{\mathrm{b},j}^l\right] + \sum_{i=1}^{N}\beta(L_i)w_i(\bar{P}_{k,l}^{(i)} - L_i^k\phi_{\mathrm{b},i}^l) \tag{2.83}$$

where $\alpha(L_i, L_j)$ and $\beta(L_i)$ are respectively the aggregation kernel and the breakage frequency, modeled as in Section 2.2.2, and

$$\bar{P}_{k,l}^{(i)} = \int_{\Omega_L}\int_{\Omega_{\phi_\mathrm{b}}} L^k\phi_\mathrm{b}^l P(L_i,\phi_{\mathrm{b},i}|\lambda,\phi_{\mathrm{b},\lambda})\,\mathrm{d}L\,\mathrm{d}\phi_\mathrm{b}, \tag{2.84}$$

is the generic order moment (k with respect to size and l with respect of composition) of the daughter distribution function, described in Section 2.2.2. For the monovariate case, the source term of a generic order moment M_k can be written as (omitting all the calculations):

$$H_k = \frac{1}{2}\sum_{i=1}^{N}\sum_{j=1}^{N}\alpha(L_i,L_j)w_i w_j\left[(L_i^3+L_j^3)^{k/3} - L_i^k - L_j^k\right] + \sum_{i=1}^{N}\beta(L_i)w_i(\bar{P}_k^{(i)} - L_i^k). \tag{2.85}$$

As for Eq. (2.83) and Eq. (2.85), all the unclosed terms of moment transport equation can be written in terms of weights and quadrature nodes. At this point, it is crucial to establish a procedure for relating weights and nodes to the underlying moment set. This is the topic of the following sections, where QBMM will be introduced.

It is worth mentioning also an important case examined in this dissertation, namely when the system is open, well-mixed, and there is continuous injection and extraction of bubbles in a liquid. The transport equation for a generic order moment k, l can be written as follows:

$$\frac{\mathrm{d}\,M_{k,l}}{\mathrm{d}t} = -\frac{(M_{k,l})_{out} - (M_{k,l})_{in}}{\tau} + \int_0^\infty k\,L^k\,G\,n(L,\phi_\mathrm{b})\mathrm{d}L + \int_0^\infty l\,\phi_\mathrm{b}^l\,\dot{\phi}_\mathrm{b}\,n(L,\phi_\mathrm{b})\mathrm{d}\phi_\mathrm{b} + H_{k,l}. \tag{2.86}$$

where τ is the bubble mean residence time and $(M_{k,l})_{in}$ is the generic moment of the inlet bubble population. By establishing an analogy with the continuous stirred tank reactor theory, it is possible to assume assume that $(M_{k,l})_{out}$ is equal to $M_{k,l}$. The importance of this case will be pointed out in the following sections.

2.3.1 Direct Simulation Monte Carlo

The method described in this section takes into account the evolution of the bubble population in a volume V, divided in N_v smaller and well-mixed subvolumes V_v (with $v = 1, 2, \dots, N_v$), called "reservoirs". Since the actual population within a single subvolume can be extremely large, it is reasonable to consider only a portion $\Delta V_v = \alpha V_v$ with $\alpha << 1$ in order to deal with a reasonable number of bubbles.

Each bubble is characterized by the indices i and v, indicating the $i-$th bubble of the subvolume ΔV_v, with size L_i and oxygen number of moles $\phi_{\mathrm{b},i}$. The method calculates the frequency of the considered events:

- Coalescence between two bubbles i and j of the same subvolume ΔV_v.
  Since coalescence is a consequence of collision between two bubbles, its rate per unit volume is formulated as follows:

$$r^{(c)}_{i,j,v} = \alpha_{i,j,v} c_{i,v} c_{j,v} \tag{2.87}$$

  where $\alpha_{i,j,v} = \alpha_v(L_{i,v}, \phi_{\mathrm{b},i,v}; L_{j,v}, \phi_{\mathrm{b},j,v})$ is the coalescence kernel, $c_{i,v}$ and $c_{j,v}$ are the numerical concentration of the $i-$th and $j-$th bubble (i.e., number of bubbles per unit volume). Considering that for only one bubble ($i-$th or $j-$th) the concentration in the subvolume ΔV_v is equal to $1/\Delta V_v$, it is possible to write the coalescence frequency as:

$$f^{(c)}_{i,j,v} = r^{(c)}_{i,j,v} \Delta V_v = \alpha_{i,j,v} c_{i,v} c_{j,v} \Delta V_v = \frac{\alpha_{i,j,v}}{\Delta V_v}. \tag{2.88}$$

- Breakage of the $i-$th bubble in subvolume ΔV_v.
  Since the breakage is a first order process depending on the hydrodynamic field, its rate per unit volume is expressed as:

$$r^{(b)}_{i,v} = \beta_{i,v} c_{i,v}, \tag{2.89}$$

  where $\beta_{i,v} = \beta_v(L_i)$ is the breakage kernel and $c_{i,v}$ the concentration of the $i-$th bubble in subvolume ΔV_v. As before, the frequency is defined as:

$$f^{(b)}_{i,v} = r^{(b)}_{i,v} \Delta V_v = \beta_{i,v}. \tag{2.90}$$

  In fact, the breakage kernel $\beta(L_i)$ has units of the inversion of time.

- Bubble i moving from subvolume ΔV_v to another reservoir.
  Inside the physical volume V, a bubble may move from subvolume ΔV_v to any point of the system: if it remains into the same reservoir, it is reasonable to assume that another identical bubble of the reservoir V_v moves into the subvolume ΔV_v, replacing the old one, thus canceling the effect of this phenomenon. On the contrary, when the bubble moves to another reservoir, it is necessary to define the frequency of this event:

$$f_{i,v}^{(m)} = \frac{1}{\tau_v}, \tag{2.91}$$

where τ_v is the average residence time of a bubble in reservoir v. It is obvious that, when a new bubble enters a different reservoir V_u, it does not directly move into the subvolume ΔV_u due to the small size of the subvolume compared to the reservoir. However, it is reasonable to assume that when a bubble moves from ΔV_v to V_u, another identical bubble moves from V_u to ΔV_u. Therefore it is possible to assume that bubble motion takes place directly among subvolumes.

- Bubble i injected into the subvolume ΔV_v from outside.
  Since a generic open system is considered, also the injection frequency is indicated with $f_{i,v}^{(i)}$, corresponding to the number of bubbles entering into the system from outside per unit time.

The total event frequency is the sum of the frequency of all possible events:

$$f^{(tot)} = \sum_{v=1}^{N_v} \left(\sum_{i=1}^{N_b(v)} \sum_{j=i+1}^{N_b(v)} f_{i,j,v}^{(c)} + \sum_{i=1}^{N_b(v)} f_{i,v}^{(b)} + \sum_{i=1}^{N_b(v)} f_{i,v}^{(m)} + f_{i,v}^{(i)} \right) \tag{2.92}$$

where $N_b(v)$ is the number of bubbles contained in ΔV_v.

If an event has occurred at time t_0, the probability for a new event of any type to take place at time $t = t_0 + \Delta t$ is described by the following law, typical of a Poisson process:

$$\Pr(\Delta t) = 1 - \exp\left(-f^{(tot)} \Delta t\right). \tag{2.93}$$

In other words, it is possible to determine the interval of quiescence Δt at which a new event occurs by means of a random variable with cumulative probability density function expressed in Eq. (2.93).

Once determined the time at which an event occurs, it is necessary to establish the nature of this event. The probability of a generic event k is defined as:

$$\Pr_k = \frac{f_k}{f^{(tot)}}. \tag{2.94}$$

After having ordered properly the list of all possible events, a random number ξ is picked from a uniform distribution between 0 and 1 and the chosen event is that with the index q, satisfying the following relation:

$$\sum_{k=1}^{q-1} \Pr_k < \xi \leq \sum_{k=1}^{q} \Pr_k. \tag{2.95}$$

This method is the so-called "inversion method" (Gillespie, 1976; Garcia et al., 1987; Kruis et al., 2000). Another method used to determine the nature of the event is the "acceptance-

rejection" procedure (Smith and Matsoukas, 1998; Tandon and Rosner, 1999), where an event k is randomly selected (independently from its actual frequency f_k: the event is accepted if

$$\xi < \frac{f_k}{\max_i f_i} \tag{2.96}$$

where ξ a uniformly distributed (between 0 and 1) random number. If the event is rejected, a new event is selected and the procedure is repeated using a new random number. However, this method is more susceptible to the goodness of the random number generator algorithm leading to larger errors compared with the more rigorous "inversion method" (Kruis et al., 2000). Therefore, the "inversion method" is used in this work.

All the information relating to the bubble population is kept in a large array $\boldsymbol{R}$, whose element $\boldsymbol{R}_{v,i,k}$ is the value of the $k-$th internal coordinate of the $i-$th bubble belonging to the subvolume ΔV_v. After the procedure determining the quiescence time Δt and the nature of the event, the array is updated according to the selected event. In the case of coalescence between bubble (i, v) and bubble (j, v), bubble (j, v) is removed by the population (canceling the k values of $\boldsymbol{R}_{v,j,k}$) and bubble (i, v) is substituted by the new formed bubble. In the case of breakage of bubble (i, v), this bubble is replaced by one of the fragments (according to the daughter distribution function) while other daughter bubbles are added to the array $\boldsymbol{R}$ as new elements. In the case of bubble injection, a new array element is added according to the boundary condition imposed. It is indeed that new internal-coordinate values follow the proper law described by the physics of the system.

The case of bubble motion requires further explanations: the matrix $\boldsymbol{P}$ is defined in such a way that its element $\boldsymbol{P}_{v,u}$ represents the probability for the bubble (i, v) to exit from the volume v and enter in volume u. It is clear that for a closed system $\boldsymbol{P}_{v,v} = 0$ and $\sum_{u=1}^{N_v} \boldsymbol{P}_{v,u} = 1$, but for an open system this is not longer true. When the bubble motion event is selected by the algorithm, the destination of the bubble is established by extracting another random number ζ from a uniform distribution between 0 and 1, following the relationship:

$$\sum_{v,k}^{u-1} \boldsymbol{P}_{v,k} < \zeta \leq \sum_{v,k}^{u} \boldsymbol{P}_{v,k}. \tag{2.97}$$

Since the mass transfer process is slower than bubble coalescence and breakage, in this work it is not treated in the same way as the other events. According to the calculated mass transfer rates, the internal coordinates of the bubble population are updated after a certain number N_e of consecutive events in order to reduce the computational effort of this procedure. By assuming that the liquid phase is well-mixed, also a variable related to the composition of the chemical species in the liquid phase is integrated with respect to time by using an explicit first-order forward scheme after N_e events. In this work, the value of N_e adopted was equal to 20, since no significant differences were detected in the solution with further reductions.

It is worth mentioning a very common issue of coalescence-breakage problems is rep-

resented by the number of the simulated bubbles during the simulation: if the coalescence prevails this number reduces, possibly leading to statistical unreliable results; whereas if breakage event is more frequent, the total number of simulated bubbles increases until a unsustainable situation is reach in terms of computational time. This issue is usually overcome by using the "doubling-halving" procedure described in Liffman (1992), in which the population is doubled or halved if the number of simulated bubble reaches a minimum or a maximum limit. However, the mass transfer process imposes the conservation of the total number of moles of the exchanged chemical species: this procedure can not be adopted in this situation and the total number of bubbles is here simply monitored over the entire simulation.

2.3.2 Quadrature Method of Moments

As previously mentioned, the closure problem typical of MOM can be solved by imposing a functional form for the NDF and QBMM use the quadrature approximation for overcome this issue. The Quadrature Method of Moments was originally formulated in the work of McGraw (1997), and it is specifically defined for monovariate NDF. In Eq. (2.82) the typical functional form given by QBMM for a monovariate NDF is already reported; moreover, by substituting the Eq. (2.82) into Eq. (2.72) it is possible to write what follows:

$$M_k = \sum_{i=1}^{N} w_i L_i^k, \tag{2.98}$$

where a generic $k-$order moment is expressed as a function of N weights and nodes of quadrature.

Since moments are the transported quantities of Eq. (2.77) and Eq. (2.78), while weights and nodes are used to formulate the unclosed terms as performed in Eq. (2.85), it is necessary to establish a procedure capable to express the quadrature weights and nodes as a function of moments themselves. This procedure is usually called "inversion algorithm" (McGraw, 1997; Marchisio et al., 2003). It is certainly possible to determine the N weights and nodes by solving the following non-linear system:

$$\begin{cases} M_0 = \sum_{i=1}^{N} w_i \\ M_1 = \sum_{i=1}^{N} w_i L_i \\ \dots \\ M_{2N-1} = \sum_{i=1}^{N} w_i L_i^{2N-1} \end{cases} \tag{2.99}$$

This non-linear system can be solved by using a non-linear equation solver (e.g., Newton-Raphson); however, this is not a very efficient method since a very good initial guess is needed to ensure convergence (Marchisio and Fox, 2013). In this part of the dissertation, an efficient and stable procedure will be explained in detail.

As this method is based on quadrature theory, some preliminary concept will be introduced. According to this theory, the NDF (as reported in Eq. (2.36)) is called weight function or measure, must be non-negative and non-null in the integration interval and all its moments of any k order (as defined in Eq. (2.72)) must exist (Gautschi, 2004; Press et al., 2007; Marchisio and Fox, 2013). Since the physical reality is here described, all these requirements are in general satisfied by the defined NDF. It is important to define the or-

thogonal polynomials (Gautschi, 2004):

$$\begin{aligned} &\{P_0(L), P_1(L), \ldots, P_i(L)\} \\ &\text{with } P_i(L) = k_{i,0}L^i + k_{i,1}L^{i-1} + \cdots + k_{i,i} \end{aligned} \tag{2.100}$$

is orthogonal in the interval of integration Ω_L, with respect to the measure function $n(L)$, if

$$\int_{\Omega_L} n(L)P_\alpha(L)P_\beta(L)\,\mathrm{d}L \begin{cases} = 0 & \text{for } \alpha \neq \beta, \\ > 0 & \text{for } \alpha = \beta. \end{cases} \tag{2.101}$$

A consequence of this definition is that the integration domain Ω_L and the weight function $n(L)$ uniquely define the family of polynomials $\{P_i(L)\}$. An important relation of the orthogonal polynomials is that:

$$P_{i+1}(L) = (L - a_i)P_i(L) - b_i P_{i-1}(L) \qquad \text{with } i = 0, 1, 2, \ldots \tag{2.102}$$

with $P_{-1}(L) = 0$, $P_0(L) = 1$ and where

$$a_N = \frac{\displaystyle\int_{\Omega_L} L\,n(L)P_i(L)P_i(L)\,\mathrm{d}L}{\displaystyle\int_{\Omega_L} n(L)P_i(L)P_i(L)\,\mathrm{d}L} \quad \text{with } i = 0, 1, 2, \ldots \tag{2.103}$$

$$b_N = \frac{\displaystyle\int_{\Omega_L} n(L)P_i(L)P_i(L)\,\mathrm{d}L}{\displaystyle\int_{\Omega_L} n(L)P_{i-1}(L)P_{i-1}(L)\,\mathrm{d}L} \quad \text{with } i = 1, 2, \ldots \tag{2.104}$$

Eq. (2.102) is the so-called "recurrence formula" of orthogonal polynomials and is an important relation used for computing the quadrature approximation. The knowledge of the recursion coefficients indicated in Eq. (2.103) and Eq. (2.104) allows to calculate the zeros of the orthogonal polynomials. In fact, the recursive relationship is capable to generate a sequence of polynomials orthogonal with respect to the weight function in the integration interval. An important feature is that, as shown in Marchisio and Fox (2013), it is possible to write the coefficients a_i and b_i in terms of the moments of the NDF. Furthermore, it is possible to demonstrate that each polynomial belonging to an orthogonal sequence has all its roots real, distinct, and strictly inside the integration interval (the entire demonstration can be found in Gautschi, 2004). Now it is clearer the choose of Gaussian quadrature to approximate the NDF (Eq. (2.82)): the roots of the orthogonal polynomials are in turn the nodes of the approximation quadrature. Moreover, Gaussian quadrature formulas are used because of its accuracy property: an interpolation formula with N equally-spaced nodes (i.e.,Newton-Cotes) has a degree of accuracy of $N - 1$, whereas a Gaussian quadrature has a degree of accuracy of $2N - 1$. However, the definition of degree of accuracy is based on

having polynomials as the integrand function, for this reason the quality of the quadrature must be assessed when another integrand function (as in the case of source term of PBE, expressed in Eq. (2.51)) is evaluated.

By using the recursive relationship of the orthogonal polynomials, it is possible to find the weights and nodes of quadrature (Wilf, 1962; Gautschi, 1997, 2004; Marchisio and Fox, 2013). The sequence of recursive relationships can be written in matrix form as:

$$L\begin{bmatrix} P_0(L) \\ P_1(L) \\ P_2(L) \\ \vdots \\ P_{N-1}(L) \end{bmatrix} = \begin{bmatrix} a_0 & 1 & & & \\ b_1 & a_1 & 1 & & \\ & b_2 & a_2 & 1 & \\ & & \ddots & \ddots & \ddots \\ & & & b_{N-1} & a_{N-1} \end{bmatrix} \begin{bmatrix} P_0(L) \\ P_1(L) \\ P_2(L) \\ \vdots \\ P_{N-1}(L) \end{bmatrix} + \begin{bmatrix} 0 \\ 0 \\ 0 \\ \vdots \\ P_N(L) \end{bmatrix}. \tag{2.105}$$

Eq. (2.105) shows that the zeros of $P_N(L)$ (i.e., the nodes of the quadrature approximation L_i) are the eigenvalues of the tridiagonal matrix appearing in the equation. Eventually, this matrix can be transformed in symmetric by means of a diagonal similarity transformation, and so preserving the eigenvalues, to give the so-called Jacobi matrix:

$$\mathbf{J} = \begin{bmatrix} a_0 & \sqrt{b_1} & & & \\ \sqrt{b_1} & a_1 & \sqrt{b_2} & & \\ & \sqrt{b_1} & a_2 & \sqrt{b_3} & \\ & & \ddots & \ddots & \ddots \\ & & & \sqrt{b_{N-1}} & a_{N-1} \end{bmatrix}. \tag{2.106}$$

This procedure transforms the ill-conditioned problem of finding the roots of a polynomial described in Eq. (2.99) into the well-conditioned problem of finding the eigenvalues and eigenvectors of a tridiagonal symmetric matrix. In the work of Wilf (1962), it is shown that the N weights can then be calculated as $w_i = M_0 j_{\alpha 1}^2$, where $j_{\alpha 1}$ represent the first component of the $\alpha-$th eigenvector $\mathbf{j}_\alpha$ of the Jacobi matrix. As previously mentioned, the coefficients a_N and b_N of Eq. (2.102) can be calculated by means of the orthogonality condition and by using the moments of the NDF. Two efficient methods for calculating the Jacobi matrix from the moments, the Product-Difference algorithm (Gordon, 1968) and Wheeler algorithm (Wheeler, 1974) will be described below. Furthermore, it is important to stress that a generic inversion algorithm is capable of calculate a full set of N weights and N nodes from a "realizable" set of $2N-1$ moment. The concept of moment realizability is introduced in the work of Wright Jr (2007), where a typical condition in which moments may corrupt is presented. The inversion of a corrupted moment set may give weights and nodes not belonging to the integration support. An adaptive version of the Wheeler algorithm was proposed by Yuan and Fox (2011), capable of checking for moment realizability and return the largest set of weights and abscissas possible (i.e., with a total number of quadrature nodes $\leq N$). Moreover, this adaptive algorithm is particularly useful for degenerate cases, where the evolution of the underlying NDF tends to be described with a number of quadrature

nodes less than the initial $N-$weighted Dirac delta functions. In such cases, the adaptive Wheeler algorithm will return the exact NDF. More details on adaptive quadrature can be found in Yuan and Fox (2011).

It is worth mentioning that if the functional form of the NDF corresponds to the weight function of a known family of orthogonal polynomials, such as Gauss-Legendre, Gauss-Jacobi, Gauss-Laguerre, Gauss-Hermite and Gauss-Chebyshev, the recursion coefficients can be calculated without using the moments and therefore Eq. (2.106) can be directly solved. This procedure is the basis of other methods, the so-called Extended Quadrature Methods of Moments (Yuan et al., 2012).

Product-Difference

A method for write the Jacobi matrix (Eq. (2.106)) is represented by the product-difference (PD) algorithm, firstly formulated by Gordon (1968) and based on the theory of continued fractions of Stieltjes. The first step consists to write the matrix $\mathbf{P}$ with components $P_{i,j}$ functions of the moments of the NDF. The procedure is the following:

$$\begin{cases} P_{i,1} = \delta_{i,1} & \text{with } i = 1, \dots, 2N+1, \\ P_{i,2} = (-1)^{i-1} M_{i-1} & \text{with } i = 1, \dots, 2N, \\ P_{i,j} = P_{1,j-1} P_{i+1,j-2} - P_{1,j-2} P_{i+1,j-1} & \text{with } i = 1, \dots, 2N+2-j \\ & \text{and } j = 3, \dots, 2N+1. \end{cases} \tag{2.107}$$

where $\delta_{i,1}$ is the Kronecker delta, M_i represents the moment of $i-$order of the NDF and N is the chosen number of quadrature nodes. It important to highlight here that also normalized moments $m_i = M_i/M_0$ can be used for construct the matrix $\mathbf{P}$; in this case the final weights must be corrected by multiplying for M_0.

The matrix $\mathbf{P}$ is necessary to determine the coefficients of the continued fraction ζ_i for in turn calculating the coefficients of Jacobi matrix $\mathbf{J}$. The relationship between $\mathbf{P}$ and ζ_i is the following:

$$\zeta_i = \frac{P_{1,i+1}}{P_{1,i} P_{1,i-1}} \quad \text{with } i = 2, \dots, 2N \text{ and } \zeta_1 = 0, \tag{2.108}$$

while a_i and b_i coefficients of Eq. (2.106) can be expressed as:

$$a_i = \zeta_{2i} + \zeta_{2i-1} \quad \text{with } i = 0, \dots, N-1, \tag{2.109}$$

$$b_i = -\sqrt{\zeta_{2i+1} \zeta_{2i}} \quad \text{with } i = 1, \dots, N-1. \tag{2.110}$$

This algorithm is very efficient, but the stability tends to decrease as the number of quadrature nodes N increases (in general when $N > 10$, as pointed out by Marchisio and Fox, 2013). Moreover the algorithm fails with distributions with zero mean (i.e., with $M_1 = 0$), because a division by zero is performed when the coefficients of the continued

fraction ζ_i are calculated. However, this is not the case of distributions with values of internal coordinate ranging between $[0, \infty)$, such as bubble size or bubble composition; the problem may arise when the integration support is between $(-\infty, \infty)$ as for the bubble velocity space. Therefore, another algorithm can be used in place of PD: the Wheeler algorithm, presented in the following section, can be applied without problems also in the latter case.

Wheeler algorithm

Wheeler (1974) proposed an alternative approach for the calculation of the coefficient of the Jacobi matrix (Eq. (2.106)). This method uses a different set of basis functions $\pi_i(L)$, rather than the powers of L. Since also $\{\pi_i(L)\}$ are orthogonal polynomials it is possible to apply the recursive relation as follows:

$$\pi_{i+1}(L) = (L - a_i')\pi_i(L) - b_i'\pi_{i-1}(L) \quad \text{for } i = 0, 1, 2, \dots \tag{2.111}$$

with $\pi_{-1} = 0$ and $\pi_0 = 1$. The coefficients a_i' and b_i' must be calculated by means of the following integrals:

$$\mu_i = \int_{\Omega_L} \pi_i(L)\, n(L)\, \mathrm{d}L \quad \text{with } i = 0, 1, \dots, 2N - 1, \tag{2.112}$$

usually referred as modified moments in contrast with the standard moment definition. It must be remarked that, also in this case, N represents the number of quadrature nodes. Now the coefficients of the modified moments a_i' and b_i' must be related to the standard moment coefficients a_i and b_i of the Jacobi matrix. This is done by defining the following intermediate quantities:

$$\sigma_{i,j} = \int_{\Omega_L} n(L)\pi_i(L)\pi_j(L)\, \mathrm{d}L, \quad \text{for } i, j \geq -1. \tag{2.113}$$

The calculation of these quantities can be performed by using the following relation, based on the orthogonality property:

$$\sigma_{i,j} = \sigma_{i-1,j+1} - \left(a_{j-1} - a_j'\right)\sigma_{i-1,j} - b_{j-1}\sigma_{i-2,j} + b_j'\sigma_{i-1,j-1} \tag{2.114}$$

where $i = 1, 2, \dots, N-1$, $j = i, i+1, \dots, 2N-i-1$ and with

$$\sigma_{-1,i} = 0 \quad \sigma_{0,i} = \mu_i \quad \text{and} \quad a_0 = a_0' + \frac{\mu_1}{\mu_0}, \; b_0 = 0. \tag{2.115}$$

Eq. (2.114) can be rewritten as a function of the coefficients of the Jacobi matrix in the

following way:

$$a_i = a'_i - \frac{\sigma_{i-1,i}}{\sigma_{i-1,i-1}} + \frac{\sigma_{i,i+1}}{\sigma_{i,i}}, \tag{2.116}$$

$$b_i = \frac{\sigma_{i,i}}{\sigma_{i-1,i-1}}. \tag{2.117}$$

A detailed derivation of this method can be found in (Wheeler, 1974). The Wheeler algorithm results in higher stability, compared with the PD algorithm: in fact, even by choosing modified moments μ_i equal to standard moments M_i (i.e., with $a'_i = b'_i = 0$), the algorithm is general more stable (Yuan and Fox, 2011; Marchisio and Fox, 2013). Moreover, it can be demonstrated that the use of the basis functions $\pi_i(L)$ allows to calculate the coefficients of the Jacobi matrix also in the case of distributions with zero mean (i.e., $M_1 = 0$).

2.3.3 Conditional Quadrature Method of Moments

This method is basically an extension of QMOM discussed in Section 2.3.2 to multivariate cases (Yuan and Fox, 2011; Buffo et al., 2013). The variables transported inside the computational domain are in this case some mixed-order moments of the multivariate NDF, for bubble population as defined in Eq. (2.71) distributed with respect to bubble size L and composition ϕ_b. The inversion algorithm must be capable of inverting the tracked moment set, taking into account the dependencies on other internal coordinates. It is important to remark that here the method is presented for the bivariate case under investigation, but there is not a serious limitation on its applicability on other cases with a larger number of the internal coordinates (Yuan and Fox, 2011; Marchisio and Fox, 2013).

The Conditional Quadrature Method of Moments is intended as a particular inversion procedure, intrinsically related to the following definition of conditional density function:

$$n(L, \phi_b) = n(L)\, p(\phi_b | L), \tag{2.118}$$

and its generic moment of order k and l:

$$M_{k,l} = \int_0^\infty n(L)\, L^k \int_0^\infty p(\phi_b | L)\, \phi_b^l \, \mathrm{d}L \, \mathrm{d}\phi_b, \tag{2.119}$$

where $p(\phi_b | L)$ is the probability of having the bubble composition ϕ_b in the infinitesimal interval $\phi_b + \mathrm{d}\phi_b$ when the bubble size L is fixed and equal to a certain value and $n(L)$ is the monovariate NDF (i.e., with only the bubble size L as internal coordinate). It is important to stress here that a preliminary choice related to the order of importance among all the internal coordinates has to be made. In general, this decision is problem-dependent: in this particular case under investigation the bubble size L is chosen in place of bubble composition ϕ_b because of coalescence and breakage kernels depend mostly on bubble size. However, other approaches are possible, as explicated by Yuan and Fox (2011) where CQMOM was applied to the Kinetic Equation for rarefied gases: by tracking a large number of moments

(and thus increasing the computational cost of the methods), the conditional density function can be defined respectively for all the considered internal coordinates, and the choice of the preliminary internal coordinate is performed from time to time, according to characteristic of the underlying NDF (i.e., the covariance of the distribution with respect to a specific internal coordinate).

By using the quadrature approximation expressed in Eq. (2.82) for the first term on the right hand side of Eq. (2.118), it is possible to write:

$$n(L) = \sum_{i_1=1}^{N_1} w_{i_1} \delta(L - L_{i_1}), \tag{2.120}$$

where w_{i_1} is the number density of bubbles with size equal L_{i_1}. It should be noticed that N_1 represents the number of quadrature nodes used to approximate only the bubble size distribution, without considering a specific dependence on bubble composition ϕ_b. In order to include this dependence, a functional form for the conditional probability density function $p(\phi_b|L)$ must be assumed. Also in this case, a sum of delta functions centered on nodes of a Gaussian quadrature approximation are is used as follows:

$$p(\phi_b|L_{i_1}) = \sum_{i_2=1}^{N_2} \widehat{w}_{i_2}(L_{i_1})\, \delta(\phi_b - \phi_{b,i_2}(L_{i_1})), \tag{2.121}$$

where the numerical fraction $\widehat{w}_{i_2}(L_{i_1})$ and the composition $\phi_{b,i_2}(L_{i_1})$ are conditioned on the value of the first internal coordinate L_{i_1} with number density w_{i_1}, while N_2 indicates the number of nodes used to represent the conditioned distribution. Since $p(\phi_b|L)$ is essentially a PDF, $\widehat{w}_{i_2}(L_{i_1})$ is actually a numerical fraction and not a density number as for w_{i_1}. By substituting Eq. (2.120) and Eq. (2.121) into Eq. (2.118), a functional form for the bivariate NDF is given in the following way:

$$n(L, \phi_b) = \sum_{i_1=1}^{N_1} w_{i_1} \delta(L - L_{i_1}) \sum_{i_2=1}^{N_2} \widehat{w}_{i_1,i_2} \delta(\phi_b - \phi_{b,i_1,i_2}), \tag{2.122}$$

where $\widehat{w}_{i_2}(L_{i_1}) = \widehat{w}_{i_1,i_2}$ and $\phi_{b,i_2}(L_{i_1}) = \phi_{b,i_1,i_2}$. Eq. (2.122) can be easily explained from a physical point of view: each of the N_1 groups of bubbles characterized by a size L_{i_1} is subdivided into N_2 groups of bubbles with different compositions ϕ_{b,i_1,i_2}. The total number of quadrature nodes N is equal to $N_1 \cdot N_2$. An important case is represented by the case in which $N_2 = 1$: in this particular case at each group of bubbles corresponds a single value of bubble size and bubble composition. As it will be shown in Chapter 4 and Chapter 5, the choice of a number of nodes $N_2 > 1$ can be pointless if the underlying NDF does not present any variance with respect to bubble composition; in other words, the quadrature is determined by the investigated problem. Moreover, it is worth mentioning that Eq. (2.122) can be rewritten in the same form as preliminarily indicated in Eq. (2.81), and this aspect will

be of crucial importance when bivariate DQMOM equations are derived in Section 2.3.4.

The structure of CQMOM inversion algorithm directly follows from Eq. (2.122). In fact, the construction of the multivariate distribution begins with the calculation of the monovariate quadrature of order N_1 for the chosen first internal coordinate L, inverting the first $2N_1$ pure moments with respect to bubble size. According to this statement, $2N_1$ pure moments with respect to the size must be transported and used to recover the N_1 monovariate weights and nodes of quadrature:

$$\begin{matrix} M_{0,0} \\ M_{1,0} \\ \vdots \\ M_{2N_1-2,0} \\ M_{2N_1-1,0} \end{matrix} \rightarrow \text{PD/Wheeler} \rightarrow \begin{matrix} w_1 & L_1 \\ w_2 & L_2 \\ \vdots & \vdots \\ w_{N_1-1} & L_{N_1-1} \\ w_{N_1} & L_{N_1} \end{matrix} .$$

By applying the quadrature approximation in Eq. (2.82) for the first part of this double integral reported in Eq. (2.119), the following expression is written:

$$M_{k,l} = \sum_{i_1=1}^{N_1} w_{i_1} L_{i_1}^k C^l(L_{i_1}), \tag{2.123}$$

where

$$C^l(L_{i_1}) = \int_0^\infty p(\phi_\text{b}|L_{i_1}) \phi_\text{b}^l \text{d}\phi_\text{b}, = \sum_{i_2=1}^{N_2} \widehat{\omega}_{i_1,i_2} \phi_{\text{b},i_1,i_2}^l \tag{2.124}$$

is the so-called conditional moment of order l with respect to bubble composition, conditioned on the value of the first internal coordinate L_{i_1}. Conditional moments are quite useful to determine the conditional numerical fraction $\widehat{\omega}_{i_1,i_2}$ and conditional abscissas ϕ_{b,i_1,i_2} by using the same inversion algorithms formulated in Section 2.3.2 for monovariate moments :

$$\begin{matrix} C^0(L_{i_1}) \\ C^1(L_{i_1}) \\ \vdots \\ C^{2N_2-2}(L_{i_1}) \\ C^{2N_2-1}(L_{i_1}) \end{matrix} \rightarrow \text{PD/Wheeler} \rightarrow \begin{matrix} \widehat{\omega}_{i_1,1} & \phi_{\text{b},i_1,1} \\ \widehat{\omega}_{i_1,2} & \phi_{\text{b},i_1,2} \\ \vdots & \vdots \\ \widehat{\omega}_{i_1,N_2-1} & \phi_{\text{b},i_1,N_2-1} \\ \widehat{\omega}_{i_1,N_2} & \phi_{\text{b},i_1,N_2} \end{matrix} ,$$

with $i_1 = 1, 2, \dots, N_1$. It is clear that the first $2N_2$ conditional moments are necessary to calculate N_1 quadratures, for each of the N_1 nodes previously calculated. These conditional moments are recovered by using Eq. (2.123), resulting in the following linear system of rank

N_1:

$$\mathbf{K}\cdot\mathbf{G}\begin{pmatrix} C^l(L_1) \\ C^l(L_2) \\ \vdots \\ C^l(L_{N_1-1}) \\ C^l(L_{N_1}) \end{pmatrix} = \begin{pmatrix} M_{0,l} \\ M_{1,l} \\ \vdots \\ M_{N_1-1,l} \\ M_{N_1,l} \end{pmatrix}, \tag{2.125}$$

where the coefficient matrices are defined as follows:

$$\mathbf{K} = \begin{pmatrix} 1 & \dots & 1 \\ L_1 & \dots & L_{N_1} \\ \vdots & \ddots & \vdots \\ L_1^{N_1-1} & \dots & L_{N_1}^{N_1-1} \end{pmatrix}, \tag{2.126}$$

and

$$\mathbf{G} = \begin{pmatrix} w_1 & & \\ & \ddots & \\ & & w_{N_1} \end{pmatrix}, \tag{2.127}$$

with $l = 0, 1, 2, \dots, 2N_2 - 1$. Eq. (2.125) has the structure typical of a Vandermonde linear system, which is a well-known ill-conditioned problem. However, as reported in Yuan and Fox (2011), this system can be numerically solved by using an efficient algorithm proposed by Rybicki (Press et al., 2007). Moreover, it is important to mention that the linear system of Eq. (2.125) becomes singular if two of the L_{i_1} nodes are identical. Therefore, in a degenerate case CQMOM fails and the particular adaptive quadrature described in Yuan and Fox (2011) represents a possible solution to this particular issue.

As previously mentioned in this dissertation, the total number of moments to track depends on the desired quadrature approximation: the number of nodes N_1 for the first internal coordinate (e.g., in this case bubble size) and the number of conditional nodes N_2 of the second internal coordinate (e.g., in this case bubble composition). Firstly the calculation of the quadrature for the first internal coordinate requires to transport the first $2N_1$ pure moments with increasing order with respect to size. Then, the $N_1 \cdot N_2$ conditional numerical fractions and nodes for the second internal coordinate are determined by means of the $N_1(2N_2 - 1)$ moments in the order indicated in Eq. (2.125). Therefore, the total number of moments composing the tracked moment set is $2N_1N_2 + N_1$ and is strictly specified by the method: in other words, the set of transported moments is formed by a fixed number of moments with a specific order k with respect to size and l with respect to composition, determined by the total number of nodes N of quadrature approximation. In Fig. 2.1 moment sets for different choices of N_1 and N_2 are reported as example. Furthermore, the method can be used coupled with an adaptive approach as previously mentioned for a degenerate case, where the total number of moments to be tracked is fixed at the beginning of the simulation using a large number of nodes N, and during the simulation the actual number of nodes used is reduced according to the instantaneous underlying NDF. Further details can be found in the

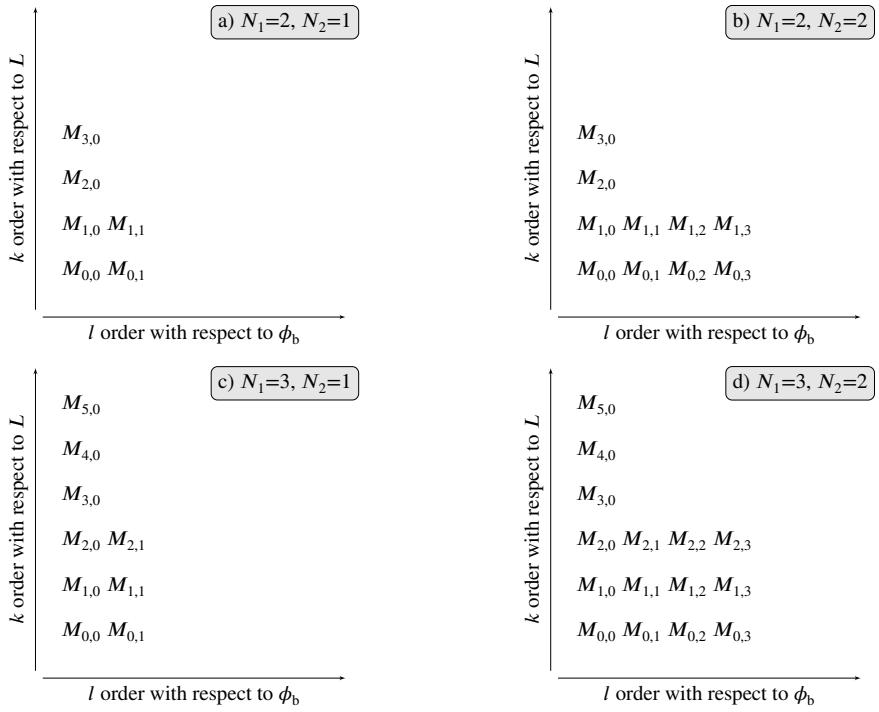

Figure 2.1: Moment sets tracked by CQMOM for different values of N_1 and N_2.

original work of Yuan and Fox (2011).

2.3.4 Direct Quadrature Method of Moments

As remarked in the original work of Marchisio and Fox (2005), the idea behind DQMOM is different from QMOM and its multivariate extension CQMOM: instead of transporting a set of moments of the NDF, with DQMOM the evolution of weights and nodes of the quadrature approximation is directly calculated in every point of the computational domain, without recurring to any inversion algorithm. The main advantage of this method is the fact that the extension to multivariate cases is straightforward, allowing to treat in the same way the distribution with respect to any internal coordinate characterizing the system (Marchisio and Fox, 2005; Zucca et al., 2007; Buffo et al., 2012). However, this method is affected by some problems relating to the proper conservation of some moments of the NDF when the advection in the physical space is described, as mentioned in Section 2.3.5 and explicated by examples in Section 4.2 and Section 5.2. In this part of the dissertation, DQMOM for the monovariate and bivariate cases presented in Section 2.2 will be discussed for the homogenous system modeled by Eq. (2.35) and Eq. (2.38); afterward, the issue relating to the physical space advection will be treated in detail.

The detailed derivation of DQMOM for a generic dispersed system can be found in Marchisio and Fox (2005), while in the works of Buffo et al. (2012, 2013) the method is applied to a gas-liquid system. In order to give an idea of all the passages, the set of governing

equations for a monovariate and spatially homogeneous system will be recovered starting from the definition of quadrature approximation (Eq. (2.82)):

$$n(L) = \sum_{i=1}^{N} w_i \, \delta(L - L_i). \tag{2.128}$$

By substituting Eq. (2.128) into Eq. (2.38), the following expression is obtained after some algebra:

$$\sum_{i=1}^{N} \delta(L - L_i) \left[\frac{\mathrm{d}w_i}{\mathrm{d}t} \right] - \sum_{i=1}^{N} \delta'(L - L_i) \left[\frac{\mathrm{d}w_i L_i}{\mathrm{d}t} - L_i \frac{\mathrm{d}w_i}{\mathrm{d}t} \right] + \sum_{i=1}^{N} w_i \frac{\partial}{\partial L} \left(G \, \delta(L - L_i) \right) = h(L). \tag{2.129}$$

where N is the total number of quadrature nodes. By applying the definition of moment transform reported in Eq. (2.72), Eq. (2.129) becomes:

$$\int_{\Omega_L} \sum_{i=1}^{N} \delta(L - L_i) \left[\frac{\mathrm{d}w_i}{\mathrm{d}t} \right] L^k \, \mathrm{d}L - \int_{\Omega_L} \sum_{i=1}^{N} \delta'(L - L_i) \left[\frac{\mathrm{d}w_i L_i}{\mathrm{d}t} - L_i \frac{\mathrm{d}w_i}{\mathrm{d}t} \right] L^k \, \mathrm{d}L + \int_{\Omega_L} \sum_{i=1}^{N} w_i \frac{\partial}{\partial L} \left(G(L) \, \delta(L - L_i) \right) L^k \, \mathrm{d}L = H_k. \tag{2.130}$$

Since integrals can be moved inside the summation sign, it is possible to write:

$$\int_{-\infty}^{+\infty} L^k \delta(L - L_i) \mathrm{d}L = L_i^k; \tag{2.131}$$

$$\int_{-\infty}^{+\infty} L^k \delta'(L - L_i) \mathrm{d}L = -k L_i^{k-1}; \tag{2.132}$$

$$\int_{-\infty}^{+\infty} \frac{\partial}{\partial L} \left(G(L) \, \delta(L - L_i) \right) L^k \, \mathrm{d}L = = -k \int_{-\infty}^{+\infty} L^{k-1} G(L) \delta(L - L_i) \mathrm{d}L = -k L_i^{k-1} G_i; \tag{2.133}$$

where $G_i = G(L_i)$. Eqs. (2.131) to (2.133) are substituted into Eq. (2.130), bringing together all left hand terms under the same summation sign:

$$\sum_{i=1}^{N} \left\{ L_i^k \left[\frac{\mathrm{d}w_i}{\mathrm{d}t} \right] + k L_i^{k-1} \left[\frac{\mathrm{d}w_i L_i}{\mathrm{d}t} - L_i \frac{\mathrm{d}w_i}{\mathrm{d}t} \right] - k w_i L_i^{k-1} G_i \right\} = H_k \tag{2.134}$$

where H_k is the source term of the $k-$order moment of the monovariate NDF, calculated with Eq. (2.85). By defining the following constitutive equations of DQMOM for the $i-$th

weight and weighted node in the following way:

$$\begin{cases} \dfrac{\mathrm{d}\, w_i}{\mathrm{d}t} = a_i; \\ \dfrac{\mathrm{d}\, w_i L_i}{\mathrm{d}t} = b_i + w_i G_i; \end{cases} \tag{2.135}$$

with $i = 1, \ldots, N$, it is possible to express Eq. (2.134) as:

$$\sum_{i=1}^{N} \left\{ (1-k) L_i^k a_i + k L_i^{k-1} b_i \right\} = H_k. \tag{2.136}$$

Eq. (2.135) and Eq. (2.136) totally determine the evolution of the NDF for a given initial condition. In fact, the $2N$ source terms a_i and b_i of Eq. (2.135) can be calculated by means of the linear system defined by Eq. (2.136), by using the source term of the first $2N-$order moments of the distribution, which are written as functions of weights and nodes of quadrature as shown in Eq. (2.83). In order to make the discussion clearer, the case with $N = 2$ is presented:

$$\begin{cases} \dfrac{\mathrm{d}\, w_1}{\mathrm{d}t} = a_1; \\ \dfrac{\mathrm{d}\, w_2}{\mathrm{d}t} = a_2; \\ \dfrac{\mathrm{d}\, w_1 L_1}{\mathrm{d}t} = b_1 + w_1 G_1; \\ \dfrac{\mathrm{d}\, w_2 L_2}{\mathrm{d}t} = b_2 + w_2 G_2; \end{cases} \tag{2.137}$$

where a_1, a_2, b_1 and b_2 are calculated by the following linear system:

$$\begin{bmatrix} 1 & 1 & 0 & 0 \\ 0 & 0 & 1 & 1 \\ -L_1^2 & -L_2^2 & 2L_1 & 2L_2 \\ -2L_1^3 & -2L_2^3 & 3L_1^2 & 3L_2^2 \end{bmatrix} \begin{bmatrix} a_1 \\ a_2 \\ b_1 \\ b_2 \end{bmatrix} = \begin{bmatrix} H_0 \\ H_1 \\ H_2 \\ H_3 \end{bmatrix}. \tag{2.138}$$

The extension to the bivariate case is straightforward. In fact, by using the same derivation strategy of the monovariate case and assuming the expression reported in Eq. (2.81) as functional form of the bivariate NDF, it is possible to write:

$$\begin{cases} \dfrac{\mathrm{d}\, w_i}{\mathrm{d}t} = a_i, \\ \dfrac{\mathrm{d}\, w_i L_i}{\mathrm{d}t} = b_i + w_i G_i, \\ \dfrac{\mathrm{d}\, w_i \phi_{\mathrm{b},i}}{\mathrm{d}t} = c_i + w_i \dot{\phi}_{\mathrm{b},i}, \end{cases} \tag{2.139}$$

with $i = 1, \dots, N$, $G_i = G(L_i, \phi_{\mathrm{b},i})$ and $\dot{\phi}_{\mathrm{b},i} = \dot{\phi}_{\mathrm{b},i}(L_i, \phi_{\mathrm{b},i})$. In order to solve Eq. (2.139) the source terms a_i, b_i and c_i must be expressed as functions of weights and nodes w_i, L_i and $\phi_{\mathrm{b},i}$. This is accomplished by forcing the evolution of the moments to be what is dictated by Eq. (2.76) resulting in the following expression:

$$\sum_{i=1}^{N} \left[(1-k-l) L_i^k \phi_{\mathrm{b},i}^l a_i + k L_i^{(k-1)} \phi_{\mathrm{b},i}^l b_i + l L_i^k \phi_{\mathrm{b},i}^{(l-1)} c_i \right] = H_{k,l}. \tag{2.140}$$

Eq. (2.140) is the bivariate counterpart of Eq. (2.136), representing a linear system as different pairs of $\{k, l\}$ values are selected. As in the monovariate case, the number of pairs depends on total number of unknown terms, in turn defined by the nodes of the quadrature N. In the case, DQMOM needs $3N$ independent relations in order to calculate the $3N$ unknown source terms appearing in Eq. (2.139). It is clear that, as with other QBMM, the accuracy of the quadrature approximation is improved by increasing the number of nodes N, resulting in higher computational costs due to the increasing number of transport equations. In a more compact form, Eq. (2.140) can be written as follows:

$$\bar{\mathbf{A}}\mathbf{s} = \mathbf{d}, \tag{2.141}$$

where

$$\mathbf{s} = [a_1, \dots, a_N, b_1, \dots, b_N, c_1, \dots, c_N]^{\mathrm{T}},$$

$$\mathbf{d} = [H_{k_1,l_1}, H_{k_2,l_2}, \dots, H_{k_{3N},l_{3N}}]^{\mathrm{T}}.$$

As detailed discussed in the literature (Fox, 2009; Buffo et al., 2012), it is important to define the linear system in such a manner that results in a full rank matrix $\bar{\mathbf{A}}$ for all possible N distinct and non-degenerate nodes (i.e., L_i for monovariate case and $L_i, \phi_{\mathrm{b},i}$ for bivariate case). As pointed out in the original work of Marchisio and Fox (2005), in the case of a monovariate distribution the source terms of the first $2N$ order moments must be used to define the $2N$ unknowns, always resulting in a full rank matrix $\bar{\mathbf{A}}$ for a non-degenerating problem: in the reported example with $N = 2$, in fact, H_0, H_1, H_2 and H_3 are evaluated before solving the linear system.

When a bivariate case is solved, this strategy relating to the mimicked moment set may be not unique (Buffo et al., 2013). As explained by Fox (2009), one strategy could be choosing linearly independent moments of a particular order $\gamma = k + l$ that lead to a full rank matrix, before including moments of higher order. Another possibility for the choice of the moments can be to track only the pure moments with respect of size and composition (Buffo et al., 2012). A different approach was used in the work of Buffo et al. (2013), in which the aim was the comparison between different QBMM: the mathematical equivalence between the methods is guaranteed only if the same moment set is tracked. With this approach the strategy behind the choice of moments is left to CQMOM, which, as explained in Section 2.3.3, strictly defines the moment set to be tracked. For example when a two-node quadrature is used ($N = 2$), it is possible to track the moment set presented as first choice in Fig. 2.1, namely

$\{k,l\} = (0,0;1,0;0,1;2,0;1,1;3,0)$. Moreover, it should be remarked that the functional form assumption for the bivariate NDF made for CQMOM and DQMOM formulations are different: Eq. (2.122) is equal to Eq. (2.81) only when $N_2 = 1$, as already pointed out in Section 2.3.3. Therefore, only in this case the two QBMM can give comparable results. Furthermore, it is worth mentioning that the choice $\{k,l\} = (0,0;1,0;0,1;2,0;1,1;0,2)$ that would use all the possible moments of global order $0,1,2$ cannot be used since it leads to a singular linear system (Buffo et al., 2013).

In contrast with CQMOM, particular attention should be paid when other terms of the PBE are taken into account with DQMOM. The simple case of continuous injection and extraction of bubbles in stagnant liquid, described with Eq. (2.86) for a generic order moment of the NDF, can be helpful to understand the problem. As mentioned in Buffo et al. (2013), it is possible to make a parallel with the theory of the numerical methods for conservation laws, where constitutive equations may be formulated in terms of conserved variables (i.e., moments) or primitive variables (i.e., weights and nodes of quadrature). Since with QMOM and CQMOM conserved variables are transported, one may think that DQMOM is a method based on balance of primitive quantities and write what follows:

$$\begin{cases} \dfrac{\mathrm{d}\, w_i}{\mathrm{d}t} = -\dfrac{(w_i)_{out} - (w_i)_{in}}{\tau} + a_i, \\ \dfrac{\mathrm{d}\, w_i L_i}{\mathrm{d}t} = -\dfrac{(w_i L_i)_{out} - (w_i L_i)_{in}}{\tau} + b_i + w_i G_i, \\ \dfrac{\mathrm{d}\, w_i \phi_{\mathrm{b},i}}{\mathrm{d}t} = -\dfrac{(w_i \phi_{\mathrm{b},i})_{out} - (w_i \phi_{\mathrm{b},i})_{in}}{\tau} + c_i + w_i \dot{\phi}_{\mathrm{b},i}, \end{cases} \tag{2.142}$$

with $(w_i)_{out}$, $(w_i L_i)_{out}$, $(w_i \phi_{\mathrm{b},i})_{out}$ assumed equal to w_i, $w_i L_i$, $w_i \phi_{\mathrm{b},i}$ respectively in a well-mixed system, and $(w_i)_{in}$, $(w_i L_i)_{in}$, $(w_i \phi_{\mathrm{b},i})_{in}$ are weights and weighted nodes of the inlet bubble distribution. However, as it will be shown in Section 4.1.2 this formulation is not able to properly conserve the evolution of the moments because is not correctly derived following the DQMOM procedure (Marchisio and Fox, 2005): in fact, bubble injection and extraction must be modeled as source/sink terms (Buffo et al., 2013), as reported in Eq. (2.86).

The proper way for writing the constitutive equations for the aforementioned case is the following one (algebraic passages are omitted for brevity):

$$\begin{cases} \dfrac{\mathrm{d}\, w_i}{\mathrm{d}t} = -a_i^{\#} + a_i, \\ \dfrac{\mathrm{d}\, w_i L_i}{\mathrm{d}t} = -b_i^{\#} + b_i + w_i G_i, \\ \dfrac{\mathrm{d}\, w_i \phi_{\mathrm{b},i}}{\mathrm{d}t} = -c_i^{\#} + c_i + w_i \dot{\phi}_{\mathrm{b},i}, \end{cases} \tag{2.143}$$

where a_i, b_i and c_i can be found through the solution of the linear system described in Eq. (2.140) and $a_i^{\#}$, $b_i^{\#}$, $c_i^{\#}$ are obtained by solving the linear system generated by the fol-

lowing expression:

$$\sum_{i=1}^{N}\left[(1-k-l)L_i^k\phi_{\mathrm{b},i}^l a_i^{\#}+kL_i^{(k-1)}\phi_{\mathrm{b},i}^l b_i^{\#}+lL_i^k\phi_{\mathrm{b},i}^{(l-1)}c_i^{\#}\right]=\frac{(M_{k,l})_{out}-(M_{k,l})_{in}}{\tau}. \quad (2.144)$$

It is important to highlight the analogy between the Eq. (2.140) and Eq. (2.144): once that the moment set is defined, the matrix $\bar{\mathbf{A}}$ is the same for calculating all the unknown terms a_i, b_i, c_i and $a_i^{\#}$, $b_i^{\#}$, $c_i^{\#}$, what changes is the vector of known terms.

A problem of different nature may occur when the advection in physical space is considered. In this case, DQMOM equations written for an inhomogeneous case, as formulated in the work of Marchisio and Fox (2005), are an example of a set of conservation laws written by using primitive variables (Buffo et al., 2013). An implicit assumption of solution smoothness in space and time was made for deriving the following equations:

$$\begin{cases}\dfrac{\mathrm{d}\,w_i}{\mathrm{d}t}+\dfrac{\partial}{\partial\mathbf{x}}\left(w_i\check{\mathbf{U}}_i\right)=a_i,\\ \dfrac{\mathrm{d}\,w_iL_i}{\mathrm{d}t}+\dfrac{\partial}{\partial\mathbf{x}}\left(w_iL_i\check{\mathbf{U}}_i\right)=b_i+w_iG_i,\\ \dfrac{\mathrm{d}\,w_i\phi_{\mathrm{b},i}}{\mathrm{d}t}+\dfrac{\partial}{\partial\mathbf{x}}\left(w_i\phi_{\mathrm{b},i}\check{\mathbf{U}}_i\right)=c_i+w_i\dot{\phi}_{\mathrm{b},i},\end{cases} \quad (2.145)$$

where $\check{\mathbf{U}}_i$ is the conditional velocity of bubbles with size L_i and composition $\phi_{\mathrm{b},i}$, namely the velocity of the i-th group of bubbles with size L_i and composition $\phi_{\mathrm{b},i}$, calculated by means of a specific momentum equation of the multifluid method, considering each group of bubble as a different phase (as explained in the work of Buffo et al., 2012). The terms a_i, b_i and c_i are calculated with the same procedure described in Eq. (2.141). It is important to remark that Eq. (2.145) are derived by assuming that the time and spatial derivatives of weights and nodes exist and are finite (Marchisio and Fox, 2005), and for this reason the fields of each quadrature weight and node must be necessarily continuous all over the computational domain. Unfortunately, weights and abscissas may be spatially discontinuous, even if the moment set is well defined (Wright Jr, 2007); in these cases DQMOM will not be able to calculate the correct evolution of the conserved variables (i.e., moments). Even when no discontinuities are present, due to the fact that the governing equations do not contain any diffusion term (for modeling reasons, as in this case) and because the only resulting diffusion is numerical, standard DQMOM fails in correctly predicting the evolution of the moments, as demonstrated by Mazzei et al. (2010, 2012). Since the quantification of the numerical diffusion coefficient is not feasible, because depends on the numerical scheme and the computational grids used, Buffo et al. (2013) formulate a new version of DQMOM, called DQMOM-Fully Conservative, capable of properly conserve in space the moments of NDF even transporting primitive quantities as weights and nodes of quadrature.

2.3.5 Direct Quadrature Method of Moments - Fully Conservative

As previously pointed out, QBMM can be essentially subdivided into two different groups of method: the former group is composed by QMOM and CQMOM in which the equations for a given moment set are discretized and solved, recurring to the inversion algorithm whenever source terms of moments are calculated. The latter group is composed by DQMOM (and its conservative counterpart DQMOM-FC), where the equations for the quadrature quantities are directly discretized and solved for a given computational domain, calculating the source terms of these quantities by means of a linear system defined in such a way that the evolution of a certain moment set of the NDF is properly described.

As remarked in Section 2.3.4, by using an analogy with the theory of numerical method for conservation laws (LeVeque, 2002; Toro, 2009), the first group of methods stems on conservative quantities calculation (i.e., moments of NDF), while the second group is based on primitive quantities. For smooth solutions in space and time, the two classes of methods are essentially equivalent, while significant differences are present when the solution contains shock waves that lead to spatial discontinuities (LeVeque, 2002; Toro, 2009); in this case the equations written in a non-conservative form are not able to provide the correct solution due to the smoothness solution assumption made for formulating the second group methods. Unfortunately, DQMOM equations for a generic inhomogeneous system are an example of a set of conservation laws written by using primitive variables, assuming that spatial and time derivatives exist and are finite, namely the solution is smooth enough to be differentiable in space and time. As pointed out in literature (Mazzei et al., 2010; Buffo et al., 2013), the cases in which weights and nodes of quadrature fields present spatial discontinuities are very frequent, especially when a diffusion term (generally capable of smoothing solutions) is not included in the model. In these cases, moreover, the numerical diffusion introduced with any discretization scheme only magnifies the solution differences between these methods and conservatives methods. Buffo et al. (2012) proposed to estimate the numerical diffusion of the discretization scheme and introduce a diffusion term in DQMOM equations capable of canceling out the numerical diffusion: this method was proved to be very effective in preserving the correct behavior of moments for a very simple 1D inhomogeneous system discretized with equally-spatial nodes, for which a method for evaluate the numerical diffusion there exist (Ferziger and Peric, 2002). However, this method can not be efficiently applied for two or three-dimensional CFD simulation, even in simple Cartesian grids.

Therefore, a new approach was proposed by Buffo et al. (2013), based on the fact that weights and nodes of quadrature may be discontinuous in space, but not in time. The idea behind this Fully-Conservative formulation (DQMOM-FC) is to rewrite the fluxes of weight and nodes in the physical space in order to preserve the correct behavior of the moments, by extending to the general inhomogenous situation the approach developed previously for homogeneous open systems (Eq. (2.143) and Eq. (2.144)). By treating also the physical advection term of moments as a source term of DQMOM equations, it is possible to write

the following equations (derivation passages are described in Buffo et al. (2013)):

$$\begin{cases} \dfrac{\mathrm{d}\, w_i}{\mathrm{d}t} = -a_i^* + a_i, \\ \dfrac{\mathrm{d}\, w_i L_i}{\mathrm{d}t} = -b_i^* + b_i + w_i G_i, \\ \dfrac{\mathrm{d}\, w_i \phi_{\mathrm{b},i}}{\mathrm{d}t} = -c_i^* + c_i + w_i \dot{\phi}_{\mathrm{b},i}, \end{cases} \tag{2.146}$$

The new values a_i^*, b_i^* and c_i^*, with respect to the DQMOM formulation given in Section 2.3.4, contain the information relating to the physical space advection of the moments tracked and are calculated by solving the linear system underlying the following expression:

$$\sum_{i=1}^{N} \left[(1-k-l) L_i^k \phi_{\mathrm{b},i}^l a_i^* + k L_i^{(k-1)} \phi_{\mathrm{b},i}^l b_i^* + l L_i^k \phi_{\mathrm{b},i}^{(l-1)} c_i^* \right] = F_{k,l}, \tag{2.147}$$

where $i = 1, 2, \ldots, N$. The term $F_{k,l}$ is the net flux over the cell faces of the generic moment $M_{k,l}$ and it must be written by using the standard FV method of fluxes discretization and recurring to the quadrature approximation. A detailed account of how to calculate these fluxes can be found in the work of Vikas et al. (2011). As it is possible to observe, the main difference compared to the original formulation is the way in which advection in physical space is treated, and as shown in Chapter 4 and Chapter 5, this slight modification allows the method to conserve properly the moments of the NDF. However, it can be proven (the detailed demonstration can be found in Marchisio and Fox, 2013) that, although DQMOM-FC is conservative in space, this method is only first-order accurate in time: this means that when a first-order forward Euler time integrator is used, an error proportional to Δt^2 is introduced by the method. Therefore, for problems intrinsically non-stationary it may be necessary to use a very small time step or an high-order time-integrator in order to minimize this error; otherwise for stationary solutions, even with a fast transient, the results are accurate and equal to those obtained with methods formulated for conservative quantities (i.e., QMOM and CQMOM).

References

Alopaeus, V., Koskinen, J., I. Keskinen, K., Majander, J., 2002. Simulation of the population balances for liquid–liquid systems in a nonideal stirred tank. part 2—parameter fitting and the use of the multiblock model for dense dispersions. Chemical Engineering Science 57, 1815–1825.

Andersson, R., Andersson, B., 2006. On the breakup of fluid particles in turbulent flows. American Institute of Chemical Engineering Journal 52, 2020–2030.

Aris, R., 1962. Vectors, Tensors, and the Basic Equations of Fluid Mechanics. Prentice-Hall, Englewood Cliffs (NJ), USA.

Bakker, A., Van den Akker, H., 1994. Gas-liquid contacting with axial flow impellers. Chemical Engineering Research and Design 72, 573–582.

Buffo, A., Vanni, M., Marchisio, D., 2012. Multidimensional population balance model for the simulation of turbulent gas–liquid systems in stirred tank reactors. Chemical Engineering Science 70, 31–44.

Buffo, A., Vanni, M., Marchisio, D., Fox, R.O., 2013. Multivariate quadrature-based moments methods for turbulent polydisperse gas-liquid systems. International Journal of Multiphase Flow 50, 41–57.

Coulaloglou, C., Tavlarides, L., 1977. Description of interaction processes in agitated liquid-liquid dispersions. Chemical Engineering Science 32, 1289–1297.

Cussler, E.L., 1997. Diffusion: Mass Transfer in Fluid Systems. Cambridge Series in Chemical Engineering, Cambridge University Press, Cambridge, UK. Second Edition.

Danckwerts, P.V., 1951. Significance of liquid-film coefficients in gas absorption. Industial and Engineering Chemistry 43, 1460–1467.

Ferziger, J.H., Peric, M., 2002. Computational Methods for Fluid Dynamics. Springer-Verlag, Berlin, Germany. Third Edition.

Fox, R., 2009. Higher-order quadrature-based moment methods for kinetic equations. Journal of Computational Physics 228, 7771–7791.

Garcia, A.L., van den Broeck, C., Aertsens, M., Serneels, R., 1987. A monte carlo simulation of coagulation. Physica A: Statistical Mechanics and its Applications 143, 535–546.

Gautschi, W., 1997. Numerical Analysis: An Introduction. Birkhäuser, Boston (MA), USA.

Gautschi, W., 2004. Orthogonal Polynomials: Computation and Approximation. Oxford University Press, Oxford, UK.

Gillespie, D.T., 1976. A general method for numerically simulating the stochastic time evolution of coupled chemical reactions. Journal of Computational Physics 22, 403–434.

Gimbun, J., Rielly, C., Nagy, Z., 2009. Modelling of mass transfer in gas–liquid stirred tanks agitated by rushton turbine and CD-6 impeller: A scale-up study. Chemical Engineering Research and Design 87, 437–451.

Godin, F.B., Cooper, D.G., Rey, A.D., 1999. Numerical methods for a population-balance model of a periodic fermentation process. American Institute of Chemical Engineering Journal 45, 1359–1364.

Gordon, R.G., 1968. Error bounds in equilibrium statistical mechanics. Journal of Mathematical Physics 9, 655–663.

Gunawan, R., Fusman, I., Braatz, R.D., 2004. High resolution algorithms for multidimensional population balance equations. American Institute of Chemical Engineering Journal 50, 2738–2749.

Higbie, R., 1935. The rate of absorption of a pure gas into a still liquid during short periods of exposure. Transaction of the Institution of Chemical Engineers 31, 364–389.

Hulburt, H., Katz, S., 1964. Some problems in particle technology: A statistical mechanical formulation. Chemical Engineering Science 19, 555–574.

Jakobsen, H.A., 2008. Chemical Reactor Modeling: Multiphase Reactive Flows. Springer-Verlag, Berlin, Germany. First Edition.

Kawase, Y., Halard, B., Moo-Young, M., 1987. Theoretical prediction of volumetric mass transfer coefficients in bubble columns for newtonian and non-newtonian fluids. Chemical Engineering Science 42, 1609–1617.

Kruis, F.E., Maisels, A., Fissan, H., 2000. Direct simulation monte carlo method for particle coagulation and aggregation. American Institute of Chemical Engineering Journal 46, 1735–1742.

Kumar, J., Peglow, M., Warnecke, G., Heinrich, S., 2008. The cell average technique for solving multi-dimensional aggregation population balance equations. Computers and Chemical Engineering 32, 1810–1830.

Laakkonen, M., Alopaeus, V., Aittamaa, J., 2006. Validation of bubble breakage, coalescence and mass transfer models for gas–liquid dispersion in agitated vessel. Chemical Engineering Science 61, 218–228.

Lamont, J.C., Scott, D.S., 1970. An eddy cell model of mass transfer into the surface of a turbulent liquid. American Institute of Chemical Engineering Journal 16, 513–519.

Lee, C.H., Erickson, L., Glasgow, L., 1987. Bubble breakup and coalescence in turbulent gas-liquid dispersions. Chemical Engineering Communications 59, 65–84.

Lehr, F., Millies, M., Mewes, D., 2002. Bubble-size distributions and flow fields in bubble columns. American Institute of Chemical Engineering Journal 48, 2426–2443.

LeVeque, R.J., 2002. Finite Volume Methods for Hyperbolic Problems. Cambridge University Press, Cambridge, UK.

Liffman, K., 1992. A direct simulation monte-carlo method for cluster coagulation. Journal of Computational Physics 100, 116–127.

Luo, H., Svendsen, H.F., 1996. Theoretical model for drop and bubble breakup in turbulent dispersions. American Institute of Chemical Engineering Journal 42, 1225–1233.

Marchisio, D., Fox, R.O., 2013. Computational Models for Polydisperse Particulate and Multiphase Systems. Cambridge Series in Chemical Engineering, Cambridge University Press, Cambridge, UK.

Marchisio, D.L., Dennis Vigil, R., O. Fox, R., 2003. Implementation of the quadrature method of moments in CFD codes for aggregation–breakage problems. Chemical Engineering Science 58, 3337–3351.

Marchisio, D.L., Fox, R.O., 2005. Solution of population balance equations using the direct quadrature method of moments. Journal of Aerosol Science 36, 43–73.

Marshall Jr., C.L., Rajniak, P., Matsoukas, T., 2011. Numerical simulations of two-component granulation: Comparison of three methods. Chemical Engineering Research and Design 89, 545–552.

Mazzei, L., Marchisio, D.L., Lettieri, P., 2010. Direct quadrature method of moments for the mixing of inert polydisperse fluidized powders and the role of numerical diffusion. Industrial & Engineering Chemistry Research 49, 5141–5152.

Mazzei, L., Marchisio, D.L., Lettieri, P., 2012. New quadrature-based moment method for the mixing of inert polydisperse fluidized powders in commercial CFD codes. American Institute of Chemical Engineering Journal 58, 3054–3069.

McGraw, R., 1997. Description of aerosol dynamics by the quadrature method of moments. Aerosol Science and Technology 27, 255–265.

Nandanwar, M.N., Kumar, S., 2008. A new discretization of space for the solution of multi-dimensional population balance equations. Chemical Engineering Science 63, 2198–2210.

Narsimhan, G., Gupta, J., Ramkrishna, D., 1979. A model for transitional breakage probability of droplets in agitated lean liquid-liquid dispersions. Chemical Engineering Science 34, 257–265.

Patruno, L., Dorao, C., Svendsen, H., Jakobsen, H., 2009. Analysis of breakage kernels for population balance modelling. Chemical Engineering Science 64, 501–508.

Petitti, M., Nasuti, A., Marchisio, D.L., Vanni, M., Baldi, G., Mancini, N., Podenzani, F., 2010. Bubble size distribution modeling in stirred gas–liquid reactors with QMOM augmented by a new correction algorithm. American Institute of Chemical Engineering Journal 56, 36–53.

Petitti, M., Vanni, M., Marchisio, D., Buffo, A., Podenzani, F., 2012. Application of the conditional quadrature method of moments for the simulation of coalescence, breakup and mass transfer in gas-liquid stirred tanks, in: Proceedings of 14th European Conference on Mixing, pp. 371–376.

Press, W.H., Teukolsky, S.A., Vetterling, W.T., Flannery, B.P., 2007. Numerical Recipes: The Art of Scientific Computing. Cambridge University Press, Cambridge, UK. Third Edition.

Prince, M.J., Blanch, H.W., 1990. Bubble coalescence and break-up in air-sparged bubble columns. American Institute of Chemical Engineering Journal 36, 1485–1499.

Ramkrishna, D., 2000. Population Balances: Theory and Applications to Particulate Systems in Engineering. Academic Press, San Diego (CA), USA. First Edition.

Smith, M., Matsoukas, T., 1998. Constant-number monte carlo simulation of population balances. Chemical Engineering Science 53, 1777–1786.

Tandon, P., Rosner, D.E., 1999. Monte carlo simulation of particle aggregation and simultaneous restructuring. Journal of Colloid and Interface Science 213, 273–286.

Toro, E.F., 2009. Riemann Solvers and Numerical Methods for Fluid Dynamics: A Practical Introduction. Springer-Verlag, Berlin, Germany. Third Edition.

Vanni, M., 2000. Approximate population balance equations for Aggregation–Breakage processes. Journal of Colloid and Interface Science 221, 143–160.

Vikas, V., Yuan, C., Wang, Z., Fox, R., 2011. Modeling of bubble-column flows with quadrature-based moment methods. Chemical Engineering Science 66, 3058–3070.

Walter, J.F., Blanch, H.W., 1986. Bubble break-up in gas—liquid bioreactors: Break-up in turbulent flows. The Chemical Engineering Journal 32, B7–B17.

Wheeler, J.C., 1974. Modified moments and gaussian quadratures. Rocky Mountain Journal of Mathematics 4, 287–296.

Wilf, H.S., 1962. Mathematics for the physical sciences. John Wiley and Sons, New York (NJ), USA.

Wright Jr, D.L., 2007. Numerical advection of moments of the particle size distribution in eulerian models. Journal of Aerosol Science 38, 352–369.

Yuan, C., Fox, R.O., 2011. Conditional quadrature method of moments for kinetic equations. Journal of Computational Physics 230, 8216–8246.

Yuan, C., Laurent, F., Fox, R.O., 2012. An extended quadrature method of moments for population balance equations. Journal of Aerosol Science 51, 1–23.

Zhao, H., Maisels, A., Matsoukas, T., Zheng, C., 2007. Analysis of four monte carlo methods for the solution of population balances in dispersed systems. Powder Technology 173, 38–50.

Zucca, A., Marchisio, D.L., Vanni, M., Barresi, A.A., 2007. Validation of bivariate DQMOM for nanoparticle processes simulation. American Institute of Chemical Engineering Journal 53, 918–931.

Chapter 3

CFD coupling

Multiphase systems can be described according to different approaches. Since the inherent complexity of these systems, there is not a definitive model that can be considered universally applicable: it should be evaluated for any kind of problem which is the most convenient one to use, accordingly to the type of system under consideration and the information to be obtained. The reason for this lack is due mainly to two factors (van Wachem and Almstedt, 2003):

- different multiphase systems (i.e., gas-solid, liquid-solid, liquid-liquid, etc..) may result into different fluid dynamic regimes (annular flow, jet flow, slug flow, bubbly flow, etc.) that are very difficult to integrate into a single model.
- the forces that arise when two or more phases are in contact (dynamic interface, coalescence, breakage, drag, etc.) usually have a complex mathematical formulation and can be not convenient to consider all types of forces existing.

It is usually possible to distinguish between methods that solve the interface profile, used in simulations where the scale of reference is that of the particle, and averaged methods, which do not address the problem of the interface, making the application to spatially larger systems easy. Among the former methods, it should be mentioned the family of Volume of Fluid (VOF) methods (Hirt and Nichols, 1981): with these it is possible to trace the interface between the continuous and the disperse phase, describing in detail the shape of the dispersed particle during its motion in the continuous fluid. The different phases are considered to be completely segregated in the computational cell (i.e., only one phase present in a single cell); an additional equation solves the evolution of the interface and can be formulated according to different point of views (Eulerian or Lagrangian or in a combination of both) (Peskin, 1977; Hirt and Nichols, 1981; Osher and Sethian, 1988; Unverdi and Tryggvason, 1992). The limitation of these methods is the high definition of the calculation grid necessary to represent in detail the shape of the dispersed particle and therefore its interface; for this reason the computational costs can be very high. These methods fall into the category of Direct Numerical Simulation (DNS) for multiphase systems and provide very

precise information, but their use is mostly limited to simple geometries and small portions of systems.

The averaged methods may be divided in two categories: Eulerian-Lagrangian and Eulerian-Eulerian methods. The Eulerian-Lagrangian approach prescribes that the flow field of the continuous phase is calculated by using the averaged Navier-Stokes equation, while the motion of each one of the particles composing the disperse phase is taken into account by calculating the trajectories of the particles moving in the continuous phase, exchanging momentum, mass and energy with the surrounding fluid. The limitation of this type of approach is related to the global amount of particles traceable; in fact, despite of the continuous increase in computing power, this amount is always restricted, and consequently the models Lagrangian-Eulerian are only applicable to certain types of systems (such as sprays or droplet). Among these methods, it is worth mentioning the Particle Source in Cell (PSIC) used for simulate gas-liquid and gas-solid systems (Migdal and Agosta, 1967; Crowe et al., 1977), but with a limit on the volume fraction of the disperse phase, since a way to account for the interactions between different particles is not expected. For high volume fractions, it is possible to use the so-called Discrete Particle Method (DPM) (Li et al., 1999; Chen and Fan, 2004; van Sint Annaland et al., 2005).

With the Eulerian-Eulerian approach, all the phases present in the multiphase system are treated as interpenetrating continua, sharing the same space and interacting through their source terms. The concept of volume fraction is essential: all the equations are written in such a way that volume fractions assume values between zero and one: the summation of these, in each cell, must be equal to one. It is clear that in this approach an average of the properties of the single dispersed particles is performed, calculating the evolution of different phases characterized by averaged quantities. Among these Eulerian-Eulerian methods, the multifluid model and the mixture model are the most important (Drew and Passman, 1999; Hjertager, 2007; Yeoh and Tu, 2010). The former solves the constitutive equations for the N different phases composing the multiphase system, while the latter uses a few equations that describe the properties of the mixture, rather than those of the individual phases. However, this latter method is more indicated when a multiphase system composed by phases with more or less the same density is considered.

Since the aim of this work is to simulate industrial scale gas-liquid systems, the multifluid model will be used. In this chapter, the constitutive equations of the model will be formulated, with particular attention to the peculiarities of gas-liquid systems and the coupling procedure with the Population Balance Equation.

3.1 Multifluid model

In general, it is possible to describe a multiphase system by means of a finite number of regions, each one containing a single phase, divided by many interfaces. The derivation of the multifluid model consists in writing the local and instantaneous mass and momentum conservation equations for each phase and, through appropriate averaging techniques, deriving the equations that describe the average characteristics of the fluid. For engineering applications, in fact, the interest is often directed towards the average properties of a fluid; the fluctuations given by turbulence are taken into account only when they may affect the macroscopic properties. As it will be clearer below, the averaging process involves the definition of sub-models for some phenomena constituting the deviating components of the averaged equations, such as the effects of turbulence and the interaction between the phases. In the next section, the constitutive equations of the multifluid model for N different phases will be presented in detail.

3.1.1 Local and instantaneous formulation

For a given region V fixed in space and shared between N different physical phases, it is possible to write the balance equation for a generic (scalar or vector) extensive quantity ψ. By indicating with $V_k \subseteq V$ the portion of the volume occupied by $k-$th phase, the control volume V is the union of the N subvolumes:

$$V = \bigcup_{k=1}^{N} V_k(t) \tag{3.1}$$

where $k = 1, ..., N$. By assuming valid the continuum hypothesis, the balance equation for ψ is the following (Ishii and Mishima, 1984; Hjertager, 2007):

$$\begin{aligned}
&\underbrace{\sum_{k=1}^{N}\left(\frac{d}{dt}\int_{V_k(t)}\rho_k\psi_k dV\right)}_{accumulation} = \\
&= \underbrace{-\sum_{k=1}^{N}\left(\int_{A_k(t)}\rho_k\psi_k(\vec{u}_k\cdot\vec{n}_k)dA\right) - \sum_{k=1}^{N}\left(\int_{A_k(t)}(\vec{J}_k\cdot\vec{n}_k)dA\right)}_{net\ flux} + \\
&+ \underbrace{\frac{1}{2}\sum_{k=1}^{N}\sum_{j=1}^{N}(1-\delta_{jk})\int_{A_{I,jk}(t)}\Phi_{I,jk}dA + \sum_{k=1}^{N}\int_{V_k(t)}\rho_k\Phi_k dV}_{source\ term},
\end{aligned} \tag{3.2}$$

where $A_{I,jk}(t)$ represents the interface between $j-$th and $k-$th phase, $A_k(t)$ the surface of volume $V_k(t)$, ρ_k the density of $k-$th phase, ψ_k a property of the fluid evaluated for the $k-$th phase, $\vec{n}_k$ the normal vector of $A_k(t)$, $\vec{u}_k$ the instantaneous velocity of $k-$th phase, $\vec{J}_k$ the

flux of ψ_k due to other phenomena, Φ_k the volumetric source term, $\Phi_{I,jk}$ the source term of the interface and δ_{jk} the Kronecker delta (equal to 1 if $i = j$ and equal to 0 if $i \neq j$). It is important to say that the interface between phases can be thought as a separation surface between the phases through which discontinuity of properties may exist. The position of the interface $A_{I,jk}(t)$ is determined by the vector:

$$\vec{r}_{I,jk} = \vec{r}_{I,jk}(x(\zeta,\eta,t), y(\zeta,\eta,t), z(\zeta,\eta,t)), \tag{3.3}$$

and the velocity of the point(ζ,η) belonging to the surface is written as:

$$\vec{u}_{I,jk} = \left(\frac{\partial \vec{r}_{I,jk}}{\partial t}\right)_{\zeta,\eta=cost.}. \tag{3.4}$$

By means of Leibniz and Gauss theorem, it is possible to rewrite the three first terms of Eq. (3.2) as a sum of volume and surface integrals (a rigorous derivation can be found in Bove, 2005):

$$\frac{d}{dt}\int_{V_k(t)} \rho_k\psi_k dV = \int_{V_k(t)} \frac{\partial}{\partial t}(\rho_k\psi_k)dV + \sum_{j=1}^{N}(1-\delta_{jk})\int_{A_{I,jk}(t)} \rho_k\psi_k\vec{u}_{I,jk}\cdot\vec{n}_{kj}dA \tag{3.5}$$

$$\int_{A_k(t)} \rho_k\psi_k\vec{u}_k\cdot\vec{n}_k dA = \int_{V_k(t)} \nabla\cdot(\rho_k\psi_k\vec{u}_k)dV - \sum_{j=1}^{N}(1-\delta_{jk})\int_{A_{I,kj}(t)} \rho_k\psi_k\vec{u}_k\cdot\vec{n}_{kj}dA. \tag{3.6}$$

$$\int_{A_k(t)} \vec{J}_k\cdot\vec{n}_k dA = \int_{V_k(t)} \nabla\cdot\vec{J}_k dV - \sum_{j=1}^{N}(1-\delta_{jk})\int_{A_{I,kj}} \vec{J}_k\cdot\vec{n}_{kj}dA. \tag{3.7}$$

By substituting Eqs. (3.5) to (3.7) into Eq. (3.2) the following expression is obtained:

$$\begin{aligned}\sum_{k=1}^{N}\int_{V_k(t)}\left[\frac{\partial}{\partial t}(\rho_k\psi_k) + \nabla\cdot(\rho_k\psi_k\vec{u}_k) + \nabla\cdot\vec{J}_k - \rho_k\Phi_k\right]dV + \\ -\sum_{k=1}^{N}\sum_{j=1}^{N}(1-\delta_{jk})\int_{A_{I,kj}}\left[(\dot{m}_{I,kj}\psi_k + \vec{J}_k\cdot\vec{n}_{kj}) + \frac{1}{2}\Phi_{I,kj}\right]dA = 0,\end{aligned} \tag{3.8}$$

where the mass exchange term $\dot{m}_{I,kj}$ per unit of area and unit time from $k-$th phase to $j-$th phase is defined as:

$$\dot{m}_{I,kj} = \rho_k(\vec{u}_k - \vec{u}_{I,kj})\cdot\vec{n_{I,kj}}. \tag{3.9}$$

Since control volume V is generic, Eq. (3.8) is valid for any $V_k(t)$ and $A_{I,kj}(t)$. Therefore, the local and instantanous balance equation has the following form:

$$\frac{\partial}{\partial t}(\rho_k\psi_k) + \nabla\cdot(\rho_k\psi_k\vec{u}_k) + \nabla\cdot\vec{J}_k - \rho_k\Phi_k = 0, \tag{3.10}$$

and the condition for the interfacial jump:

$$\psi_j \dot{m}_{I,jk} + \psi_k \dot{m}_{I,kj} + \vec{J}_j \cdot \vec{n}_{I,jk} + \vec{J}_k \cdot \vec{n}_{I,kj} = \Phi_{I,jk}. \tag{3.11}$$

Eq. (3.10) and Eq. (3.11) are valid for any ψ_k, properly providing $\vec{J}_k$, Φ_k and $\Phi_{I,kj}$. Mass, momentum, chemical species and energy balance equation are written in the form of Eq. (3.10) and Eq. (3.11) (Hjertager, 2007). Since in this work, an isothermal system is modeled, only first three balance equation will be reported below.

Mass balance for $k-$th phase can be written as:

$$\frac{\partial \rho_k}{\partial t} + \nabla \cdot (\rho_k \vec{u}_k) = 0 \tag{3.12}$$

and the jump condition as:

$$\dot{m}_{I,jk} + \dot{m}_{I,kj} = 0. \tag{3.13}$$

Momentum balance equation for $k-$th phase is:

$$\frac{\partial}{\partial t}(\rho_k \vec{u}_k) + \nabla \cdot (\rho_k \vec{u}_k \vec{u}_k) = \nabla \cdot \bar{\bar{T}}_k + \rho_k \cdot \vec{b}_k, \tag{3.14}$$

and the interfacial jump condition:

$$\dot{m}_{I,jk} \vec{u}_j + \dot{m}_{I,kj} \vec{u}_k + \bar{\bar{T}}_j \cdot \vec{n}_{I,jk} + \bar{\bar{T}}_k \cdot \vec{n}_{I,kj} = \vec{m}^{\sigma}_{jk}, \tag{3.15}$$

where $\bar{\bar{T}}$ represents the stress tensor, $\vec{b}_k$ is the vector representing the sum of the forces acting on $k-$th phase and m^{σ}_{jk} is the superficial traction, which has the dimension of stress and is defined as:

$$m^{\sigma}_{jk} = 2H_{jk}\sigma \vec{n}_{I,jk} - \nabla_{I,jk}\sigma, \tag{3.16}$$

where σ is the interfacial tension, H_{jk} the interface curvature e $\nabla_{I,jk}\sigma$ is the gradient of interfacial tension between $j-$th and $k-$th phases (Aris, 1962). For the mass fraction Y_k of a chemical species:

$$\frac{\partial}{\partial t}(\rho_k Y_k) + \nabla \cdot (\rho_k Y_k \vec{u}_k) = -\nabla \vec{F}_{Y,k} + \rho_k \Psi_k \tag{3.17}$$

and the interfacial jump condition:

$$\dot{m}_{I,jk} Y_j + \dot{m}_{I,kj} Y_k + \vec{F}_{Y,j} \cdot \vec{n}_{I,jk} + \vec{F}_{Y,k} \cdot \vec{n}_{I,kj} = \Psi_{I,kj} \tag{3.18}$$

where $\vec{F}_{Y,k}$ is the molecular flux of Y in the $k-$th phase according to Fick law, Ψ_k is the volumetric generation rate of Y of $k-$th phase and $\Psi_{I,kj}$ is the interfacial generation rate of Y per unit area of the interface jk.

Eqs. (3.12) to (3.18) describe in detail all the fluid dynamics aspects of a generic multiphase system. Since the final aim of this work is to develop a methodology for predicting

the behavior of industrial scale systems, averaging techniques can be helpful to reduce the level of detail of the simulation.

3.1.2 Averaging techniques

Averaging techniques commonly used in the multiphase modeling can be essentially of three types: time average, spatial average or ensemble average. As pointed out by Drew and Passman (1999), the averaged equations for multiphase flows were historically derived by means of volume averaging, in which the averaging procedure was performed on a volume larger than the characteristic volume of the secondary phase. Therefore, all the information lost on the scales smaller than the averaging scale need to be accounted for through sub-grid models, which may be derived empirically, analytically or numerically (Hjertager, 2007). However, in this way, the model is sensitive to the choice of averaging volume (Drew and Passman, 1999); with the ensemble averaging, the obtained equations are the same to those derived with the volume averaging technique and from the mathematical point of view are independent of the choice of volume control. Therefore, the latter method will be used.

In deriving conservation laws for each phase on the desired domain it is important to distinguish between phases during the averaging procedure. The mathematical tool used for performing this distinction is the so-called "indicator function", specifically defined to isolate each phase from others even in the microscale description. Defining the space of all possible events $\mathscr{E}$ of a given system $\mathscr{P}$, the local and instantaneous formulation of a generic variable f defined in $\mathscr{P}$ can be written as $f(\vec{r}, t; \mu)$, where $\vec{r} \in \mathscr{R}$ is the vector of position coordinates, t is the time and $\mu \in \mathscr{E}$ is a particular realization of $\mathscr{P}$. The indicator function for the $k-$th phase in any realization μ is defined as:

$$X_k(\vec{r}, t; \mu) = \begin{cases} 1 & \text{if } \vec{r} \in \text{phase } k \text{ in realization } \mu \\ 0 & \text{otherwise} \end{cases} \tag{3.19}$$

By using the phase indicator function is possible to describe the behavior of a single phase in completely separate way from the entire multiphase system, ignoring all the other phases and interfaces. Moreover, the definition of Eq. (3.19) is useful to the derivation of averaged equations, for example:

$$\frac{\partial X_k}{\partial t} + \vec{u}_{I,jk} \cdot \nabla X_k = 0, \tag{3.20}$$

namely the derivatives of phase indicator function is equal to zero. The term ∇X_k can be written as:

$$\nabla X_k = \left(\frac{\partial X_k}{\partial n} \right) \vec{n}_{I,kj} = \delta(\vec{r} - \vec{r}_{I,kj}) \vec{n}_{I,kj} \tag{3.21}$$

where $\delta(\vec{r} - \vec{r}_{I,kj})$ is the Dirac delta function for the interface between $j-$th and $k-$th.

Now it is important to define the ensemble average of f in the following way:

$$\langle f(\vec{r}, t; \mu) \rangle^{\mathscr{E}} = \int_{\mathscr{E}} f(\vec{r}, t; \mu) \, \mathrm{d}m(\mu) \tag{3.22}$$

where $dm(\mu)$ is the density for the probability on the set of all events $\mathscr{E}$. It can be shown that for the ensemble average the following relationships are valid (Drew and Passman, 1999):

- according to Leibnitz theorem:

$$\left\langle X_k \frac{\partial f}{\partial t} \right\rangle^{\mathscr{E}} = \left\langle \frac{\partial X_k f}{\partial t} \right\rangle^{\mathscr{E}} - \left\langle f_{kj} \frac{\partial X_k}{\partial t} \right\rangle^{\mathscr{E}} \tag{3.23}$$

- according to Gauss theorem:

$$\langle X_k \nabla f \rangle^{\mathscr{E}} = \langle \nabla (X_k f) \rangle^{\mathscr{E}} + \langle f_{kj} \nabla X_k \rangle^{\mathscr{E}} \tag{3.24}$$

where f_{kj} represent the value of the function f evaluated on $k-$th phase region of the interface kj. Moreover, also the so-called Reynolds rules are valid:

$$\begin{aligned}
\langle f + g \rangle &= \langle f \rangle + \langle g \rangle \\
\langle \langle f \rangle g \rangle &= \langle f \rangle \langle g \rangle \\
\langle \text{cost.} \rangle &= \text{cost.} \\
\left\langle \frac{\partial f}{\partial t} \right\rangle &= \frac{\partial \langle f \rangle}{\partial t} \\
\langle \nabla f \rangle &= \nabla \langle f \rangle \\
\langle \nabla \cdot f \rangle &= \nabla \cdot \langle f \rangle
\end{aligned} \tag{3.25}$$

By multiplying Eq. (3.10) for the phase indicator function X_k e and applying the ensemble averaging, the following equation is obtained:

$$\begin{aligned}
\frac{\partial}{\partial t} \langle X_k \rho_k \psi_k \rangle + \nabla \cdot \langle X_k \rho_k \psi_k \vec{u}_k \rangle = -\langle X_k \vec{J}_k \rangle + \langle X_k \rho_k \Phi_k \rangle + \\
- \frac{1}{V} \sum_{j=1}^{N} (1 - \delta_{jk}) \int_{A_{I,kj}} [\dot{m}_{I,kj} \psi_k + \vec{J}_k \cdot \vec{n}_{I,kj}] dA
\end{aligned} \tag{3.26}$$

The average equation for the interface jump condition can be written multiplying Eq. (3.11) for the gradient of indicator phase function ∇X_k and performing the averaging procedure:

$$\frac{1}{V} \int_V [\psi_j \dot{m}_{I,jk} + \psi_k \dot{m}_{I,kj} + \vec{J}_j \vec{n}_{I,jk} + \vec{J}_k \vec{n}_{I,kj}] dV = \frac{1}{V} \int_V \Phi_{I,jk} dV \tag{3.27}$$

3.1.3 Constitutive equations of multifluid model

Constitutive equations of the model can be written in compact form by means of the following defined averages (Drew and Passman, 1999):

1. phase average:
$$\psi_k = \frac{\langle X_k \psi_k \rangle}{\alpha_k} \tag{3.28}$$
where α_k is the volume fraction of $k-$th phase and is defined as ensemble average of the phase indicator function X_k (i.e., $\alpha_k = \langle X_k \rangle$) and the following relationship is valid:
$$\sum_{K=1}^{N} \alpha_k = 1; \tag{3.29}$$

2. interfacial area per unit volume expressed as:
$$A_k = -\langle \vec{n}_k \cdot \nabla X_k \rangle \tag{3.30}$$
where $\vec{n}_k$ is the unit normal vector to $k-$th phase;

3. density weighted average (or Favre average) written as:
$$\hat{\psi}_k = \frac{\langle X_k \rho_k \psi_k \rangle}{\alpha_k \bar{\rho}_k}. \tag{3.31}$$

The balance equation for the for a Favre-averaged generic quantity of $k-$th phase $\hat{\psi}$ can be written as:

$$\frac{\partial}{\partial t}(\alpha_k \bar{\rho}_k \hat{\psi}_k) + \nabla \cdot (\alpha_k \bar{\rho}_k \hat{\psi}_k \hat{\vec{u}}_k) = -\nabla \cdot \left[\alpha_k \left(\hat{\vec{J}}_k + \vec{J}_k^T\right)\right] + (\alpha_k \bar{\rho}_k \hat{\Phi}_k) + \\ - \frac{1}{V} \sum_{j=1}^{N} (1 - \delta_{jk}) \int_{A_{I,kj}} [\dot{m}_{I,kj} \psi_k + \vec{J}_k \cdot \vec{n}_{I,kj}] dA \tag{3.32}$$

where $\vec{J}_k^T$ is originated by averaging procedure of the advective term. This unclosed term contains the information relating to the turbulence of the system. The vector (or tensor if ψ_k is a vector field) $\vec{J}_k^T$ can be formulated in the following way:

$$\vec{J}_k^T = \bar{\rho}_k \left(\widehat{\psi_k \vec{u}_k} - \hat{\psi}_k \hat{\vec{u}}_k\right) \tag{3.33}$$

Below the averaged constitutive equations for a generic multiphase system are presented. As seen in Section 3.1.1, at least three relationship are necessary to describe the evolution of an isothermal system:

- mass conservation
$$\frac{\partial}{\partial t}(\alpha_k \bar{\rho}_k) + \nabla \cdot (\alpha_k \bar{\rho}_k \hat{\vec{u}}_k) = \Gamma_k \tag{3.34}$$

- momentum conservation (Navier-Stokes)
$$\frac{\partial}{\partial t}(\alpha_k \bar{\rho}_k \hat{\vec{u}}_k) + \nabla \cdot (\alpha_k \bar{\rho}_k \hat{\vec{u}}_k \hat{\vec{u}}_k) = \nabla \cdot \left[\alpha_k \left(\hat{\bar{\vec{T}}}_k + \bar{\vec{T}}_k^T\right)\right] + (\alpha_k \bar{\rho}_k \vec{g}) + \Gamma_k \hat{\vec{u}}_k + \vec{M}_{I,k} \tag{3.35}$$

- mass fraction of the Y_k chemical species conservation

$$\frac{\partial}{\partial t}(\alpha_k \bar{\rho}_k \hat{Y}_k) + \nabla \cdot (\alpha_k \bar{\bar{u}}_k \hat{Y}_k) = -\nabla \cdot \alpha_k (\hat{\bar{\bar{F}}}_{Y,k} + \hat{\bar{\bar{F}}}^T_{Y,k}) + \hat{Y}_{kj} \cdot \Gamma_k + \alpha_k \bar{\rho}_k \hat{\Psi}_k \tag{3.36}$$

where $\bar{\bar{T}}^T_k$ represent the Reynolds stress tensor generated by the averaging procedure. Furthermore, the right-hand side terms of Eq. (3.36) represent respectively the mass exchange within $k-$th phase due to concentration gradient, mass transfer from other phases to $k-$th and the generation rate of Y in phase k (e.g., due to chemical reaction). Γ_k is the mass exchange term between phases defined as:

$$\Gamma_k = -\frac{1}{V} \sum_{j=1}^{N} (1 - \delta_{jk}) \int_{A_{I,kj}} \dot{m}_{I,kj} dA \tag{3.37}$$

while the term $\vec{M}_{I,k}$ takes into account the interfacial forces between phases:

$$\vec{M}_{I,k} = -\frac{1}{V} \sum_{j=1}^{N} (1 - \delta_{jk}) \int_{A_{I,kj}} \left[\dot{m}_{I,kj} \vec{u}_k - \bar{\bar{T}}_k \cdot \vec{n}_{I,kj} \right] dA \tag{3.38}$$

For the mass conservation, the interface jump condition is:

$$\frac{1}{V} \int_{A_{I,kj}} [\dot{m}_{I,jk} + \dot{m}_{I,kj}] dA = 0, \tag{3.39}$$

and for momentum conservation:

$$\frac{1}{V} \int_{A_{I,kj}} \left[\vec{u}_j \dot{m}_{I,jk} + \vec{u}_k \dot{m}_{I,kj} - \bar{\bar{T}}_j \cdot \vec{n}_{I,jk} - \bar{\bar{T}}_k \cdot \vec{n}_{I,kj} \right] dA = -\frac{1}{V} \int_{A_{I,kj}} \vec{m}^{\sigma}_{jk} dA. \tag{3.40}$$

Therefore the following constraints are valid for the mass exchange:

$$\sum_{k=1}^{N} \Gamma_k = 0, \tag{3.41}$$

and for momentum exchange:

$$\sum_{k=1}^{N} [\Gamma_k \vec{u}_k + \vec{M}_{I,k}] = \frac{1}{2} \sum_{k=1}^{N} \sum_{j=1}^{N} \frac{1}{V} (1 - \delta_{kj}) \int_{A_{I,kj}} \vec{m}^{\sigma}_{jk} dA = \vec{M}_{\sigma}. \tag{3.42}$$

3.2 Closure relations for multifluid model

The multifluid model written in the form expressed in Section 3.1.3 can not be directly solved since there are terms not directly depending on averaged fluid quantities. These unclosed

terms can be divided in three groups:

1. self-interaction terms ($\bar{\bar{T}}_k$);
2. terms of interaction between phases (Γ_k, $\vec{M}_{I,k}$, $\vec{M}_\sigma$);
3. turbulence terms ($\bar{\bar{T}}_k^T$).

Moreover, the thermodynamic state of the system must be defined through equations of state, linking the different thermodynamic variables. The closures of the aforementioned terms together with state equations defines the constitutive laws for a given system. In the next section, the laws of closure for the multifluid model will be derived, with special mention to gas-liquid in which the dispersed phase are bubbles.

3.2.1 Self-interaction term

The viscous stress tensor $\bar{\bar{T}}_k$ of the $k-$th phase can be formulated as sum of two different components, a pressure term and a shear stress term (Aris, 1962):

$$\bar{\bar{T}}_k = -p_k \bar{\bar{I}} + \bar{\bar{\tau}}_k. \tag{3.43}$$

The shear stress tensor is modeled according to the Newtonian strain-stress relationship:

$$\bar{\bar{\tau}}_k = \zeta_k \left(\nabla \cdot \hat{\vec{u}}_k \right) \bar{\bar{I}} + 2\mu_k \left[\bar{\bar{S}}_k - \frac{1}{3} \nabla \cdot \hat{\vec{u}}_k \bar{\bar{I}} \right], \tag{3.44}$$

where $\bar{\bar{I}}$ is the identity matrix and the strain-rate tensor is defined as:

$$\bar{\bar{S}}_k = \frac{1}{2} \left(\nabla \cdot \hat{\vec{u}}_k + \left(\nabla \cdot \hat{\vec{u}}_k \right)^T \right). \tag{3.45}$$

The bulk viscosity ζ_k is generally assumed equal to zero for all phases, while the dynamic viscosity μ_k is usually equal to the value of the laminar viscosity, different for each phase (for the dispersed gas phase is usually assumed equal to zero). The effects of secondary phases and temperature on this term is in general neglected in first approximation, especially when an isothermal system is studied, as in examined case. Furthermore, it is possible to state that by neglecting the effect of surface tension, as if the different phases were not separated, the same pressure is shared by all the phases:

$$p_k = p_{I,k} = p. \tag{3.46}$$

3.2.2 Interaction terms between phases

The formulation of the term Γ_k depends on the process (i.e., evaporation, condensation, mass transfer, etc.) that one wants to simulate. If there is an exchange of mass, Γ_k equal to zero; in the case of mass transfer, this term must be defined according the underlying theory, as in Section 2.2.1.

The force acting on the interface of $k-$th phase $\vec{M}_{I,k}$ is usually expressed with a sum of an average interfacial pressure, a shear rate acting on the interface and a term accounting for the forces acting on the bubbles:

$$\vec{M}_{I,k} = p_{I,k}\nabla\alpha_k - \bar{\bar{\tau}}_{I,k}\nabla\alpha_k + \vec{M}^e_{I,k}. \tag{3.47}$$

In this manner, it is possible to rewrite the right-hand side of Eq. (3.35) in the following way:

$$\begin{aligned}\nabla\cdot\left(\alpha_k\bar{\bar{\hat{T}}}_k\right) + (\alpha_k\bar{\rho}_k\vec{g}) + \Gamma_k\hat{\vec{u}}_k + \vec{M}_{I,k} = \\ = -\alpha_k\nabla p_k + \nabla\cdot\left(\alpha_k\bar{\bar{\tau}}_k\right) + (p_{I,k}-p_k)\nabla\alpha_k - \tau_{I,k}\nabla\cdot\alpha_k + (\alpha_k\bar{\rho}_k\vec{g}) + \Gamma_k\hat{\vec{u}}_k + \vec{M}^e_{I,k},\end{aligned} \tag{3.48}$$

where $\vec{M}^e_{I,k}$ represents the external forces per unit volume acting on the interface between the continuous phase and the $k-$th disperse phase. Since the external forces are of different nature, $\vec{M}^e_{I,k}$ is a linear combination of various acting forces. Moreover, it is possible to consider the gas-liquid system composed by a continuous (or primary) phase (with $k = 1$) and $N-1$ disperse phases, each one representing a group of bubbles characterized by a value of size, composition and velocity. By assuming that interfacial forces act only between continuous and disperse phases, a reasonable assumption for low gas hold-up, the external forces term for the primary phase results in (Ishii and Mishima, 1984):

$$\vec{M}_{I,1} = \sum_{k=2}^{N}(\vec{M}^D_{I,k} + \vec{M}^L_{I,k} + \vec{M}^{VM}_{I,k} + \vec{M}^B_{I,k} + \vec{M}^{TD}_{I,k}), \tag{3.49}$$

while for the secondary phases:

$$\vec{M}_{I,k} = -\vec{M}^D_{I,k} - \vec{M}^L_{I,k} - \vec{M}^{VM}_{I,k} - \vec{M}^B_{I,k} - \vec{M}^{TD}_{I,k} \qquad k = 2, ..., N. \tag{3.50}$$

The different terms in Eq. (3.49) and Eq. (3.50) represent respectively contributions of drag, lift, virtual mass, Basset and turbulent dispersion forces. Since each term of Eq. (3.49) and Eq. (3.50) are forces per unit volume, $\vec{M}_{I,k}$ is expressed in the following way:

$$\vec{M}_{I,k} = \frac{\alpha_k}{V_b}\vec{F}_{I,k}, \tag{3.51}$$

where V_b is the volume of the single bubble. In the case of bubbles with spherical shape, it is possible to write:

$$V_b = \frac{\pi}{6}\bar{d}^3_{b,k} \tag{3.52}$$

where $\bar{d}_{b,k}$ is the diameter of the bubbles belonging to the $k-$th group of bubbles.

This way to express $\vec{M}_{I,k}$ respects the jump condition at the interface as specified in Eq. (3.40). In the following sections, the meaning of the terms entering Eq. (3.49) and Eq. (3.50) and their formulation from modeling point of view will be treated.

3.2.3 Drag force

The relative stationary motion between an immersed body and the surrounding fluid (primary or continuous phase) generates the drag force. This force acts on single bubbles and has an influence on the global hold-up of the disperse phase, as well as on flooding point and heat and mass transfer coefficients. Drag force $\vec{F}_{I,k}^{\,D}$ has two different contributions: the first is linked to the surface friction due to the shear rates acting on the surface of the immersed body. The second is related to the shape of the body and is generated by the non-uniform pressure distribution caused by the relative (or slip) velocity between the object and the fluid (Bird et al., 2002). Therefore, the drag force is expressed in terms of the projection area A of the body, the slip velocity and the so-called drag coefficient $C_{D,k}$:

$$\vec{F}_{I,k}^{\,D} = \frac{1}{2}\rho_1 C_{D,k} A |\vec{u}_k - \vec{u}_1|(\vec{u}_k - \vec{u}_1). \tag{3.53}$$

In general $C_{D,k}$ depends on the characteristics of the continuous phase according to the following definition of Reynolds number for dispersed systems:

$$\mathrm{Re} = \frac{\rho_1 \bar{d}_{b,k} |\vec{u}_k - \vec{u}_1|}{\mu_1}, \tag{3.54}$$

where μ_1 is the dynamic viscosity of the continuous phase. For spherical particles $\bar{d}_{b,k}$ is the diameter, while for particles of other shapes an equivalent diameter can be conveniently defined. In Fig. 3.1 the behavior of drag coefficient $C_{D,k}$ is reported for a solid spherical particle as a function of Re.

For low Reynolds numbers (Re < 1), the drag coefficient is inversely proportional to the values of Re. For these values, the non-linear advective term of Navier-Stokes equation is negligible with respect to the viscous term and the stationary momentum balance equation for the incompressible continuous phase can be written in the following form:

$$\nabla p = \mu_l \nabla^2 \vec{u}_1. \tag{3.55}$$

The solution of this equation was provided by Stokes, giving the name to the fluid regime that one has for these conditions. The drag force acting on a solid particle immersed in a Stokesian fluid results equal to:

$$\vec{F}_D = 3\pi\mu_1 \bar{d}_{b,k} |\vec{u}_k - \vec{u}_1|(\vec{u}_k - \vec{u}_1), \tag{3.56}$$

where $|\vec{u}_k - \vec{u}_1|$ is absolute value the slip velocity. By substituting Eq. (3.56) into Eq. (3.53), it is possible to express the drag coefficient as:

$$C_{D,k} = \frac{\vec{F}_D}{0,5\rho_1 A(\vec{u}_k - \vec{u}_1)} = \frac{24}{\mathrm{Re}} \tag{3.57}$$

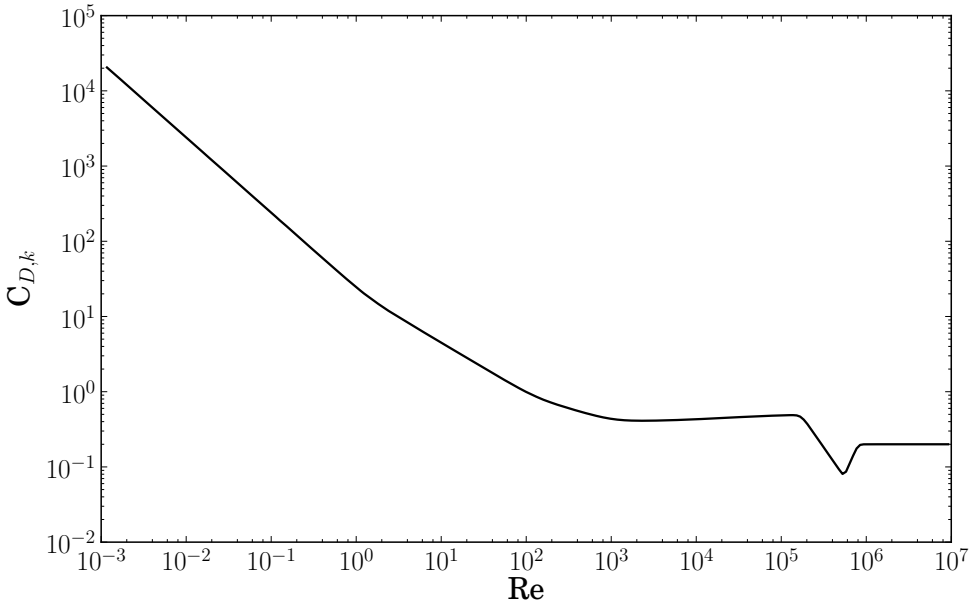

Figure 3.1: Values of the drag coefficient $C_{D,k}$ in function of the Reynolds number for a solid shperical shere.

where $A = \pi \vec{d}_{b,k}^2/4$ represents the projection area. For values of Re > 1, the assumption underlying the Stokesian regime is no more valid, since the fluid inertia begins to show its importance and the behavior of $C_{D,k}$ deviates from Eq. (3.57). As is it possible to observe in Fig. 3.1, for values of Reynolds number ranging between 10^3 and $2,5 \cdot 10^5$ (Newton regime), the drag coefficient $C_{D,k}$ assumes an almost constant values equal to 0.44. In the zone between the two regimes (1<Re<10^3), it is possible to use the following drag coefficient proposed by Schiller and Naumann (1933):

$$C_{D,k} = \frac{24}{\mathrm{Re}}(1 + 0.15\mathrm{Re}^{0.687}). \tag{3.58}$$

For Re>$2,5 \cdot 10^5$ the values of drag coefficient $C_{D,k}$ strongly reduce due to the transition boundary layer of the from laminar to turbulent condition.

Hadamard e Rybczynski extended the Stokes relationship for $C_{D,k}$ to the case of a fluid sphere with viscosity μ_k immersed in a fluid with viscosity μ_1 (Crowe, 2006). The drag force acting on the fluid particle can be written in the following way:

$$\vec{F}_D = 2\pi\mu_1 A|\vec{u}_k - \vec{u}_1|\frac{3\lambda + 2}{\lambda + 1}, \tag{3.59}$$

where $\lambda = \mu_k/\mu_1$. The solid sphere represents a limiting case of Eq. (3.59) for $\lambda = \infty$, while the case of a bubble in a liquid can be approximated with $\lambda = 0$. In this latter case, the

following relationship is obtained:

$$C_{D,k} = \frac{16}{\mathrm{Re}}. \tag{3.60}$$

A fluid sphere rising or falling in a viscous liquid is subjected to the force of gravity, buoyancy and drag. In stationary conditions, the forces sum to zero, and the sphere is moving at a constant speed called terminal velocity (Clift et al., 1978). For a viscous sphere in Stokes regime, the terminal velocity is:

$$U_T = \frac{2}{3}\vec{g}A^2\frac{(\rho_1 - \rho_k)}{\mu_1}\frac{\lambda + 1}{3\lambda - 2} \tag{3.61}$$

This value should be considered as an upper limit, since the impurities present in real systems have an effect on the coefficient λ which is difficult to quantify. Furthermore, it is important to define the Eötvös number (Eo) in the following way:

$$\mathrm{Eo} = \frac{d_{b,k}^2 g|\rho_1 - \rho_k|}{\sigma}, \tag{3.62}$$

representing the ratio between buoyancy and superficial forces. For $\mathrm{Eo} \leq 4$, the size of the fluid sphere is small and tends to behave like solid spheres, instead for $\mathrm{Eo} > 4$ its behavior is more similar to that described by the equations of Hadamard e Rybczynski.

For high values of Reynolds number, the non linear advective term of Navier-Stokes equation becomes important: this implies that the vorticity and its gradients around the sphere are transported by the fluid; in these cases the drag coefficient cannot be calculated with a theoretical approach but can be estimated by means of empirical or semi-empirical expressions obtained by many authors. The experimental campaigns carried out for the determination of $C_{D,k}$ mainly consider a single not rotating particle or bubble, in motion through a fluid medium of infinite length and stagnant, therefore moving with a constant terminal velocity. Moreover correlations were developed to describe the swarm effect of on drag force; in fact the presence of many neighboring particles or bubbles generates interference that lead to a reduction of the slip velocity between the phases and this aspect should be consider in $C_{D,k}$ models. It is worth mentioning that rising or falling fluid spheres may change their shape according to different fluid dynamics conditions. The different shape regimes are shown in Fig. 3.2, according to Eötvös (Eo), Reynolds (Re) and Morton (Mo), this latter defined as:

$$\mathrm{Mo} = \frac{g\mu_1^4|\rho_1 - \rho_k|}{\rho_1^2\sigma^3}. \tag{3.63}$$

Some of the more popular drag correlations for gas-liquid systems will be reported below.

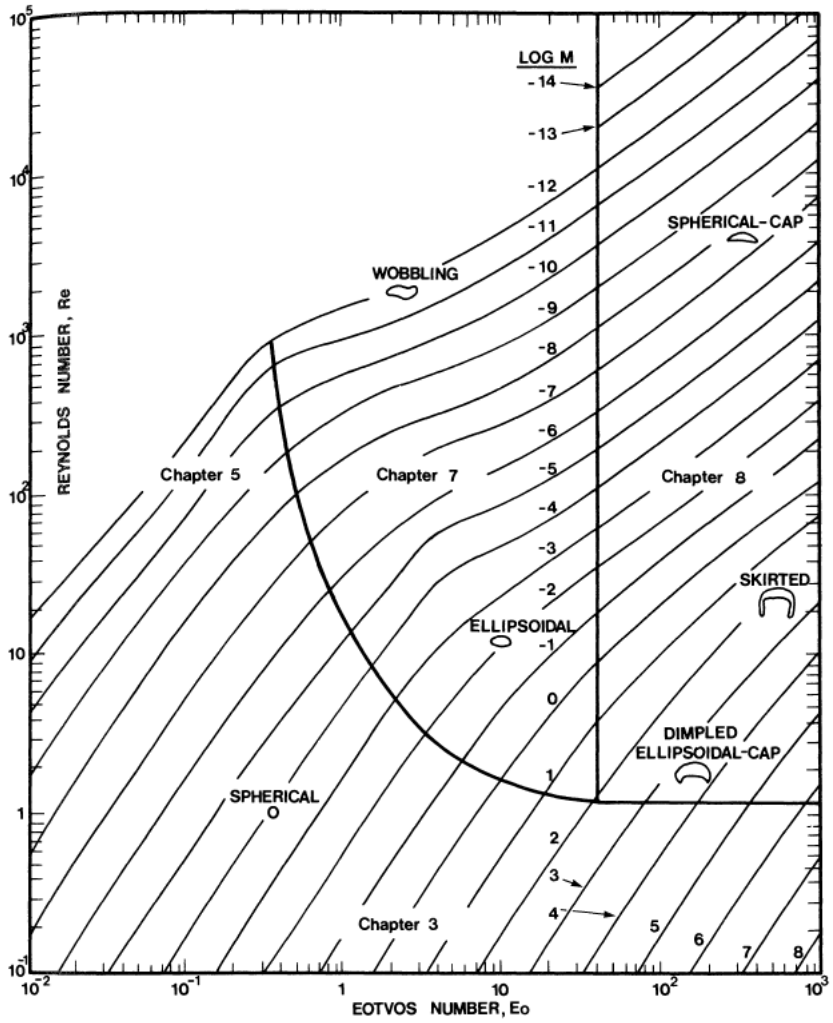

Figure 3.2: Shape regimes for falling or rising drops and bubbles in water. (Clift et al., 1978)

$C_{D,k}$ proposed by Schiller and Naumann

The well-known Schiller and Naumann correlation (Schiller and Naumann, 1933), valid for isolated solid spheres in liquids, has the following form:

$$C_{D,k} = \begin{cases} \frac{24}{\mathrm{Re}}(1 + 0.15\mathrm{Re}^{0.687}) & \text{if } \mathrm{Re} \leq 1000 \\ 0.44 & \text{if } \mathrm{Re} > 1000 \end{cases} \tag{3.64}$$

This correlation is here mentioned for its widespread implementation in CFD codes; it should not be used for the simulation of gas-liquid systems.

Drag correlation based on terminal velocity

Experiments on individual air bubbles in distilled water were conducted by Peebles and Garber (1953); Haberman and Morton (1956), which has been chosen because the contaminants in the primary stage have a significant influence on $C_{D,k}$.Taking into account the balance of forces acting on a single bubble rising in a primary stage considered of infinitesimal length, can be derived the following drag coefficient form:

$$C_{D,k} = \frac{4}{3}\frac{(\rho_1 - \rho_k)\bar{d}_{b,k}g}{\rho_1 \hat{\bar{u}}_t} \tag{3.65}$$

where $\hat{\bar{u}}_t$ is the terminal velocity of the rising bubble experimentally measured. The terminal velocity $\hat{\bar{u}}_t$ for a pure air water system can be calculated by means of the Grace correlation (Clift et al., 1978):

$$\hat{\bar{u}}_t = \sqrt{\left(\frac{2.14\sigma}{\rho_1 d_{b,k}} + 0.505 g d_{d,k}\right)} \qquad d_{b,k} \geq 1.3\mathrm{mm}. \tag{3.66}$$

Eq. (3.66) gives an expression to the central part of the curve shown in Fig. 3.3.

$C_{D,k}$ according to Tomiyama

Recently, Tomiyama et al. (1998) developed different correlations for air-water systems with different of purity of water:

- for a pure system:

$$C_{D,k} = \max\left[\min\left(\frac{16}{\mathrm{Re}}(1 + 0.15\mathrm{Re}^{0.687}), \frac{48}{\mathrm{Re}}\right), \frac{8}{3}\frac{Eo}{Eo + 4}\right] \tag{3.67}$$

- for a slightly contaminated water:

$$C_{D,k} = \max\left[\min\left(\frac{24}{\mathrm{Re}}(1 + 0.15\mathrm{Re}^{0.687}), \frac{72}{\mathrm{Re}}\right), \frac{8}{3}\frac{Eo}{Eo + 4}\right] \tag{3.68}$$

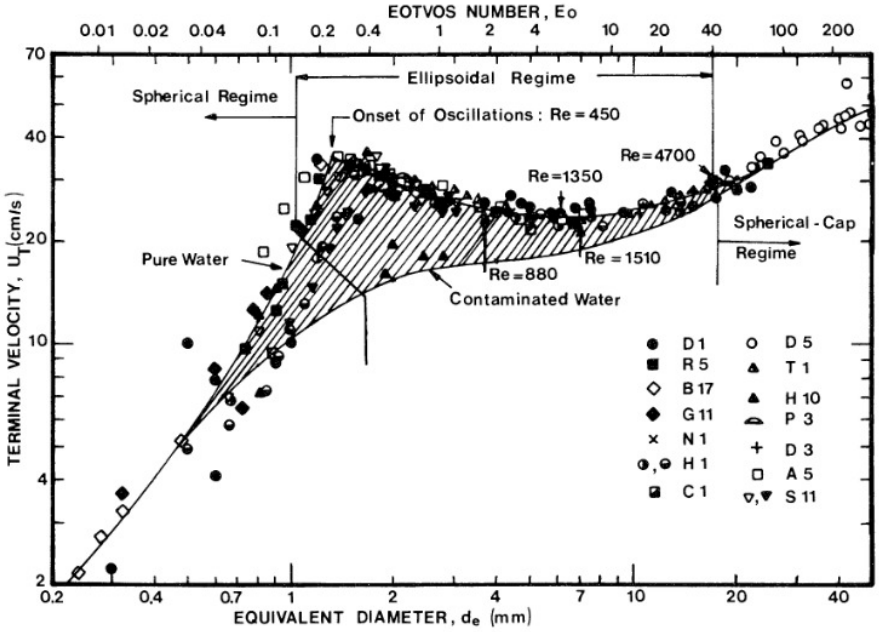

Figure 3.3: Terminal velocity for a single air bubble in water at 20°C. (Clift et al., 1978)

- for a fully contaminated water:

$$C_{D,k} = \max\left[\frac{24}{\mathrm{Re}}(1 + 0.15\mathrm{Re}^{0.687}), \frac{8}{3}\frac{Eo}{Eo+4}\right] \tag{3.69}$$

$C_{D,k}$ for swarm of bubbles

The motion of bubbles in water at different hold-up values was studied by Ishii and Zuber (1979), in order to determine the influence of swarms of bubbles on the drag coefficient. For this reason, they proposed an approach based on a mixture viscosity, namely a modified value of the viscosity of the primary phase that takes account of the additional resistance to the motion of the bubbles caused by a high concentration of bubbles themselves. The following correlation for the identified flow regimes was proposed:

$$C_{D,k} = \begin{cases} \dfrac{24}{\mathrm{Re}_m} & \text{Stokes Regime} \\ \dfrac{24}{\mathrm{Re}_m}(1 - 0.1\mathrm{Re}_m^{0.75}) & \text{Undistorted Particle Regime} \\ \dfrac{4\bar{d}_{b,k}}{6} f(\alpha_k)\sqrt{\dfrac{g(\rho_1 - \rho_k)}{\sigma}} & \text{Distorted Particle Regime} \\ \dfrac{8}{3}(1-\alpha_k)^2 & \text{Churn Turbulent Regime} \end{cases} \tag{3.70}$$

where

$$\mathrm{Re}_m = \frac{\bar{d}_{b,k}\rho_1|\hat{\vec{u}}_1 - \hat{\vec{u}}_k|}{\mu_m} \tag{3.71}$$

is the Reynolds number based on mixture viscosity μ_m. The function $f(\alpha_k)$ depends on relative viscosity between continuous and dispersed phases and can be expressed as follows:

$$f(\alpha_k) = \begin{cases} (1-\alpha_k)^{-0.5} & \text{for } \mu_1 \gg \mu_k \\ (1-\alpha_k)^{-1.0} & \text{for } \mu_1 \approx \mu_k \\ (1-\alpha_k)^{-1.5} & \text{for } \mu_1 \ll \mu_k \end{cases} \tag{3.72}$$

However, the swarm effect becomes significant for high local volume fraction of the dispersed phase, generally more than 20 %.

Turbulence effect on $C_{D,k}$

For solid particles larger than the typical length scale of turbulence, the dimensions and the characteristics of the boundary layer surrounding the particles are modified by the turbulent fluctuations and changing according to the drag force. For fluid particles, experimental studies showed that turbulence causes a reduction of the slip velocity. The model proposed by Bakker and Van den Akker (1994) takes this effect into account, based on the fact that the increase of momentum transport around the bubble can be related to the ratio between the size of the bubble and the length of the scale of turbulence. These authors introduce the concept of effective viscosity, defined as the sum of the molecular viscosity and of a term proportional to the eddy viscosity. In the case the $k-\epsilon$ model for the turbulence is used, effective viscosity can be written as:

$$\mu_{eff} = \mu_l + C\rho_l\frac{k^2}{\epsilon} \tag{3.73}$$

where k is the turbulent kinetic energy, ϵ is its rate of dissipation and C is a fitting parameter. The drag coefficient will be calculated by means of this modified Reynolds number:

$$\mathrm{Re}_{eff} = \frac{\bar{d}_{b,k}\rho_1|\vec{u}_1 - \vec{u}_k|}{\mu_{eff}} \tag{3.74}$$

This correlation is able to predict the decrease of slip velocity with increasing turbulence, and this damping is particularly significant for bubbles with diameter less than 5 mm. This seems reasonable, since larger bubbles fluctuates also in stagnant fluids, the turbulent fluctuations therefore play a minor role on their drag coefficient.

3.2.4 Other interfacial forces

Among interfacial forces, the drag force is certainly the most important of those listed in Eq. (3.49) and Eq. (3.50). Often, other forces are neglected in a first approximation and are evaluated only in a second time in order to reach a more accurate prediction of the system dynamics. It is very common procedure to consider only the drag force for the simulation of aerated stirred tank reactors, where the motion of the bubbles is imposed by the impeller (Petitti et al., 2010); in bubble columns also other forces, especially lift and virtual mass may have an effect on the predicted flow pattern. Nevertheless, they are often neglected even in this case especially in the simulation of laboratory scale rectangular columns (Diaz et al., 2008). Models for other interfacial forces are listed below, in order of importance.

Lift force

The lift force acting on the bubbles is able to induce a lateral shift of the rising motion, tending to bring the bubbles to the walls of the vessel. Through numerous experiments it was shown that this lateral shift depends strongly on the size of the bubble (for example, the small bubbles tend to go towards the walls, while the larger ones at the center of the vessel).The lift force represents the transverse force due to vorticity, evaluated in the center of the particle subject to such a force. The general expression for the lift force is the following (Drew and Lahey Jr, 1987):

$$F_d^L = \alpha_k \rho_1 C_L (\hat{\vec{u}}_k - \hat{\vec{u}}_1) \times \vec{\omega}_1, \tag{3.75}$$

where C_L is the lift coefficient. The following expression for $\vec{\omega}_1$ is given:

$$\vec{\omega}_1 = \nabla \times \hat{\vec{u}}_1. \tag{3.76}$$

For systems at low Reynolds number, the lift coefficient C_L for small bubbles rising in an air-water system ranges between 0.25 and 0.3 (Zun, 1980). A correlation for calculating C_L after numerous experiments in the case of a single bubble in air-water system was proposed by Tomiyama et al. (2002):

$$C_L = \begin{cases} \min[0.288 \tanh(0.121\mathrm{Re}), f(Eo)] & \text{se } Eo < 4 \\ f(Eo) & \text{se } Eo \geq 4 \end{cases} \tag{3.77}$$

where

$$f(Eo) = 0.00105 Eo^3 - 0.0159 Eo^2 - 0.0204 Eo + 0.474. \tag{3.78}$$

Another correlation was proposed by Hibiki and Ishii (2007), accounting for the swarm effect on lift force:

$$C_L = \xi \sqrt{[C_L^{\text{low Re}_m}(\mathrm{Re}_m, G_S)]^2 + C_L^{\text{high Re}_m}(Re_m, G_S)]^2}, \tag{3.79}$$

where Re_m is:

$$\mathrm{Re}_m = \frac{2\rho_1 \left|\hat{\bar{u}}_k - \hat{\bar{u}}_1\right| \bar{d}_{b,k}}{\mu_m}, \tag{3.80}$$

and G_S:

$$G_S = \left| \frac{\bar{d}_{b,k}}{\hat{\bar{u}}_k - \hat{\bar{u}}_1} \nabla \hat{\bar{u}}_1 \right|. \tag{3.81}$$

In practice, C_L is supposed to be constituted by the contribution of two different terms, the first acting at low Re_m ($\mathrm{Re}_m < 1000$):

$$C_L^{\text{low Re}_m} = \frac{6}{\pi^2 (2 Re_m G_S)^{1/2}} \frac{2.255}{(1 + 0.1 Re_m / G_S)^{3/2}}, \tag{3.82}$$

and the second term is important for high values of Re_m:

$$C_L^{\text{high Re}_m} = \frac{1}{2} \left(\frac{1 + 16 Re_m^{-1}}{1 + 29 Re_m^{-1}} \right). \tag{3.83}$$

The coefficient ξ takes into account the shape of the bubbles and can be expressed as:

$$\xi = 2 - \exp(0.136 Eo^{1.11}). \tag{3.84}$$

Turbulent dispersion force

As already mentioned, turbulent fluctuations are capable of strongly modifying the flow field of multiphase system, and the effect on the interfacial forces may be in some cases not negligible. Turbulent energy may be dissipated acting on different aspects of the disperse phase: size of the bubble, interfacial area, slip velocity and turbulent intensity of the continuous phase. Because of the difficulties related to the experimental techniques, it is difficult to isolate different effects of the turbulence and therefore formulate a unique model. As already seen, some authors took into account this phenomenon by modifying the drag coefficient (Bakker and Van den Akker, 1994); on the contrary some others expressed a new force able to consider the modifications on the disperse phase inducted by turbulence. Among these it is possible to mention the work of Lopez de Bertodano (1998), proposing the following model for a single bubble:

$$F_d^{TD} = -C_{TD} \rho_1 k_1 \nabla \alpha_k, \tag{3.85}$$

where C_{TD} is the turbulent dispersion coefficient (ranging between 0.1 and 0.5) and k_1 represents the turbulent kinetic energy of the continuous phase. The following model for a single bubble moving in a vertical cylinder, also accounting for wall effects was proposed by Podowski (2009):

$$F_d^{TD} = C_{TD} \rho_1 \nabla \cdot (\alpha_1 \bar{\bar{T}}_k^T), \tag{3.86}$$

with a coefficient C_{TD} equal to 2/3.

Virtual mass force

The drag force takes into account the interactions between the liquid and the bubbles in a field of uniform motion under the stationary conditions. If bubbles were accelerated in relation to the liquid, the liquid surrounding the bubble would be accelerated as well. This additional contribution is the so-called force of additional mass or virtual mass. The concept of virtual mass force can be understood by considering the change of kinetic energy of the liquid surrounding a bubble in acceleration. In a potential flow, acceleration induces a resistant force on a sphere equal to half the mass of the fluid displaced by the acceleration of the bubble. The general expression for this force is the following (Drew and Lahey Jr, 1987):

$$F_d^{VM} = \alpha_k \bar{\rho}_1 C_{VM} \left[\left(\frac{D}{Dt}\hat{\vec{u}}_k - \frac{D}{Dt}\hat{\vec{u}}_1 \right) + (\hat{\vec{u}}_1 - \hat{\vec{u}}_k) \cdot (\nabla\hat{\vec{u}}_k - \nabla\hat{\vec{u}}_1) \right] \tag{3.87}$$

where the virtual mass coefficient C_{VM} is function of the volume fraction α_k and for a single bubble ranges between 0.25 e 0.5. For very diluted solid particles in a fluid, it is possible to use the value calculated for a sphere in a potential flow, equal to 0.5. For gas-liquid systems, the following relationship was proposed by Wijngaarden and Jeffrey (1976):

$$C_{VM} = C_{VMP}(1 + 2.78\alpha_k), \tag{3.88}$$

where C_{VMP} represents the value of C_{VM} for a single bubble. It is important to remark that this force is usually neglected when the motion of the disperse phase can be assumed as stationary.

Basset force

The Basset force is the viscous force due to acceleration relative between the two phases, continuous and dispersed, and the development of the boundary layer near the interfacial surface. This force can be neglected when the motion of a stationary system is described and should be considered for the modeling of non-stationary flows. However, the relative importance compared to the drag force is such that even in this last case it is often neglected. The Basset force can be expressed as follows (Drew and Lahey Jr, 1987):

$$F_d^B = \frac{9}{\bar{d}_{b,k}} \alpha_1 \sqrt{\frac{\rho_1 \mu_1}{\pi}} \int_0^t \frac{a(r,t)}{\sqrt{t-\tau}} d\tau, \tag{3.89}$$

where for $a(r,t)$ is the acceleration between phases, given by the following relation:

$$a(r,t) = \left(\frac{D}{Dt}\vec{u}_1 - \frac{D}{Dt}\vec{u}_1 \right) - (\vec{u}_k - \vec{u}_1) \times (\nabla \times \vec{u}_l). \tag{3.90}$$

3.2.5 Turbulence closure

The averaging procedure of the advective term of the Navier-Stokes equation for the generic phase k brings to the definition of the so-called Reynolds stress tensor $\bar{\bar{T}}_k^T$, which takes into

account that part of the turbulent spectrum which is not resolved with the averaging process. While nowadays strengths and weaknesses of all the models for single phase systems are well-known, for multiphase flows, the turbulence modeling has still a number of not fully clarified aspects. As previously remarked, although accurate methods (such as Direct Numerical Simulation (DNS) or Large Eddy Simulation (LES)) allow to have a clearer view of the phenomenon, it is non-feasible to apply them to simulations of large systems due to the excessive details provided and the huge computational cost. In this sense, it should be considered the work of Kataoka and Serizawa (1989) and then Lopez de Bertodano and Saif (1997), which have derived and extended the well-known $k-\epsilon$ model for single phase systems to multiphase systems. Comparing the case of N generic phases with the single phase $k-\epsilon$, the number of terms that need to be modeled is larger and it is difficult to give a physical meaning for each term, making it extremely complex the treatment of turbulence in multiphase systems.

The multiphase $k-\epsilon$ is the common choice among other Reynolds-Averaged Navier-Stokes (RANS) models, because is a good trade off between accuracy and computational costs. However, recent work has shown that Large Eddy Simulations (LES) and Very Large Eddy Simulations (VLES) can be applied to bubbly flows for systems of small size, allowing to better describe the fluid dynamics of the systems compared to RANS prediction (Deen et al., 2001).

Since the final aim of this dissertation is to describe turbulent industrial scale systems, the following approaches are taken into account:

- *turbulence model only for the liquid phase*: standard $k-\epsilon$ model is used for the liquid phase and an additional term accounting for the turbulence inducted by the bubbles can be included.
- *mixture turbulence model*: when the ratio of densities between different phases in the systems is close to 1 or when the global gas hold-up is small, it is possible to solve the transport equation for k and ϵ referred to the mixture of the phases involved.

$k-\epsilon$ Turbulence Model only for the liquid phase

This model calculates the turbulent energy k and the its dissipation rate ϵ only for the liquid phase. Therefore, the equations have the following form (Kataoka and Serizawa, 1989):

$$\frac{\partial}{\partial t}(\alpha\bar{\rho}k)_1 + \nabla\cdot(\alpha\bar{\rho}\hat{\bar{u}}k)_1 = \nabla\cdot\left(\alpha\frac{\mu_T}{\sigma_k}\nabla k\right)_1 + \alpha_1\left[G_1 - \bar{\rho}\epsilon + P_{b,k}\right]_1, \tag{3.91}$$

$$\frac{\partial}{\partial t}(\alpha\bar{\rho}\epsilon)_1 + \nabla\cdot(\alpha\bar{\rho}\hat{\bar{u}}\epsilon)_1 = \nabla\cdot\left(\alpha\frac{\mu_T}{\sigma_\epsilon}\nabla\epsilon\right)_1 + \alpha_1\left[\frac{\epsilon}{k}(C_1G_1 - C_2\bar{\rho}\epsilon) + P_{b,\epsilon}\right]_1. \tag{3.92}$$

where the C_1 and C_2 are model parameters, indicated in Table 3.1. The term relating to the production of turbulent kinetic energy G_1 is defined as follows:

$$G_1 = \bar{\bar{\tau}}_1 : \nabla\hat{\bar{u}}_1, \tag{3.93}$$

where $\bar{\bar{\tau}}_1$ is defined according to Eq. (3.44). The turbulent viscosity $\mu_{T,1}$ is modeled in the following way:

$$\mu_{T,1} = C_\mu \bar{\rho} \frac{k_1^2}{\epsilon_1} \tag{3.94}$$

where C_μ is a constant. It should be remarked that when the two terms $P_{b,k}$ and $P_{b,\epsilon}$ relating to the additional turbulent kinetic energy produced or dissipated due to the work induced by the bubbles are equal to 0, the model has the form of the standard $k-\epsilon$ model. These two terms can be expressed, according to Sato and Sekoguchi (1975):

$$P_{b,k} = C_b \vec{M}_1^D \cdot (\hat{\vec{u}}_k - \hat{\vec{u}}_1) \tag{3.95}$$

$$P_{b,\epsilon} = C_{be}(1-\alpha_1)\hat{\rho}_1 \frac{k_1^{3/2}}{d_b} \tag{3.96}$$

where $\vec{M}_1^D$ is the drag force per unit volume expressed as in Eq. (3.51), d_b is the bubble diameter and C_b and C_{be} are two model constants. C_b usually ranges from 0.02 to 0.75, meaning that from 2 to 75 percent of the bubble-induced turbulence goes into the large eddy structure of the continuous phase, while C_{be} from 0.02 to 0.2. However, these large variations in the two constants indicate the problems with this turbulence model for bubbly flows (Hjertager, 2007), and, as said before, the two production terms are usually neglected (Zhang et al., 2006).

Table 3.1: Constants of the $k-\epsilon$ model.

C_μ	C_1	C_2	σ_k	σ_ϵ
0.09	1.44	1.92	1.0	1.3

$k-\epsilon$ Mixture Turbulence Model

As previously remarked, this model is based on the assumption that properties and mean velocities of the mixture are sufficient to describe the behavior of the turbulence of the multiphase system. It is possible to write the equations for k and ϵ in the following way (Yeoh and Tu, 2010):

$$\frac{\partial \rho_m k}{\partial t} + \nabla \cdot (\rho_m \hat{\vec{u}}_m k) = \nabla \cdot \left(\frac{\mu_{T,m}}{\sigma_k} \nabla k \right) + G_{k,m} - \rho_m \epsilon \tag{3.97}$$

$$\frac{\partial \rho_m \epsilon}{\partial t} + \nabla \cdot (\rho_m \hat{\vec{u}}_m \epsilon) = \nabla \cdot \left(\frac{\mu_{T,m}}{\sigma_\epsilon} \nabla \epsilon \right) + \frac{\epsilon}{k}(C_1 G_{k,m} - C_2 \rho_m \epsilon) \tag{3.98}$$

where ρ_m (mixture density) and $\hat{\vec{u}}_m$ (mixture velocity) are defined as:

$$\rho_m = \sum_{i=1}^{N} \alpha_i \rho_i, \tag{3.99}$$

$$\hat{\vec{u}}_m = \frac{\sum_{i=1}^{N} \alpha_i \rho_i \hat{\vec{u}}_i}{\sum_{i=1}^{N} \alpha_i \rho_i}, \tag{3.100}$$

For the turbulent viscosity of the mixture $\mu_{T,m}$ the following expression is used:

$$\mu_{T,m} = \rho_m C_\mu \frac{k^2}{\epsilon}, \tag{3.101}$$

and the production of turbulent kinetic energy $G_{k,m}$ can be expressed as:

$$G_{k,m} = \mu_{T,m}(\nabla \hat{\vec{u}}_m + \nabla \hat{\vec{u}}_m^T) : \nabla \hat{\vec{u}}_m \tag{3.102}$$

The constant used with this model are the same for the single phase $k - \epsilon$ model, reported in Table 3.1.

3.2.6 Summary of the multifluid model equations

The final set of the equations is the following, neglecting all the interfacial forces except drag force:

- Mass conservation

$$\frac{\partial}{\partial t}(\alpha_k \bar{\rho}_k) + \nabla \cdot \left(\alpha_k \bar{\rho}_k \hat{\vec{u}}_k \right) = \Gamma_k \tag{3.103}$$

$$\sum_{k=1}^{N} \alpha_k = 1 \qquad k = 1, ..., N \tag{3.104}$$

$$\sum_{k=1}^{N} \Gamma_k = 0 \tag{3.105}$$

- Momentum conservation (Navier-Stokes equation) for the continuous phase ($k = 1$)

$$\begin{aligned} &\frac{\partial}{\partial t}\left(\alpha_1 \bar{\rho}_1 \hat{\vec{u}}_1 \right) + \nabla \cdot \left(\alpha_1 \bar{\rho}_1 \hat{\vec{u}}_1 \hat{\vec{u}}_1 \right) = -\alpha_1 \nabla p + \alpha_1 \bar{\rho}_1 \vec{g} + \Gamma_1 \hat{\vec{u}}_1 + \\ &+\nabla \left(\alpha_1 (\mu_1 + \mu_{T,1}) \left(\nabla \hat{\vec{u}}_1 + \left(\nabla \hat{\vec{u}}_1 \right)^T \right) \right) - \nabla \cdot \left(\alpha_1 \mu_1 \left(\frac{1}{3} \nabla \hat{\vec{u}}_1 \bar{\bar{I}} \right) \right) \\ &- \sum_{k=2}^{N} \frac{3}{4} \bar{\rho}_1 \alpha_k \frac{C_{D,k}}{\bar{d}_{b,k}} \left| \hat{\vec{u}}_k - \hat{\vec{u}}_1 \right| \left(\hat{\vec{u}}_k - \hat{\vec{u}}_1 \right) \end{aligned} \tag{3.106}$$

- Momentum conservation for the $N-1$ disperse phases ($k = 2, \dots, N$)

$$\frac{\partial}{\partial t}\left(\alpha_k \bar{\rho}_k \hat{\bar{u}}_k\right) + \nabla \cdot \left(\alpha_k \bar{\rho}_k \hat{\bar{u}}_k \hat{\bar{u}}_k\right) = -\alpha_k \nabla p + \alpha_k \bar{\rho}_k \vec{g} + \Gamma_1 \hat{\bar{u}}_1 + \\ - \frac{3}{4} \bar{\rho}_1 \alpha_k \frac{C_{D,k}}{\bar{d}_{b,k}} \left|\hat{\bar{u}}_k - \hat{\bar{u}}_1\right| \left(\hat{\bar{u}}_k - \hat{\bar{u}}_1\right) \tag{3.107}$$

- Conservation of the $\hat{Y}_k$ chemical species in the $k-$th phase ($k = 1, \dots, N$)

$$\frac{\partial}{\partial t}(\alpha_k \bar{\rho}_k \hat{Y}_k) + \nabla \cdot (\alpha_k \bar{\vec{u}}_k \hat{Y}_k) = -\nabla \cdot \alpha_k (\hat{\bar{F}}_{Y,k} + \hat{\bar{F}}^T_{Y,k}) + \hat{Y}_{kj} \cdot \Gamma_k + \alpha_k \bar{\rho}_k \hat{\Psi}_k \tag{3.108}$$

3.3 Coupling with Population Balance Equation

In the previous sections, the constitutive equations of the multifluid model were derived for a very general case, in which the multiphase system is composed by one continuous phase and $N-1$ disperse phases. With this approach, it is possible to calculate the velocity $\hat{\bar{u}}_k$ of the $k-$th disperse phase with volume fraction α_k and characteristic diameter $\bar{d}_{b,k}$. Now that the methodologies for solving the Population Balance Equation (PBE) and for calculating the flow-field of a gas-liquid are introduced, the so-called PBM-CFD coupling procedure will be presented.

As already reported in Section 2.3, by using a QBMM the entire population of the dispersed bubbles can be subdivided into N different groups, each one of them corresponding to a node of the quadrature approximation reported in Eq. (2.81), in turn composed by bubbles with the same size and composition. In light of that, two different approaches are possible:

- Assign a volume fraction α_k and a velocity $\hat{\bar{u}}_k$ of the multifluid for each one of the N quadrature nodes of the QBMM (Fan et al., 2004).
- Consider only one volume fraction and one velocity for all the bubbles of the disperse phase (Petitti et al., 2010).

It is clear that the first method has a higher computational cost compared to second one due to the larger number of equations to solve, however represents a good choice when bubble sizes distribution is wide, in order to catch segregation phenomena (more evident in other kind of multiphase flows, such as granular systems). The second approach is a time saving procedure, which has its validity if the population of bubbles has more or less the same terminal velocity (Montante et al., 2007; Petitti et al., 2010; Buffo et al., 2012), a typical situation for bubble size ranging between 2 to 10 mm, as it is possible to observe in Fig. 3.3. As with QBMM the moments of the population or the quadrature approximation itself can be transported, these two approaches will be further explained in the following sections.

3.3.1 Transport of moments - QMOM/CQMOM/DQMOM-FC

As already remarked in this dissertation, with QMOM and CQMOM the evolution of the moments of the bubble distribution can be tracked in space and time. This means that the equations for a moment set are coupled to multifluid equations and solved by the methods. Otherwise with DQMOM-FC the advective term is rewritten in terms of the velocity of the moments. Therefore it is important to define the velocity of the moments, coupled with the calculated values of the multifluid model. The velocity of a generic order bivariate moment, appearing in the moment transport equation (Eq. (2.73)), is defined in the following way (Eq. (2.74)):

$$\check{\mathbf{U}}_{k,l} = \frac{\iint_0^\infty \check{\mathbf{U}}_\mathrm{b}(L,\phi_\mathrm{b})\, n(L,\phi_\mathrm{b})\, L^k \phi_\mathrm{b}^l \,\mathrm{d}L\,\mathrm{d}\phi_\mathrm{b}}{\iint_0^\infty n(L,\phi_\mathrm{b})\, L^k \phi_\mathrm{b}^l \,\mathrm{d}L\,\mathrm{d}\phi_\mathrm{b}} \tag{3.109}$$

where $\check{\mathbf{U}}_\mathrm{b}(L,\phi_\mathrm{b})$ representing the average bubble velocity conditioned over the values of bubble size and composition and is calculated by means of the multifluid model.

If all the bubbles share the same flow field $\check{\mathbf{U}}_\mathrm{b}$, it is possible to take it out to sign of integral and write the following statement:

$$\check{\mathbf{U}}_{k,l} = \check{\mathbf{U}}_\mathrm{b}, \tag{3.110}$$

namely, all the moments of the tracked set moves in the physical domain with the same velocity $\check{\mathbf{U}}_\mathrm{b}$, calculated considering only two phases, one continuous and one dispersed. It is important to notice that $\check{\mathbf{U}}_\mathrm{b}$ is not a function of size L and composition ϕ, but it is necessary to indicate a characteristic diameter for solving the Navier-Stokes equations, appearing in the formulation of the interfacial forces term (Eq. (3.51)). A common approach is represented by the following choice (Petitti et al., 2010):

$$d_b = d_{32} = \frac{M_{3,0}}{M_{2,0}}, \tag{3.111}$$

namely the Sauter diameter is locally calculated through moments and used for the velocity of the gas phase.

When N different disperse phases are considered, each one for N quadrature node approximation, it is possible to rewrite Eq. (3.109) as:

$$\check{\mathbf{U}}_{k,l} = \frac{\sum_{i=1}^{N} \check{\mathbf{U}}_{\mathrm{b},i}\, w_i\, L_i^k \phi_{\mathrm{b}_i}^l}{\sum_{i=1}^{N} w_i\, L_i^k \phi_{\mathrm{b}_i}^l} \tag{3.112}$$

where $\check{\mathbf{U}}_{\mathrm{b},i} = \check{\mathbf{U}}_{\mathrm{b},i}(L_i,\phi_{\mathrm{b},i})$ is calculated by the multifluid approach considering L_i as the

size of the characteristic bubble and the volume fraction of the $i-$th phase as:

$$\alpha_i = w_i k_V L_i^3 \tag{3.113}$$

where k_V is the volumetric shape factor. The derivation of the equations for the monovariate case is straightforward and here are not reported.

3.3.2 Transport of quadrature - DQMOM

When the N quadrature weights and nodes are directly tracked with DQMOM, the more common strategy adopted is to calculate the evolution of N different disperse phase and use the calculated velocity of the $i-$th phase for transporting the quadrature quantities as expressed in Eq. (2.145). In order to reduce the number of equations, Fan et al. (2004) proposed the following approach for the $i-$th quadrature node (or disperse phase):

$$\frac{\partial}{\partial t}\left(\alpha_i \rho_\mathrm{b}\right) + \nabla \cdot \left(\alpha_i \rho_\mathrm{b} \mathbf{U}_{\mathrm{b},i}\right) = \rho_\mathrm{b}\left(3k_V L_i^2 b_i - 2k_V L_i^3 a_i\right), \tag{3.114}$$

$$\frac{\partial}{\partial t}\left(\alpha_i \rho_\mathrm{b} L_i\right) + \nabla \cdot \left(\alpha_i \rho_\mathrm{b} L_i \mathbf{U}_{\mathrm{b},i}\right) = \rho_\mathrm{b}\left(4k_V L_i^3 b_i - 3k_V L_i^4 a_i\right), \tag{3.115}$$

$$\frac{\partial}{\partial t}\left(\alpha_i \rho_\mathrm{b} \phi_{\mathrm{b},i}\right) + \nabla \cdot \left(\alpha_i \rho_\mathrm{b} \phi_{\mathrm{b},i} \mathbf{U}_{\mathrm{b},i}\right) = \rho_\mathrm{b}\left(k_V L_i^3 c_i + \phi_{\mathrm{b},i}\left(3k_V L_i^2 b_i - 3k_V L_i^3 a_i\right)\right), \tag{3.116}$$

where a_i, b_i and c_i are calculated through Eq. (2.140) and the volume fraction α_i is defined as

$$\alpha_i = w_i k_V L_i^3 \tag{3.117}$$

where k_V is the volumetric shape factor. Due to the peculiarities of the method, DQMOM was usually used with more than two disperse phases. However it is possible to write the governing equations for weights and nodes of quadrature considering only one disperse phase, namely combined with a two-phase flow description. The set of equations solved will be the following:

$$\begin{cases} \dfrac{\partial\, w_i}{\partial t} + \nabla \cdot \left(w_i \check{\mathbf{U}}_\mathrm{b}\right) = a_i, \\ \dfrac{\partial\, w_i L_i}{\partial t} + \nabla \cdot \left(w_i L_i \check{\mathbf{U}}_\mathrm{b}\right) = b_i + w_i\, G_i, \\ \dfrac{\partial\, w_i \phi_{\mathrm{b},i}}{\partial t} + \nabla \cdot \left(w_b \phi_{\mathrm{b},i} \check{\mathbf{U}}_\mathrm{b}\right) = c_i + w_i\, \dot{\phi}_{\mathrm{b},i}, \end{cases} \tag{3.118}$$

with velocity field $\check{\mathbf{U}}_\mathrm{b}$ shared by all the quadrature weights and nodes and the total gas volume fraction α defined as:

$$\alpha = \sum_{i=1}^{N} w_i k_V L_i^3. \tag{3.119}$$

Also in this case, the derivation for the monovariate case is trivial.

References

Aris, R., 1962. Vectors, Tensors, and the Basic Equations of Fluid Mechanics. Prentice-Hall, Englewood Cliffs (NJ), USA.

Bakker, A., Van den Akker, H., 1994. Gas-liquid contacting with axial flow impellers. Chemical Engineering Research and Design 72, 573–582.

Lopez de Bertodano, M.A., 1998. Two fluid model for two-phase turbulent jets. Nuclear Engineering and Design 179, 65–74.

Lopez de Bertodano, M.A., Saif, A.A., 1997. Modified k-ϵ model for two-phase turbulent jets. Nuclear Engineering and Design 172, 187–196.

Bird, R.B., Stewart, W.E., Lightfoot, E.N., 2002. Transport Phenomena. John Wiley & Sons, Inc., New York (NJ), USA. Second Edition.

Bove, S., 2005. Computational fluid dynamics of gas-liquid flows including bubble population balances. Ph. D. Thesis. Aalborg University. Esbjerg, Denmark.

Buffo, A., Vanni, M., Marchisio, D., 2012. Multidimensional population balance model for the simulation of turbulent gas–liquid systems in stirred tank reactors. Chemical Engineering Science 70, 31–44.

Chen, C., Fan, L.S., 2004. Discrete simulation of gas-liquid bubble columns and gas-liquid-solid fluidized beds. American Institute of Chemical Engineering Journal 50, 288–301.

Clift, R., Grace, J.R., Weber, M.E., 1978. Bubbles, Drops, and Particles. Academic Press, New York (NJ), USA.

Crowe, C., Stock, D., Sharma, M., 1977. The particle-source-in cell (PSI-CELL) model for gas-droplet flows. ASME Journal of Fluid Engineering 99, 325–332.

Crowe, C.T., 2006. Multiphase Flow Handbook. CRC Taylor and Francis Group, Boca Raton (FL), USA.

Deen, N., Solberg, T., Hjertager, B., 2001. Large eddy simulation of the gas-liquid flow in a square cross-sectioned bubble column. Chemical Engineering Science 56, 6341–6349.

Diaz, M.E., Montes, F.J., Galan, M.A., 2008. Experimental study of the transition between unsteady flow regimes in a partially aerated two-dimensional bubble column. Chemical Engineering and Processing 47, 1867–1876.

Drew, D., Lahey Jr, R., 1987. The virtual mass and lift force on a sphere in rotating and straining inviscid flow. International Journal of Multiphase Flow 13, 113–121.

Drew, D.A., Passman, S.L., 1999. Theory of Multicomponent Fluids. Springer-Verlag, New York (NJ), USA.

Fan, R., Marchisio, D.L., Fox, R.O., 2004. Application of the direct quadrature method of moments to polydisperse gas–solid fluidized beds. Powder Technology 139, 7–20.

Haberman, W.L., Morton, R.K., 1956. An experimental study of bubbles moving in liquids. Transaction of the American Society of Civil Engeneers 121, 227–252.

Hibiki, T., Ishii, M., 2007. Lift force in bubbly flow systems. Chemical Engineering Science 62, 6457–6474.

Hirt, C., Nichols, B., 1981. Volume of fluid (VOF) method for the dynamics of free boundaries. Journal of Computational Physics 39, 201–225.

Hjertager, B.H., 2007. Multi-fluid CFD analysis of chemical reactors, in: Marchisio, D.L., Fox, R.O. (Eds.), Multiphase Reacting Flows: Modelling and Simulation. Springer-Verlag, Vienna, Austria. number 492 in CISM International Centre for Mechanical Sciences, pp. 125–179.

Ishii, M., Mishima, K., 1984. Two-fluid model and hydrodynamic constitutive relations. Nuclear Engineering and Design 82, 107–126.

Ishii, M., Zuber, N., 1979. Drag coefficient and relative velocity in bubbly, droplet or particulate flows. American Institute of Chemical Engineering Journal 25, 843–855.

Kataoka, I., Serizawa, A., 1989. Basic equations of turbulence in gas-liquid two-phase flow. International Journal of Multiphase Flow 15, 843–855.

Li, Y., Zhang, J., Fan, L.S., 1999. Numerical simulation of gas–liquid–solid fluidization systems using a combined CFD-VOF-DPM method: bubble wake behavior. Chemical Engineering Science 54, 5101–5107.

Migdal, D., Agosta, V.D., 1967. A source flow model for continuum gas-particle flow. Journal of Applied Mechanics 34, 860–865.

Montante, G., Paglianti, A., Magelli, F., 2007. Experimental analysis and computational modelling of gas - liquid stirred vessels. Chemical Engineering Research and Design 85, 647–653.

Osher, S., Sethian, J.A., 1988. Fronts propagating with curvature-dependent speed: algorithms based on hamilton-jacobi formulations. Journal of Computational Physics 79, 12–49.

Peebles, F.N., Garber, H.J., 1953. Studies on the motion of gas bubbles in liquid. Chemical Engineering Progress 42, 88–97.

Peskin, C.S., 1977. Numerical analysis of blood flow in the heart. Journal of Computational Physics 25, 220–252.

Petitti, M., Nasuti, A., Marchisio, D.L., Vanni, M., Baldi, G., Mancini, N., Podenzani, F., 2010. Bubble size distribution modeling in stirred gas–liquid reactors with QMOM augmented by a new correction algorithm. American Institute of Chemical Engineering Journal 56, 36–53.

Podowski, M., 2009. On the consistency of mechanistic multidimensional modeling of gas/liquid two-phase flows. Nuclear Engineering and Design 239, 933–940.

Sato, Y., Sekoguchi, K., 1975. Liquid velocity distribution in two-phase bubble flow. International Journal of Multiphase Flow 2, 79–95.

Schiller, L., Naumann, A., 1933. Uber die grundlegende berechnung bei der schwekraftaufbereitung. Zeitung des Vereins Deutscher Ingenieure 44, 318–320.

van Sint Annaland, M., Deen, N., Kuipers, J., 2005. Numerical simulation of gas–liquid–solid flows using a combined front tracking and discrete particle method. Chemical Engineering Science 60, 6188–6198.

Tomiyama, A., Kataoka, I., Zun, I., Sakaguchi, T., 1998. Drag coefficients of single bubbles under normal and micro gravity conditions. JSME international journal. Ser. B, Fluids and thermal engineering 41, 472–479.

Tomiyama, A., Tamai, H., Zun, I., Hosokawa, S., 2002. Transverse migration of single bubbles in simple shear flows. Chemical Engineering Science 57, 1849–1858.

Unverdi, S.O., Tryggvason, G., 1992. A front-tracking method for viscous, incompressible, multi-fluid flows. Journal of Computational Physics 100, 25–37.

van Wachem, B., Almstedt, A., 2003. Methods for multiphase computational fluid dynamics. Chemical Engineering Journal 96, 81–98.

Wijngaarden, L.V., Jeffrey, D.J., 1976. Hydrodynamic interaction between gas bubbles in liquid. Journal of Fluid Mechanics 77, 27–44.

Yeoh, G.H., Tu, J., 2010. Computational Techniques for Multiphase Flows. Butterworth-Heinemann, Oxford, UK.

Zhang, D., Deen, N., Kuipers, J., 2006. Numerical simulation of the dynamic flow behavior in a bubble column: A study of closures for turbulence and interface forces. Chemical Engineering Science 61, 7593–7608.

Zun, I., 1980. Transverse migration of bubbles influenced by walls in vertical bubbly flow. International Journal of Multiphase Flow 6, 583–588.

Chapter 4

Results on simplified systems

In Chapter 2, multivariate Quadrature-Based Moment Methods (QBMM) in the context of gas-liquid systems were presented and discussed in detail from the theoretical point of view. It was shown that they are part of a particular family called Methods of Moments (MOM), and that they are based on the use of a quadrature approximation for overcoming the inevitable closure problem (Hulburt and Katz, 1964; McGraw, 1997). As explained in Section 2.3, with QBMM only the evolution of integral properties of the distribution (i.e., moments) can be tracked in space and time, integrating out the information relating to the actual shape of the number density function (NDF) and by assuming the functional form of NDF as a summation of delta functions centered on nodes of quadrature approximation (McGraw, 1997; Marchisio and Fox, 2005). This approximation allows to solve the population balance equation, both for monovariate and multivariate cases, reducing the computational costs compared to other solution methods; for this reason QBMM are particularly suitable to be coupled with CFD codes (Fan et al., 2004; Zucca et al., 2006; Petitti et al., 2010). However, although the quadrature approximation is in general very accurate, a comparison with alternative "exact" methods is always needed in order to assess the accuracy of QBMM by varying the total number of quadrature nodes N when different processes are considered (Zucca et al., 2007; Buffo et al., 2012). For this reason, in the first section of this chapter the results of the comparison between different QBMM and the Direct Simulation Monte Carlo (DSMC) for a very simple zero-dimensional system will be shown and discussed.

Since the final aim of the work is to develop a reliable and accurate methodology for performing mass transfer predictions in different gas-liquid equipments, it is crucial to verify QBMM also in the case of inhomogeneous systems, in which also advection in physical space has an influence on the evolution in space and time of the NDF. As reported in Chapter 1, several issues may jeopardize the results of QBMM simulations: for example the "moment corruption" problem, namely the generation of invalid moment sets, may arise with QMOM/CQMOM when standard high-order spatial discretization schemes are used for transporting the moments of the NDF (Wright Jr, 2007; Petitti et al., 2010). Another well-known issue is related to the fact that when the transport equations for moments are purely hyperbolic (i.e. pure advection of the NDF) and when there are spatial discontinuities in the

NDF, the spatial continuity assumption used to derive DQMOM is not valid anymore (Buffo et al., 2013; Marchisio and Fox, 2013). Even if the spatial solution is smooth, moments of the NDF may not properly be conserved whenever the moment transport equation contains spatial diffusion terms that are smaller than or comparable with numerical diffusion, that every Finite-Volume scheme (FV) introduces (Mazzei et al., 2010, 2012). For these reasons, in the second section of this chapter the results of the implementation different QBMM for a mono-dimensional system will be presented, with particular attention to the described problems and to the grid-independence conditions, that always must be verified for the solution of similar cases. The results presented in this work are based on recently published works (Buffo et al., 2012, 2013).

4.1 Zero-dimensional system

4.1.1 Test case description

As previously mentioned, it is very important to verify and validate QBMM through comparison with alternative methods as a reference for the solution quality. For this purpose, Direct Simulation Monte Carlo (DSMC) technique (described in Section 2.3.1) was chosen among other methods as alternative to QBMM due to its implementation simplicity and because it can be easily extended to simulate multivariate problems as in this case. It is important to stress here that the important parameter of DSMC simulation, the total number of notional bubbles undergoing randomly selected events, must be high enough to ensure statistical reliability of the results but also must be affordable from the computational point of view, especially for memory requirements. A common strategy adopted in other works for obtaining sensible results is to average a certain number of different realizations of the same system (Zucca et al., 2007). In this case, the average of ten different realizations with 10,000 bubbles was considered a good trade off between accuracy and computational costs after a series of preliminary tests.

A summary of all the simulations carried out for this zero-dimensional homogeneous system is reported in Table 4.1; in each case different processes were selected in order to cover a wide spectrum of possibilities and the results obtained with DQMOM and CQMOM were compared to DMSC predictions. As pointed out in Section 2.3, QBMM for homogeneous systems result in a system of Ordinary Differential Equations, solved here with the standard Matlab integrator `ode15s` (a quasi-constant step size implementation of the numerical differentiation formulas, as explained in Shampine and Reichelt, 1997). In all cases the studied system was composed of water and air, as continuous and disperse phases respectively. The physical properties are reported in Table 4.2. The variable H is the dimensionless Henry constant based on concentrations (i.e., $HC_i^G = C_i^L$). It is important to notice that the value used in these simulations is two order magnitude larger than the physical one, with the aim of seeing a significant variation of oxygen concentration in the gas phase during mass transfer; although this value does not represent any real gas-liquid system, this artifact is

Table 4.1: Summary of simulations carried out for the homogeneous case.

Case	Coalescence kernel		Breakage	Mass	Continuous	Chemical
	Size depend.	Comp. depend.	kernel	transfer	gas flow	reaction
1	Laakkonen	No	Laakkonen	No	No	No
2	Laakkonen	Yes	Laakkonen	No	No	No
3	Laakkonen	No	Laakkonen	Yes	No	No
4	Laakkonen	No	Laakkonen	No	$\tau = 1$ s	No
5	Laakkonen	No	Laakkonen	Yes	$\tau = 1$ s	No
6	Laakkonen	No	Laakkonen	Yes	$\tau = 1$ s	Fast

Table 4.2: Physical properties used in numerical simulations.

ρ_c	998.2	kg m^{-3}
ρ_b	1.255	kg m^{-3}
μ_c	$1.0 \cdot 10^{-3}$	Pa s
σ	0.07	N m^{-1}
$\mathscr{D}$	$1.970 \cdot 10^{-9}$	m^2 s^{-1}
H	3.18	[−]

nevertheless useful to test and validation purposes.

In order to assess the accuracy of the quadrature approximation underlying QBMM equations, different simulations with a variable number of nodes of the quadrature (from two to four) were carried out. As remarked in Section 2.3.4, all of the N nodes of DQMOM have different values of both internal coordinates. On the contrary, with CQMOM the value of the first internal coordinate is shared by N_2 nodes for the second internal coordinate. When $N_2 = 1$ and the same set of moments is tracked in spatially homogenous systems, CQMOM and DQMOM are mathematically equivalent and the obtained results are the same. As it was pointed out in the work of Yuan and Fox (2011), CQMOM can be particularly efficient when the population is distributed with a certain variance over the second internal coordinate, and $N_2 > 1$ helps to capture some specific properties of the studied system. In this work, different simulations were performed with the aim of finding the possible situations in which a quadrature with $N_2 > 1$ is required; size-dependent or size-composition dependent coalescence, breakage, mass transfer, inlet or depletion of bubbles and fast chemical reaction in the liquid bulk were considered.

As shown in Table 4.1, breakage frequency, daughter distribution function, coalescence kernel and efficiency formulations used in this study are based on the works of Laakkonen et al. (2006, 2007), indicated in Eqs. (2.55), (2.64), (2.66) and (2.68) at Pages 27 and 30 to 32 respectively. Although a comparison between different kernels available in the literature will be certainly very interesting, it is out of the aims of this study. In previous works (Petitti et al., 2010, 2012; Buffo et al., 2012), it was shown that the set of kernels used in this work is particularly suitable for describing gas-liquid systems, and for this reason it was here widely investigated. Moreover, it is important to remind that the composition dependence, indicated in Table 4.1 and expressed in Eq. (2.70) at Page 32, is based on the work of Marshall Jr. et al. (2011) on particular solid-fluid systems. Although this might not represent any realistic

Table 4.3: Initial conditions for QBMM simulations: log-normal distribution with respect to bubble size and constant oxygen concentration. Units: generic moment $M_{k,l}$ in $\mathrm{m}^{k-3}\ \mathrm{mol}^{l}$, weights w_i in m^{-3}, size L_i in m, moles $\phi_{\mathrm{b},i}$ in mol

CQMOM				
$M_{0,0}$ $1.8286 \cdot 10^{7}$	$M_{1,0}$ $6.7086 \cdot 10^{4}$	$M_{2,0}$ $2.5173 \cdot 10^{2}$	$M_{3,0}$ $9.6615 \cdot 10^{-1}$	$M_{4,0}$ $3.7925 \cdot 10^{-3}$
$M_{5,0}$ $1.5226 \cdot 10^{-5}$	$M_{6,0}$ $6.2521 \cdot 10^{-8}$	$M_{7,0}$ $2.6256 \cdot 10^{-10}$	$M_{0,1}$ 4.3303	$M_{1,1}$ $1.6998 \cdot 10^{-2}$
$M_{2,1}$ $6.8243 \cdot 10^{-5}$	$M_{3,1}$ $2.8022 \cdot 10^{-7}$	$M_{0,2}$ $1.2559 \cdot 10^{-6}$	$M_{1,2}$ $5.2744 \cdot 10^{-9}$	$M_{2,2}$ $2.2655 \cdot 10^{-11}$
$M_{3,2}$ $9.9517 \cdot 10^{-14}$	$M_{0,3}$ $4.4604 \cdot 10^{-13}$	$M_{1,3}$ $2.0037 \cdot 10^{-15}$	$M_{2,3}$ $9.2036 \cdot 10^{-18}$	$M_{3,3}$ $4.3206 \cdot 10^{-20}$
DQMOM				
$N = 2$		w_1 $1.1157 \cdot 10^{7}$	L_1 $3.2258 \cdot 10^{-3}$	$\phi_{\mathrm{b},1}$ $1.4912 \cdot 10^{-7}$
		w_2 $7.1291 \cdot 10^{6}$	L_2 $4.3619 \cdot 10^{-3}$	$\phi_{\mathrm{b},2}$ $3.7403 \cdot 10^{-7}$
$N = 3$		w_1 $5.3797 \cdot 10^{6}$	L_1 $2.9524 \cdot 10^{-3}$	$\phi_{\mathrm{b},1}$ $1.1535 \cdot 10^{-7}$
		w_2 $1.1446 \cdot 10^{7}$	L_2 $3.8375 \cdot 10^{-3}$	$\phi_{\mathrm{b},2}$ $2.5329 \cdot 10^{-7}$
		w_3 $1.4601 \cdot 10^{6}$	L_3 $4.9846 \cdot 10^{-3}$	$\phi_{\mathrm{b},3}$ $5.5511 \cdot 10^{-7}$
$N = 4$		w_1 $2.3732 \cdot 10^{6}$	L_1 $2.7504 \cdot 10^{-3}$	$\phi_{\mathrm{b},1}$ $9.3254 \cdot 10^{-8}$
		w_2 $1.0745 \cdot 10^{7}$	L_2 $3.5030 \cdot 10^{-3}$	$\phi_{\mathrm{b},2}$ $1.9266 \cdot 10^{-7}$
		w_3 $4.9635 \cdot 10^{6}$	L_3 $4.3875 \cdot 10^{-3}$	$\phi_{\mathrm{b},3}$ $3.7856 \cdot 10^{-7}$
		w_4 $2.0419 \cdot 10^{5}$	L_4 $5.5902 \cdot 10^{-3}$	$\phi_{\mathrm{b},4}$ $7.8296 \cdot 10^{-7}$

gas-liquid system, the assessment of the accuracy of QBMM with similar kernels is still interesting in other application areas (Buffo et al., 2013). The mass transfer coefficient, k_L, was calculated by means of the Lamont and Scott correlation as reported in Eq. (2.48) at Page 25, while the effect of a fast chemical reaction was obtained by setting the concentration of oxygen in liquid phase equal to zero at each time step without accounting for a mass transfer enhancement. As already mentioned, the value chosen for Henry constant and the selection of composition dependent kernels are justified by the testing purposes. However, the modeling of a chemical reaction in liquid phase coupled with a detailed description of the dispersed phase by means of Population Balance Models will certainly be the subject of future studies.

As far as the different variables involved are concerned, a crucial role is played by the turbulent dissipation rate, ϵ, or more specifically for zero-dimensional systems its volume-averaged value, that determines the prevalence of bubble coalescence on breakage. In fact, such value is present in both kernels (Eqs. (2.55), (2.66) and (2.68)) and in the mass transfer coefficient correlation (Eq. (2.48)): for this reason two different values of ϵ was preliminarily investigated in order to find the more critical situation for the quadrature accuracy. Here only the results obtained using ϵ equal to $4.82 \cdot 10^{-2}\ \mathrm{m^2/s^3}$ will be shown, in which bubble coalescence is stronger than breakage. In this case, the error of the quadrature is higher probably due to the fact that coalescence is a second order process compared to breakage, which is a common first order process, representing therefore a more challenging problem.

Another important aspect of a zero-dimensional simulation is represented by the initial conditions chosen for the bubble population: in this work all the predictions were obtained by prescribing the presence of bubbles inside the control volume. Although the total number of notional bubbles already present inside the system at the beginning of the DSMC simulations was set equal to 10,000 and kept in a certain range by the DSMC algorithm, the value of the subvolume of the domain in which all the bubbles are contained was calculated in such a way that the global gas volume fraction of the system was equal to 0.5. This gas hold-up is important to characterize the physics of the system: in fact, the greater the number of bubbles inside a volume, the more these will tend to coalesce. It is indeed true that a similar global hold-up value is difficult to find in real gas-liquid system, but it is quite common as a local value in CFD simulations. For example, higher gas volume fractions are usually imposed as inlet boundary condition, according to the procedure described by Ranade (2002). Smaller volume fraction values were preliminarily tested, but the most significant results in terms of assessment of quadrature error were obtained with the initial global gas hold-up equal to 0.5. The shape of the initial bubble distribution was assumed to be a log-normal distribution with respect to the size with a mean of 3.7 mm and a standard deviation of 15% of the mean value, but with the same oxygen concentration of $8.56\ \mathrm{mol/m^3}$ in all bubbles (corresponding to the concentration of oxygen in air at 25 °C and 1 atm). The described initial condition had to be prescribed in the form of initial moments for CQMOM and of initial weights and nodes for DQMOM: in order to compare the results given by different methods, these values were obtained by the initialization of the DSMC. The numerical values are reported in Table 4.3.

4.1.2 Results and discussion

Since it would be too confusing to extensively represent all cases considered, only the salient results will be shown and discussed. In Fig. 4.1 the time evolution of some lower-order moments of the NDF is reported for Case 1, in which only bubble coalescence and breakage were described. It should be noticed that in Fig. 4.1 the time evolution of only some tracked moments is plotted. As already remarked, the tracked moment set changes according to the chosen total number of quadrature nodes ($N = 2, 3, \dots$). Since the subset: $M_{0,0}$, $M_{1,0}$, $M_{2,0}$, $M_{3,0}$, $M_{0,1}$ and $M_{1,1}$ are the six moments transported in all the cases (see Fig. 2.1), only their evolution will be commented in this section. Furthermore, it is very important to remind here that the represented moments have a clear physical meaning: $M_{0,0}$ is the total number of bubbles per unit volume, $M_{1,0}$ is the total bubble size per unit volume, $M_{2,0}$ is proportional to the total area of bubbles per unit volume, $M_{3,0}$ is proportional the total gas fraction and $M_{0,1}$ is the total number of oxygen moles in the gas phase per unit volume. The first three moments decrease as a result of a prevailing coalescence, whereas $M_{3,0}$ and $M_{0,1}$ remain constant, because coalescence and breakage do not have an influence on the global gas hold-up and on the total moles of oxygen in the gas phase. The physical meaning of mixed-order moments is not straightforward and their evolution with respect to time is usually difficult to predict intuitively; however, as it will become clearer later, some of them are important to conserve crucial properties of the bubble population.

In Fig. 4.2 the evolution of moments is shown in the case with coalescence, breakage and mass transfer. In this case $M_{3,0}$ and $M_{0,1}$ decrease with time as a consequence of mass transfer. In fact, the gas volume fraction and the oxygen moles are reduced by the mass exchanged with the liquid. The comparison between MC and QBMM simulations results in good agreement: the evolution in time is correctly reproduced, with a slight error due to the quadrature approximation. Moreover, the moment evolutions are identical with CQMOM and DQMOM, as evident in Fig. 4.1 and Fig. 4.2. In fact for this simple spatially homogeneous system the two methods are mathematically equivalent when the moment set is identical.

Mean percentage integral errors calculated during all the time evolution of some moments are reported in Table 4.4 with an increasing number of quadrature nodes: for all the cases examined the error between the "exact" Monte Carlo solution and the QBMM solution for the moments with order smaller than four with respect to bubble size and for $M_{0,1}$ and $M_{1,1}$, which are the moments included in all the tracked moment set, is below 10%, even when the total number of nodes is equal to two, a remarkable result considering the computational savings achieved. If we look at the higher-order moments, especially the pure moments with respect to bubble size which are not included in the moment set tracked by the QBMM, the relative error increases, reaching values up to 50.1% in some cases. But when the total number of quadrature nodes increases, the quadrature accuracy improves also for higher order moments, with an error below 15% in every case considered.

Particular attention should be paid to Fig. 4.3, where the comparison obtained with a two and three-node quadrature is shown for Case 1, in terms of mean gas oxygen concentration

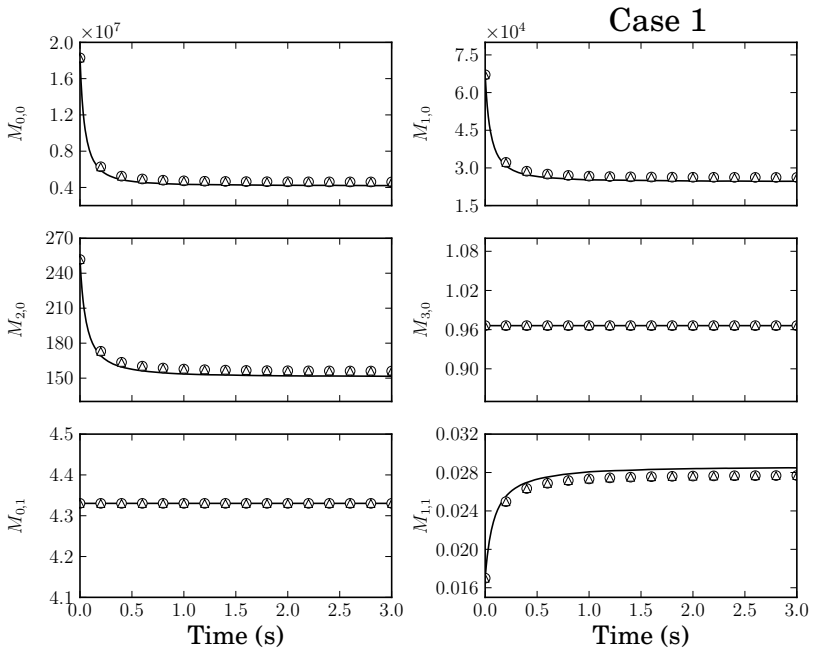

Figure 4.1: Time evolution of some lower order moments of the NDF for a homogeneous system, in case of coalescence (size-dependent kernel) and breakage. Black line: MC method. Circles: CQMOM with $N_1 = 3$ and $N_2 = 1$. Triangles: DQMOM with $N = 3$. Units of a generic moment $M_{k,l}$: $\mathrm{m}^{k-3}\ \mathrm{mol}^{l}$. Time in seconds.

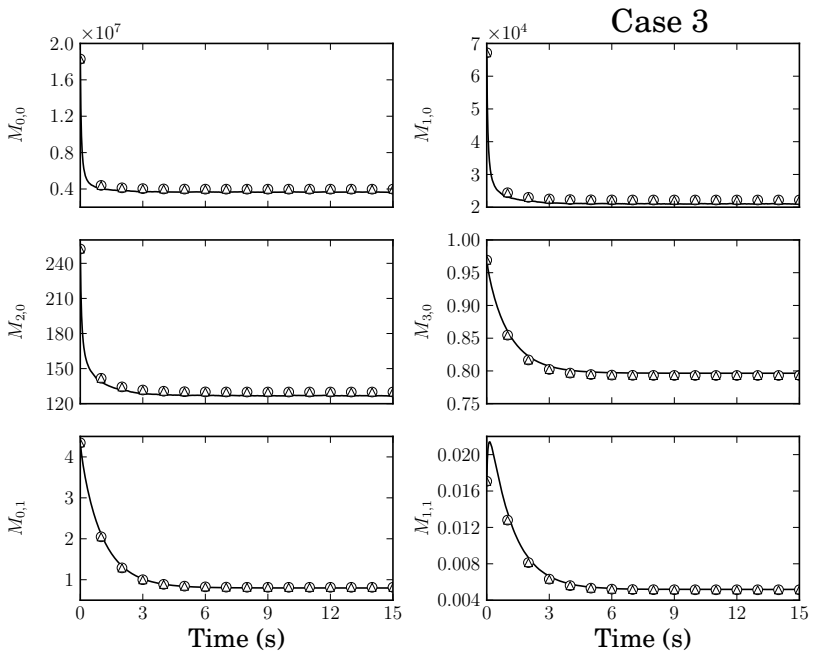

Figure 4.2: Time evolution of some lower order moments of the NDF for a homogeneous system, in case of coalescence (size-dependent kernel), breakage and mass transfer. Black line: MC method. Circles: CQMOM with $N_1 = 3$ and $N_2 = 1$. Triangles: DQMOM with $N = 3$. Units of a generic moment $M_{k,l}$: $\mathrm{m}^{k-3}\ \mathrm{mol}^{l}$. Time in seconds.

Table 4.4: Mean percentage error of QBMM for the examined cases.

	$\boldsymbol{M}_{0,0}$	$\boldsymbol{M}_{1,0}$	$\boldsymbol{M}_{2,0}$	$\boldsymbol{M}_{3,0}$	$\boldsymbol{M}_{4,0}$	$\boldsymbol{M}_{5,0}$	$\boldsymbol{M}_{6,0}$	$\boldsymbol{M}_{7,0}$	$\boldsymbol{M}_{0,1}$	$\boldsymbol{M}_{1,1}$	$\boldsymbol{M}_{2,1}$	$\boldsymbol{M}_{3,1}$
Case 1												
N=2	9.2	7.3	4.3	0.	6.2	14.8	26.2	41.1	0.	6.0	14.4	25.7
N=3	7.9	5.3	2.6	0.	2.6	5.4	8.3	11.8	0.	2.6	5.4	8.3
N=4	7.6	5.2	2.6	0.	2.8	5.6	8.6	11.6	0.	2.8	5.6	8.6
Case 2												
N=2	10.5	8.1	4.7	0.	3.7	4.5	5.6	8.5	0.	6.4	8.3	6.6
N=3	7.6	5.1	2.5	0.	2.5	5.1	7.8	10.1	0.	2.5	5.1	7.8
N=4	7.4	5.0	2.6	0.	2.7	5.5	8.3	11.2	0.	2.7	5.5	8.3
Case 3												
N=2	10.1	7.9	4.6	0.5	6.5	22.3	38.3	50.1	2.1	6.5	21.4	44.6
N=3	7.9	5.2	2.3	0.5	3.3	6.2	8.2	6.9	1.9	1.8	4.7	6.2
N=4	7.7	5.1	2.4	0.4	3.3	6.4	9.5	12.7	3.2	1.7	3.4	6.4
Case 4												
N=2	5.5	5.2	3.6	0.4	3.9	5.8	5.6	4.1	0.4	6.3	9.5	9.4
N=3	6.1	4.7	2.5	0.4	3.1	6.5	10.1	13.5	0.4	3.1	6.5	10.1
N=4	5.6	4.2	2.3	0.4	3.0	6.1	9.6	13.2	0.4	3.0	6.1	9.6
Case 5												
N=2	5.6	5.3	3.6	0.7	4.1	6.0	5.7	4.1	1.1	6.5	9.7	9.7
N=3	5.9	4.3	2.1	0.8	3.8	7.2	10.9	14.5	2.7	6.0	9.6	13.5
N=4	5.3	3.8	1.7	0.9	3.8	7.1	10.7	14.5	3.4	6.6	10.1	13.9
Case 6												
N=2	5.6	5.3	3.4	0.7	4.4	6.1	5.2	2.7	2.2	7.1	10.0	9.1
N_1=2 N_2=2	5.6	5.3	3.5	0.6	4.3	6.1	5.2	2.8	2.0	6.9	10.2	9.8
N=3	5.7	4.2	2.1	0.7	3.4	6.8	10.3	13.6	2.3	5.4	8.9	12.6
N_1=3 N_2=2	5.7	4.3	2.2	0.6	3.4	6.7	10.3	13.6	2.1	5.2	8.7	12.6
N=4	5.3	3.9	2.0	0.7	3.4	6.6	10.1	13.7	2.2	5.0	8.3	11.8
N_1=4 N_2=2	5.3	4.0	2.1	0.6	3.3	6.6	10.1	13.8	2.0	4.9	8.2	11.8

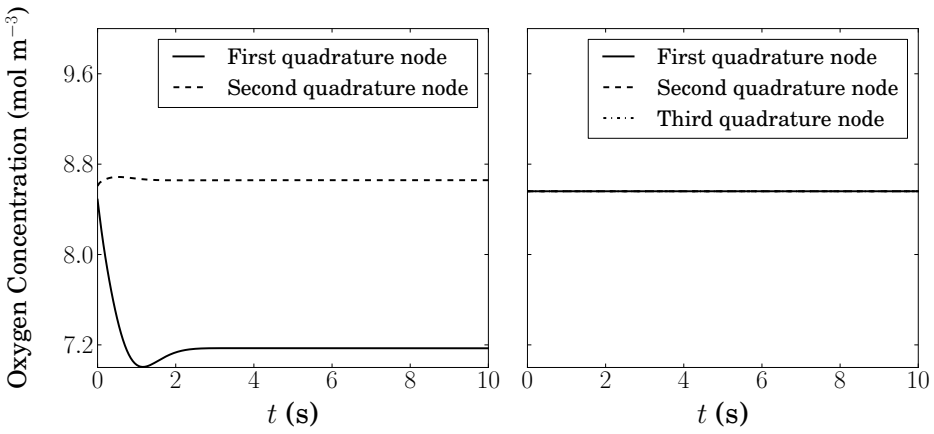

Figure 4.3: Time evolution of oxygen concentration for each quadrature node representing the population of bubbles for the Case 1. Left: two-node quadrature ($N = 2$). Right: three-node quadrature ($N = 3$).

and oxygen concentration calculated for each i-th quadrature node, defined respectively as:

$$C_{gas} = \frac{M_{0,1}}{k_V M_{3,0}}, \tag{4.1}$$

$$C_i = \frac{\phi_{\mathrm{b},i}}{k_V L_i^3}. \tag{4.2}$$

As already explained with Fig. 4.1, since bubbles in this simple case coalesce and break-up in the absence of mass transfer, the global oxygen concentration in the gas phase has to remain constant. Since $M_{0,1}$ and $M_{3,0}$ are included in the tracked moment set and are properly conserved even when $N = 2$, the average concentration in gas phase remains constant in both cases shown in Fig. 4.3. This means that the moment set evolution is correct and that moments are realizable. However, also the concentration for each quadrature node should stay constant and equal to the initial value, but for the case of two nodes this condition is not respected, showing a non-physical behavior, as if the concentration may vary over time even without mass transfer. The fact that the quadrature approximation, still representing a realizable moment set, explores forbidden and unphysical regions of phase space, means that this is an unrelizable reconstruction of the NDF, as is therefore labelled as unrelizable quadrature. This wrong behavior is probably due to the fact that a particular moment $M_{2,1}$ related to the specific surface area and their oxygen concentration must be included into the transported set. In fact, when this moment is tracked as with $N = 3$, the evolution of the oxygen concentration for each node in time is constant as expected. This example highlights the importance of checking always not only the realizability of the moments but also that of the quadrature.

In Fig. 4.4 the time evolution of some lower-order moments of the NDF calculated with QBMM for Case 4 is reported. The continuous injection/extraction of bubbles, added to

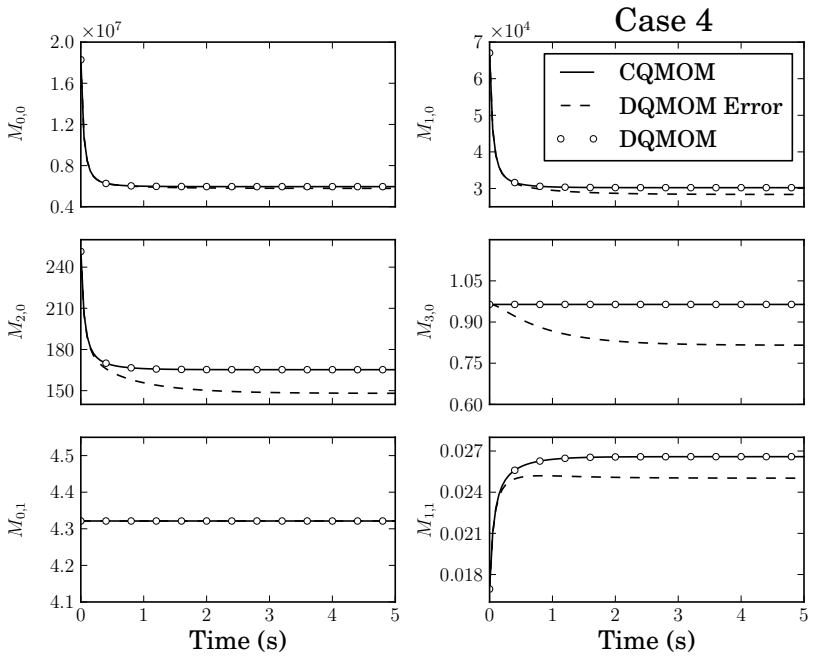

Figure 4.4: Time evolution of some lower order moments of the NDF for a homogeneous system, in case of coalescence (size-dependent kernel), breakage and continuous injection/extraction of bubbles. CQMOM with $N_1 = 3$ and $N_2 = 1$. DQMOM with $N = 3$. Units of a generic moment $M_{k,l}$: $\mathrm{m}^{k-3}\ \mathrm{mol}^{l}$. Time in seconds.

coalescence and breakage, does not modify the volume fraction and the total number of oxygen moles, because the initial condition corresponds in this case to the steady state hold-up and oxygen moles. In fact, $M_{3,0}$ and $M_{0,1}$ remain constant in time with CQMOM and with DQMOM. On the contrary if we try to solve Eq. (2.142) reported at Page 54, shown in the figure with the label "DQMOM Error", we obtain the non-physical behavior shown in Fig. 4.4 highlighting the importance of a correct implementation of DQMOM.

It is interesting to discuss more in detail the evolution of the variance in the second internal coordinate (i.e., bubble composition), since this is strictly related to the number of nodes to be used in that direction (i.e., N_2 of CQMOM) kept equal to one in the previous simulations. As already pointed out before, under this constraint and for this simple zero dimensional system CQMOM and DQMOM are mathematically equivalent. For this reason, different initial conditions/boundary conditions were also tested and investigated (both with MC and CQMOM) in order to understand under what conditions variance is generated and sustained for the problem under investigation, resulting therefore in NDF that might require quadratures with more than one node in the second internal coordinate. One of them is shown in Fig. 4.5, where the size/composition NDF of the bubbles is represented at different times for a particular population: a bivariate normal distribution with a mean of 3.7 mm and $2.27 \cdot 10^{-7}$ mol of oxygen and with a standard deviation of 15% of the mean size and composition in both directions. This specific initial condition was studied as a simple starting

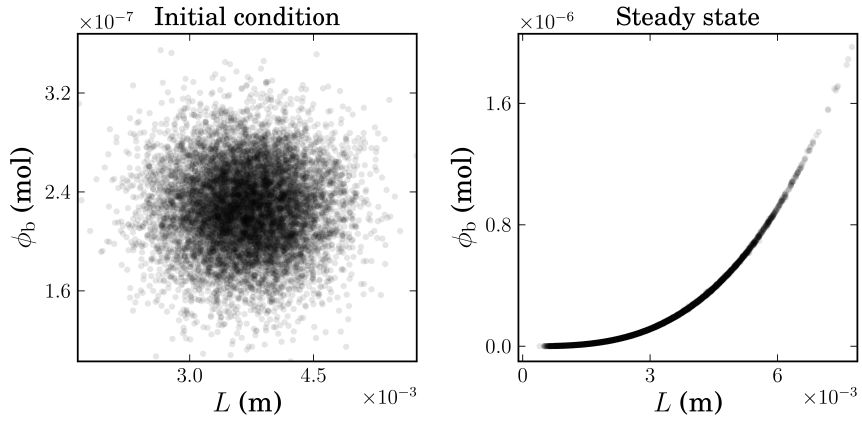

Figure 4.5: Representation of the NDF on the plane bubble size/bubble composition obtained by MC simulation considering coalescence and breakage (both depending only on bubble size). On the left the initial distribution at $t = 0$ s, on the right the distribution after 15 s, when the steady state is reached.

point in which there exists variance in the second coordinate direction, although it may not reflect any realistic system. As clearly shown in Fig. 4.5, after a short transient the population of bubbles moves toward a steady state in which a functional relationship between bubble size and bubble composition is established, namely

$$\phi_b = C_f k_V L^3, \tag{4.3}$$

where C_f is the final equilibrium oxygen concentration equal within all bubbles. As the transient is quite fast and the variance in the direction of the second internal coordinate is negligible, there is no need for this particular case to have $N_2 > 1$ when using CQMOM. Even in the case of continuous injection and extraction of bubbles with mass transfer (Case 5), no significant variance is detected at the steady state, as shown in Fig. 4.6. In fact, the rate of inter-bubble mixing, caused by coalescence and breakage is much higher than the rate of mass transfer (even though here the Henry constant is fixed to a much higher value than physical reality) and consequently the concentration of oxygen in the bubbles becomes quickly uniform.

However, the multivariate description is still needed. As it is possible to see in Fig. 4.7, where the time evolution of the oxygen concentration for each bubble node (of DQMOM and CQMOM) for the Case 5 is shown. In fact, small bubbles tend to exchange mass faster than the bigger ones and, more importantly, with different dynamics. It is important to highlight here that only if the lines overlapped, namely all the bubbles moved towards the equilibrium with the same oxygen concentration, it would not be necessary the use of multivariate population balances.

The last zero dimensional spatially homogeneous case investigated, was that of mass

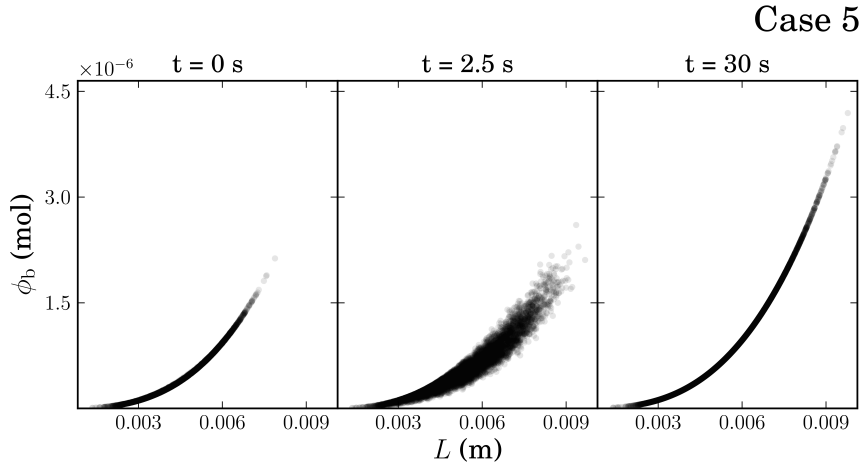

Figure 4.6: Representation of the NDF on the plane bubble size/bubble composition obtained by MC simulation considering coalescence (depending only on bubble size), breakage, continuous injection and extraction of bubbles and mass transfer. On the left the initial condition for the distribution, on the center the distribution after 2.5s and on the right the distribution after 30 s, when the steady state is reached.

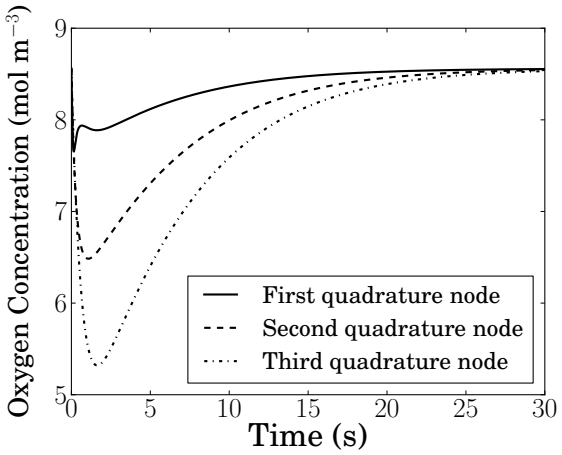

Figure 4.7: Time evolution of oxygen concentration for each quadrature node representing the population of bubbles for the Case 5 with $N = 3$. Solid line: small sized bubbles. Dashed line: medium sized bubbles. Dash-dotted line: large sized bubbles.

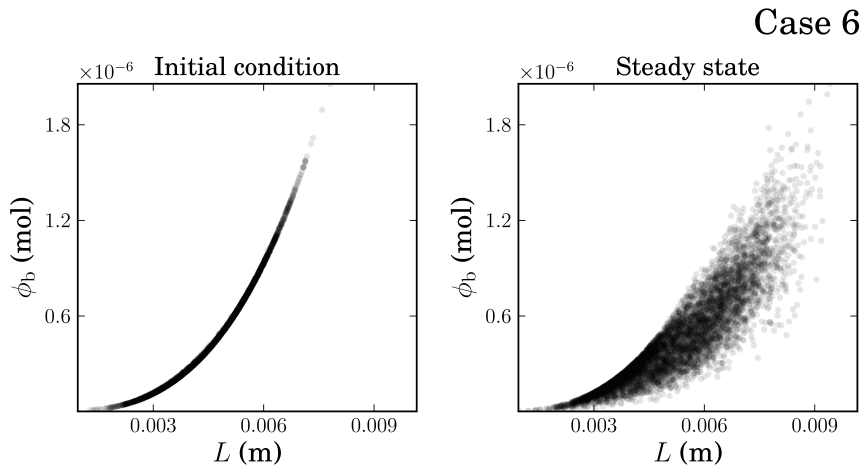

Figure 4.8: Representation of the NDF on the plane bubble size/bubble composition obtained by MC simulation considering coalescence (depending only on bubble size), breakage, continuous injection and extraction of bubbles, mass transfer and fast chemical reaction. On the left the initial distribution at $t = 0$ s, on the right the distribution after 30 s, when the steady state is reached.

transfer combined with a fast chemical reaction, which instantaneously consumes the oxygen molecules in liquid phase. Fig. 4.8 represents the bubble population at different times for Case 6: in this case the chemical reaction in the liquid phase is able to generate variance in the second internal coordinate direction, but it is still insufficient to justify the use of $N_2 > 1$ with CQMOM. In fact, the values of the mean percentage error reported in Table 4.4 using only one node in the direction of the second internal coordinate are comparable to those obtained in other cases, and an increase in N_2 does not show a significant reduction. However, this conclusion is not valid in general and further studies are desirable in order to assess this point.

4.2 Mono-dimensional system

4.2.1 Test case description

The governing equations of CQMOM, DQMOM and DQMOM-FC were numerically solved to simulate coalescence and breakage of a population of bubbles inside a mono-dimensional system in which the gas phase flows and the liquid is stagnant. As previously said, this case is particularly helpful to verify the implementation and highlight possible difficulties that may arise when also the motion of bubbles in physical space is taken into account. This turns out to be very useful in understanding as the "moment corruption" problem, when moments are transported (CQMOM) and the non-conservation of the moment set, when primitive variables are transported (DQMOM). In this very simple test case, the bubble velocity $\check{\mathbf{U}}_b$ (appearing in the moment velocity term $\check{\mathbf{U}}_{k,l}$ of Eq. (2.74)) was assumed constant and uni-

form (in physical space, time and internal-coordinate space) and equal to 1 m/s, while the total length of the mono-dimensional domain was equal to 1 m. No diffusion term was included in the equation of this case study; this assumption is justified by the fact that molecular and turbulent diffusion is generally negligible when compared to advection due to the relatively large size of the bubbles. Moreover, only a two-node quadrature is considered, namely six moments are tracked into the domain: $M_{0,0}$, $M_{1,0}$, $M_{2,0}$, $M_{3,0}$, $M_{0,1}$ and $M_{1,1}$. At the inlet of this system, a log-normal distribution with the characteristics described in Section 4.1.1 was prescribed as boundary condition (see Table 4.3); for the outlet all the derivatives were set equal to zero in order to allow the bubble to exit from the domain. This mono-dimensional system is discretized by means of the standard Finite-Volume approach. Properties at the face on the boundary in between two cells was reconstructed with the simple First-Order upwind scheme and time integration was carried out by using the standard adaptive solver `ode15s` of Matlab (Shampine and Reichelt, 1997). A particular initial condition was implemented: in the first half of the domain the same distribution of the inlet boundary was assumed, while in the second half the bivariate distribution indicated in Section 4.1.2 was prescribed. In this way, in each zone the moment set is realizable and can be inverted by CQMOM algorithm; however particular attention should be paid in the calculation of fluxes near the discontinuity at the half of the mono-dimensional system.

4.2.2 Results and discussion

In Fig. 4.9 the result of QBMM verification is shown for the simple 1-D system described above, in which bubbles flow with uniform velocity and undergo coalescence and breakage. The use of the First-Order upwind scheme allows to have realizable moment set in all the domain (Desjardins et al., 2008), even during the very first time steps when the discontinuity due to the prescribed initial condition may potentially lead to moment corruption. Furthermore, it is possible to observe that the original version of DQMOM (Marchisio and Fox, 2005) and reported in Section 2.3.4, is not capable of preserving the correct evolution of the moment set; on the contrary with DQMOM-FC the moments are properly conserved, restoring the expected mathematical equivalence with CQMOM. Increasing the number of the grid nodes, as shown in Fig. 4.10, the accuracy of the original version of DQMOM is improved, explaining why this non-conservation problem can be treated as a numerical diffusion. However, with DQMOM-FC the moment set is correctly reproduced. It is in particular interesting to observe the evolution of $M_{3,0}$ and $M_{0,1}$. Since these moments are conserved during the coalescence and break-up, as their source terms are null, their evolution should be a straight horizontal line. This is however true (for any number of grid nodes) only for CQMOM and DQMOM-FC. It is worth mentioning that these conservation errors due to spatial discretization are detected in moments of global order (i.e., $k + l$) equal to or greater than two. In fact, moments of global order smaller than two are linear combination of the primitive variables actually transported (i.e., weights and weighted nodes or abscissas), whereas higher-order moments are non-linear combinations of these variables. This means that the original DQMOM is capable of conserving only moments of global order

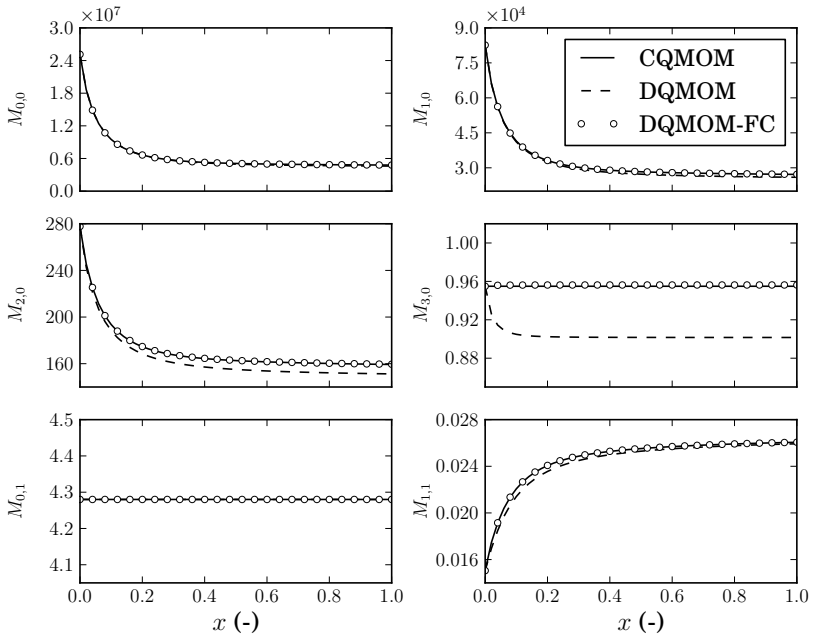

Figure 4.9: Steady state spatial evolution of moments calculated with QBMM, in the case of coalescence and breakage with bubbles moving into the domain with a residence time $\tau = 1$. Units of a generic moment $M_{k,l}$: m^{k-3} mol^{l}. Time in seconds. Dimensionless x-coordinate discretized with 50 grid nodes

zero and of an additional global order (usually one since the method is formulated in terms of weighted nodes or abscissas, as formulated in Section 2.3.4).

In order to make sure that the behaviors observed are intrinsic properties of the methods and not artifacts caused by the fact that different methods might need finer grids than others a grid-independence study has been performed. Fig. 4.11 shows these results for the tracked moments with different methods. In this simple one-dimensional case the number of grid nodes was varied between 5 and 1000. The CQMOM solution with 1000 nodes was considered "exact" since no significant differences were detected in the solution with further refinements. Then the moments predicted with CQMOM, DQMOM and DQMOM-FC with grid nodes varying between 5 and 500 were used to calculate the error with respect to the "exact" solution. As it is seen only CQMOM and DQMOM-FC are capable of conserving (in the Finite-Volume sense) all the moments, including those of global order equal to or higher than two. The error for $M_{3,0}$ (i.e., global order $3 > 2$), whose source term is null considering only coalescence and breakup, is of the order of magnitude of the round-off error only for CQMOM and DQMOM-FC (even with 5 grid nodes), whereas DQMOM, which transports primitive variables, fails in conserving this moment. The error for $M_{0,1}$ is instead for all the methods as small as the order of magnitude of the round-off error, because this moment of global order 1 (smaller than 2) can be correctly predicted also by DQMOM. The error for all the other moments (with non-zero source term) confirms that in general CQMOM and

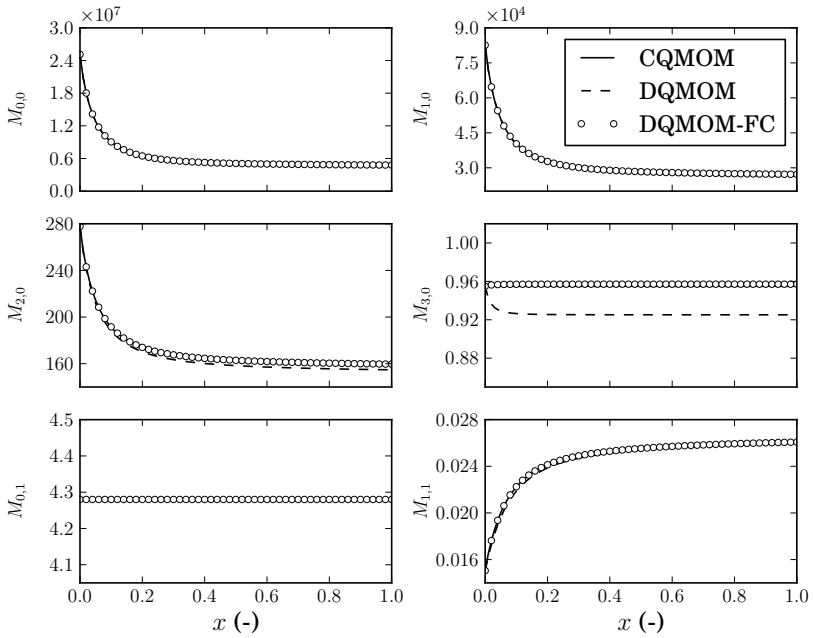

Figure 4.10: Steady state spatial evolution of moments calculated with QBMM, in the case of coalescence and breakage with bubbles moving into the domain with a residence time $\tau = 1$. Units of a generic moment $M_{k,l}$: m^{k-3} mol^{l}. Time in seconds. Dimensionless x-coordinate discretized with 100 grid nodes

DQMOM-FC are more accurate than DQMOM, notwithstanding the grid refinement.

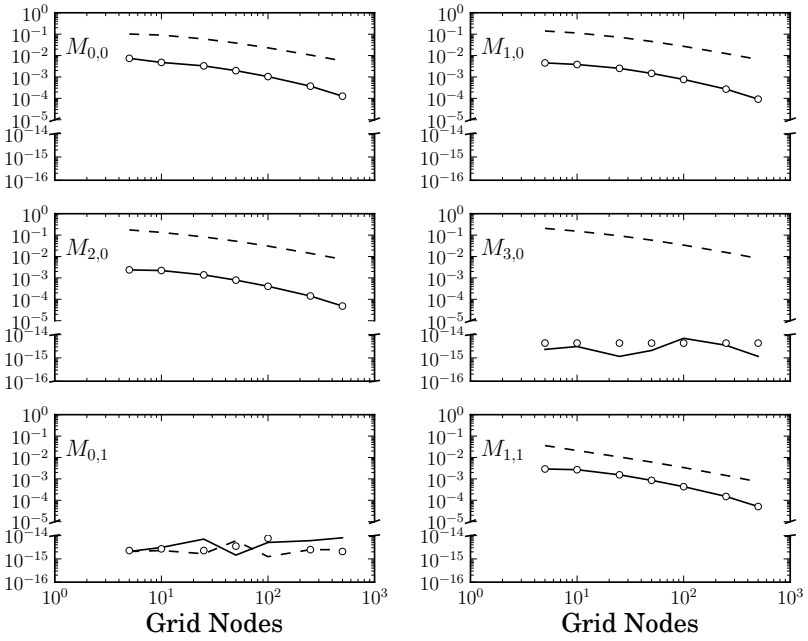

Figure 4.11: Relative error of the tracked moments with respect to the "exact" solution, in one point of the computational domain in function of the total number of grid nodes in the mono-dimensional inhomogeneous case considering coalescence and breakage. The "exact" solution is obtained considering 1000 grid nodes. Continuous line: CQMOM. Dotted line: DQMOM. White circles: DQMOM-FC.

References

Buffo, A., Vanni, M., Marchisio, D., 2012. Multidimensional population balance model for the simulation of turbulent gas–liquid systems in stirred tank reactors. Chemical Engineering Science 70, 31–44.

Buffo, A., Vanni, M., Marchisio, D., Fox, R.O., 2013. Multivariate quadrature-based moments methods for turbulent polydisperse gas-liquid systems. International Journal of Multiphase Flow 50, 41–57.

Desjardins, O., Fox, R., Villedieu, P., 2008. A quadrature-based moment method for dilute fluid-particle flows. Journal of Computational Physics 227, 2514–2539.

Fan, R., Marchisio, D.L., Fox, R.O., 2004. Application of the direct quadrature method of moments to polydisperse gas–solid fluidized beds. Powder Technology 139, 7–20.

Hulburt, H., Katz, S., 1964. Some problems in particle technology: A statistical mechanical formulation. Chemical Engineering Science 19, 555–574.

Laakkonen, M., Alopaeus, V., Aittamaa, J., 2006. Validation of bubble breakage, coalescence and mass transfer models for gas–liquid dispersion in agitated vessel. Chemical Engineering Science 61, 218–228.

Laakkonen, M., Moilanen, P., Alopaeus, V., Aittamaa, J., 2007. Modelling local bubble size distributions in agitated vessels. Chemical Engineering Science 62, 721–740.

Marchisio, D., Fox, R.O., 2013. Computational Models for Polydisperse Particulate and Multiphase Systems. Cambridge Series in Chemical Engineering, Cambridge University Press, Cambridge, UK.

Marchisio, D.L., Fox, R.O., 2005. Solution of population balance equations using the direct quadrature method of moments. Journal of Aerosol Science 36, 43–73.

Marshall Jr., C.L., Rajniak, P., Matsoukas, T., 2011. Numerical simulations of two-component granulation: Comparison of three methods. Chemical Engineering Research and Design 89, 545–552.

Mazzei, L., Marchisio, D.L., Lettieri, P., 2010. Direct quadrature method of moments for the mixing of inert polydisperse fluidized powders and the role of numerical diffusion. Industrial & Engineering Chemistry Research 49, 5141–5152.

Mazzei, L., Marchisio, D.L., Lettieri, P., 2012. New quadrature-based moment method for the mixing of inert polydisperse fluidized powders in commercial CFD codes. American Institute of Chemical Engineering Journal 58, 3054–3069.

McGraw, R., 1997. Description of aerosol dynamics by the quadrature method of moments. Aerosol Science and Technology 27, 255–265.

Petitti, M., Nasuti, A., Marchisio, D.L., Vanni, M., Baldi, G., Mancini, N., Podenzani, F., 2010. Bubble size distribution modeling in stirred gas–liquid reactors with QMOM augmented by a new correction algorithm. American Institute of Chemical Engineering Journal 56, 36–53.

Petitti, M., Vanni, M., Marchisio, D., Buffo, A., Podenzani, F., 2012. Application of the conditional quadrature method of moments for the simulation of coalescence, breakup and mass transfer in gas-liquid stirred tanks, in: Proceedings of 14th European Conference on Mixing, pp. 371–376.

Ranade, V.V., 2002. Computational Flow Modeling for Chemical Reactor Engineering. Academic Press, San Diego (CA), USA.

Shampine, L.F., Reichelt, M.W., 1997. The matlab ODE suite. SIAM Journal on Scientific Computing 18, 1–22.

Wright Jr, D.L., 2007. Numerical advection of moments of the particle size distribution in eulerian models. Journal of Aerosol Science 38, 352–369.

Yuan, C., Fox, R.O., 2011. Conditional quadrature method of moments for kinetic equations. Journal of Computational Physics 230, 8216–8246.

Zucca, A., Marchisio, D.L., Barresi, A.A., Fox, R.O., 2006. Implementation of the population balance equation in CFD codes for modelling soot formation in turbulent flames. Chemical Engineering Science 61, 87–95.

Zucca, A., Marchisio, D.L., Vanni, M., Barresi, A.A., 2007. Validation of bivariate DQMOM for nanoparticle processes simulation. American Institute of Chemical Engineering Journal 53, 918–931.

Chapter 5

Results on realistic systems

From the industrial point of view, aerated stirred tanks and bubble columns are the most common examples of turbulent gas-liquid systems; numerous reactions, such as oxidation, hydrogenation, halogenation and biological fermentation are usually carried out in such equipments. Most of these processes need a turbulent flow condition, an important factor that controls the interfacial area between phases and, consequently, mass and heat transfer rates. Since this has an impact on the process economy, extensive experimental comparison have been performed in the past to identify the different fluid dynamics regimes, and to assign to each of them appropriate correlations to calculate mass transfer rates for design and scale-up (Calderbank, 1958). Nevertheless, these empirical or semi-empirical correlations do not have a general validity and their use is limited to specific configurations and operating conditions close to those under which they were derived, considering only volume-averaged properties of the system, neglecting the significant spatial inhomogeneities that exist even in laboratory scale equipment and that in turn affect global properties.

An illuminating example is constituted by the estimation of mass transfer rates in bubble columns. In fact, the operating conditions and the design variables of these system play a crucial role in the determination of all the main fluid dynamics characteristics. Moreover, the hydrodynamics is very difficult to describe due to the unsteady nature of the flow, caused by the simultaneous processes that occur at different spatial and time scales. The liquid recirculation inside the column is inducted by the rising bubbles, in turn subjected to coalescence and breakage at smaller scales that modify in size and shape. Local interfacial area for gas-liquid mass transfer depends on the Bubble Size Distribution (BSD), which may sensibly vary in different zones of the column. Numerous zero-dimensional or mono-dimensional models for the estimation of the volumetric mass transfer coefficient, $k_L a$, have been formulated through the years (for a thorough review, see Cachaza Gianzo, 2011), but they are all applicable to particular cases, as basic assumptions of these refer to specific fluid dynamic regimes.

Another example is that of gas–liquid stirred tank reactors, where the hydrodynamic is completely determined by the mechanic agitation. Also in this case, however, the interfacial area for mass transfer depends on the BSD, which is known to vary according to different op-

erating conditions, and for the same operating conditions, from point to point in the system. In fact, higher bubble break-up frequency are detected near the impeller, due to the high shear rates, resulting in BSD skewed towards lower diameters, whereas in stagnant zones far from the impeller bubbles tend to accumulate and coalesce, resulting in a BSD shifted to larger bubble diameters.

Moreover, it should be considered that bubbles are distributed not only with respect to size, but also velocity and composition and a possible approach, as described in Chapter 3, is to combine Computational Fluid Dynamics (CFD) with Population Balance Modeling (PBM) in an Eulerian-Eulerian framework with the aim of correctly predicting the evolution in space and time of the dispersed phase, including local and global mass transfer fluxes in industrial-scale equipments.

In this Chapter, the coupled CFD-PBM fully predictive approach will be applied to the simulation of mass transfer rates for a realistic bubble column and an aerated stirred tank reactor, both experimentally studied by Cachaza Gianzo (2011) and Laakkonen et al. (2006), respectively. The obtained results will be eventually compared with the experimental data available for those configurations.

5.1 CFD simulation of a pseudo 2D bubble column.

5.1.1 Introduction

In the latest years, rectangular bubble columns have been investigated by many groups (Pfleger et al., 1999; Pfleger and Becker, 2001; Buwa et al., 2006; Diaz et al., 2008a) due to the easy setup and the possibility to better visualize the flow without any optical distortion. Moreover this particular configuration has several fluid dynamic characteristics of larger cylindrical bubble columns and is particularly suited to be studied computationally because of the lower volume and regular shape; both aspects help to achieve good quality grids, reducing the global computational cost (Buwa and Ranade, 2002).

Different experimental techniques can be used to characterize the nature of the gas-liquid flow inside rectangular bubble columns: measurement of the wall pressure fluctuations is one of the simplest ways to characterize the dynamics of such systems (Drahoš et al., 1991; Letzel et al., 1997), but also laser-Doppler anemometry (Becker et al., 1994, 1999; Borchers et al., 1999; Pfleger et al., 1999) and particle image velocimetry (Lin et al., 1996; Mudde and Simonin, 1999) were successfully applied for the same purpose. Furthermore, high-speed cameras and oxygen probes have been used to carry out measurements of BSD and mass transfer rates (Cachaza Gianzo, 2011).

From the modeling point of view, all these data allow to study on different aspects and easily validate simulation results. The dimension of the computational grid was one of the first points addressed: Pfleger et al. (1999) have performed simulations both with two-dimensional (2-D) and three-dimensional (3-D) domain, showing that turbulent viscosity obtained with a 2-D simulation is 5-10 times higher than the viscosity values obtained

in 3-D simulation of the same identical column and for this artificially increased viscosity the oscillatory motion of the plume is damped with 2-D simulations. Pfleger et al. (1999); Sokolichin and Eigenberger (1999); Mudde and Simonin (1999) have stressed on the importance of an adequate grid resolution to properly catch the experimentally observed dynamics. In the work of Deen et al. (2001), different turbulence models are compared showing that Large Eddy Simulation (LES) with a proper subgrid model may improve the description of the fluid dynamics usually obtained with the Reynolds-average Navier-Stokes equations (RANS) approach, although this latest model represents the only feasible way for describe industrial-scale systems; Zhang et al. (2006) have shown that RANS results can be improved by choosing the proper bubble-induced turbulence model. Another important investigated aspect is represented by the boundary conditions: Ranade (2002) has speculated about common practices both for inlet and outlet conditions without giving a unique optimal choice. Recently, Zhang (2007) has pointed out the necessity to include the free surface into the computational domain when the system involves mass transfer.

Most of these attempts to describe the behavior of rectangular bubble columns assume the bubble population as composed of a single bubble size, usually used as a fitting parameter to capture the global gas hold-up value (Pfleger and Becker, 2001). Although in air-water dispersions, bubble slip velocity is not very sensitive to the value of bubble diameter ranging between 1 to 10 mm (see Fig. 3.3 at Page 80), bubble size distribution locally varies as a consequence of coalescence and break-up processes and this deeply affects the estimation of gas-liquid interfacial area. The recent interest of coupled CFD-PBM approaches is so explained: Buwa and Ranade (2002) have used the commercial code FLUENT for the two-phase fluid dynamics description coupled with user-defined functions (UDF) implementing the so-called non-uniform multi-group model, a particular method Classes Method, for five bubble groups. Diaz et al. (2008b) have carried out simulations using the commercial code CFX using the build-in population balance module including the non-uniform multi-group model for ten different classes of bubbles.

As reported in Chapter 2, Quadrature-Based Moment Methods (QBMM) have the great advantage of increasing the accuracy of the population balance description by reducing the overall computational cost compared with other solution methods. In a previous work of my group (Buffo et al., 2013) the importance of having a deep control on the implementation of the governing equations was remarked; in commercial codes it can be very difficult to achieve a proper combination between CFD software and user-defined routines for Population Balance Equations, can be very difficult to achieve especially in terms of stability of the code. The open source alternative to the commonly known CFD codes, OpenFOAM, reached in later years a good level of maturity and nowadays it is widely used in different scientific areas both in the industry and in academic institutions. All the parts of the code are available under the GPL license over the internet and can be fully modifiable according to different needs.

The aim of the work is so to implement and validate QBMM inside the OpenFOAM framework. A preliminary implementation of the Quadrature Method of Moments was tested

by simulating the partially aerated rectangular bubble column experimentally studied by Diaz et al. (2008b,a); Cachaza Gianzo (2011) and directly comparing the results obtained with the experiments. This work will be described in the following subsections.

5.1.2 Test case description

The simulated experimental apparatus consists of a 0.2 m wide, 1.8 m high and 0.04 m deep polymethyl methacrylate bubble column. The column was filled with tap water up to 0.45 m from the bottom at room temperature and atmospheric pressure, while air was fed through an aluminum sparger composed of eight centered holes of 1 mm of diameter and 6 mm pitch. A sketch of this setup is shown in Fig. 5.1. The superficial gas velocity U_G was varied from 2.4 to 21.3 m/s by means of the appropriate combination of volumetric flow meters.

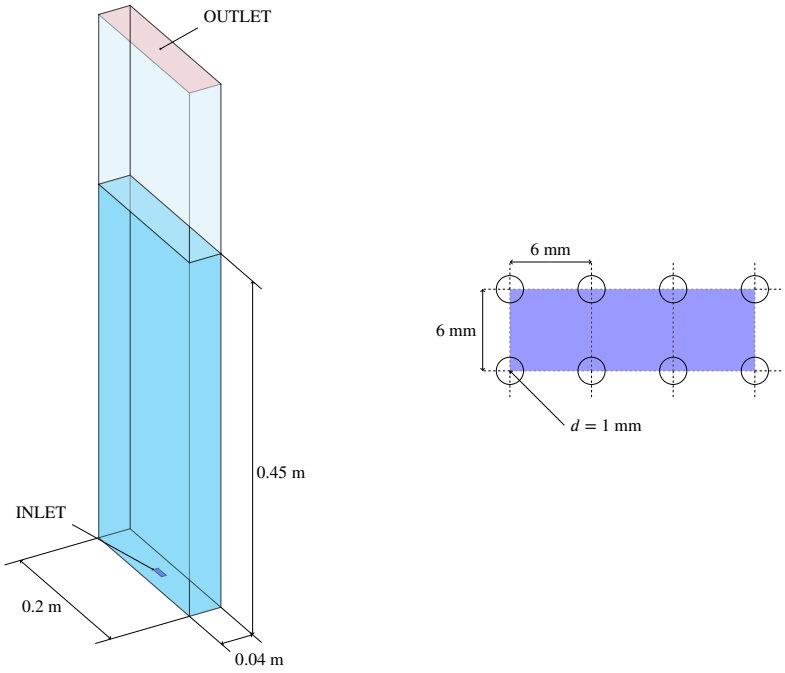

Figure 5.1: Left: Schematic representation of the rectangular bubble column simulated. Right: Gas distributor scheme; colored area represents the modeled sparger surface.

Comparison with the numerical simulations is carried out between different sets of experimental data:

- Global gas hold-up, measured through the manometric method, that evaluates the static pressure difference between two pressure sensors located at wall of the column.
- Plume Oscillation Period (POP), performed by means of the transformation of the pressure time series from the time domain to the frequency domain and the subsequent identification of the characteristic frequency of the peak in the low frequency band (0 - 1 Hz).

- Visual observations, carried out by means of a digital video system.
- Mean Sauter diameter (d_{32}), obtained after manipulation of high-speed digital camera frames through an image processing software. Although the exact position of the camera is unknown (Cachaza Gianzo, 2011), this value helps to understand what happens in the central part of the column in terms of Bubble Size Distribution (BSD).

Further details about the experimental setup can be found in the literature (Diaz et al., 2008b,a; Cachaza Gianzo, 2011).

5.1.3 Methods and numerical details

The standard OpenFOAM solver `compressibleTwoPhaseEulerFoam`, based on the two-phase Eulerian-Eulerian equations for compressible systems, was modified in order to include a Population Balance module (a description of the coupled PBM-CFD methodology was reported in Section 3.3). This module is designed to allow further expansions, as different solution methods, as well as other closures for turbulence and interfacial forces and different coalescence/breakage kernels. A preliminary implementation of the Quadrature Method of Moments (QMOM) was performed and verified, then the obtained results were eventually compared with the experimental data. In Fig. 5.2 an outline of the solver structure is shown.

The main guidelines of the solution procedure are summarized below:

- Compressibility effect disabled by default (isothermal system);
- Drag coefficient calculated by means of Eq. (3.65) assuming constant terminal velocity equal to 20 $^{cm}/_{s}$ for all the bubble sizes. Other interfacial forces are neglected;
- Standard $k - \epsilon$ model for the turbulence in the liquid phase. Turbulent viscosity in the gas phase was not taken into account because, in this phase, turbulent transport of momentum is negligible in comparison to advection because of the large size of the bubbles;
- Four moments of the Bubble Size Distribution calculated (M_0, M_1, M_2, M_3), corresponding to a two-node quadrature approximation;
- Coalescence kernel and efficiency indicated in Eq. (2.66) and Eq. (2.68). Brekage frequency and daughter distribution function reported in Eq. (2.55) and Eq. (2.62);
- Source terms of moments calculated in a specific range of gas volume fraction (i.e., $1.0 \cdot 10^{-4} < \alpha_G < 0.8$). In the other regions are assumed equal to zero;
- Free surface contained inside the computational domain.

Three different non-uniform hexahedrical grids, reported in Fig. 5.3, with the purpose of addressing a proper spatial resolution were investigated. An adaptive version of the first

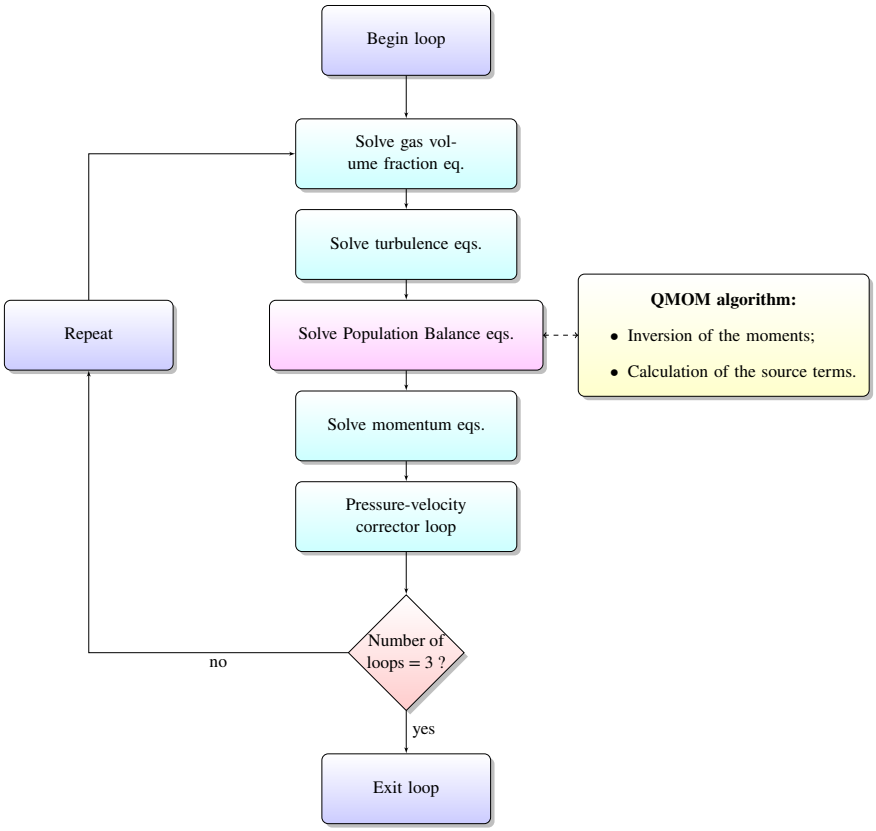

Figure 5.2: Schematic representation of a single time step of the segregated OpenFOAM solver coupled with QMOM.

order backward Euler discretization scheme was used for time integration: time step Δt is chosen so that the following Courant-Friedrichs-Lewy condition is respected:

$$\mathrm{CFL} = \Delta t \sum_{i=1}^{n=3} \frac{U_{r,i}}{\Delta x_i} < 1, \tag{5.1}$$

where $U_{r,i}$ is the relative velocity between gas and liquid in the i-th direction and Δx_i is the cell size in the same direction. For the sake of numerical stability, the value of Δt can not be larger than 0.025 s. Spatial discretization schemes and boundary conditions are summarized in Table 5.1. The physical constants used in all the simulations are reported in Table 5.2.

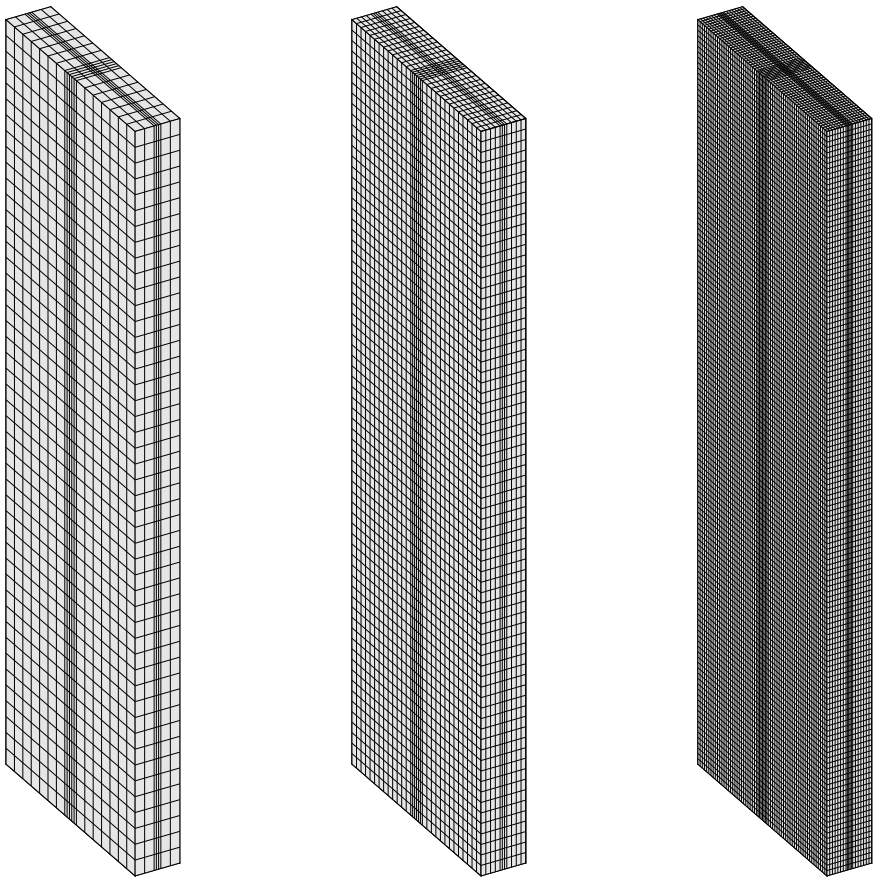

Figure 5.3: Mesh used in the numerical simulations. From left to right: coarse (17 width × 7 depth × 45 height), medium (32 × 11 × 70), fine (62 × 19 × 128).

Special mention deserves the inlet condition for the gas phase; in fact the sparger was modeled through a rectangle with an area equal to the total area enclosed by the 8 holes (Fig. 5.1). The volume fraction of gas α_G imposed at this surface is fixed and equal to 0.5 in all the performed simulations; the inlet gas velocity was calculated according to the

Table 5.1: Numerical schemes and boundary conditions adopted in the simulations

Variable	Scheme	Inlet	Outlet	Wall
Gas vol. frac.	Limited Second Order Upwind	0.5	Gradient zero	Gradient zero
Gas velocity	Limited Second Order Upwind	Depends on flow rate	Gradient zero with backflow	Free-slip wall
Liquid velocity	Limited Second Order Upwind	0.0 $^{m}/_{s}$	Gradient zero	No-slip wall
Pressure	First Order Upwind	Gradient zero	1 bar	Gradient zero
k	Limited Second Order Upwind	Based on Turbulence Intensity equal to 5% and Length Scale equal to the hole diameter	$1 \cdot 10^{-4}$ $^{m^2}/_{s^2}$ (backflow only)	Gradient zero
ϵ	Limited Second Order Upwind		$1 \cdot 10^{-5}$ $^{m^2}/_{s^3}$ (backflow only)	Gradient zero
Moments	First Order Upwind	Log-normal distrib.	Gradient zero	Gradient zero

Table 5.2: Physical properties used in numerical simulations.

$\rho_{liq.}$	998.2	$^{kg}/_{m^3}$
ρ_{gas}	1.255	$^{kg}/_{m^3}$
$\mu_{liq.}$	$1.0 \cdot 10^{-3}$	Pa s
σ	0.07	$^{N}/_{m}$

following expression:

$$\text{Inlet Gas Velocity} = \frac{\text{Gas Flow Rate}}{\text{Modelled Sparger Area} \cdot \text{Gas Volume Fraction}}. \tag{5.2}$$

The complex mechanism of bubble formation and detachment from the hole of the sparger was modeled by assuming a log-normal distribution as inlet Bubble Size Distribution, according to the work of Petitti et al. (2010). The k-th order moment was calculated as follows:

$$M_k = M_0 \exp\left\{ k\mu + \frac{k^2\sigma^2}{2} \right\}, \tag{5.3}$$

where M_0 is the moment of order zero, namely the total number of bubbles per unit volume and μ and σ are the two parameters of the log-normal distribution. By assuming the mean m of the bubble distribution equal to the bubble diameter calculated with the correlation of Geary and Rice (1991) valid for holed spargers and the standard deviation $\sqrt{v}$ of the distribution equal to 15% of the mean value m as in the works of Laakkonen et al. (2007);

Petitti et al. (2010), it is possible to calculate μ and σ in the following way:

$$\mu = \log\left(\frac{m^2}{\sqrt{v+m^2}}\right), \tag{5.4}$$

$$\sigma = \sqrt{\log\left(\frac{v}{m^2}+1\right)}. \tag{5.5}$$

The value of the moment of order zero M_0 can be calculated by considering the following equality:

$$\text{Gas vol. frac.} = k_V M_3 = k_V M_0 \exp\left\{3\mu + \frac{9\sigma^2}{2}\right\}, \tag{5.6}$$

where k_V is the volumetric shape factor (equal to $\pi/6$ for a sphere) and M_3 is the moment of order three with respect to bubble size.

Five different operating conditions (at different superficial velocity U_G) were simulated, in order to compare the obtained results with the experimental data available. The results of this comparison are shown in the following section.

5.1.4 Results and discussion

Mesh size analysis

As previously mentioned, the influence of the mesh resolution on the results was studied in order to keep under control the computational time (similar work was done by Diaz et al. (2008b)). Three different grids were generated: coarse, medium and fine (as reported in Fig. 5.3) and in Table 5.3 the obtained results are compared with the experimental data for the case with $U_G = 2.4\,\text{mm/s}$.

Table 5.3: Mesh size effect on calculated gas hold-up, Plume Oscillation Period and Sauter Diameter compared with experiments for $U_G = 2.4\,\text{mm/s}$.

Grid size	**Number of cells**	**Hold-up**	**POP** (s)	d_{32} (mm)
Coarse	5355	0.64%	7.78	5.78
Medium	24640	0.62%	10.57	6.92
Fine	150784	0.57%	11.71	5.93
Experim.		0.69%	11.37	6.83

As it can be observed, all numerical results slightly differ from the experiments. While the global gas hold-up decreases with the grid resolution, POP increases and the mean Sauter diameter d_{32} shows a non-monotonic trend. Similar results varying the cell size were obtained by Diaz et al. (2008b) for the same system under investigation. Although it is not possible to say that a grid independence condition is achieved, the medium mesh represents a good trade off between accuracy and computational costs and will be used in the rest of the work. However, it should be remarked that both numerical global gas volume fraction and POP are strongly influenced by the interfacial force closure (i.e., drag force) and a tuning

of the terminal velocity U_T will provide better agreement with experiments. Regarding the difference between experimental and simulated d_{32} values, as it was previously pointed out, it might be due not only to the choice of coalescence and breakup kernel constants, but also to the uncertainty of the exact camera position (Cachaza Gianzo, 2011).

Effect of increasing gas flow rate

In Fig. 5.4 some experimental camera frames of the characteristic flow inside the column are compared with the simulation results of gas hold-up and water superficial velocity for different values of the superficial gas velocity U_G. As it is possible to see the predicted results reproduce the central bubble plume and its oscillating motion from side to side. The liquid phase descends along the sidewalls of the column, without escaping from the domain due to the fact that walls are higher than the free surface; the conservation of the liquid mass is a crucial aspect in the prediction of mass transfer rates (Buffo et al., 2012). The local value of gas hold-up at different U_G is in good agreement with the experimental pictures. The region with the higher bubble density is the central plume for all the simulated cases, but at the lowest investigated gas flow rate bubbles are not trapped into the liquid recirculation and tend to stay only in the central region and spread over all the column section only when the plume approaches the free surface. As the superficial velocity U_G is increased to higher values, smaller bubbles tend to move with the liquid vortices downwards along the side walls, resulting in a better aeration in the bubble column. This situation is also confirmed by other plots that show the liquid velocity field and the profile of the mean bubble diameter, d_{32} (Fig. 5.5). Contour plots of d_{32} show that, with the increase of the gas superficial velocity, smaller bubbles tend to stay in the liquid recirculation path, whereas bigger bubbles are concentrated into the central plume zone where coalescence and breakage occur with faster rates due to turbulence.

Table 5.4: Comparison of experimental data and calculated results for global gas volume fraction (hold-up), POP and mean Sauter diameter varying the superficial gas velocity U_G.

Superf. vel. (mm/s)	**Hold-up**	**POP** (s)	d_{32} (mm)
2.4	0.62%	10.10	6.01
Exp.	0.69%	11.37	6.83
7.1	1.61%	8.26	6.28
Exp.	1.81%	5.69	7.05
11.9	2.45%	5.83	6.89
Exp.	2.63%	4.27	6.50
16.6	3.36%	3.80	7.01
Exp.	3.36%	3.01	6.40
21.3	4.19%	3.84	7.96
Exp.	4.10%	2.84	7.73

In Table 5.4 another comparison between simulations and experiments in terms of average values as global gas hold-up, POP and mean Sauter diameter as a function of the

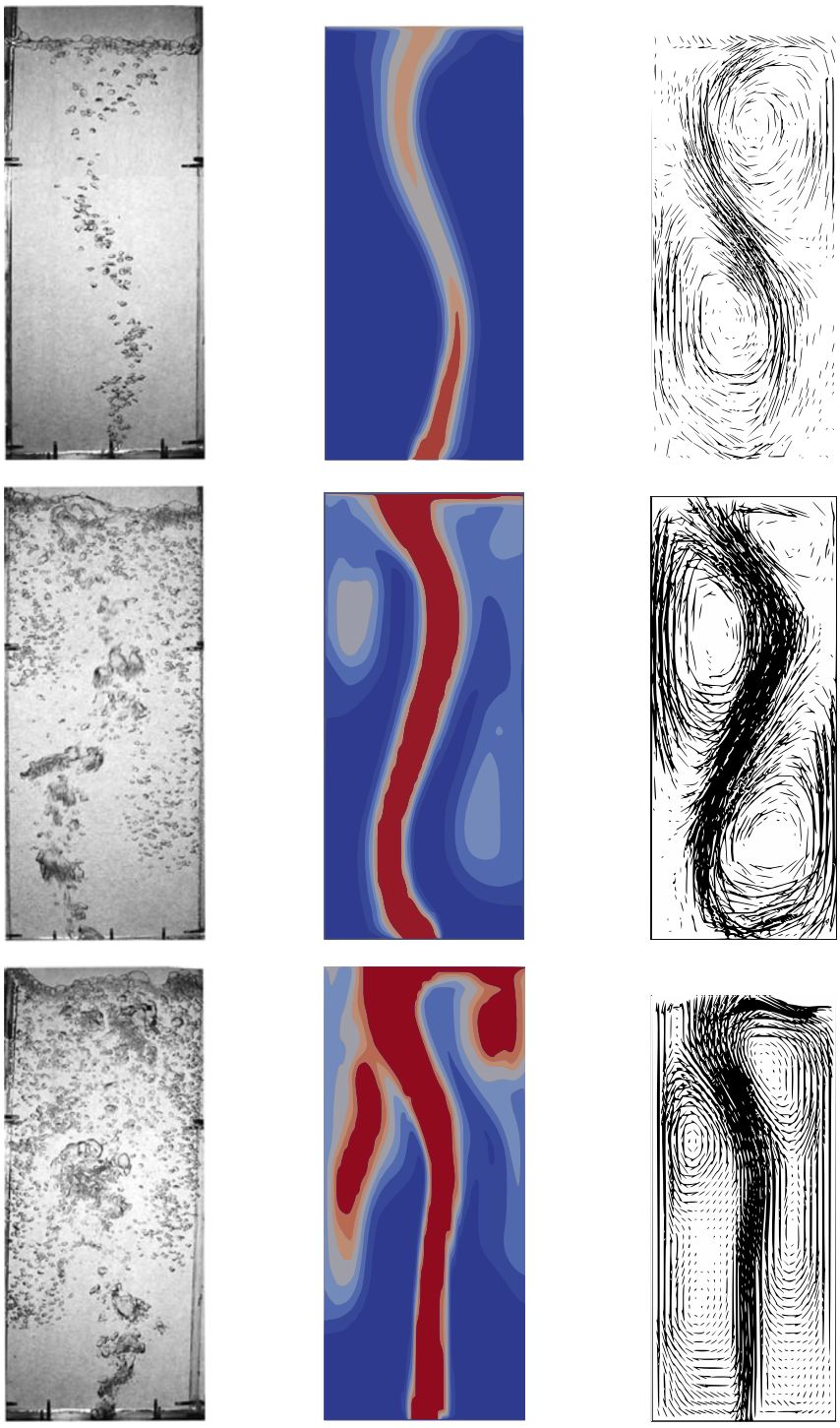

Figure 5.4: Comparison between experimental and computational frames at different values of gas superficial velocity. From top to bottom: $U_G = 2.4\,\text{mm/s}$; $11.9\,\text{mm/s}$ and $21.3\,\text{mm/s}$. From left to right: high speed camera frame. Gas hold-up distribution [0 (blue), > 0.1 (red)]. Water superficial velocity field.

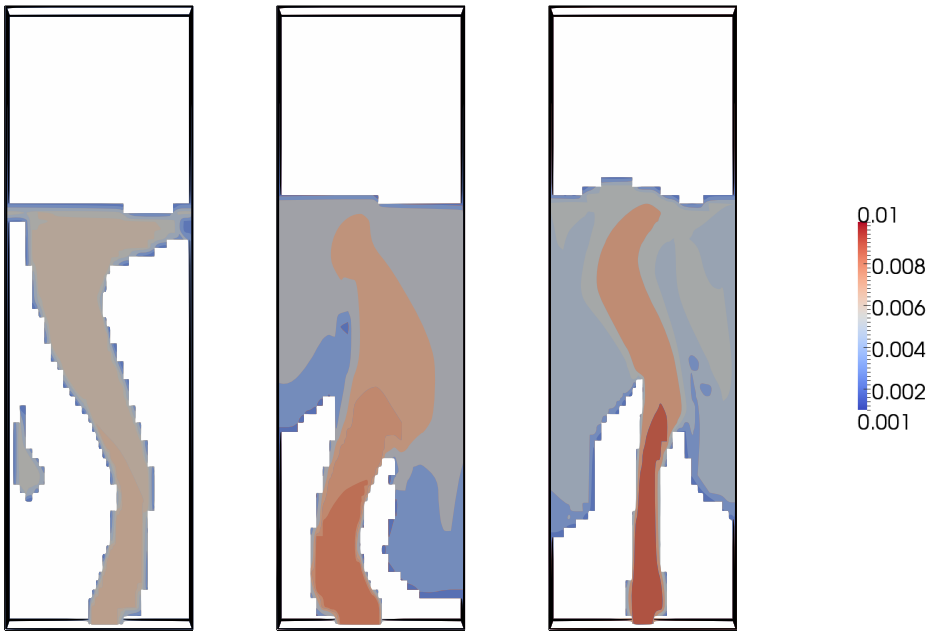

Figure 5.5: Contour plot of mean Sauter diameter d_{32} for different superficial velocity U_G. From left to right: 2.4 mm/s, 11.9 mm/s, 21.3 mm/s. Units in meter.

superficial gas velocity U_G is reported. The change of global gas hold-up at different flow rates is a crucial characterization for a bubble column because it is usually performed in order to experimentally identify the different flow regimes (Ruzicka et al., 2001; Zahradník et al., 1997). In Fig. 5.6 the measured global gas hold-up values are compared with the predicted ones. As it can be clearly seen, very good agreement is detected both in terms of absolute values and trends; similar trends can be explained by the existence of unique flow regime, the vortical flow regime(Diaz et al., 2008b), as clearly visible in Fig. 5.4. Furthermore, a similar agreement proves that the choice of the drag coefficient is appropriate, at least for this flow regime: it is interesting to stress here that bubble size diameter is no longer used as a model fitting parameter (Pfleger and Becker, 2001) for catching the experimental value of global gas hold-up, but it is calculated with the population balance model. As already mentioned, the terminal velocity of the bubble U_T is here assumed equal to 20 cm/s for all the bubbles. This is a reasonable value because, from experimental evidence, the rising velocity of a single bubble in stagnant water is about 25 cm/s for bubble sizes ranging between 2-10 mm (see Fig. 3.3 at Page 80); this value must be in some way reduced in order to account for the effect of other bubbles (i.e., the local gas volume fraction) and of turbulence of the system (Montante et al., 2007; Petitti et al., 2010). In this case it is possible to say that 20 cm/s is an appropriate value for the system under investigation, but further studies are required both from the experimental and theoretical point of view to formulate a drag law valid for different flow regimes.

The characteristic oscillating behavior of the bubble plume is an essential trait of the partially aerated bubble column. From the experimental side, the measurements of this wavelike

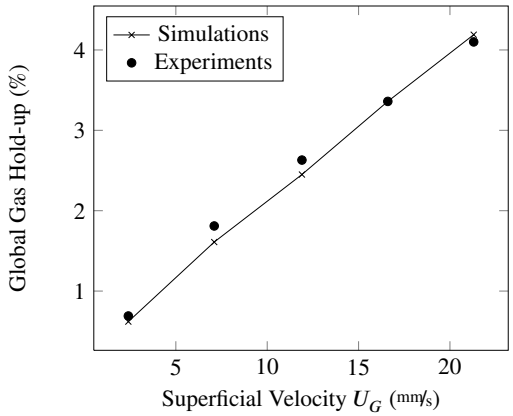

Figure 5.6: Comparison between experimental data and predicted global gas hold-up for different superficial gas velocities.

motion is usually carried out by means of time series analysis of pressure sensors data located at different points in the equipment. In the examined case, the spectrum of pressure fluctuations was recorded at a frequency of 15 Hz for 20 min in order to minimize the statistical error, then low-pass filtered at the frequency of 1 Hz before the calculation of the Plume Oscillation Period (POP) (Cachaza Gianzo, 2011). Otherwise, the calculation of the POP from the simulations is usually based on the number of cycles of the horizontal liquid velocity profile at the central point of the column. This method is feasible at low superficial gas velocity, but at high gas flow rates the number of cycles cannot be easily identified due to chaotic motion of the plume. For this reason, the horizontal liquid velocity data are transformed from time domain to the frequency domain using a Fast Fourier Transform algorithm (Diaz et al., 2008b). In Fig. 5.7 the comparison between experimental and predicted POP values is reported. As it is possible to see from the experimental observations, at low U_G values, the POP is high and rapidly decreases as gas superficial velocity decreases until a constant value is reached. This evolution has been related to the evolution of the bubble size distribution (Buwa and Ranade, 2002), as coalescence and breakage rapidly increase at low gas superficial velocity but then reach a pseudo steady-state at higher U_G values. The predictions of the model do not fully capture this trend and the calculated POP decreases almost monotonically with the gas superficial velocity. This is probably due to the turbulence models that seems to be inadequate to describe the observed dispersion behavior.

Fig. 5.8 shows the evolution of the mean Sauter diameter d_{32} with respect to the gas superficial velocity. As it was previously pointed out, the exact position of the camera used in the experiments is unknown, moreover assuming that the values reported in literature are averaged over all the snapshots analyzed by the software (Cachaza Gianzo, 2011). For this reason the comparison with the experiments should not be intended here as a validation but only as a qualitative feedback for QMOM results. More interesting is the comparison between the predicted d_{32} and the value imposed at the inlet by the Geary and Rice correlation: the average bubble size at the center of the column increases much less with the gas flow

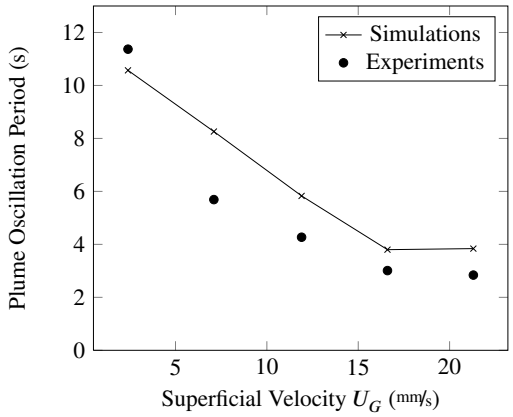

Figure 5.7: Comparison between experimental data and predicted Plume Oscillation Period for different superficial gas velocities.

rate than the bubble size at inlet. This fact shows that the relative importance of break-up process over coalescence increases with U_G, due to the enhancement of turbulent induced collisions at higher gas flow rates.

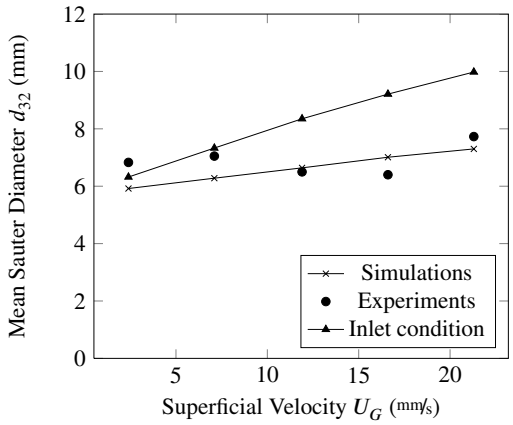

Figure 5.8: Comparison between experimental and predicted mean Sauter diameter at the center of the column and the inlet value calculated with the correlation of Geary and Rice (1991) for different superficial gas velocities.

5.1.5 Conclusions

In this part of the work, QBMM were implemented in a open source CFD code OpenFOAM, overcoming all the issues that may arise when new equations must be solved and coupled with the fluid dynamic description in a commercial CFD code (Buffo et al., 2013). The new code obtained from the modification of the standard solver `compressibleTwoPhaseEulerFoam` is stable and parallelized, providing a solid base for further expansions.

For assessing the reliability of the implementation, the partially aerated rectangular bub-

ble column of the work of Diaz et al. (2008b,a); Cachaza Gianzo (2011) was modeled and the obtained results was compared with the experimental data available at different superficial gas velocities. The performed analysis shows that there is in general a good agreement with the experiments for the compared variables: global gas hold-up trend with respect of U_G was correctly reproduced by the model, while the comparison of POP and mean Sauter diameter is still satisfactory despite of the approximations introduced by the model and the impossibility of extracting data from simulations with the same procedures used in the experiments.

However, it was shown that the calculated moments of the bubble size distribution may give detailed and local information of mass transfer interfacial area between the two phases, necessary for carrying out mass transfer simulations of oxygen in water. As seen in Section 4.1.2 for zero-dimensional systems, the smaller bubbles have higher mass transfer rates than larger ones because of a higher interfacial area and tend to reach the equilibrium with the liquid more quickly; for this reason not only the bubble size, but also bubble concentration is needed for a proper description of the mechanism. Therefore, this work will continue with the implementation of a multivariate population balance solver, CQMOM, in the same open source framework with aim of validating the model with the dissolved oxygen profiles available in literature.

5.2 Multivariate QBMM verification on a 2D bubble column

5.2.1 Introduction

As previously reported, in the latest years the coupled PBM-CFD approach has attracted the interest of the scientific and industrial communities as a powerful tool to predict dispersed systems involving a certain degree of poly-dispersity. In the most popular commercial codes (i.e., CFX, FLUENT) new specific modules for the solution of the monovariate PBE using different methods were introduced in order to meet the user needs. However, an official implementation of a multivariate PBE solution method does not exist, and this will be the focus of the rest of this Chapter.

As pointed out elsewhere (Buffo et al., 2013), the implementation of PBE solution methods in CFD codes is not a straightforward operation. Although the main commercial CFD codes have the possibility of introducing additional equations, some important information, such as phase fluxes at different cell faces, are the results of internal routines, completely hidden to the programmer and for which there is no proper documentation. For this reason, it is crucial to verify every implemented part of the code in order to point out programming errors and in order to overcome numerical difficulties that may arise when new quantities, strongly coupled with the fluid dynamic description, like the moments of the bubble distribution, are transported. Only after this verification is performed the validation via comparison with experiments can be carried out.

Therefore, the implementation in the commercial code ANSYS FLUENT 13 and the ver-

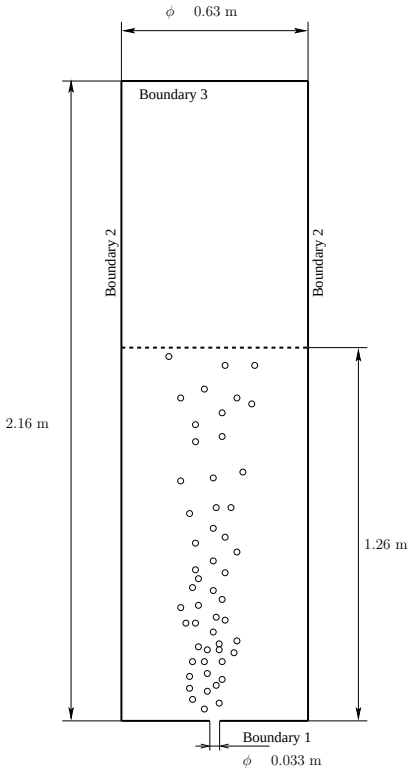

Figure 5.9: Schematic representation of the two-dimensional rectangular bubble column modeled.

ification of different QBMM for a very simple 2D bubble column will be treated in this part of the dissertation, showing in detail the criteria used for verifying the code and establishing the guidelines of initial and boundary conditions. The result of the comparison between different QBMM will be also shown and discussed. Moreover, mass transfer tests were also carried out, in order to point out the differences between modeling without population balances, with a monovariate approach and with a multivariate approach the comparison is done in terms of global mass transfer coefficient and the results of this comparison will be presented and discussed.

5.2.2 Test case description

In Fig. 5.9 a schematic representation of the simulated system is reported. The aim of the work is to verify the implemented population balance module without validation. The geometry is constituted by a simple two-dimensional rectangular grid with 11,230 non-uniform cells, with a gas sparger situated at the bottom of the column and the outlet at the top. The air bubbles are injected in stagnant pure water and therefore the liquid starts moving only due to the action of bubbles. At the beginning of the simulation, the free surface between phases is placed at a height of 1.26 m.

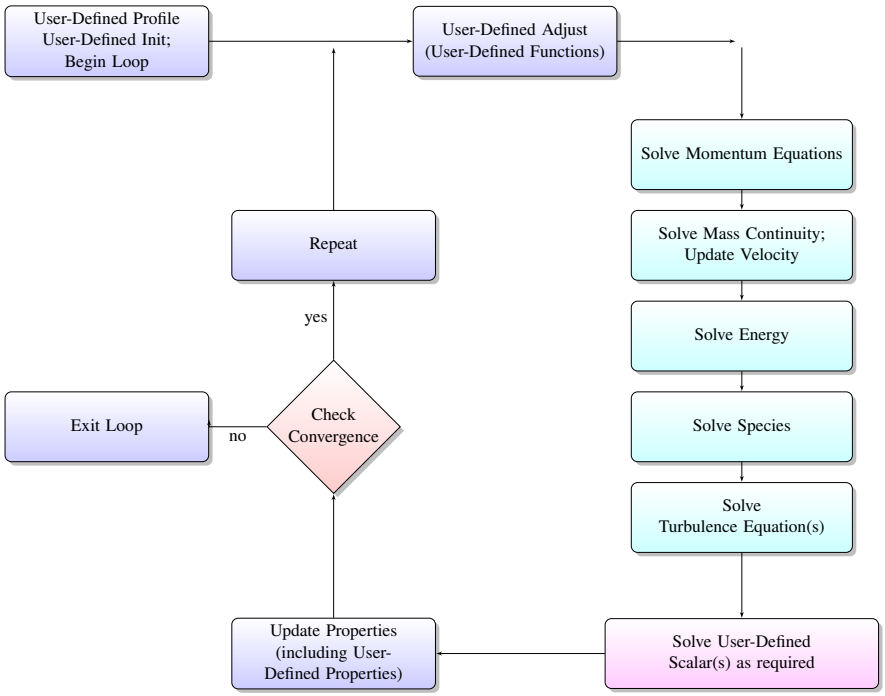

Figure 5.10: Schematic representation of a single inner iteration of the segregated pressure-based solver of FLUENT.

5.2.3 Methods and numerical details

As previously mentioned, different QBMM were coupled to the commercial CFD code ANSYS FLUENT 13. The Population Balance Equations were implemented by means of a User-Defined Functions (UDF) and Scalars (UDS), a framework specifically designed for coupling new equations into the preexisting CFD code. Although a complete description of the coupling procedure is reported in Section 3.3, in this section the salient details will be recalled.

A generic User-Defined Scalar, ψ, can be introduced into the set of solved equations in the context of the multifluid solver and calculated by means of the following equation:

$$\frac{\partial}{\partial t}\left(\alpha_i \rho_i \psi\right) + \nabla_{\mathbf{x}} \cdot \left(\alpha_i \rho_i \mathbf{U}_i \psi - \left(\alpha_i \Gamma_i \nabla_{\mathbf{x}} \psi\right)\right) = S \tag{5.7}$$

where α_i, ρ_i, $\mathbf{U}_i$ and Γ_i are respectively volume fraction, density, velocity and diffusion coefficient of the $i-$th phase, while S is the source term. It should be noticed that Eq. (5.7) is mass conservative with respect to the $i-th$ phase, namely the sum of advective and diffusive fluxes discretized at different faces of a single computational cell within a time step is equal to zero (when S is equal to zero). A schematic rapresentation of the solver is reported in Fig. 5.10.

In the actual PBE implementation ψ and S may represent different quantities, depending on the method used. As explained in Section 2.2, molecular or turbulent diffusion is neg-

ligible for all the scalars that refer to bubble properties, as moments for QMOM/CQMOM and weights and weighted nodes for DQMOM/DQMOM-FC. For CQMOM, the relation between the solved scalar ψ and the generic-order moment $M_{k,l}$ is the following:

$$\psi = \frac{M_{k,l}}{\alpha_i} \tag{5.8}$$

$$S = \rho_i \left[H_{k,l} - \sum_{j=1}^{N} k\, w_j\, L_j^{k-1}\, \phi_{\mathrm{b},j}^{l}\, G(L_j, \phi_{\mathrm{b},j}) - \sum_{j=1}^{N} l\, w_j L_j^{k} \phi_{\mathrm{b},j}^{l-1} \dot{\phi}_{\mathrm{b}}(L_j, \phi_{\mathrm{b},j}) \right], \tag{5.9}$$

which is the approach described in Section 3.3.1. Assuming that all bubbles move the same velocity, namely using a two-fluid approach with a liquid continuous phase and a single gaseous dispersed phase (i.e., $i = 1$), it is theoretically possible to recover the transport equation for a generic order moment as reported Eq. (2.73) at Page 34 by substituting Eq. (5.9) into Eq. (5.7). As mentioned in Section 3.3, this assumption is reasonable when the BSD ranges between 1 to 10 mm (Petitti et al., 2010; Buffo et al., 2013), as in this case. It is not clear, however, how the advective fluxes of a generic scalar are calculated; for this reason the discretization scheme used not only for the moments, but also all for the other calculated variables First-Order Upwind was used.

For DQMOM and DQMOM-FC respectively, the generic scalar ψ must be substituted by the model variables w_j, $w_j L_j$ and $w_j \phi_{\mathrm{b},j}$ in the following way:

$$\begin{cases} \psi = \dfrac{w_j}{\alpha_i} & S = \rho_i a_j, \\ \psi = \dfrac{w_j L_j}{\alpha_i} & S = \rho_i \left[b_j, + w_j G_j \right] \\ \psi = \dfrac{w_j \phi_j}{\alpha_i} & S = \rho_i \left[c_j + w_j \dot{\phi}_{\mathrm{b},j} \right], \end{cases} \tag{5.10}$$

$$\begin{cases} \psi = \dfrac{w_j}{\alpha_i} & S = \rho_i \left[a_j + a_j^* \right], \\ \psi = \dfrac{w_j L_j}{\alpha_i} & S = \rho_i \left[b_j + b_j^*, + w_j G_j \right], \\ \psi = \dfrac{w_j \phi_j}{\alpha_i} & S = \rho_i \left[c_j + c_j^* + w_j \dot{\phi}_{\mathrm{b},j} \right], \end{cases} \tag{5.11}$$

with $j = 1, \ldots, N$ is the quadrature node index. Also in this case, it is possible to recover DQMOM formulation as written in Eq. (2.145) at Page 55 by substituting Eq. (5.10) into Eq. (5.7), and DQMOM-FC formulation expressed in Eq. (2.146) at Page 57 by substituting Eq. (5.11) into Eq. (5.7). In order to perform a fair comparison between the different QBMM, it is necessary to adopt the same assumptions everywhere: First-Order Upwind discretization schemes for all the variables and the two-fluid approach (i.e., only one gas phase considered). Moreover, the calculation of the source term of QBMM was performed only in a certain

Table 5.5: Boundary conditions used for two-dimensional CFD simulation

Boundary	BC for gas phase	BC for liquid phase
1	$\alpha = 0.5$ $U = 1.4236$ m s^{-1}	$\alpha = 0.5$ $U = 0.0$ m s^{-1}
2	Free slip wall	No-slip wall
3	Pressure outlet with backflow equal to 1	Pressure outlet

range of gas volume fraction (i.e., $1.0 \times 10^{-4} < \alpha_G < 0.8$), in order to consider bubble collisions only when bubbles are in an adequate number and do not constitute the continuous phase.

The turbulent behavior of the systems was taken into account by means of the $k - \epsilon$ mixture turbulent model indicated in Section 3.2.5. The drag coefficient entering in the interfacial force of the two-fluid model was calculated in terms of the bubble terminal velocity reported in Eq. (3.65) at Page 79, which was assumed to be constant and equal to 20 cm/s. It is important to remark that the mean bubble diameter in Eq. (3.65) is calculated as a function of moments through the definition of Sauter diameter d_{32} reported in Eq. (3.111) at Page 90. Other interfacial forces were neglected in first approximation. Bubble breakage frequency, daughter distribution function, coalescence kernel and efficiency were formulated with models reported in Eqs. (2.55), (2.64), (2.66) and (2.68) at Pages 27 and 30 to 32 respectively (Laakkonen et al., 2006; Petitti et al., 2010), while for the mass transfer coefficient the model of Lamont and Scott (1970) expressed in Eq. (2.48) at Page 25 was implemented.

In Table 5.5 the conditions imposed at boundaries are reported for gas and liquid phases, while in Table 5.6 a scheme of all the performed simulations is reported. The inlet air bubble population was a log-normal distribution as in Section 5.1.3, with parameters calculated assuming a mean diameter equal to 3.7 mm and a standard deviation equal to 15 % of the mean diameter value. The generic-order moment $M_{k,l}$ is calculated by means of the following expression:

$$M_{k,l} = M_{0,0} \left(k_V C_{O_2}\right)^l \exp\left\{(k + 3l)\,\mu + \frac{(k + 3l)^2\,\sigma^2}{2}\right\} \tag{5.12}$$

where μ, σ and $M_{0,0}$ are calculated with Eqs. (5.4) to (5.6) and C_{O_2} is inlet oxygen concentration assumed equal to 8.56 mol/m^3. Weights and weighted nodes of quadrature needed for the inlet conditions of DQMOM/DQMOM-FC simulations can be found applying the CQMOM inversion algorithm described in Section 2.3.3 to the corresponding inlet moment set.

Table 5.6: Summary of the simulations carried out.

QBMM	Quadrature nodes	Mass transfer	Number of scalars
CQMOM	2	No	6
CQMOM	3	No	9
DQMOM	2	No	6
DQMOM-FC	2	No	6
No	-	Yes	2
QMOM	2	Yes	6
QMOM	3	Yes	8
CQMOM	2	Yes	7
CQMOM	3	Yes	10

5.2.4 Results and discussion

CQMOM implementation

As previously said, the CQMOM implementation was tested and verified in order to point out numerical issues. The typical result of a CQMOM simulation is shown in Fig. 5.11, where the contour plots of volume fraction, mean Sauter diameter and some of the transported moments are reported considering a system with only coalescence and breakage with a two-node quadrature.

The physical meaning for most of these quantities is explained in Chapter 4; here it is important to remark that, by means of this approach, the evolution of the multidimensional NDF is tracked in every point of the computational domain. In fact, as shown in Fig. 5.11 the mean Sauter diameter, calculated with Eq. (3.111), changes from point to point into the bubble column as a consequence of coalescence and breakage processes. In order to have this information, six moments have to be transported (i.e., $M_{0,0}$, $M_{1,0}$, $M_{2,0}$, $M_{3,0}$, $M_{0,1}$, $M_{1,1}$) for calculating the two nodes of the quadrature approximation through the inversion algorithm, used in turn to evaluate the source terms of the moments. It is important to remark that the moment inversion and the source term calculation are carried out only when the local gas volume fraction ranges between 1.0×10^{-4} and 0.8, as the description of the disperse phase (i.e., bubbles) with the population balance makes sense only under these conditions. As a consequence, the equations for the tracked moments are solved also above the free liquid surface for stability reasons, but without calculating the source term and setting it to zero. The unphysical contour plot for the moment reported is explained by the fact that all the moments were initialized equal to zero at the initial time. However, what happens above the liquid level does not influence the results in the area of interest, namely the gas-liquid dispersion.

Other important variables to be monitored for verification purposes are the source terms of the moment of order three with respect to size and the source term of the moment of order one with respect to composition, that must be equal to zero, if mass transfer process is not active. As reported in Fig. 5.11, the calculated values for these quantities in all the cells of the domain are near the machine precision as expected. This means that bubble coalescence

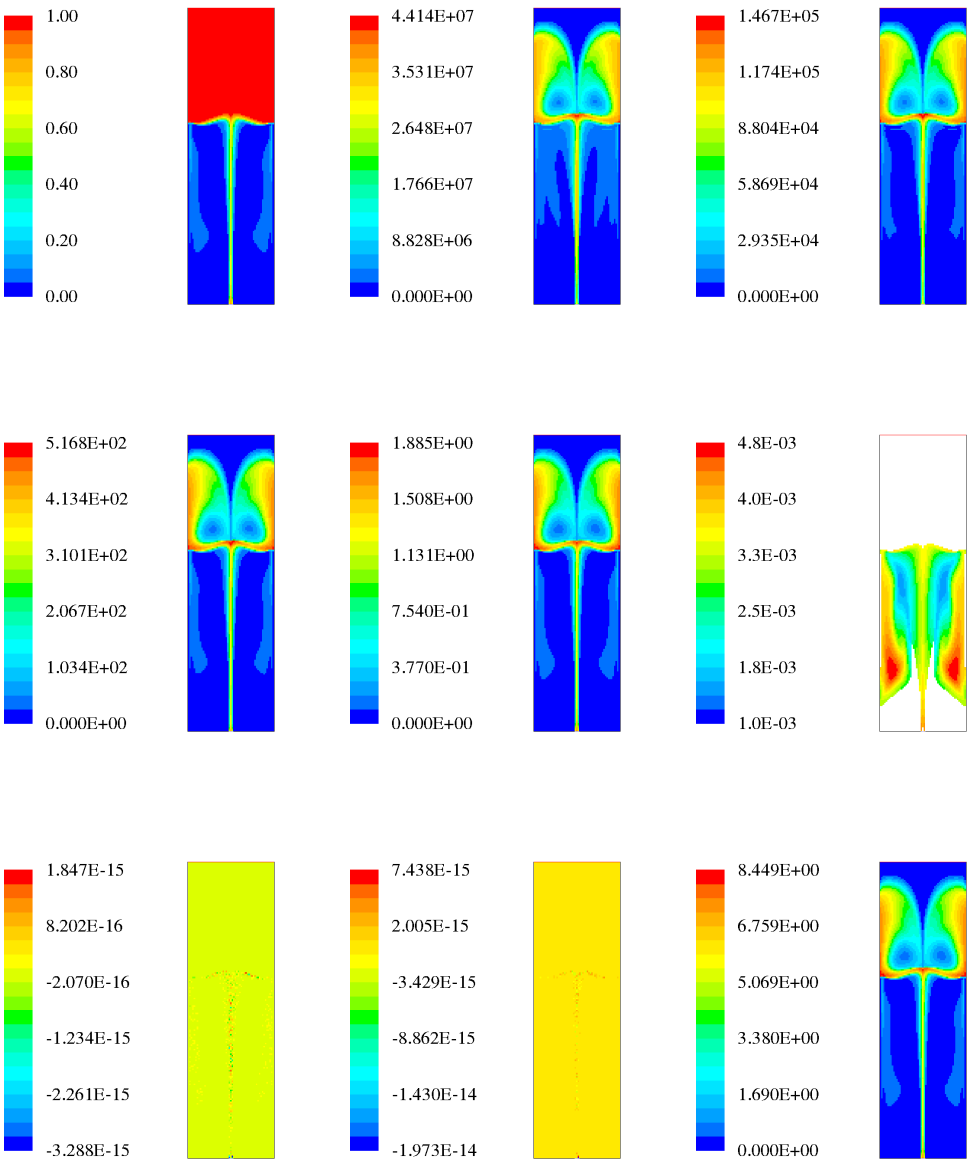

Figure 5.11: From left to right: 1) First row: Profiles of gas volume fraction, $M_{0,0}$, $M_{1,0}$; 2) Second row: $M_{2,0}$, $M_{3,0}$, mean Sauter diameter *sau* (m); 3) Third row: source term of $M_{3,0}$, source term of $M_{0,1}$ and $M_{0,1}$ for the case considering only bubble coalescence and break-up calculated using CQMOM with a two-node quadrature approximation after 15 s. Units of a generic order moment $M_{k,l}$: m^{k-3} mol^{l}.

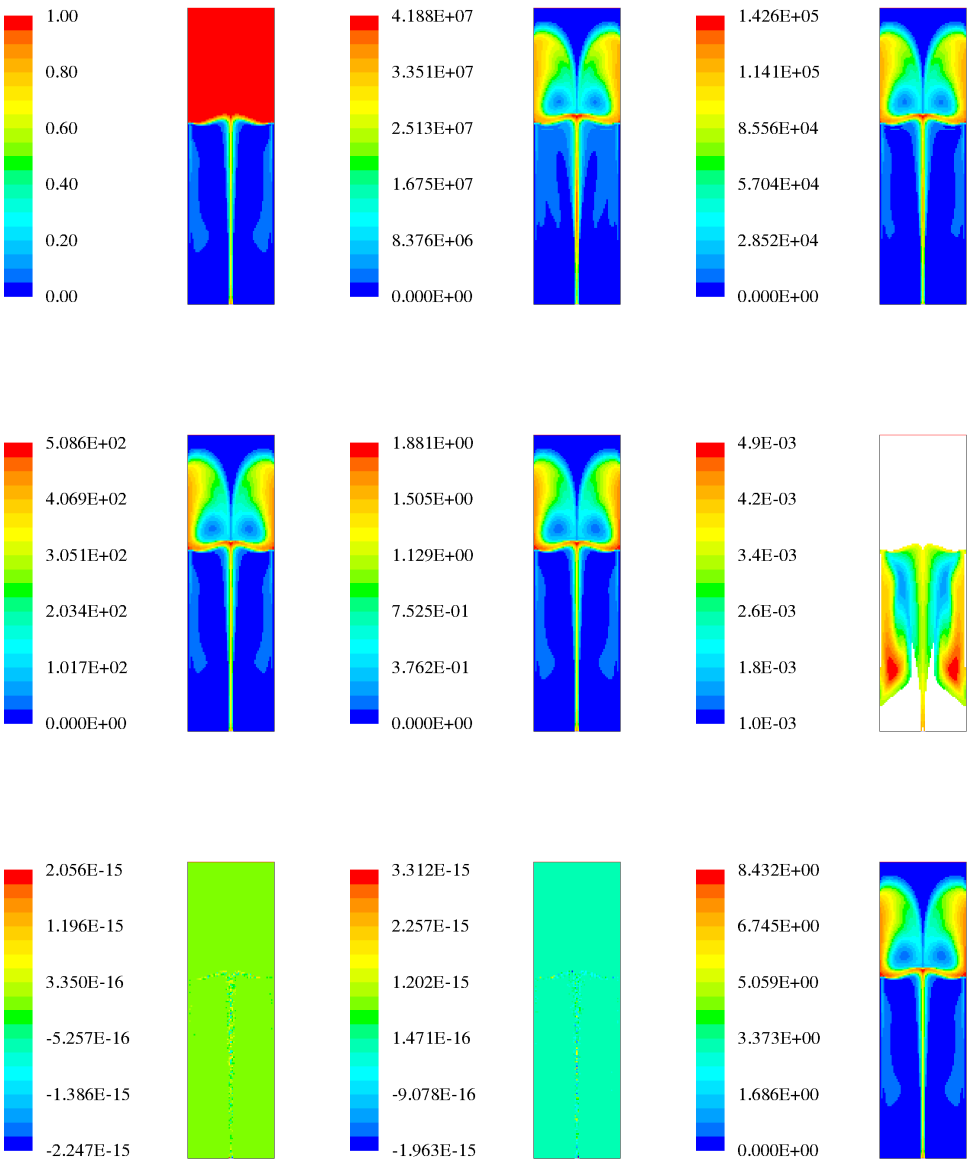

Figure 5.12: From left to right: 1) First row: Profiles of gas volume fraction, $M_{0,0}$, $M_{1,0}$; 2) Second row: $M_{2,0}$, $M_{3,0}$, mean Sauter diameter *sau* (m); 3) Third row: source term of $M_{3,0}$, source term of $M_{0,1}$ and $M_{0,1}$ for the case considering only bubble coalescence and break-up calculated using CQMOM with a three-node quadrature approximation after 15 s. Units of a generic order moment $M_{k,l}$: m^{k-3} mol^{l}.

and breakage do not change $M_{3,0}$ and $M_{0,1}$ maintaining constant the gas holdup and the total number of oxygen moles, as seen in Chapter 4 for simplified systems.

As pointed out in Section 2.3, it is possible to improve the accuracy of the approximation by increasing the number of nodes of the quadrature, namely a larger number of moments must be included into the transported set. In Fig. 5.12 the results obtained considering a three-node quadrature (moment set: $M_{0,0}$, $M_{1,0}$, $M_{2,0}$, $M_{3,0}$, $M_{4,0}$, $M_{5,0}$, $M_{0,1}$, $M_{1,1}$, $M_{2,1}$) are shown. By looking the contour plots, especially the source terms of the moments, similar conclusions can be drawn also in this case.

However, particular attention should be devoted to the gas phase oxygen concentration that will be used for expressing the driving force for mass transfer estimation. It is interesting to compare results obtained with two and three-node quadrature approximations in terms of global oxygen concentration, calculated by means of Eq. (4.1), and in terms of oxygen concentration for each of $i-$th nodes as expressed in Eq. (4.2). This comparison are reported in Fig. 5.13. As explained in Chapter 4, the case with coalescence and breakage is particularly helpful for verification purposes. In fact, since bubbles in this simple case coalesce and break-up in the absence of mass transfer, the global oxygen concentration in the gas phase, shown in Fig. 5.13, has to remain constant and the corresponding contour plot has to give a flat profile since it is the ratio of two conserved quantities. The fact that the mean gas oxygen concentration has the same value also above the free surface is due an assumption used inside the subroutine; this explains why in the other contour plots, the concentration fields are defined only in the disperse phase and are equal to zero in the other zones. As it is possible to see both quadrature approximations with $N = 2$ and $N = 3$ respect this constraint, as the contour plots of the global oxygen concentration in the gas in the case of no mass transfer are completely flat and equal to the inlet values.

Furthermore, also the concentration for each quadrature node should be constant and equal to the inlet value but, as it is possible to see in Fig. 5.13, for the case of two nodes this condition is not respected, showing a non-physical behavior, already detected in the zero-dimensional case (Fig. 4.3), amplified here by the fact that the oxygen concentration for the first internal coordinate is non-physically negative in some points of the domain. This situation in which the moments are correctly predicted (i.e., $M_{3,0}$ and $M_{0,1}$), and therefore their values are realizable, but the quadrature approximation generates reconstructed NDF that samples the phase space in "forbidden" regions, is defined as unrealizable quadrature. This unrealizable reconstructed NDF is due to the fact that a particular moment, $M_{2,1}$, related to the covariance of the distribution must be included into the transported set and must be used to reconstruct the NDF and the quadrature approximation. When this moment is transported and used into the inversion algorithm, as in the case of three-node quadrature, the contour plots of the oxygen concentrations for each node are flat profiles (see second row of Fig. 5.13).

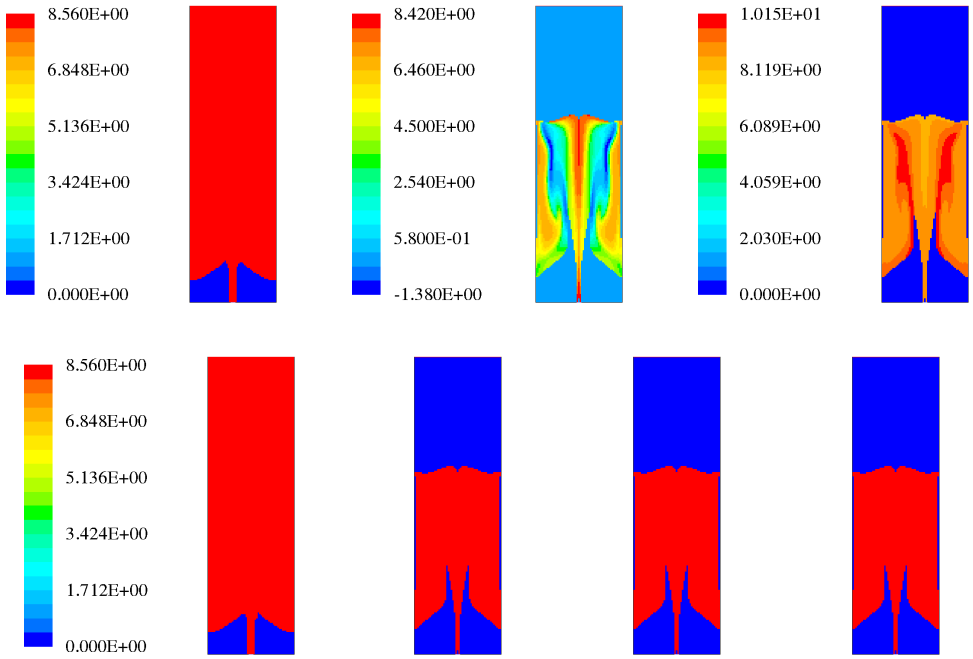

Figure 5.13: First row from left to right: Mean oxygen concentration ($^{mol}/_{m^3}$) in the gas phase and oxygen concentration calculated for the first and second quadrature nodes in the case of coalescence and breakage with a 2 node quadrature after 15 s. In the second row, the same variables for a 3 node quadrature.

DQMOM implementation

Also the implementations of DQMOM and DQMOM-FC were verified, considering only bubble coalescence and breakage, limiting the investigation only to the case of the two-node quadrature . In Fig. 5.14 and Fig. 5.15 are shown the weights and the weighted nodes transported by the methods, mean diameter, mean oxygen concentration and gas volume fraction profiles for the two different QBMM. As it can be clearly seen from the figures, DQMOM does not allow to calculate properly the mean oxygen concentration in the gas phase because, as already seen in the mono-dimensional case Section 4.2, is not capable of preserving the correct evolution of the moment set. It is worth mentioning that these errors are detected in moments $M_{k,l}$ of global order (i.e., $k + l$) equal to or greater than two (Marchisio and Fox, 2005). In fact, moments of global order smaller than two are linear combination of the primitive variables actually transported (i.e., weights and weighted nodes or abscissas), whereas higher-order moments are non-linear combinations of these variables. This means that the original DQMOM is capable of conserving only moments of global order zero and of order one. Moreover, it is possible to say that the unphysical contour plot of the mean oxygen concentration in gas phase, shown in Fig. 5.14, is due to $M_{3,0}$, namely the local volume fraction might be under/overestimated with this method.

On the contrary with DQMOM-FC the moments are properly conserved as the mean oxygen concentration contour plot is able to show. However, it is very important to remark

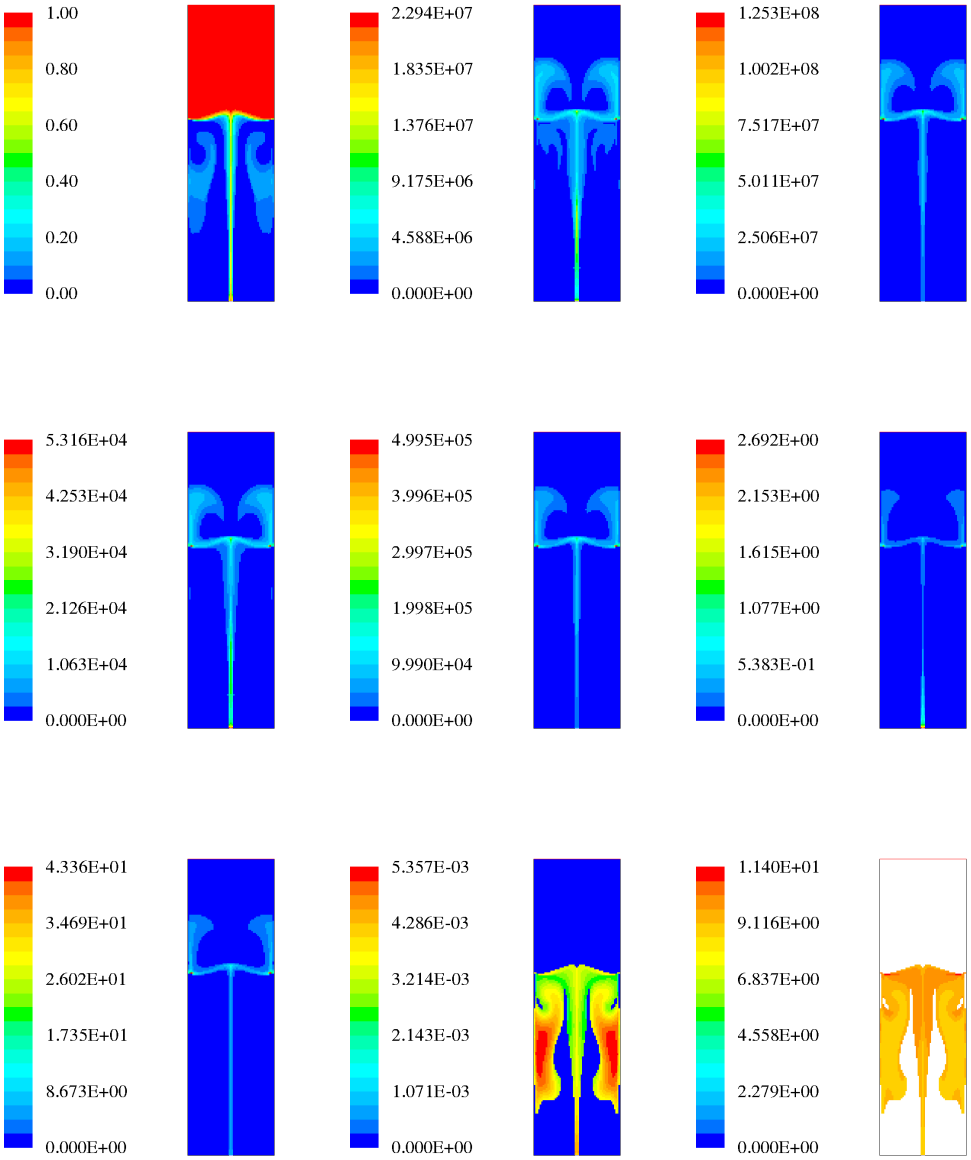

Figure 5.14: From left to right: 1) First row: Profiles of gas volume fraction, w_1 (m^{-3}), w_2 (m^{-3}); 2) Second row: $w_1 L_1$ (m^{-2}), $w_2 L_2$ (m^{-2}), $w_1 \phi_{b,1}$ (mol m^{-3}); 3) Third row: $w_2 \phi_{b,2}$ (mol m^{-3}), mean Sauter diameter d_{32} (m) and mean oxygen concentration ($^{mol}/_{m^3}$) in the gas phase for the case considering only bubble coalescence and break-up calculated using DQMOM with a 2 nodes quadrature approximation after 12 s.

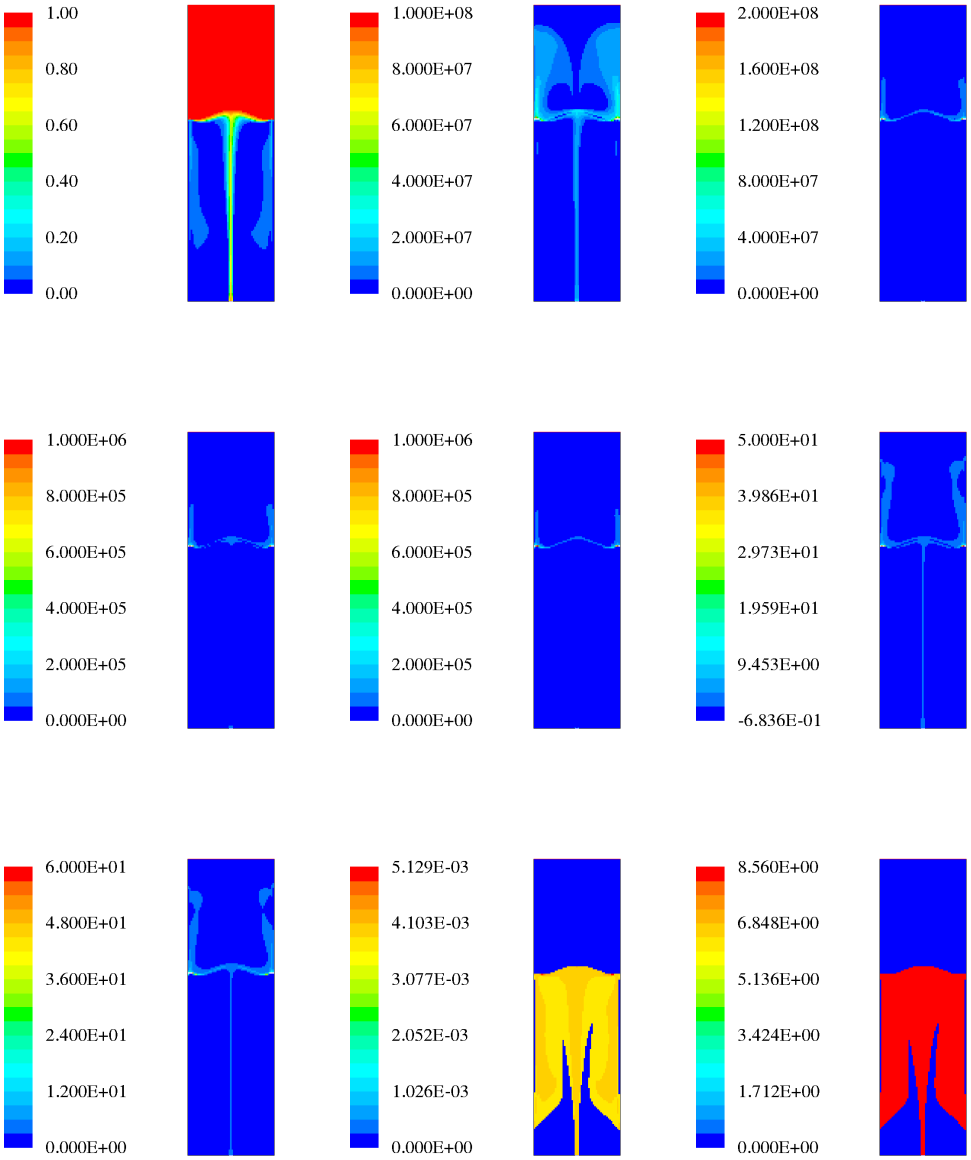

Figure 5.15: From left to right: 1) First row: Profiles of gas volume fraction, w_1 (m^{-3}), w_2 (m^{-3}); 2) Second row: $w_1 L_1$ (m^{-2}), $w_2 L_2$ (m^{-2}), $w_1 \phi_{b,1}$ (mol m^{-3}); 3) Third row: $w_2 \phi_{b,2}$ (mol m^{-3}), mean Sauter diameter d_{32} (m) and mean oxygen concentration ($^{mol}/_{m^3}$) in the gas phase for the case considering only bubble coalescence and break-up calculated using DQMOM-FC with a 2 nodes quadrature approximation after 10.5 s.

that the maximum time step value used to achieve stability with DQMOM-FC was $5.0 \cdot 10^{-5}$ s versus 0.05 s of CQMOM and DQMOM, greatly increasing the total computational time with respect to the other two methods. The main reason of this big difference stays into the fact that DQMOM-FC is capable of conserve moments in space but is only a second order accurate method with respect to time, as pointed out in Section 2.3.5. Furthermore, the numerical implementation of the method is another important aspect: while CQMOM and DQMOM use the stable and optimized built-in user-defined scalar structure with additional source term, DQMOM-FC calculation are carries out by means of an external program specifically created to manage the large set of ODEs that the moment flux calculations involve, without resorting to the optimized FLUENT subroutines. This is due to the impossibility of performing these calculations for the fluxes, as dictated by the DQMOM-FC algorithm, inside FLUENT.

The comparison between different QBMM for this particular test case showed that CQMOM is a stable and efficient algorithm, able to automatically conserve the physical quantities of interest, while DQMOM suffers from the impossibility of conserving all the quantities of interest, unless its fully conservative version is used. This latter seems to cure the problem, but the current implementation in commercial codes is still inadequate to simulate large systems.

Mass transfer test

As reported in Table 5.6 five different types of mass transfer simulation were performed for this particular configuration and, in the absence of experimental data for this system, the results of the different methodologies are compared with each other in Fig. 5.16. The comparison is done for the oxygen saturation curve, namely the time evolution of mean oxygen concentration in the liquid phase. All the curves showed a similar behavior with some differences. It is important to stress here that the simulation without the PBM requires an arbitrary assumption on the mean bubble size and completely neglects the poly-dispersity of gas-phase. Therefore not only the predictions will be different from those of the PBM (and potentially wrong) but they will be highly affected by the value chosen for the constant mean bubble size. For the particular value used here (i.e., $d_b = 3.7$ mm) the predictions reported in Fig. 5.16 over predicts the average liquid oxygen accumulation.

As already pointed out elsewhere in this dissertation, PBM gives the opportunity to take

Table 5.7: Computational time required for 10 seconds of mass transfer simulation.

Method	Quadrature nodes	Simulation time (s)	Ratio
No PBM	-	30692	-
QMOM	2	51648	168.28%
QMOM	3	80062	260.86%
CQMOM	2	79374	258.61%
CQMOM	3	132509	431.74%

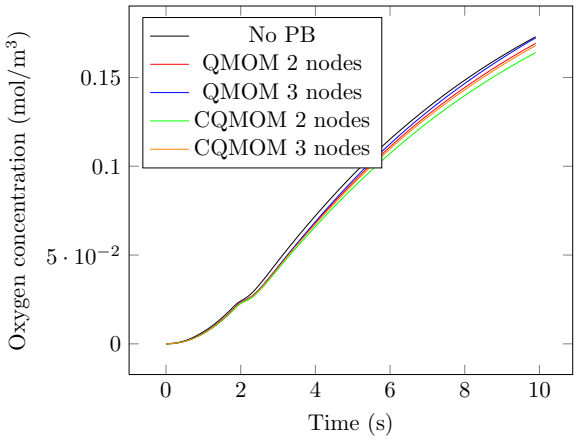

Figure 5.16: Oxygen saturation curve in the liquid phase, calculated with different methodologies.

into account the polydispersity of the system: the choice between monovariate and multivariate is, in general, due to the nature of the problem and to the required accuracy for describing the system under study. In this case, the main difference between monovariate (only size dependent population balance) and bivariate (size-composition dependent population balance) is the capacity to describe not only the interfacial area, but also the driving force of mass transfer. Comparing the predictions in Fig. 5.16 highlights that a higher transfer rate for the monovariate than for the bivariate description, as shown in Fig. 5.16, due to the fact that the monovariate description neglects that smaller bubbles exchange mass faster than larger ones and the concentration of the species transferred tends to decrease more rapidly thereby reducing the global mass transfer coefficient. A preliminary computation time analysis, reported in Table 5.7, demonstrates that the monovariate method is faster than the bivariate one due to the lower number of moments transported. However, the use of a closed commercial code does not allow to optimize certain aspects of the implementation. For example, the assumption of an unique terminal velocity for all the bubbles allows to solve the moment equations only at the end of the time iteration, just after the fluid dynamics calculation: this possibility is excluded by the solver. Therefore an analysis of the computational times will be more significant when it is available an optimized implementation of CQMOM in a open source CFD code.

Fig. 5.16 also shows the effect of increasing the number of quadrature nodes in the description of the bubble population and its impact on the overall oxygen transfer rate. The curves with three nodes, both with QMOM and CQMOM, indicate a faster oxygen absorption due to a better description of the interfacial area. In the case of CQMOM, it is very important to monitor for verification purposes the evolution with the time of the oxygen concentration calculated for each quadrature node in the case of the two and three-node quadrature. In fact, as previously pointed out in absence of mass transfer, oxygen concentrations for two nodes quadrature have non-physical values and, as Fig. 5.17 shows, the mass

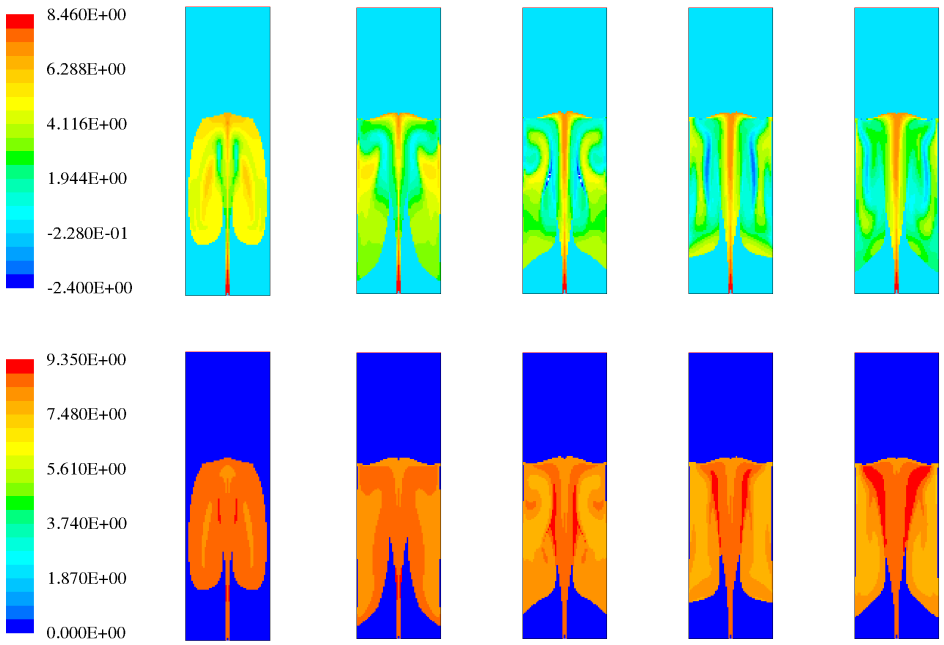

Figure 5.17: Time evolution of oxygen concentration ($^{mol}/_{m^3}$) calculated for first and second quadrature node (first and second rows) in the case of coalescence, breakage and mass transfer after 2, 4, 6, 8 and 10 seconds (left to right) calculated by means of CQMOM with 2 nodes.

transfer tends to amplify this wrong behavior, resulting in time to negative concentrations in some zones of the domain. Otherwise, with a three-node quadrature (Fig. 5.18), the nodes of quadrature approximations representing oxygen concentrations have always acceptable values, i.e., positive and smaller than the inlet values.

5.2.5 Conclusions

In this section, the implementation of different QBMM inside the commercial CFD code FLUENT was discussed and verified in order to point out numerical issues. Although DQMOM and DQMOM-FC are solid methods to treat different multivariate problems, it was demonstrated that, in the case of gas-liquid flows, the former method fails because of the underestimation of the gas volume fraction and the consequently wrong calculation of the average oxygen concentration of the gas phase; while the latter method was implemented by means of an external program without resorting to the optimized user-defined subroutines framework, requiring a very smaller time step compared to the other methods.

CQMOM instead was proved to be stable and ready to be used for the simulation of realistic system for validation purposes. However, also in this case some issues related to the oxygen concentration were found: when only six moments are used for representing the bubble size and composition distribution, the oxygen concentration field calculated for each quadrature node may become nonphysical or unrealizable, because the transported moment set does not include an important higher order moment (i.e., $M_{2,1}$), while the mean oxygen

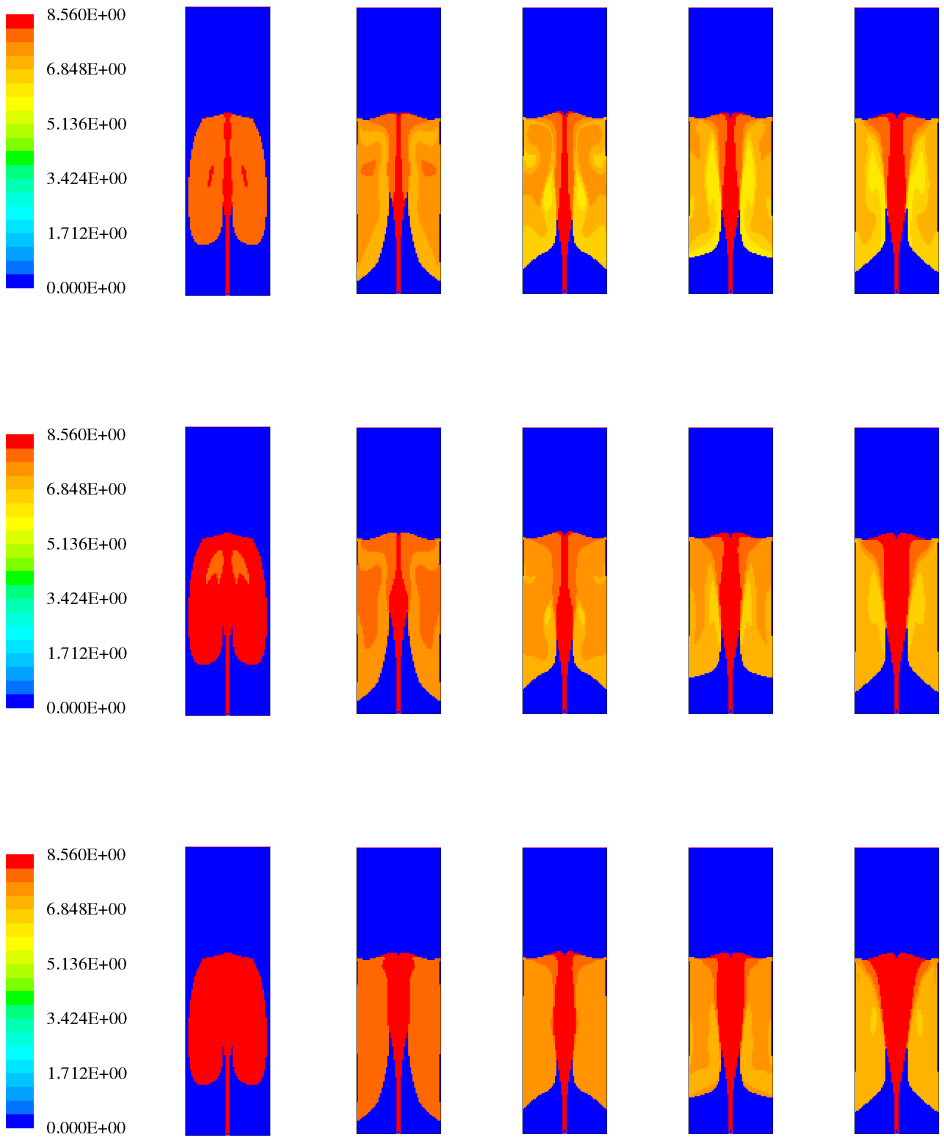

Figure 5.18: Time evolution of oxygen concentration (mol/m^3) calculated for first, second and third quadrature node (first, second and third rows) in the case of coalescence, breakage and mass transfer after 2, 4, 6, 8 and 10 seconds (left to right) calculated by means of CQMOM with 3 nodes.

concentration is properly calculated because of a ratio of conserved moments. When nine moments included in the moment set, namely a three-node quadrature is used, all the oxygen concentrations are correctly placed in phase space. Moreover, this situation also was confirmed when oxygen mass transfer was studied. However, also in the case of three-node quadrature the oxygen concentrations need to be monitored and prevent them from becoming negative with an appropriate correction. In the next section, a possible approach will be presented and discussed.

In conclusion, different approaches in the simulation of mass transfer tests were compared in terms of computational time and the evolution of mean oxygen concentration in the liquid phase. Although the simulation without population balance was proved to be the fastest of all, an important part of the gas liquid physics is completely neglected; by using a monovariate or multivariate approaches to account for the bubble population, a difference in the results is observed, meaning that problem of course affected by the amount of physics considered. The analysis of computational time for the different methodologies showed that the controlling parameter is the total number of variables to be tracked. Nevertheless, this significant difference in computational time may be due to the implementation strategy of the additional equations in the commercial code FLUENT. The optimized CQMOM implementation in a open CFD source code might provide a more significant comparison.

5.3 Mass transfer simulation in a stirred tank reactor

5.3.1 Introduction

CFD modeling of aerated stirred tanks initially focused on single-phase liquid systems, with very simplified two-dimensional approaches (Harvey and Greaves, 1982; Placek et al., 1986; Pericleous and Patel, 1987), where the impeller and the baffles were considered as sources/sink of momentum and the system was modeled assuming an axial-symmetric geometry, in order to give only a qualitative idea of the flow pattern, without resolving its three-dimensional structures. With the increase of computational power, three-dimensional simulations became feasible and were performed (Ranade et al., 1989; Ranade and Joshi, 1990; Kresta and Wood, 1991), but still with the stirrer modeled as a momentum source or by means of ad-hoc boundary conditions; these methods were limited by a difficulty closure process. To overcome this issue, several approaches have been developed such as Sliding Mesh (SM) and Multiple Reference Frame (MRF) (Luo et al., 1994; Tabor et al., 1996; Wechsler et al., 1999). Especially the latter one has become a standard in the simulation of rotating items because it is computationally cheap and can be also used in steady-state descriptions. With this method, the computational domain is divided in two zones: one rotating with the impeller, while the other one fixed in an inertial reference frame. The information between the two zones is exchanged by means of particular boundary conditions. Good agreement with the experimental measurements of flow velocity was obtained by Luo et al. (1994), while Wechsler et al. (1999) compared the results obtained by SM and MFR in

the prediction of trailing vortices, demonstrating that the MFR approach represents a good trade-off between computational costs and accuracy.

As mentioned in Chapter 1, one of the first works accounting for the presence of a Bubble Size Distribution (BSD) in gas-liquid stirred tanks was that of (Bakker and Van den Akker, 1994), who formulated a population balance model, based on the solution of an additional equation for the bubble number density. Good agreement with experimental data for global gas hold-up and mass transfer coefficient was found, with the exception of the impeller discharge zone, where the turbulent dissipation rate reaches the highest values; the same approach was also adopted by other authors (Lane et al., 2002; Kerdouss et al., 2006; Moilanen et al., 2008). In all cases, good predictions were obtained by adjusting some empirical constants introduced in the model; however a proper phenomenological description of the probability and rate of bubbles collisions and bubble-eddy collisions was replaced by a less complicated approach based on the critical Weber number. With this approach, the local bubble size varies from point to point in the domain, but in every single point a non-physical mono-disperse distribution is considered; this is due to the fact that the constitutive equations for only 2 moments of the bubble size distribution, the moment of order zero (i.e., the total number of bubble per unit volume) and the moment of order three with respect to bubble size (i.e., the moment proportional to the gas volume fraction) were solved.

To overcome this issue, it is necessary to solve a complete population balance model (PBM). As already pointed out in Chapter 2, different methods exist for its solution, but only a few of them can be used coupled with the fluid dynamic flow description in a CFD framework. Various Classes Methods (CM) were firstly coupled with CFD for the description of gas-liquid stirred tanks, as in the work of Montante et al. (2008); Kerdouss et al. (2008); the main disadvantage of these methods is represented by the large number of classes (and so the number of equations) to reach a satisfactory accuracy, thus consequently increasing the computational costs, without considering that the extension to multivariate problems for these methods is absolutely not trivial. An attractive way to solve the population balance equation with a low computational cost is represented by the methods of moments (MOM), where the evolution of the bubble population is calculated by transporting only few low order moments of the distribution. As previously mentioned, a particular group of MOM is the Quadrature-based Method of Moments (QBMM), where a quadrature formula is used to approximate the shape of the distribution. QBMM were applied both in the monovariate (QMOM) (Petitti et al., 2010) and multivariate (DQMOM) (Buffo et al., 2012) cases for description of the 194 L baffled gas-liquid stirred tank reactor, experimentally investigated by Laakkonen et al. (2006). Simulations considering bubble coalescence and breakage were carried out and the results were validated with the experimental data available of Bubble Size Distribution, both intended as a mean Sauter diameter profile over all the reactor and as a local BSD in a singular point of the domain. In the work of (Petitti et al., 2012), it is seen as Conditional Quadrature Method of Moments can be successfully used in the context of gas-liquid systems and it is particularly suitable for multivariate problems due to its conservation properties.

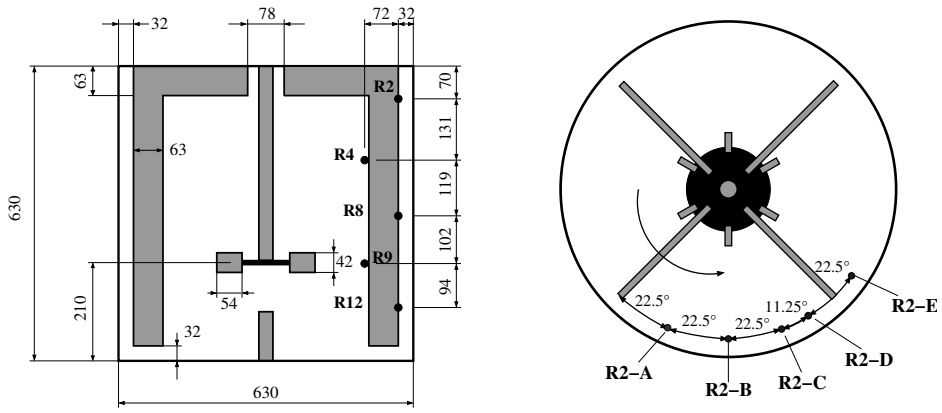

Figure 5.19: Representation of the simulated stirred tank and location of the sample points in which BSD data were measured (Dimensions in mm). (a) Sample points are located on 45°plane between baffles. (b) Plane located at 70 mm below the upper surface.

The results presented in this section are based on the description of the gas-liquid interfacial area with DQMOM (Buffo et al., 2012) and a complete mass transfer simulation performed with CQMOM (Petitti et al., 2012).

5.3.2 Test case description

The configuration studied in this part of the work has been firstly investigated from the experimental and modeling point of view by Laakkonen et al. (2006, 2007). The vessel dimensions and the position of the measurement points are reported in Fig. 5.19. This reactor is a 194 liter tank with four baffles (with a particular configuration with upper extensions, specifically designed for having a flat liquid profile on the free surface), agitated by a standard six-blade Rushton turbine with a circular metal porous sparger with external diameter of 3.3 cm and pores with an average diameter of 15 μm, situated about at 10.5 cm under the impeller.

For this particular air-water system, detailed local measurements of BSD in different points of the reactor and mass transfer rates are available for model validation. The experimental technique used for measuring the bubble size distribution was the Capillary Suction Probe, in which bubbles are forced to pass into capillaries of different sizes and a light sensor takes into account the number of bubbles and their volume. The oxygen adsorption curve in the liquid phase was instead determined by means of an oxygen probe positioned in a specific point of the reactor, having previously fluxed only nitrogen into the system.

5.3.3 Methods and numerical details

The computational grid was created with GAMBIT, whereas simulations were carried out by using FLUENT 12: population balance equations and the drag force formulation in Eq. (3.65) based on bubble terminal velocity were implemented through User-Defined Func-

tions and Subroutines and by solving additional equations for User-Defined Scalars as explained in Section 5.2. Same submodels for bubble coalescence, breakage and massa transfer were used also in this case. The motion of the Rushton turbine was modeled by using the Multiple Reference Frame (MFR) approach (Wechsler et al., 1999), in order to reduce the computational time requested for each simulation. Thanks to geometrical symmetry and periodicity only half of the stirred tank was considered. Approximately 230,000 hexahedrical cells were used to discretize the reactor; further grid refinement did not significantly improve the accuracy of solution. Mass trasfer simulations required an extension of the geometry in the upper part for including also the free surface, in order to conserve the total mass of liquid inside the domain. In the latter case, approximately 150,000 celles were added to the reactor mesh. The simulation results were compared with the experimental data for the different measurement points and for a wide range of operating conditions. The air flow rate ranged from 0.018 to 0.093 volumes of gas per volume of reactor per minute (vvm) and the stirring rate ranged between 155 and 250 rpm, with global hold-up values up to 1.5 %.

As already said before, both DQMOM and CQMOM were applied to the same geometry for different purposes: DQMOM is used to obtain detailed information on the gas-liquid interfacial area and validate the model with the experimental BSD data, whereas CQMOM is used for simulating the mass transfer experiments and comparing the obtained results with the experimental data available. For this reason, in the first case a steady-state approach was used and in the second case a transient situation solved by means of a First-Order Implicit time integrator was considered. It should be remarked that DQMOM implementation is slightly different than the one reported in Section 5.2: here the two nodes the multiphase system are calculated by means of a multifluid approach, considering one continuous liquid phase (water) and two dispersed gaseous phases (air) whose volume fractions, characteristic composition, sizes and velocities are calculated by solving the appropriate equations (see Eq. (3.116)). With CQMOM instead, only two phases (continuous liquid and dispersed gas) were used in the description of the system and ten additional scalar were transported, 9 moments of the multidimensional bubble distribution (i.e., three-node quadrature approximation. Moment set: $M_{0,0}$, $M_{1,0}$, $M_{2,0}$, $M_{3,0}$, $M_{4,0}$, $M_{5,0}$, $M_{0,1}$, $M_{1,1}$, $M_{2,1}$) and the concentration of oxygen in the liquid phase. The main difference between the two methods lies not only in the number of quadrature nodes, but especially in considering a velocity for each node of quadrature in the first case and only one velocity for all the bubbles in the second case. In Section 5.1 it was demonstrated that the latter method does not represent a serious limitation for the flow description in the case in which bubble size ranges between 2-10 mm, because they have approximately the same terminal velocity (as pointed out in Section 3.3.1), although the former approach is formally more rigorous.

Boundary conditions for this system are defined as follows. Non-slip and impermeability boundary conditions at walls are assumed for both the continuous and the dispersed phase. However, as demonstrated by Zhang et al. (2006), the simulations are quite insensitive to the actual wall condition used for the gas phase, because of the low gas volume fraction near the wall. A different approach was used for DQMOM simulations in terms of inlet condition:

the gas enters into the reactor by means of the porous sparger considering a constant inlet velocity of 9.94 m/s has been imposed at the whole section for the two gas phases and the overall gas volume fraction was calculated by matching the relative gassing rate, that varied between 0.018 and 0.093 vvm. With CQMOM, a different approach was adopted in order to reduce the inlet gas velocity magnitude in order to use a proper time step for integration: a volume fraction of 0.5 was assumed at the sparger surface and the gas velocity was calculate to recover the right gas flow rate, as explained in Section 5.1. The liquid velocity components on the gas sparger were assumed equal to zero. The upper surface of the vessel was modeled as a pressure outlet; the condition of backflow changed according to the simulations carried out: in all the cases gas bubbles could exit from the system but, without considering the free surface as done with DQMOM steady state description, the flow that enters into the surface it is composed only by the liquid phase. Whereas with CQMOM, in which the gas-liquid free surface is modeled, the flow that enters into the outlet surface is only composed by gas phase. Although the former approach is not completely satisfying at the theoretical level, this condition is a good compromise between accuracy and ease of solution. Zhang et al. (2006) compared such a simplified approach with a more rigorous simulation in which the gas zone above the free surface is taken into account and did not found relevant differences in the results of the two approaches. In addition, it should be observed that in an aerated stirred tank reactor the flow pattern is largely determined by the motion imposed by the stirrer, and the outlet boundary condition is not able to amend this situation. However, when mass transfer is taken into account, an approach that allows to conserve the total mass of liquid over the entire simulation is strictly required and a more costly geometry from a computational point of view is needed.

The PBM requires to set boundary conditions for the different bubbles groups with DQMOM and for different moments with CQMOM that enter into the system through the sparger. Experimental study of bubble formation at metal porous spargers has been conducted for a water-air system by Kazakis et al. (2008) for similar superficial velocity and mean diameter of pores; as a results of their work, the BSD above the sparger can be modeled as a log-normal distribution with a standard deviation of 0.15 of the mean size, with a mean bubble size ($d_{b,\,inlet}$) calculated by the following correlation:

$$d_{b,\,inlet} = 7,35 \left[\mathrm{We}^{-1,7} \mathrm{Re}^{0,1} \mathrm{Fr}^{1,8} \left(\frac{d_p}{d_s} \right)^{1,7} \right]^{1/5}, \tag{5.13}$$

where the dimensionless numbers of Froude (Fr), Weber (We), Reynolds (Re) are defined

as follows:

$$\mathrm{Fr} = \frac{U_{gs}}{d_s\, g}, \tag{5.14}$$

$$\mathrm{We} = \frac{\rho_c U_{gs}^2 d_s}{\sigma}, \tag{5.15}$$

$$\mathrm{Re} = \frac{\rho_c U_{gs} d_s}{\mu_c}, \tag{5.16}$$

and where U_{gs} is the gas superficial velocity based on sparger area, d_s is the sparger diameter and d_p is the mean pore size. The values of the inlet moments were calculated by means of Eq. (5.12) considering a mean oxygen concentration of 8.56 $\mathrm{mol/m^3}$. The inlet values of weights and nodes of the quadrature approximation of DQMOM were recovered through the CQMOM algorithm Section 2.3.3. Thanks to this procedure the inlet volume fractions for the two different bubble classes (α_1, α_2), their characteristic sizes (L_1, L_2) and their compositions ($\phi_{\mathrm{b},1}$, $\phi_{\mathrm{b},2}$) have been prescribed at the inlet surface of the sparger.

5.3.4 Results and discussion

Bubble size distribution with DQMOM

As previously mentioned, the results reported in this paragraph refer to comparison with experimental data from the work of Laakkonen et al. (2006, 2007); the prediction of gas distribution profiles, global hold-up and power consumption for this particular configuration are out of the scope of this work. For a complete discussion of these topics, see Petitti et al. (2009, 2010), where comparisons of power consumption and global hold-up show a good agreement with experimental data for similar configuration and operating conditions simulated here.

The results of a typical DQMOM simulation coupled with the CFD description are shown in Fig. 5.20. As it has been already said before, only two nodes of the quadrature approximation (i.e., $N = 2$) have been considered for modeling the population of bubbles: these nodes can be thought of as two different groups of bubbles with characteristic volume fractions (α_1, α_2), sizes (L_1, L_2), composition ($\phi_{\mathrm{b},1}$, $\phi_{\mathrm{b},2}$) and velocities ($U_{\mathrm{b},1}$, $U_{\mathrm{b},2}$), which exchange mass and momentum with the continuous liquid phase and interact with each other by means of coalescence and breakage. Through this approach it is possible to track the evolution of the multidimensional NDF in every point of the computational domain.

An example of the comparison between experimental data and modeling predictions for one operating condition is reported in Fig. 5.21, where the physical quantity compared, the mean Sauter diameter d_{32}, has been calculated from the PBM-CFD simulations as reported in Eq. (3.111). As it is seen, weights and nodes calculated directly by resorting to DQMOM properly predict the local value of the mean Sauter Diameter experimentally observed. In general, this model shows a good approximation of the experimental trends under all the operating conditions investigated (see Table 5.8). It is important to point out here that all

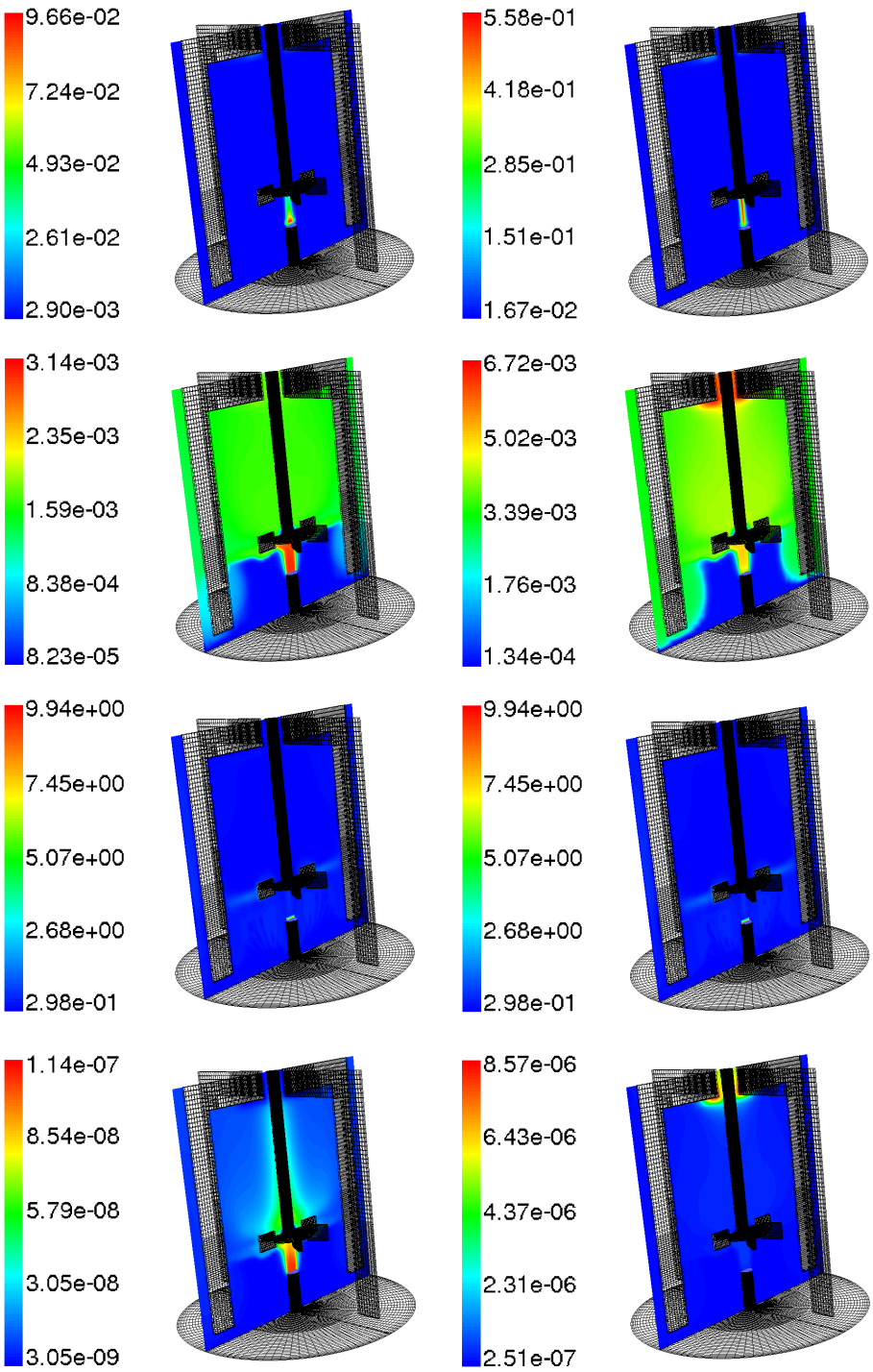

Figure 5.20: Contour plots of gas volume fraction (first row), bubble size (m) (second row), bubble velocity (m s^{-1}) (third row) and bubble composition (mol) (fourth row) for the two nodes of quadrature approximation, in the case of stirring rate of 155 rpm and gassing rate of 0.018 vvm.

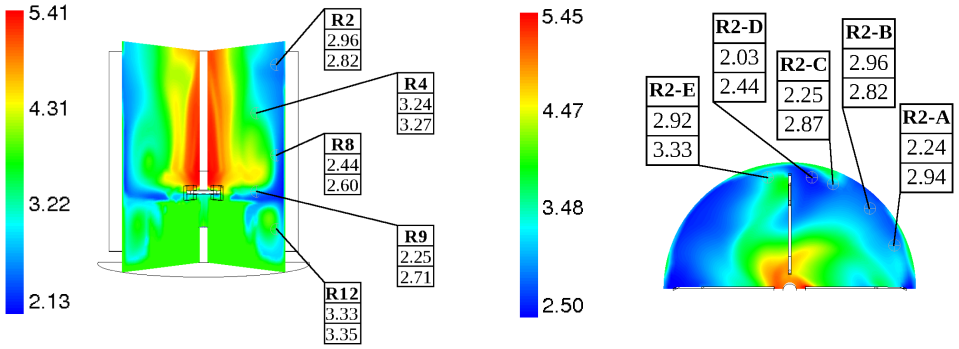

Figure 5.21: Contour plots of the local d_{32} (mm) and comparison between experimental (first row) and predicted values (second row), in the indicated points. Operating condition: 250 rpm, 0.093 vvm. (a) Axial planes at 45°between baffles. (b) Horizontal plane located at 70 mm below the upper surface.

Table 5.8: Experimental and simulated mean Sauter diameter d_{32} (mm) in five different points of the stirred tank.

Stirring rate (rpm)	Gassing rate (vvm)		**R2**	**R4**	**R8**	**R9**	**R12**
155	0.018	Exp.	2.37	2.48	2.29	1.65	3.31
		Sim.	3.10	2.56	2.57	2.63	3.09
220	0.041	Exp.	2.56	3.34	2.57	1.76	3.81
		Sim.	2.66	3.04	2.47	2.50	3.20
220	0.052	Exp.	2.74	2.93	2.17	2.01	3.18
		Sim.	2.45	3.31	2.55	2.65	3.57
250	0.093	Exp.	2.96	3.24	2.44	2.25	3.33
		Sim.	2.82	3.27	2.60	2.71	3.35

the parameters of the PBM-CFD model (especially in the coalescence and breakage kernels) are mainly derived from theory and are not adjusted in this work to fit the experimental data. Therefore the satisfactory agreement with experiments is a remarkable result.

A trend for the mean Sauter diameter (d_{32}) from experiments and simulations in different points of the vessel is clearly observable since d_{32} measured in **R12** is higher than what measured in **R4** and **R8**, whereas d_{32} measured in **R2** is generally bigger than in **R9**. Moreover, the mean Sauter diameter increases when increasing the gas flow rate. In fact, as more bubbles are present in the system, they tend to coalesce more frequently. The values of mean Sauter diameter measured in zone **R2** and **R8** are almost the same and differ only at higher flow rates. In these latter cases, d_{32} measured in **R2** is higher than in **R8**, and, near the upper surface, around the shaft of the impeller and under the baffles, coalescence plays an important role due to bubbles accumulation. The agreement is quite good also in the horizontal plane located 70 mm below the upper surface (see Fig. 5.21): coalescence prevails downwind of baffles (**R2-E**) due to stationary vortices; breakage plays an important role upwind of baffles instead (**R2-D**).

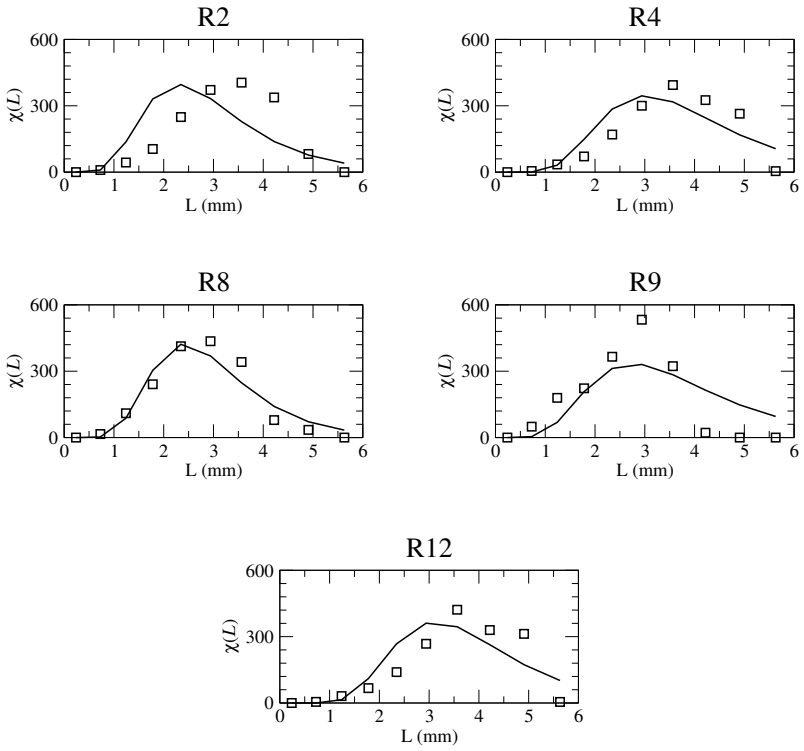

Figure 5.22: Comparison between the local BSD reconstructed from the moments (continuous line) with the experimental one (white squares) in the different measurements points. BSDs are expressed in terms of volume density $\chi(L)$.

As shown in Table 5.8, a better agreement is reached with the increase of the gas flow and stirring rate. In fact, at 155 RPM all the predicted d_{32} are larger than the experimental ones and also the spatial distribution trend into the system is not clearly detected. At 220 RPM, the experimental data are recovered by the PBM-CFD simulation with good accuracy. For this operating condition, the smallest bubbles remain at the proximity of the impeller, as well as the largest ones are confined in the lower zone of the reactor, where a gas recirculation path is present. At the maximum rotational speed considered, 250 RPM, a very good qualitative agreement is recorded: when the gas flow rate is 0.052 vvm, a slight disagreement in plane near the impeller (i.e., $d_{32,\mathbf{R9}} > d_{32,\mathbf{R2}}$) is observed. However, with the increasing of the gas flow rate up to 0.093 vvm, the observed experimental trend is restored, as confirmed by the progressive enhancement of coalescence near the upper surface of the vessel.

The experimental BSDs and the modelled BSDs are compared in Fig. 5.22 for one operating condition. The reconstruction of the predicted BSD was carried out by resorting to the tracked moments, assuming a log-normal distribution. The comparison of the local BSDs was performed in terms of volume density function $\chi(L)$, defined as follows:

$$\chi(L) = \frac{n(L)k_V L^3}{\int_0^\infty n(L)k_V L^3 dL} \tag{5.17}$$

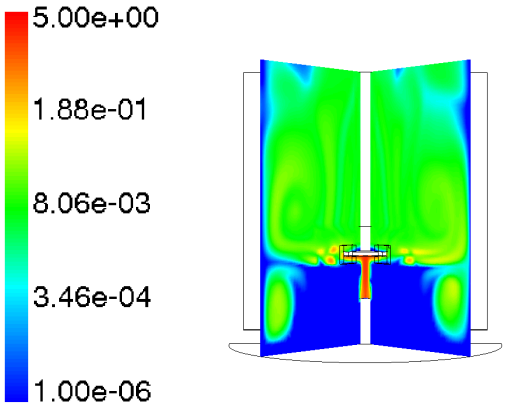

Figure 5.23: Contour plot of the local mass transfer coefficient $k_L a$ (s^{-1}) calculated in the PBM-CFD simulation with DQMOM (logarithmic scale). Operating condition: 250 rpm, 0.093 vvm.

As it is possible to see from the results obtained, the agreement with the experimental data is acceptable, even if the number of nodes of the quadrature approximation is very small.

In Fig. 5.23, the contour plot of the local volumetric mass transfer coefficient for the entire geometry, $k_L a$, calculated by means of the local values of gas fractions and characteristic bubble sizes, is reported. This value differs strongly from point to point into the reactor, because of turbulence induced by the motion of the impeller. In fact, on the impeller plane, bubbles are forced to break-up by high turbulence shear stresses, significantly increasing the number of bubbles and significantly reducing their size. For this reason, in this zone both the interfacial area per unit of volume, a, and the mass transfer coefficient, k_L, reach their maximum values. On the contrary, the portion of volume in the bottom of the vessel not interested by the gas recirculation shows a mass transfer coefficient that tends to zero.

As already remarked in this dissertation (see Sections 4.2 and 5.2), by using DQMOM the moments of bubble distribution with global order greater than two might be not properly conserved during simulations and, consequently some important quantities involved in mass transfer rates calculation could be not correctly defined. For this reason, the same configuration was studied also with CQMOM when the oxygen mass transfer problem is taken into account.

Mass transfer test with CQMOM

In Fig. 5.24, Fig. 5.25 and Fig. 5.26, the contour plot of the local volumetric mass transfer coefficient $k_L a$, the local mass transfer coefficient k_L and the specific volumetric area a for different operating conditions are reported respectively. As already said for Fig. 5.23 in the case of DQMOM, these values change significantly from point to point into the domain, due to turbulence fluctuations induced by the stirrer motion. In this case, it is possible to

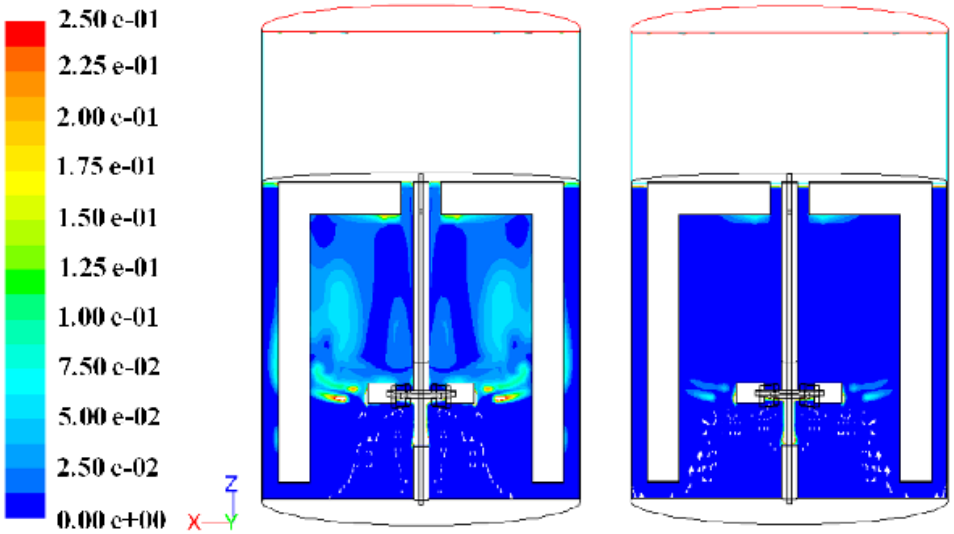

Figure 5.24: Contours of $k_L a$ (1/s) for two different operating conditions investigated after 200 s. Left: 250 rpm and 0.052 vvm. Right: 155 rpm and 0.018 vvm.

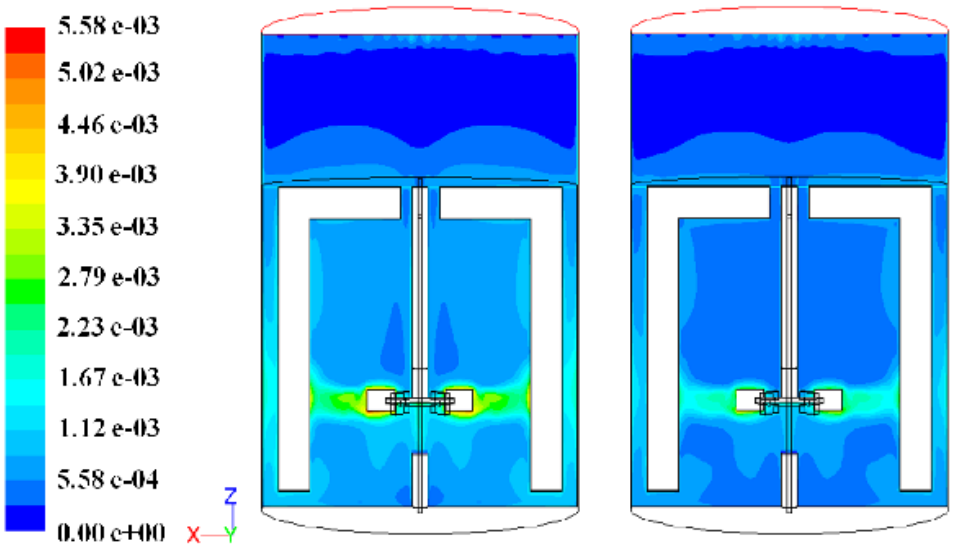

Figure 5.25: Contours of k_L (m/s) for two different operating conditions investigated after 200 s. Left: 250 rpm and 0.052 vvm. Right: 155 rpm and 0.018 vvm.

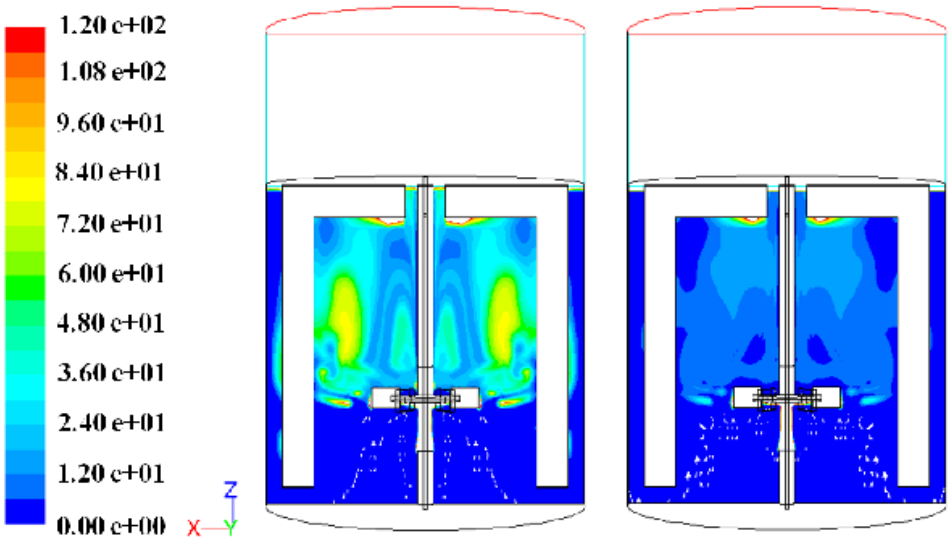

Figure 5.26: Contours of the specific surface area of bubbles (1/m) for two different operating conditions investigated after 200 s. Left: 250 rpm and 0.052 vvm. Right: 155 rpm and 0.018 vvm.

observe the relative importance of the different terms composing the local volumetric mass transfer coefficient $k_L a$ and the effect of higher gas flow rates and stirrer rotational speed: local values of mass transfer coefficient k_L are higher with the increasing of mechanical agitation. The effects of higher gas flow rates and rotational speeds are more evident in Fig. 5.26 for the specific volumetric area a, especially looking the order of magnitude of the reported values. In fact, Fig. 5.24 shows how the impact of bubble size distribution is important when compared to the mass transfer coefficient k_L; on the impeller plane, bubble breakage is the most frequent processes due to higher turbulence shear stresses, and changing the shape of bubble distribution towards smaller sizes. Above this zone, bubble coalescence increases in importance but the significant number of bubbles present has its effect on the $k_L a$ profile. Whereas, the bottom part of the vessel starts to be interested by the gas recirculation only higher gas flow rates and the mass transfer coefficient here tends to zero.

The results of the comparison between the predicted mean Sauter diameter d_{32} with the experimental data available are shown in Fig. 5.27. Also with CQMOM the experimental trend of bubble diameters are qualitative well described: as previously said, smaller bubbles prevail on the horizontal plane seen by the stirrer, whereas larger bubbles are observed in the zones with higher gas hold-up near to the shaft. From the quantitative point of view, it is important remark that d_{32} values are extracted from a snapshot of the system at 200 s; for this reason the reported profile differ from the predictions obtained in a previous work (Petitti et al., 2010) with QMOM without mass transfer, that result in a better agreement with the experimental data.

The typical results of mass transfer tests are reported in Fig. 5.28, where the measurement of oxygen absorption in the liquid phase are compared with the simulation results obtained.

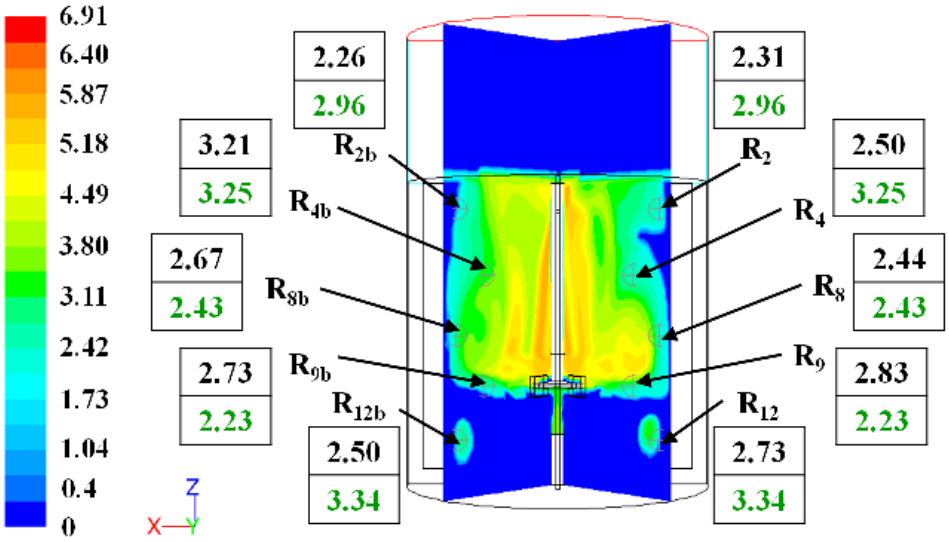

Figure 5.27: Comparison of the predicted d_{32} (mm) with the experimental data (in green), for the case at 250 rpm and 0.093 vvm after 200 s. The value zero is plotted for the d_{32} where the PBM is not solved.

As it is possible to observe from the figure, two different values of the coefficient appearing in Lamont and Scott correlation (see Eq. (2.48)) were tested. The value of 1.13 proposed by Kawase et al. (1987) results in the best agreement with the experimental data, although the quality of the results deteriorates with increasing of gas flow rate and stirring speed. This behavior could be explained with missing dependency in the mass transfer coefficient correlation or, more probably, in a underestimation of the gas-liquid interfacial area probably due to consider all bubbles with spherical shape factor.

Other typical results of mass transfer test are the contour plots of mean oxygen concentration in gas phase and in liquid phase reported in Fig. 5.29. The concentration profile in liquid phase shows another effect of mixing, that keeps a similar flat profile (changing only on magnitude) during all the mass transfer simulation. In fact, as soon as the moles of oxygen pass from the gas phase to the liquid, these are rapidly distribute within the reactor due to the combined effect of viscosity molecular and turbulent viscosity. In gas phase, instead, it is possible to see a deviation from the flat profile, as expected when the mass transfer process occurs. From the figure it is possible to notice a very limited variation of oxygen concentration from point to point into the reactor, justified by the fact that the solubility of oxygen in water liquid is low and there are only few moles of oxygen passing into the liquid phase; most of them comes out from the upper part of the reactor.

5.3.5 Conclusions

In this part of the work, the results obtained with a multidimensional PBM approach for the simulation of an aerated stirred tank reactor were presented and discussed. Two different

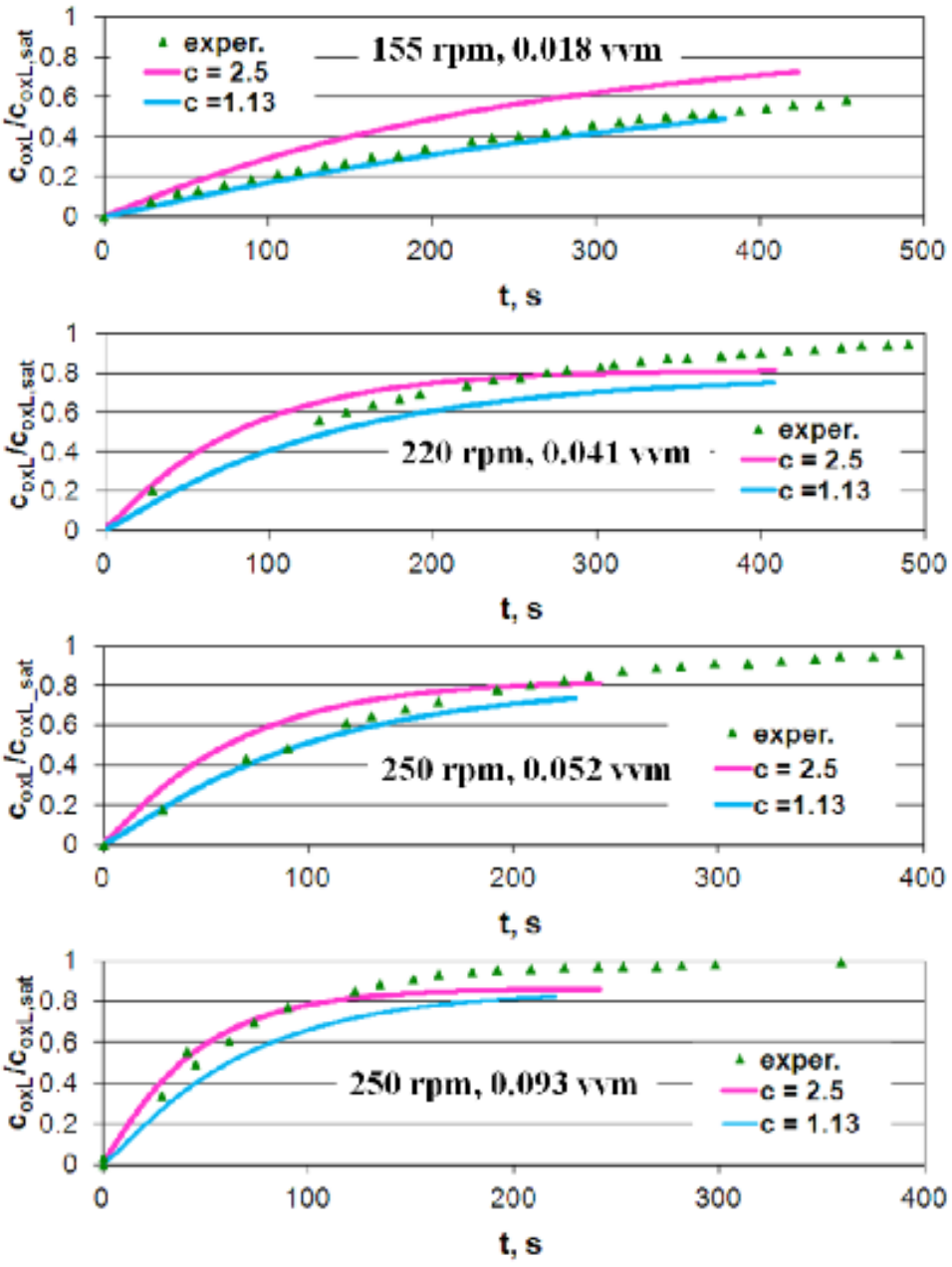

Figure 5.28: Comparison of the predicted temporal evolution of the dimensionless oxygen concentration in the liquid with the experimental data for the operating conditions investigated and for different constant values of Lamont and Scott k_L correlation.

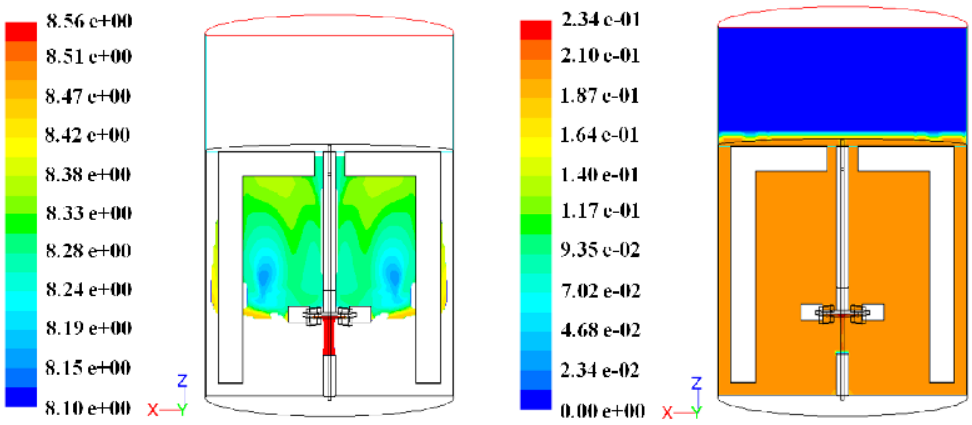

Figure 5.29: Contours of oxygen concentration (mol/m^3) at 250 rpm and 0.052 vvm after 200 s. Left: Concentration in the gas phase. Right: Concentration in the liquid phase.

QBMM were coupled to the commercial CFD code FLUENT to predict the evolution of the gas-liquid system for a real stirred reactor, for which experimental data concerning local BSD and mass transfer rate are available (Laakkonen et al., 2006). Results of DQMOM predictions with two quadrature nodes showed that bubble size distribution and mean Sauter diameter predictions are in qualitative and quantitative agreement with experiments, in spite of the intrinsic non-conservative approach of the method.

As far as mass transfer was investigated to reproduce the experimental oxygen absorption curve in liquid phase, CQMOM was successfully employed. With this method, it is possible to accurately track the evolution of the bubble distribution both in terms of size and composition. The mean Sauter diameter profiles show also with this method a satisfactory agreement with the experimental data available. Moreover, a fitting procedure relating to the coefficient appearing in Lamont and Scott k_L correlation was carried out, showing that the value proposed by Kawase et al. (1987) gives a satisfactory agreement when the predicted absorption curves are compared with the experiments, especially at lower stirring speeds and gassing rates.

References

Bakker, A., Van den Akker, H., 1994. Gas-liquid contacting with axial flow impellers. Chemical Engineering Research and Design 72, 573–582.

Becker, S., De Bie, H., Sweeney, J., 1999. Dynamic flow behaviour in bubble columns. Chemical Engineering Science 54, 4929–4935.

Becker, S., Sokolichin, A., Eigenberger, G., 1994. Gas-liquid flow in bubble columns and loop reactors: Part II. comparison of detailed experiments and flow simulations. Chemical Engineering Science 49, 5747–5762.

Borchers, O., Busch, C., Sokolichin, A., Eigenberger, G., 1999. Applicability of the standard k-ε turbulence model to the dynamic simulation of bubble columns. part II: comparison of detailed experiments and flow simulations. Chemical Engineering Science 54, 5927–5935.

Buffo, A., Vanni, M., Marchisio, D., 2012. Multidimensional population balance model for the simulation of turbulent gas–liquid systems in stirred tank reactors. Chemical Engineering Science 70, 31–44.

Buffo, A., Vanni, M., Marchisio, D., Fox, R.O., 2013. Multivariate quadrature-based moments methods for turbulent polydisperse gas-liquid systems. International Journal of Multiphase Flow 50, 41–57.

Buwa, V.V., Deo, D.S., Ranade, V.V., 2006. Eulerian-lagrangian simulations of unsteady gas-liquid flows in bubble columns. International Journal of Multiphase Flow 32, 864–885.

Buwa, V.V., Ranade, V.V., 2002. Dynamics of gas-liquid flow in a rectangular bubble column: experiments and single/multi-group CFD simulations. Chemical Engineering Science 57, 4715–4736.

Cachaza Gianzo, E.M., 2011. Hydrodynamics and mass transfer effects in bubble columns. Ph. D. Thesis. Universidad de Salamanca. Salamanca, Spain.

Calderbank, P.H., 1958. Physical rate processes in industrial fermentation. part i.: the interfacial area in gas–liquid contacting with mechanical agitation. Transaction of the Institution of Chemical Engineers 36, 443—463.

Deen, N., Solberg, T., Hjertager, B., 2001. Large eddy simulation of the gas-liquid flow in a square cross-sectioned bubble column. Chemical Engineering Science 56, 6341–6349.

Diaz, M.E., Iranzo, A., Cuadra, D., Barbero, R., Montes, F.J., Galan, M.A., 2008a. Numerical simulation of the gas-liquid flow in a laboratory scale bubble column influence of bubble size distribution and non-drag forces. Chemical Engineering Journal 139, 363–379.

Diaz, M.E., Montes, F.J., Galan, M.A., 2008b. Experimental study of the transition between unsteady flow regimes in a partially aerated two-dimensional bubble column. Chemical Engineering and Processing 47, 1867–1876.

Drahoš, J., Zahradník, J., Punčochář, M., Fialová, M., Bradka, F., 1991. Effect of operating conditions on the characteristics of pressure fluctuations in a bubble column. Chemical Engineering and Processing 29, 107–115.

Geary, N.W., Rice, R.G., 1991. Bubble size prediction for rigid and flexible spargers. American Institute of Chemical Engineering Journal 37, 161–168.

Harvey, P.S., Greaves, M., 1982. Turbulent flow in an agitated vessel. i. predictive model. Transaction of the Institution of Chemical Engineers 60, 195–210.

Kawase, Y., Halard, B., Moo-Young, M., 1987. Theoretical prediction of volumetric mass transfer coefficients in bubble columns for newtonian and non-newtonian fluids. Chemical Engineering Science 42, 1609–1617.

Kazakis, N., Mouza, A., Paras, S., 2008. Experimental study of bubble formation at metal porous spargers: Effect of liquid properties and sparger characteristics on the initial bubble size distribution. Chemical Engineering Journal 137, 265–281.

Kerdouss, F., Bannari, A., Proulx, P., 2006. CFD modeling of gas dispersion and bubble size in a double turbine stirred tank. Chemical Engineering Science 61, 3313–3322.

Kerdouss, F., Bannari, A., Proulx, P., Bannari, R., Skrga, M., Labrecque, Y., 2008. Two-phase mass transfer coefficient prediction in stirred vessel with a CFD model. Computers and Chemical Engineering 32, 1943–1955.

Kresta, S.M., Wood, P.E., 1991. Prediction of the three-dimensional turbulent flow in stirred tanks. American Institute of Chemical Engineering Journal 37, 448–460.

Laakkonen, M., Alopaeus, V., Aittamaa, J., 2006. Validation of bubble breakage, coalescence and mass transfer models for gas–liquid dispersion in agitated vessel. Chemical Engineering Science 61, 218–228.

Laakkonen, M., Moilanen, P., Alopaeus, V., Aittamaa, J., 2007. Modelling local bubble size distributions in agitated vessels. Chemical Engineering Science 62, 721–740.

Lamont, J.C., Scott, D.S., 1970. An eddy cell model of mass transfer into the surface of a turbulent liquid. American Institute of Chemical Engineering Journal 16, 513–519.

Lane, G., Schwarz, M., Evans, G., 2002. Predicting gas-liquid flow in a mechanically stirred tank. Applied Mathematical Modelling 26, 223–235.

Letzel, H., Schouten, J., Krishna, R., Van den Bleek, C., 1997. Characterization of regimes and regime transitions in bubble columns by chaos analysis of pressure signals. Chemical Engineering Science 52, 4447–4459.

Lin, T.J., Reese, J., Hong, T., Fan, L.S., 1996. Quantitative analysis and computation of two-dimensional bubble columns. American Institute of Chemical Engineering Journal 42, 301–318.

Luo, J.Y., Issa, R., Grosman, A., 1994. Prediction of impeller induced flows in mixing vessels using multiple frames of reference. Institution of Chemical Engineers Symposium Series 136, 549–556.

Marchisio, D.L., Fox, R.O., 2005. Solution of population balance equations using the direct quadrature method of moments. Journal of Aerosol Science 36, 43–73.

Moilanen, P., Laakkonen, M., Visuri, O., Alopaeus, V., Aittamaa, J., 2008. Modelling mass transfer in an aerated 0.2 m^3 vessel agitated by rushton, phasejet and combijet impellers. Chemical Engineering Journal 142, 95–108.

Montante, G., Horn, D., Paglianti, A., 2008. Gas-liquid flow and bubble size distribution in stirred tanks. Chemical Engineering Science 63, 2107–2118.

Montante, G., Paglianti, A., Magelli, F., 2007. Experimental analysis and computational modelling of gas - liquid stirred vessels. Chemical Engineering Research and Design 85, 647–653.

Mudde, R., Simonin, O., 1999. Two- and three-dimensional simulations of a bubble plume using a two-fluid model. Chemical Engineering Science 54, 5061–5069.

Pericleous, K., Patel, M., 1987. Modelling of tangential and axial agitators in chemical reactors. PCH. Physicochemical hydrodynamics 8, 105–123.

Petitti, M., Marchisio, D., Vanni, M., Baldi, G., Mancini, N., Podenzani, F., 2009. Effect of drag modeling on the prediction of critical regime transitions in agitated gas-liquid reactors with bubble size distribution modeling. Multiphase Science and Technology 21, 95–106.

Petitti, M., Nasuti, A., Marchisio, D.L., Vanni, M., Baldi, G., Mancini, N., Podenzani, F., 2010. Bubble size distribution modeling in stirred gas–liquid reactors with QMOM augmented by a new correction algorithm. American Institute of Chemical Engineering Journal 56, 36–53.

Petitti, M., Vanni, M., Marchisio, D., Buffo, A., Podenzani, F., 2012. Application of the conditional quadrature method of moments for the simulation of coalescence, breakup and mass transfer in gas-liquid stirred tanks, in: Proceedings of 14th European Conference on Mixing, pp. 371–376.

Pfleger, D., Becker, S., 2001. Modelling and simulation of the dynamic flow behaviour in a bubble column. Chemical Engineering Science 56, 1737–1747.

Pfleger, D., Gomes, S., Gilbert, N., Wagner, H.G., 1999. Hydrodynamic simulations of laboratory scale bubble columns fundamental studies of the eulerian-eulerian modelling approach. Chemical Engineering Science 54, 5091–5099.

Placek, J., Tavlarides, L., Smith, G., Fort, I., 1986. Turbulent flow in stirred tanks. II. a two-scale model of turbulence. American Institute of Chemical Engineering Journal 31, 1113–1120.

Ranade, V., Joshi, J., 1990. Flow generated by a disc turbine. part II. mathematical modelling and comparison with experimental data. Chemical Engineering Research and Design 68, 34–50.

Ranade, V., Joshi, J., Marathe, A., 1989. Flow generated by pitched blade turbines II: simulation using k-e model. Chemical Engineering Communications 81 , 1989, 225–248.

Ranade, V.V., 2002. Computational Flow Modeling for Chemical Reactor Engineering. Academic Press, San Diego (CA), USA.

Ruzicka, M., Zahradník, J., Drahoš, J., Thomas, N., 2001. Homogeneous-heterogeneous regime transition in bubble columns. Chemical Engineering Science 56, 4609–4626.

Sokolichin, A., Eigenberger, G., 1999. Applicability of the standard k-ε turbulence model to the dynamic simulation of bubble columns: Part i. detailed numerical simulations. Chemical Engineering Science 54, 2273–2284.

Tabor, G., Gosman, A., Issa, R., 1996. Numerical simulation of the flow in a mixing vessel stirred by a rushton turbine, in: Institution of Chemical Engineers Symposium Series, pp. 25–34.

Wechsler, K., Breuer, M., Durst, F., 1999. Steady and unsteady computations of turbulent flows induced by a 4/45° pitched-blade impeller. Journal of Fluids Engineering, Transactions of the ASME 121, 318–329.

Zahradník, J., Fialová, M., Růžička, M., Drahos, J., Kaštánek, F., Thomas, N., 1997. Duality of the gas-liquid flow regimes in bubble column reactors. Chemical Engineering Science 52, 3811–3826.

Zhang, D., 2007. Eulerian modeling of reactive gas-liquid flow in a bubble column. Ph. D. Thesis. University of Twente. Twente, the Netherlands.

Zhang, D., Deen, N., Kuipers, J., 2006. Numerical simulation of the dynamic flow behavior in a bubble column: A study of closures for turbulence and interface forces. Chemical Engineering Science 61, 7593–7608.

Chapter 6

Conclusions

In this dissertation, various aspects related to the formulation and the solution of the Population Balance Models (PBM) for the simulation of mass transfer in gas-liquid systems are discussed. In Chapter 2 the derivation of the PBM for gas-liquid systems is reported; this modeling framework is however general enough to be applied to any dispersed multiphase system. Two different formulations are proposed: a monovariate PBM, in which the state of the population of the dispersed gaseous phase (i.e. bubbles) is described by means of one internal coordinate, namely bubble size, and a bivariate PBM, in which not only bubble size, but also bubble composition is used to characterize the distribution. Moreover, an overview of the common phenomenological models for bubble collision and mass transfer is included; however only those representing an acceptable good trade off between accuracy and ease of implementation are actually used in the simulations. Chapter 2 ends with the description of a very promising class of approximate solution methods for PBM, namely the Quadrature-based Moment Methods (QBMM), and with the application of QBMM to the problem investigated in this thesis.

Chapter 3 introduces the governing equations for the fluid dynamics of a gas-liquid system, obtained by starting from the local and instantaneous balance equations for each phase and by applying the proper averaging technique, resulting in the popular multifluid model. Appropriate submodels for the closure of the governing equations are here provided, with particular attention to the modeling of interfacial forces and turbulence. Since all this is necessary to describe and numerically calculate the motion of bubbles in a spatially inhomogeneous system through Finite-Volume schemes, some aspects related to the coupling with the PBM approach are discussed.

In Chapter 4, the methodology presented in the previous chapters is applied to the description of simplified systems: first the predictions given by QBMM are compared with Monte Carlo simulations of bubble coalescence, breakage, injection/extraction and mass transfer for a zero-dimensional system. The results of this comparison (by using CQMOM and DQMOM) show that a good accuracy is achieved by using a reduced number of quadrature nodes ($N \leq 4$) and therefore solving a very limited number of equations. However, some issues related to mass transfer are detected: in this case it is shown that as at least three

quadrature nodes are needed to properly calculate the bubble concentration of the chemical species on interest. Furthermore, mass transfer tests show that the bivariate formulation helps to better describe the physics of the system. In fact, only considering both the distributions versus bubble size and bubble composition the evolution of the system is properly simulated. This aspect becomes of fundamental importance in the case of fast chemical reactions, where a variance with respect to bubble composition may be generated and sustained. In this particular case, CQMOM performs slightly better than DQMOM due to its quadrature assumption, but further studies are needed to point out the actual usefulness of this approach to chemical reactions.

When the advection in physical space is taken into account, even in a very simplified mono-dimensional system, the original DQMOM formulation, written in terms of primitive quantities, may suffer from the incapability of properly conserving important conservative quantities of bubble population, as the moments of the distribution. These cases arise when, for example, the turbulent transport of bubble momentum is negligible compared to advection and the dominant diffusion mechanism is numerical diffusion. In this cases a conservative formulation, DQMOM-FC is tested and proven to be very efficient in preserving the correct evolution in space and time of the moments of the bubble distribution. Results also show that CQMOM is a very stable and efficient algorithm, in fact by transporting the moments, it automatically conserves the physical quantities of interest. The inversion algorithm was found to be very stable and moments always invertible as long as first-order upwind was used as spatial discretization scheme.

In Chapter 5 QBMM are coupled to different CFD codes to predict the evolution of the dispersed gaseous phase for different realistic gas-liquid systems. As mass transfer is an non-stationary process that takes place for long time periods, particular attention is paid to the QBMM implementation in order to reduce the computational costs; this is, for example, the reason why a reduced number of quadrature nodes is used. Results concerning averaged quantities of the distribution show that even with only two quadrature nodes the PBM-CFD simulations are in qualitative and quantitative agreement with experiments. However, the issue related to mass transfer is still present and the obtained results confirm that a three quadrature nodes should be used. Furthermore, the results collected in Chapter 5 show the impact of the details of the numerical implementation of QBMM in CFD codes on stability and on the final computational costs. The commercial CFD code used (i.e., FLUENT) provides an environment to implement additional equations, that lacks flexibility, resulting in a poor management of the computing resources available. In this sense, the use of open source codes, here used to describe a monovariate bubble distribution, is found to be very promising and certainly will be extended to multivariate cases in the future.

Among different QBMM, it was observed that the use of solution methods based on conservative quantities (i.e., QMOM and CQMOM) is recommended, since for different reasons DQMOM and DQMOM-FC are not suitable for simulate mass transfer in spatially inhomogeneous systems. The former method fails because of the underestimation of the gas volume fraction and the consequent wrong calculation of the means oxygen concentration in

the gas phase; while the latter method may require a very short time step compared, making the overall computational costs unacceptable.

Eventually the simulation of real gas-liquid systems (i.e., a stirred tank reactor and a bubble column), for which experimental data concerning the local bubble size distribution (BSD) and mass transfer are performed. The results show how the proposed methodology is effective: in general very good agreement with the experimental data is observed for all the operating conditions investigated, without a tedious tuning of model parameters.

In conclusion, in this dissertation the coupled QBMM and CFD methodologies is proven to be applied to the simulation of mass transfer in real gas-liquid systems. The future possible developments on this topic may be the inclusion of thermal effects and the presence of chemical reactions.